Searching for Heavy Higgs Bosons Using Events with Leptons and Missing Transverse Momentum with the ATLAS Detector

vorgelegt von
Fang-Ying Tsai
aus Taichung, Taiwan

zur Erlangung des Doktorgrades
an der Fakultät für Mathematik, Informatik und Naturwissenschaften
Fachbereich Physik der Universität Hamburg

Hamburg
2020

Eidesstattliche Erklärung

Hiermit versichere ich an Eides statt, die vorliegende Dissertationsschrift selbst verfasst und keine anderen als die angegebenen Hilfsmittel und Quellen benutzt zu haben. Die eingereichte schriftliche Fassung entspricht der auf dem elektronischen Speichermedium. Die Dissertation wurde in der vorgelegten oder einer ähnlichen Form nicht schon einmal in einem früheren Promotionsverfahren angenommen oder als ungenügend beurteilt.

Hamburg, den 30. Juli 2020.

Fang-Ying Tsai

Gutachter der Dissertation	Dr. Sarah Heim
	Prof. Dr. Peter Schleper
Zusammensetzung der Prüfungskommission	Dr. Sarah Heim
	Prof. Dr. Peter Schleper
	Prof. Dr. Kerstin Tackmann
	Prof. Dr. Gudrid Moortgat-Pick
	Prof. Dr. Dieter Horns
Vorsitzender des Prüfungsausschusses	Prof. Dr. Dieter Horns
Datum der Disputation	26 Oktober 2020
Vorsitzender Fach-Promotionsausschusses PHYSIK	Prof. Dr. Günter Sigl
Leiter des Fachbereichs PHYSIK	Prof. Dr. Wolfgang Hansen
Dekan der MIN-Fakultät	Prof. Dr. Heinrich Graener

Acknowledgements

Foremost, I would like to express my sincere thankfulness to my research advisor, Dr. Sarah Heim, for continuously inspiring and supporting me during my years as a graduate student at DESY. Thank you for guiding me throughout my research and teaching me how to present work as clearly as possible.

Thank you to Dr. Doug Schaefer for helping and giving me the opportunity to work on the $E_{\mathrm{T}}^{\mathrm{miss}}$ in ATLAS. The hours spent working with you are countless, but it was always a pleasure. In addition, I would also like to thank all the convenors for every opportunity and your patience: Dr. Emma Tolley, Dr. Jeanette Lorenz, Dr. Maximilian Swiatlowski, and Prof. David Miller. A big thanks also to the entire $ll\nu\nu$ analysis team and all the people at CERN and DESY who worked with me to make my Ph.D. project a reality.

I would like to thank all my friends who reviewed this thesis; Dr. Stefan Richter, Dr. Kurt Brendlinger, Dr. Eric Takasugi, Dr. Ted Liang, Hamish Teagle, Emily Thompson, Jordi Sabater, Toni Mäkelä, Dr. Yee Chinn Yap, Dr. Antonio Vagnerini, and Doug. I would especially like to thank Dr. William Leight for the detailed comments and Prof. Yuhsin Tsai for guidance on the chapter that covers theory.

Thanks to all my colleagues and friends at DESY; Pieter, Romain, Ivy, Max, Vincent, Matteo, Jihyun, Roger, Federico, Eloisa, Artem, Alessandro B, Alessandro G, Surabhi, Dario, Sonia, Marco, Yu-Heng, Jose, Nils, Ruchi, Jan, Judith, Xingguo, Marianna, Yi, Filip, Janik, Jonas, Alicia, Alessia, Pablo, David, and including friends who read my thesis. I will leave Hamburg with tears in my eyes.

I am grateful to my pastors and friends from my home church and churches in Hamburg for their prayers and caring. I will never forget that more than a hundred people's valuable prayers were sent from Taiwan. I will also never forget my friends, James Liang and his family, who took care of me when I just arrived in Hamburg, and Drew Barham, who strengthened my faith and brought me so many joys.

Last but not least, I would like to thank my parents and my sister for their love, sacrifices, and continued support to complete this research work.

Abstract

An additional heavy Higgs boson is predicted by many models, such as the two-Higgs-doublet model (2HDM). This thesis presents a data-driven method to estimate the dominant ZZ background in the search for the decay of such a heavy scalar particle to a pair of Z bosons in the $ZZ \to \ell^+\ell^-\nu\bar{\nu}$ (l = electrons, muons, ν = neutrinos) final state. Currently, the $ZZ \to \ell^+\ell^-\nu\bar{\nu}$ background is estimated from simulated Monte Carlo samples, and it contributes to the largest systematic uncertainties in the analysis. The idea of the $Z\gamma$ method is to make use of the similarity of the ZZ and $Z\gamma$ processes, especially in the regions where the mass difference between the Z and the photon does not matter. The $ZZ/Z\gamma$ cross-section ratio is calculated as a function of the $\nu\nu$ (or photon) transverse momentum by the Matrix and Sherpa generators. The ratio is then applied to the $Z\gamma$ events in data, together with a correction of the photon reconstruction efficiency to mimic the production of the ZZ background. The systematic uncertainties on the estimate and comparisons of the results of the method with the Monte-Carlo-based estimate are presented as well. In such searches, the missing transverse momentum ($E_{\mathrm{T}}^{\mathrm{miss}}$) reconstruction is crucial. Studies on the electron-jet overlap removal in the $E_{\mathrm{T}}^{\mathrm{miss}}$ algorithms reducing fake $E_{\mathrm{T}}^{\mathrm{miss}}$ are shown. The main experimental results presented use the full ATLAS Run-2 data sample (2015−2018) in proton-proton collisions at $\sqrt{s} = 13$ TeV centre-of-mass energy, corresponding to 139 fb^{-1}. No significant excess over the Standard Model prediction is observed. Therefore, exclusion limits on the production cross-section times the branching ratio of a heavy Higgs boson decaying to ZZ are set at a 95% confidence level.

Zusammenfassung

Ein zusätzliches schweres Higgs-Boson wird von vielen über das Standardmodell hinausgehenden Theorien vorhergesagt, wie zum Beispiel dem Two-Higgs-Doublet-Model (2HDM). Der dominante Untergrund in der Suche nach dem Zerfall eines solchen schweren Higgs-Bosons im Zerfallskanal $ZZ \rightarrow \ell^+\ell^-\nu\bar{\nu}$ (l = Elektronen, Myonen, ν = Neutrinos) ist die Produktion eines Z-Boson Paares. Die in der aktuellen ATLAS-Analyse verwendete Methode benutzt zur Abschätzung dieses Untergrundes Monte Carlo generierte Datensätze. Die assoziierten Unsicherheiten dominieren die systematischen Unsicherheiten der Suche. Diese Arbeit präsentiert eine datenbasierte Methode, die $Z\gamma$-Methode, um den ZZ-Untergrund abzuschätzen und die systematischen Unsicherheiten zu reduzieren. Dafür nutzt die $Z\gamma$-Methode die Ähnlichkeit zwischen den ZZ- und $Z\gamma$- Prozessen aus, besonders in Regionen, in denen die Massendifferenz zwischen dem Z-Boson und dem Photon vernachlässigbar ist. Das Verhältnis der Wirkungsquerschnitte von $ZZ/Z\gamma$ wird als Funktion des Transversalimpuls des $\nu\nu$-Systems und des Photons mit Hilfe der Generatoren Matrix und Sherpa berechnet. Dieses Verhältnis wird dann zusammen mit einer Korrektur der Rekonstruktionseffizienz der Photonen auf die $Z\gamma$-Ereignisse aus den experimentellen Daten angewandt, um die Produktion des ZZ-Untergrunds zu imitieren. Die systematischen Unsicherheiten der $Z\gamma$-Methode werden präsentiert und die Ergebnisse mit der Monte Carlo basierten Abschätzung des ZZ-Untergrunds verglichen. Da für die diskutierte Analyse eine korrekte Rekonstruktion des fehlenden Transversalimpulses $E_{\mathrm{T}}^{\mathrm{miss}}$ unerlässlich ist, werden ebenso Studien über den overlap removal des $E_{\mathrm{T}}^{\mathrm{miss}}$-Algorithmus, die falsch rekonstruierte $E_{\mathrm{T}}^{\mathrm{miss}}$ reduzieren, gezeigt. Die experimentellen Ergebnisse berücksichtigen die gesamten von ATLAS in Run-2 in Proton-Proton-Kollisionen bei $\sqrt{s} = 13$ TeV gesammelten Daten (2015−2018), die einer integrierten Luminosität von 139 fb^{-1} entsprechen. Es wird keine signifikante Abweichung von der Standardmodellvorhersage beobachtet. Es werden Ausschlussgrenzen für den Produktionswirkungsquerschnitt mal der ZZ Zerfallsbreite eines schweren Higgs-Bosons für ein Konfidenzlevel von 95% gezeigt.

Contents

Chapter 1

Introduction

> what is seen was not made out of what was visible.
>
> — Hebrews 11:3

Throughout history, people have tried to categorise what are the common principles of all things, what are the smallest constituents of matter, and how to analyse them to simplify this astonishingly complex world. In the classical Greek natural philosophy, there are four fundamental elements, earth, water, air, and fire. The first milestone of the modern atomic theory was set by J.J. Thomson's electromagnetic tube in 1896. He measured the ratio of the mass to the charge of the particle and discovered the first subatomic particle, the electron. Soon after in 1909, Ernest Rutherford and his student set up a projectile experiment to explore the structure of matter and found particles were scattered by a core at the centre of the atom. Based on these experiments, Rutherford proposed a model describing the atom as a tiny and heavy charged nucleus surrounded by electrons. The nucleus is made of protons, which are oppositely charged with respect to electrons, and electrically neutral neutrons (today, we understand the model of the atom better with modern quantum mechanics in terms of electron shells and subshells where electrons reside around the nucleus). An abundance of particles, sometimes referred to as zoo, was discovered in particle accelerators starting in the 1940s. The new particles were given exotic names, such as pions, sigmas, lambdas, and Latin letters when the Greek alphabet was exhausted. This taxonomy was not more orderly or elegant than Mendeleev's periodic table until Murray Gell-Mann and George Zweig independently came up with the key insight, that the zoological particles were made of smaller particles (quarks), which could be identified by looking at patterns in terms of symmetries. The classification frames fundamental particles into three generations. Nowadays, physicists are still trying to understand why they are arranged effectively in these particular patterns.

Particle experiments can give a more profound insight into strong and electroweak forces. Maxwell's equations do not only describe that electricity and magnetism are intimately connected but further demonstrate that the electric and magnetic fields travel through space as waves. In 1933, Fermi published his landmark theory for beta decay, unveiling the weak interaction and the existence of the neutrino. A few decades later in the 1960s, the electromagnetic force and weak force were merged into a combined electroweak force. Scientists are dreaming of a theory of everything that could go even further and unify these forces including gravity into a single force. In 1905, Albert Einstein published a paper about the photoelectric effect, picturing light as a stream of particles called photons. Further force-carrying particles, such as the gluons were discovered at the electron-positron collider PETRA at DESY in 1979, and $W^{\pm}$, and Z bosons were discovered at the Super Proton Synchrotron at CERN in 1983.

In 2012, the Higgs boson was discovered at the Large Hadron Collider, which finally confirmed a critical aspect of the Standard Model. This discovery completes the Standard Model describing elementary particles and their interactions. However, the Standard Model cannot explain observations in the cosmos that suggest that ordinary matter makes up only about 5% of the universe. Besides, it does not describe one of the four known forces, namely gravity. There are many more open questions in particle physics. With increasing intensity of the particle beams and a growing data set, the LHC might shed light on what lies beyond the Standard Model.

Two models, the simplest extension of the electroweak Higgs sector and a warped-geometry higher-dimensional model, are used to explore the fundamental laws of nature in this thesis. The Standard Model and the theoretical structure of the Two-Higgs-Doublet model and the Randall–Sundrum model are introduced in Chapter 2. Chapter 3 describes the LHC and the ATLAS detector. Chapter 4 focuses on MC generators. Chapter 5 describes the reconstruction and identification of particles in ATLAS. In Chapter 6, the search for an additional heavy Higgs boson in the $\mathrm{H} \to ZZ \to \ell^+\ell^-\nu\bar{\nu}$ final state is described (published in Ref. [1]), including the event selection and background estimates. The dominant background in the analysis is the SM ZZ production, with one Z decaying into two charged leptons and the other into two neutrinos. A novel method to estimate the ZZ background is detailed in Chapter 6 as well. The methodology is based on the substitution of a γ with a Z-boson. The ZZ estimate from $Z\gamma$ events and detailed systematics are presented. The summary of my Ph.D. project is given in Chapter 7.

Author's contribution

The author is part of ATLAS, a 3000 person collaboration, which built and operates the ATLAS detector at the Large Hadron Collider. Members of the collaboration are in charge of filtering, reconstructing and analysing the recorded data. Each study and result performed as part of the collaboration has direct input from many other people. The main contributions of the author are highlighted below.

Neutrinos and other particles that are invisible to the ATLAS detector can be reconstructed through missing transverse momentum ($E_{\mathrm{T}}^{\mathrm{miss}}$). The $E_{\mathrm{T}}^{\mathrm{miss}}$ calculation is challenging as it depends on the reconstruction of all objects in the detector. The author studied one particular challenging aspect of the $E_{\mathrm{T}}^{\mathrm{miss}}$ calculation, which is how the algorithm deals with jets and electrons that are nearby and can often not be separated unambiguously. Treating these cases incorrectly can lead to fake $E_{\mathrm{T}}^{\mathrm{miss}}$, impacting the discovery potential for searches for new invisible particles. In addition to evaluating the performance of the $E_{\mathrm{T}}^{\mathrm{miss}}$ reconstruction, using various metrics, the author's studies on overlap removal and improvements to the $E_{\mathrm{T}}^{\mathrm{miss}}$ calculation based on particle flow jets lead to a significant reduction of this fake $E_{\mathrm{T}}^{\mathrm{miss}}$. The performed studies and improvements benefit all analyses with $E_{\mathrm{T}}^{\mathrm{miss}}$ in the final states, including searches for supersymmetric particles.

The author contributed to the search for new physics in the $\ell\ell$ + $E_{\mathrm{T}}^{\mathrm{miss}}$ final state (where ℓ = electron or muon), which includes the search for $X \to ZZ \to \ell^{+}\ell^{-}\nu\bar{\nu}$, Z + dark matter, including the case where the dark matter could come from the decay of a Higgs boson. Of these, only the first search was already made public, so the thesis focuses on it.

The author's main contribution is the development of a new data-driven method to estimate the dominant background in these searches, which comes from the Standard Model production of two Z bosons, decaying into two charged leptons and two neutrinos. The standard estimation of this background is based on Monte Carlo simulation and contributes the leading systematic uncertainties to the searches. The author developed and performed all experimental aspect of the new method, including the selection, data-MC comparisons in the control region, closure checks and systematic uncertainties. She was only supported by other people in the evaluation of the theoretical uncertainties.

While the resulting background estimate was not used in the published results, mainly due to the dominant statistical uncertainties, it serves as an extremely important cross check of the modelling of the ZZ background in the non-trivial phase space selected by the analysis. The author also makes suggestion for alternative uses of the $Z\gamma$ control region, for further improvements and points out areas that need more study in the light of the requirement for more and more precise background estimates for future searches.

Chapter 2

Theoretical Overview

The Standard Model (SM) of particle physics describes the nature of fundamental forces and particles, including the existence of the Higgs boson. In this chapter, Section 2.1 discusses the SM. Section 2.1.1 covers the details of the electromagnetic and weak interactions. A discussion of the Higgs mechanism and how it is incorporated in the electroweak (EW) unification is given in Section 2.1.2. Section 2.2 quantifies the abundance of Higgs bosons produced at the Large Hadron Collider. The SM is known to be incomplete as it does not explain several observations and it suffers from theoretical issues, which are summarised in Section 2.3. In the following sections, two possible theoretical extensions to address the shortcomings of the SM are discussed. The Two-Higgs-doublet model (2HDM) which extends the scalar sector to enrich the particle phenomenology is described in Section 2.4. Section 2.5 introduces the Randall-Sundrum (RS) Model to address the problem of gravity, the main missing puzzle piece in the SM.

2.1. The Standard Model Particles and Forces

In the SM, particles are divided into two categories, bosons and fermions, which can be distinguished according to their spin, a quantum number describing the internal form of angular momentum. Bosons have an integer multiple of spin, such as a spin 0 or 1. In contrast, fermions possess half integers of spin, e.g., spin of 1/2, 3/2, 5/2. Both leptons and quarks are spin 1/2 fermions, and they constitute the building blocks of matter. The charged leptons are grouped into three generations with their corresponding neutrinos, (e, ν_e), (μ, ν_μ) and (τ, ν_τ). There are six flavours of quarks, falling into three generations, (up(u), down(d)), (charm(c), strange(s)), and (top(t), bottom(b)) as shown in Table 2.1.1. Each particle has an associated antiparticle with the same mass but with opposite physical charges.

The particles that act as carriers of forces have spin of 1 and therefore are called bosons as shown in Table 2.1.2. The electromagnetic force is mediated by the photon (γ) for charged particles, which is described by Quantum Electrodynamics (QED). The $W^{\pm}$ and Z bosons are the mediators for the weak force acting on all leptons and quarks. The gluons are the mediators of the strong force.

There is an additional force called gravity but the corresponding force carrier, the graviton, has not been discovered. If a hypothetical graviton exists, it must have a spin of 2. More about the graviton will be discussed in Section 2.5. The SM includes a Higgs boson and the Higgs field is thought to give mass to the other particles. More details about the Higgs boson are discussed in Section 2.1.3.

Fermion (spin 1/2)						
Generation	Leptons			Quarks		
	particle	charge	mass [MeV]	particle	charge	mass [MeV]
1^{st}	electron (e^-)	-1	0.5109	down (d)	$-\frac{1}{3}$	4.7
	e neutrino (ν_e)	0	$< 2 \times 10^{-6}$	up (u)	$+\frac{2}{3}$	2.2
2^{nd}	muon (μ^-)	-1	105.66	strange (s)	$-\frac{1}{3}$	96
	μ neutrino (ν_μ)	0	$< 2 \times 10^{-6}$	charm (c)	$+\frac{2}{3}$	1.28×10^3
3^{rd}	tau (τ^-)	-1	1776.86	bottom (b)	$-\frac{1}{3}$	4.18×10^3
	τ neutrino (ν_τ)	0	$< 2 \times 10^{-6}$	top (t)	$+\frac{2}{3}$	173.1×10^3

Table 2.1.1.: The properties of leptons and quarks. See Ref. [2] for a discussion on the definition of the quark masses.

Gauge Bosons (spin 1)				
Forces	particle	charge	mass [GeV]	Range [m]
Strong	gluon (g)	0	0	10^{-15}
Electromagnetism	photon (γ)	0	0	∞
Weak	Z boson (Z)	0	91.19	10^{-18}
	W boson ($W^\pm$)	±1	80.39	10^{-18}
Scalar Bosons (spin 0)				
	Higgs boson (h)	0	125.09	

Table 2.1.2.: The properties of bosons [2].

Quarks and anti-quarks are arranged into groups to form composite particles. Quarks have colour charges, but the composite particles made out of quarks are colour neutral. Using a simplified picture, the quark model was proposed by Murray Gell-Mann and George Zweig in the 1960s. Mesons contain a quark and an anti-quark adding up to an integer spin, either ±1 or 0 as integer spin bosons, while baryons contain three quarks with the summed-up spin of $\pm3/2$ or $\pm1/2$ forming spin-half fermions. On 26 March 2019, LHCb announced evidence for the existence of exotic baryons called pentaquark[1] consisting of four quarks and one anti-quark [3] (see Section 4.1 for a discussion of the quark content of hadrons, including valence and sea quarks).

Collections of identical bosons and fermions must satisfy the Spin-statistics theorem. Bosons (symmetric wave function) obey Bose-Einstein statistics, which indicate that bosons tend to occupy the same quantum state, while fermions (anti-symmetric wave function) obey Fermi–Dirac statistics, which account for atomic orbitals as prescribed by the Pauli exclusion principle.

[1]Each quark has a baryon number 1/3 and anti-quark has a baryon number -1/3.

Quantum Field Theory

Quantum Field Theory (QFT) is a theoretical framework that mathematically pictures all subatomic particles as localized vibrations of the corresponding quantum fields. The idea of QFT is that these fields, which fill out the ordinary space, can interact with one another.

In relativistic physics, particle trajectories are described by functions in space-time:

$$x^\mu = (x^0, x^1, x^2, x^3) \equiv (t, x, y, z). \tag{2.1.1}$$

The path a particle takes minimises the action, S, in any physical system. This phenomenon is called the *principle of least action*, for which the smallest sum of the Lagrangian for all the points is along the chosen path. Calculating the action variation for a field configuration (ϕ) via the partial integration becomes:

$$\begin{aligned}\delta S &= \int_v d^4x \left[\frac{\partial \mathcal{L}}{\partial \phi}\delta\phi + \frac{\partial \mathcal{L}}{\partial(\partial_\mu \phi)}\partial_\mu \delta\phi\right], \\ &= \int_v d^4x \left[\frac{\partial \mathcal{L}}{\partial \phi} - \partial_\mu\left(\frac{\partial \mathcal{L}}{\partial(\partial_\mu \phi)}\right)\right]\delta\phi + \frac{\partial \mathcal{L}}{\partial(\partial_\mu \phi)}\delta\phi\Big|_{t_a}^{t_b},\end{aligned} \tag{2.1.2}$$

where v is a 4-dim space-time volume that is of interest, $\mathcal{L}$ is the Lagrangian density, ∂_μ is a space-time derivative, and $\delta\phi$ represents the small perturbation from the 'true' field. The second term integrates to zero from the boundary conditions on $\delta\phi$. In this case, the variation of the fields at the boundary does not affect the local physics process. As the perturbation of the action S should be zero ($\delta S = 0$) to minimize the action, the Lagrangian yields the equation of motions, which is known as the Euler-Lagrange equation:

$$\frac{\partial \mathcal{L}}{\partial \phi} = \partial_\mu \frac{\partial \mathcal{L}}{\partial(\partial_\mu \phi)}. \tag{2.1.3}$$

Noether symmetries are transformations acting on the fields ϕ that leave the Lagrangian of a system unchanged. For instance,

$$\phi(x) \to \phi'(x) = \phi(x) + \alpha\Delta\phi(x), \tag{2.1.4}$$

where α is an infinitesimal parameter, and $\Delta\phi(x)$ describes the transformation. The key is figuring out symmetric transformations that leave ϕ and thus the Lagrangian unchanged:

$$\mathcal{L} \to \mathcal{L} + \alpha\Delta\mathcal{L}. \tag{2.1.5}$$

This $\alpha\Delta\mathcal{L}$ can be obtained by varying the fields [4]:

$$\begin{aligned}\alpha\Delta\mathcal{L} &= \frac{\partial \mathcal{L}}{\partial \phi}(\alpha\Delta\phi) + \left(\frac{\partial \mathcal{L}}{\partial(\partial_\mu \phi)}\right)\partial_\mu(\alpha\Delta\phi) \\ &= \alpha\left[\frac{\partial \mathcal{L}}{\partial \phi} - \partial_\mu(\frac{\partial \mathcal{L}}{\partial_\mu \phi)})\right]\Delta\phi + \alpha\partial_\mu(\frac{\partial \mathcal{L}}{\partial(\partial_\mu \phi)}\Delta\phi).\end{aligned} \tag{2.1.6}$$

The first term is zero due to the Euler-Lagrange equation.

Noether's theorem states that every differentiable symmetry of the action of a physical system has a corresponding conservation law. Instead of stating that simple numbers of some physical quantity - energy, momentum, *etc.* - do not vary over time, one can develop a general form of *conserved currents*. The continuity equation, $\partial_\mu \mathcal{J}^\mu = 0$, represents the conservation of mass or energy in dynamics. The conserved current $\mathcal{J}^\mu$ is a vector with the charge density and 3-dim current density. For the transformation to be symmetry, the Lagrangian can be varied by $\partial_\mu \mathcal{J}^\mu$, so that $\Delta\mathcal{L} = \partial_\mu \mathcal{J}^\mu = \partial_\mu(\frac{\partial\mathcal{L}}{\partial(\partial_\mu\phi)}\Delta\phi)$.

Electromagnetic Interaction

The QED Lagrangian for a spin-1/2 field interacting with the electromagnetic field is given as:

$$\mathcal{L}_{QED} = \bar{\psi}(i\gamma^\mu D_\mu - m)\psi - \frac{1}{4}F_{\mu\nu}F^{\mu\nu}, \tag{2.1.7}$$

where ψ is a 4 component fermion that carries an electric charge, and $D_\mu \equiv \partial_\mu - ieA_\mu$ is the gauge covariant derivative. A vector field A_μ must transform as $A_\mu \to A_\mu - \partial_\mu\lambda(x)$ to make the Lagrangian gauge invariant. Due to gauge invariance, a term like $M^2 A_\mu A^\mu$ cannot appear in the Lagrangian, which means the A-field describes a massless particle, namely the photon. e is the strength of the phase transformation, which can be interpreted as a charge q = -$|e|$. $F_{\mu\nu} = \partial_\mu A_\nu$ - $\partial_\nu A_\mu$ is the electromagnetic field tensor. m is the mass of the electron or positron, and γ^μ are the Dirac matrices.

The QED Lagrangian is invariant under a local U(1) phase transformation $\psi(x) \to e^{ie\lambda(x)}\psi(x)$. The conserved Noether current for this transformation is $j^\mu = \bar{\psi}\gamma\psi$, which consists of the electromagnetic charge density and 3-dim current density. This conserved current can be verified by:

$$\partial_\mu j^\mu = (\partial_\mu\bar{\psi})\gamma^\mu\psi + \bar{\psi}\gamma^\mu(\partial_\mu\psi) = im\bar{\psi}\psi - im\bar{\psi}\psi = 0, \tag{2.1.8}$$

where $i\gamma^\mu\partial_\mu\psi = m\psi$ and $i\partial_\mu\bar{\psi}\gamma^\mu = -m\bar{\psi}$ is derived from the equations of motion [5].

Strong Interaction

Likewise, the gauge invariant QCD Lagrangian can be written as:

$$\mathcal{L}_{QCD} = \Sigma_q \left(\bar{\psi}_{qi}\gamma^\mu \left[\delta_{ij}\partial_\mu + ig(G^\alpha_\mu t^{ij}_\alpha)\right]\psi_{qj} - m\bar{\psi}_{qi}\psi_{qi}\right) - \frac{1}{4}G^\alpha_{\mu\nu}G^{\mu\nu}_\alpha, \tag{2.1.9}$$

where ψ_q is a 4 component fermion that carries a colour index i (=red, green, blue). The colour state can be rotated by 3 $\times$ 3 unitary matrices, t_α, which are generators of the SU(3) colour group. There are eight mediators in QCD: G^α_μ is the 4-vector potential of the gluons fields (α = 1,...8). The symbol $G^{\mu\nu}_\alpha$ represents the gauge invariant gluon field strength tensor. $G^{\mu\nu}_\alpha = \partial^\mu G^\nu_\alpha$ - $\partial^\nu G^\mu_\alpha$ - $gf^{\alpha\beta\gamma}G^\mu_\beta G^{nu}_\gamma$, $f^{\alpha\beta\gamma}$ are structure constants of the SU(3) colour group, and $g = \sqrt{4\pi\alpha_s}$ corresponds to the strong coupling. The coupling constant, α_s, is an effective constant, which depends on four-momentum Q^2 transferred (see the running coupling paragraph for details in Section 4.1).

2.1.1. Weak Interaction and Electroweak Theory

In 1933, Enrico Fermi formulated the first model of the weak interaction, known as Fermi's interaction. The interaction was formulated in terms of QFT. As illustration of the Fermi interaction, in the following, the muon decay is discussed. Fermi's Lagrangian density describing four fermions fields by the product of four Dirac fields for the muon decay $\mu^- \to e^- + \nu_\mu + \bar{\nu}_e$ is given as:

$$\mathcal{L} = \frac{G_F}{\sqrt{2}} \bar{\psi}_{\nu_\mu} \gamma_\mu (1-\gamma_5) \psi_\mu \bar{\psi}_e \gamma^\mu (1-\gamma_5) \psi_{\nu_e}, \tag{2.1.10}$$

where G_F is the interaction term of the Fermi Lagrangian with dimensions of mass to the power -2, making it non-renormalisable. The γ_μ term is a 4×4 matrix, $(1-\gamma_5)$ is the chirality operator, and it plays the role of projecting the Dirac field onto the left-handed components. The weak force has a left-handed preference, which has been verified in the experiment by Chien-Shiung Wu [6]. The muon lifetime given the Lagrangian density can therefore be computed, and then be compared to the experimental measurement, which is about 10^{-6}s [7].

The weak interaction fermion couples to the weak force corresponding to a conserved current, $\partial^\mu \mathcal{J}^\alpha_\mu = 0$ where $\alpha = 1$, 2, and 3, under the $SU(2)_L$ symmetry in which the muon current is defined as:

$$\mathcal{J}^1_\mu = \bar{\ell}^\mu_L \gamma_\mu \tau^+ \ell^\mu_L, \tag{2.1.11}$$

where τ^+ is a 2×2 matrix. Its hermitian conjugate τ^-, which is the transpose matrix of τ^+, forms the second current, $\mathcal{J}^2_\mu$.

The third current is expected from group theory, and it forms as:

$$\begin{aligned} \mathcal{J}^3_\mu &= \bar{\ell}^\mu_L \gamma_\mu [\tau^+, \tau^-] \ell^\mu_L \\ &= \bar{\nu}^\mu_L \gamma_\mu \nu^\mu_L - \bar{\mu}^\mu_L \gamma_\mu \mu^\mu_L. \end{aligned} \tag{2.1.12}$$

These three currents, $\mathcal{J}^1_\mu$, $\mathcal{J}^2_\mu$ and $\mathcal{J}^3_\mu$, appear as the consequence of $SU(2)_L$. The first two currents correspond to the charge currents and the third current is a neutral current. However, there is no neutral current in the early phenomenology of the weak interaction Fermi Lagrangian. The neutral current of electromagnetism does not fit in $SU(2)_L$ because $\mathcal{J}^3_\mu$ involves only left-handed fermions and it contains the neutrino term. Enlarging the gauge group to satisfy the current conservation and also to include the electroweak current was then proposed:

$$SU(2)_L \otimes U(1)_Y. \tag{2.1.13}$$

To build a gauge invariant theory, the recipe is to replace the ordinary derivative of the fermion fields by covariant derivatives:

$$\partial_\mu \psi \to D_\mu \psi = \partial_\mu \psi - igT^A W^A_\mu \psi - ig' B_\mu \frac{Y}{2} \psi, \tag{2.1.14}$$

where g and g' are the relevant coupling constants. T^A are the weak isospin operators, $T^A = \frac{\sigma_i}{2}$ $(i = 1, 2, 3)$, where σ_i are the Pauli matrices. W^A_μ are the 3 real vector fields related to SU(2). W^1_μ and W^2_μ are two electrically charged bosons under SU(2). B_μ is the vector boson related to U(1).

To identify the neutral electroweak current, Glashow-Weinberg jointly proposed replacing B_μ and W^3_μ by the linear combination of A^μ and Z^μ in 1968:

$$\begin{pmatrix} B_\mu \\ W^3_\mu \end{pmatrix} = \begin{pmatrix} \cos\theta_w & -\sin\theta_w \\ \sin\theta_w & \cos\theta_w \end{pmatrix} \begin{pmatrix} A^\mu \\ Z^\mu \end{pmatrix}. \tag{2.1.15}$$

The neutral current interaction then reads:

$$\begin{aligned} \mathcal{L} = &\bar{\psi}\gamma_\mu[g\sin\theta_w T_3 + g'\cos\theta_w \tfrac{Y}{2}]\psi A^\mu \\ &+\bar{\psi}\gamma_\mu[g\cos\theta_w T_3 - g'\sin\theta_w \tfrac{Y}{2}]\psi Z^\mu, \end{aligned} \tag{2.1.16}$$

where A^μ represents the photon. For particles with different electric charge, the neutral electromagnetic current can be written in units of the proton charge (e): $\mathcal{J}^{em}_\mu = e\bar{\psi}\gamma_\mu Q\psi$ where Q is the electric charge. Comparing $\mathcal{J}^{em}_\mu$ and Equation 2.1.16 with A^μ, eQ can be written in the form of:

$$eQ = g\sin\theta_w T_3 + g'\cos\theta_w \frac{Y}{2}. \tag{2.1.17}$$

After the mixing of the B and W^0 that produces the photon and the Z, the new quantum number Y (hyper-charge) is introduced by setting $g\sin\theta_w = g'\cos\theta_w = e$, $\mathrm{Q} = T_3 + \frac{Y}{2}$. This can be rearranged into the relation:

$$Y = 2(Q - T_3). \tag{2.1.18}$$

The first evidence of the weak neutral currents was confirmed at the Gargamelle bubble chamber at CERN in 1973 [8]. The Z boson was soon to been discovered at the SPS accelerator at CERN in 1983. However, the mass term for the Z and W bosons is forbidden by gauge invariance according to Yang-Mills theory. The Higgs field addresses the problem of the origin of mass of SM particles and unitarises the WW scattering, which will be discussed in Section 2.1.2 and 2.1.3.

2.1.2. The Goldstone Boson: Spontaneous Breakdown of Symmetry

The gauge vector field can acquire a mass term by introducing an additional scalar field. This mechanism is know as the Goldstone theorem, which preserves gauge invariance by defining a non-linear realization of a gauge transformation. The principle behind this theorem is to define a different way of achieving a gauge transformation. The Lagrangian for an U(1) gauge field A_μ coupling to a self-interacting complex scalar field ϕ is:

$$\mathcal{L} = D_\mu(\phi)^+ D^\mu(\phi) - V(\phi) - \frac{1}{4}F_{\mu\nu}F^{\mu\nu} + L_{GFH}, \tag{2.1.19}$$

where L_{GFH} is a Feynman gauge fixing term, which is needed to obtain an easier calculation for the whole Lagrangian. The covariant derivative acting on the scalar field is:

$$D^\mu\phi(x) = \partial^\mu\phi(x) - ieA^\mu\phi(x). \tag{2.1.20}$$

The quantum numbers remain unchanged under the Nambu–Goldstone transformation:

$$\phi(x) \to e^{ie\lambda(x)}\phi(x), A^{\mu} \to A^{\mu} + \partial^{\mu}\lambda(x). \tag{2.1.21}$$

The gauge invariance with respect to this gauge transformation can be seen by taking the scalar field in quadrature. The potential associated with the phase is dropped using a gauge transformation meaning a Goldstone mode is shifted into the gauge field A_{μ}. The scalar potential has dimensions of the field to the fourth power, hence it is re-normalisable in four dimensions as shown in the following equation:

$$V(\phi) = \lambda|\phi^4|^2 + a|\phi|^2 + b. \tag{2.1.22}$$

Expanding the ϕ around the vacuum expectation value (VEV), where the minimum of the potential meets the origin, one can rewrite the scalar field in a non-linear way: $\phi = (H+v)e^{i\frac{G}{v}}$ (H and G, which are referred to as the Higgs boson and the Goldstone bosons, respectively, are real scalar fields without VEVs). The scalar potential becomes:

$$V(\phi) = \lambda H^4 + 2\lambda v^2 H^2. \tag{2.1.23}$$

Substituting the scalar potential (Eq. 2.1.23) and covariant derivative (Eq. 2.1.20) back into the Lagrangian (Eq. 2.1.19), the free Lagrangian density becomes:

$$\mathcal{L}_0 \sim \partial_{\mu}H\partial^{\mu}H - 2\lambda v^2 H^2(x) + \partial_{\mu}G\partial^{\mu}G - \partial_{\mu}A_{\nu}\partial^{\mu}A^{\nu} + e^2v^2A_{\mu}A^{\mu}, \tag{2.1.24}$$

where $\partial_{\mu}H\partial^{\mu}H$ is the kinematic term for the Higgs boson, $\partial_{\mu}G\partial^{\mu}G$ is the kinematic term for the Goldstone bosons and $\partial_{\mu}A_{\nu}\partial^{\mu}A^{\nu}$ is the kinematic term for the vector boson. The shape of the propagators that represents the target particle moving between incoming and outgoing particles show up in the Lagrangian. For example, the Feynman propagator for the Higgs field in momentum space is $\frac{1}{k^2-2\lambda v^2+i\epsilon}$, and the $2\lambda v^2$ term corresponds to the mass term, m_H^2. Similarly, the propagator for the vector boson is $\frac{g^{\mu\nu}}{k^2-e^2\nu^2+i\epsilon}$. Some terms, such as $A_{\mu}\partial_{\mu}G$ in $\mathcal{L}_0$, are absorbed by the gauge choice, $\mathcal{L}_{GFH}$. The vector field has the dimension of the mass (e^2v^2) as an expansion around the vacuum expectation. As a result, the $\mathcal{L}_0$ is no longer invariant under the gauge transformation of the A, meaning a U(1) symmetry is broken for perturbations around the VEV. The massive vector bosons can be longitudinally polarized because the massless Goldstone bosons become the longitudinal polarization of the massive vector fields.

2.1.3. The Higgs Boson

In order to be consistent with Fermi's four-fermion interaction of the β decay, the vector fields are required to be massive. The way out of this cul-de-sac is described in Section 2.1.2 using the concept of spontaneous breakdown involving Goldstone bosons where the scalar field has a real and an imaginary component. In the SM, one can define the simplest doublet scalar field as:

$$\phi = \begin{pmatrix} \phi^+ \\ \phi^0 \end{pmatrix}, \tag{2.1.25}$$

where the superscripts + and 0 indicate the electric charge (Q) of the components. An additional U(1) Y is needed in order to let only a neutral scalar field acquire a VEV. This means electromagnetism is unbroken by the scalar VEV, and the scalar VEV yields the breaking scheme as: $SU(2)_L \otimes U(1)_Y \to U(1)_Q$.

The transformation for the scalar field can be written as follows:

$$\begin{pmatrix} \phi^+ \\ \phi^0 + \frac{v}{\sqrt{2}} \end{pmatrix} \to e^{ig\alpha(x)\frac{\tau^+}{2}} e^{ig'\beta(x)\frac{Y_\phi}{2}} \begin{pmatrix} \phi^+ \\ \phi^0 + \frac{v}{\sqrt{2}} \end{pmatrix}. \tag{2.1.26}$$

The symbol g is the weak interaction coupling strength, g' is the coupling strength of the hypercharge interaction, $\alpha(x)$ and $\beta(x)$ are the position parameter elements for the SU(2) and U(1), respectively, and the matrices τ are the Pauli matrices.

One can also parametrise the Higgs field with the Unitarity gauge[2]

$$\begin{pmatrix} \phi^+ \\ \phi^0 + \frac{v}{\sqrt{2}} \end{pmatrix} = \frac{1}{\sqrt{2}} e^{i\frac{\tau^i\theta^i(x)}{2}} \begin{pmatrix} 0 \\ H(x) + v \end{pmatrix}, \tag{2.1.27}$$

where H(x) is a real scalar field. The covariant derivative of ϕ is:

$$D_\mu \phi = \left(\partial_\mu + igT^i W^i_\mu + i\frac{1}{2}g' B_\mu\right)\phi, \tag{2.1.28}$$

where W^i_μ and B_μ are $SU(2)_L$ and $U(1)_Y$ gauge bosons, respectively (W^i_μ can be written in terms of the generators: $W_\mu = W^i_\mu T^i$). $T^i = \frac{\tau^i}{2}$ (τ^i are three Pauli matrices). The Higgs potential V(ϕ) is required from re-normalisability and gauge invariance to take the form:

$$V(\phi) = -\mu^2\phi^+\phi + \lambda(\phi^+\phi)^2. \tag{2.1.29}$$

The λ represents self-interactions among the Higgs fields, and it is positive. The quadratic term μ^2 must be greater than zero to develop a non-zero VEV leading to a non-trivial minimum $\phi_0^2 = \frac{\mu^2}{2\lambda}$. The vector boson mass terms show up by taking the square of the covariant derivative, $(D^\mu\phi)^+(D_\mu\phi)$:

$$\begin{aligned} \left| D_\mu \begin{pmatrix} \phi^+ \\ \phi^0 + \frac{v}{\sqrt{2}} \end{pmatrix} \right|^2 &\in \frac{1}{2}\frac{v^2}{4}[g^2(W^1_\mu + W^2_\mu)(W^{\mu 1} - iW^{\mu 2}) + (g'B_\mu - gW^3_\mu)^2] \\ &\in \frac{v^2}{4}[g^2 W^+_\mu W^{-\mu} + \frac{1}{2}(g^2 + g'^2)Z_\mu Z^\mu]. \end{aligned} \tag{2.1.30}$$

Equation 2.1.30 shows $m_W^2 = \frac{1}{4}g^2v^2$ and $m_Z^2 = \frac{1}{4}(g^2 + g')v^2$ where g and g' satisfy the relation of $g\sin\theta_w = g'\cos\theta_w$ and so the weak mixing angle is:

$$\tan\theta_w = \frac{g'}{g}, \sin\theta_w = \frac{g'}{\sqrt{g' + g'^2}}, \cos\theta_w = \frac{g}{\sqrt{g^2 + g'^2}}. \tag{2.1.31}$$

[2] Picking a Gauge is a mathematical procedure to remove unphysical fields, while adding additional degrees of freedom in the field. The corresponding gauge fixing terms of the Feynman Lagrangian can be written as:
$\mathcal{L} = -\frac{1}{2\xi}(\partial_\mu A^\mu)$
$\xi = 1$ is for the Feynman–'t Hooft gauge.
$\xi \to \infty$ is for the Unitarity gauge or Landau gauge.

The Higgs mechanism successfully gives masses to the bosons, though a priori fermions cannot receive their masses by the same process. A non-gauge interaction turns out to be responsible for fermion mass generation.

The Yukawa interaction between the Higgs field and massless quark (with a prime sign) and lepton fields in the SM Lagrangian reads:

$$\begin{aligned}\mathcal{L}_{Yukawa} &= -\bar{q}' h'_D d'_R(\phi + \frac{v}{\sqrt{2}}) + \bar{q}' h'_u u'_R(\phi + \frac{v}{\sqrt{2}})^c - \bar{\ell}' h_L e_R \phi + \frac{v}{\sqrt{2}} + h.c. \\ &= \frac{v}{\sqrt{2}}[\bar{d'_L} h'_d d'_R + \bar{u'_L} h'_u u'_R + \bar{\ell'_L} h'_L e'_R] + \\ &+ \phi[\bar{d'_L} h'_d d'_R + \bar{u'_L} h'_u u'_R + \bar{\ell'_L} h'_L e'_R] + h.c.,\end{aligned} \tag{2.1.32}$$

where q$\prime$ is a doublet matrix representing a collection of left-handed quarks, q$\prime$ = $\begin{pmatrix} u'_L \\ d'_L \end{pmatrix}$, h'_D is a complex matrix that describes the so-called Yukawa couplings between the single Higgs doublet and the down type quarks as a constant in the generation space, d'_R is right-handed down-type quarks, $\phi + \frac{v}{\sqrt{2}}$ is a Higgs doublet where $v = \begin{pmatrix} 0 \\ v \end{pmatrix}$, u'_R stands for right-handed up-type quarks, $(\phi + \frac{v}{\sqrt{2}})^c$ forms charge conjugate objects ($\phi^c = \epsilon\phi^*$)[3], $\ell' = \begin{pmatrix} \nu'_L \\ e'_L \end{pmatrix}$, and e_R stands for a right-handed electron.

The first term related to the constant v (VEV) in Equation 2.1.32 can be diagonalized using single value decomposition[4]:

$$\frac{v}{\sqrt{2}}[\bar{d'_L} U_d^+ h_d V_d d'_R + \bar{u'_L} U_u^+ h_u V_u u'_R + \bar{\ell'_L} U_L^+ h_L V_L e'_R]. \tag{2.1.33}$$

New fields can be defined with a unitary rotation in space where the phase can be absorbed into each quark field, such as: $d_R = V_d d'_R$, $d_L = U_d d'_L$, $u_R = V_u u'_R$, $u_L = U_u u'_L$, $\ell_R = V_L \ell'_R$ and $\ell_L = U_L \ell'_L$. The remaining complex phases then cause CP violation. The diagonal mass terms for each fermion can be seen as $-\frac{hv}{\sqrt{2}}\bar{\psi}\psi$ in Equation 2.1.34:

$$\frac{v}{\sqrt{2}}[\bar{d_L} h_d d_R + \bar{u_L} h_u u_R + \bar{\ell_L} h_L \ell_R]. \tag{2.1.34}$$

The left-handed down-type quarks are rotated by the matrix U_d and the left-handed up-type quarks are rotated by the different matrix U_u. This causes the charge current generation mixing, which is described by the Cabibbo-Kobayashi-Maskawa (CKM) matrix.

2.2. Higgs Boson Hunting at the LHC

The Higgs boson was discovered in 2012 by the ATLAS and CMS collaborations [9], and the subsequent property measurements have not shown any deviations from the predictions

[3] ϵ is an anti-symmetry matrix in 2-dimension for a doublet field:
$\epsilon = \begin{pmatrix} 0 & -1 \\ -1 & 0 \end{pmatrix}$

[4] Factorized procedure: $h' = U^+ h V$ where U and V are 2 unitary matrices. $UU^+ = I$ and $VV^+ = I$

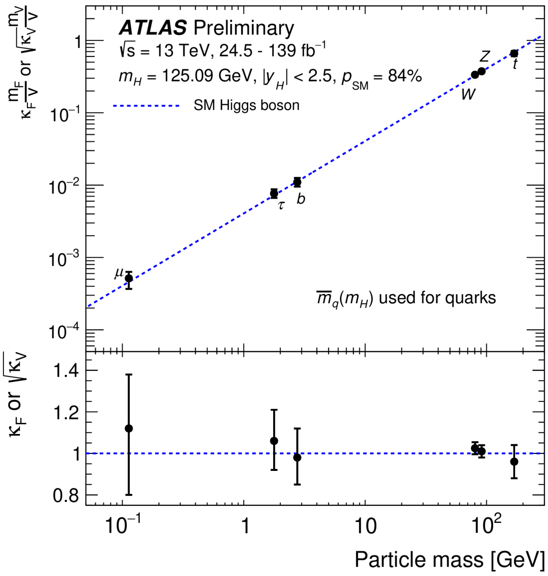

Figure 2.2.1.: The coupling of the Higgs boson to fermions (μ, τ, b, t) and bosons (W, Z) as a function of the particles' mass. The diagonal line indicates the SM prediction. The coupling modifiers are measured assuming no BSM contributions to the Higgs boson decays, and the SM structure of loop processes. Image from Ref. [10].

of the SM. Figure 2.2.1 shows a significant test of the connection between the mass of fermions and bosons and the Higgs field interactions with them. The measurement of the coupling for each particle, assuming no BSM contributions to the Higgs boson decays and the SM structure of loop processes, is consistent with the SM predictions with a p-value of $p_{SM} = 84\%$ [10]. The ATLAS-CMS combined measured mass of the Higgs boson is 125.09 $\pm$ 0.24 GeV [11].

The Higgs boson can be produced through four main production channels in pp collisions at the Large Hadron Collider. The signal contribution includes the gluon fusion (ggF) production, vector boson fusion (VBF), the associated production of the Higgs boson with a W or Z boson (VH), and the Higgs boson production in association with top-quarks (ttH). Their Feynman diagrams as shown in Figure 2.2.2 indicate the different signatures that can be used to identify the Higgs boson. This section will discuss the two production processes with the largest predicted cross-sections, ggF and VBF.

In the SM, the gluon fusion production of the Higgs boson is the dominant process as shown in Figure 2.2.3. Since gluons are massless, they do not couple directly to the Higgs boson, hence a fermion loop is needed to connect gluons and the Higgs boson. Due to the strong coupling of the Higgs boson to the top quark, a Higgs boson is mainly produced via a top quark loop. Figure 2.2.2 (a) shows the tree level diagram of ggF.

The vector boson fusion is the second leading production process. The VBF production mechanism is a process by which either W or Z bosons fuse together to create the Higgs boson. The W or Z boson is radiated by a quark via the weak interaction. Its signal has a particular geometry: jets in the final state prefer to be forward in the detector, while the Higgs and its decay products are expected to be in the central detector.

The Higgs boson is unstable, and decays into other fundamental particles almost immediately.

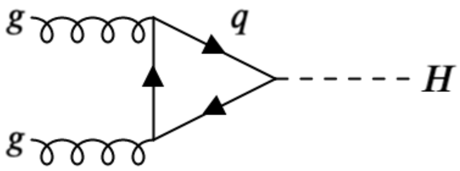

(a)

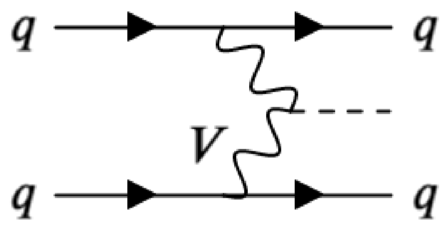

(b)

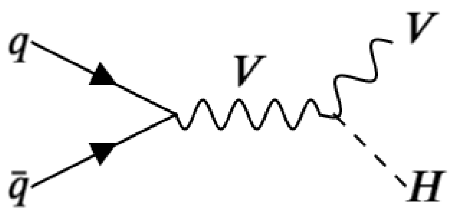

(c)

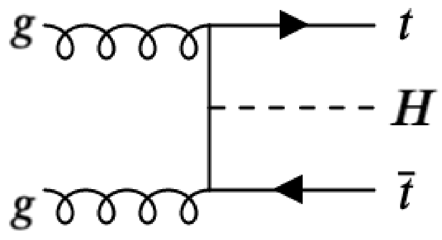

(d)

Figure 2.2.2.: The dominant Higgs boson production modes in proton-proton collisions. (a) gluon-gluon fusion, (b) vector boson fusion, (c) W and Z associated production, (d) tt associated production.

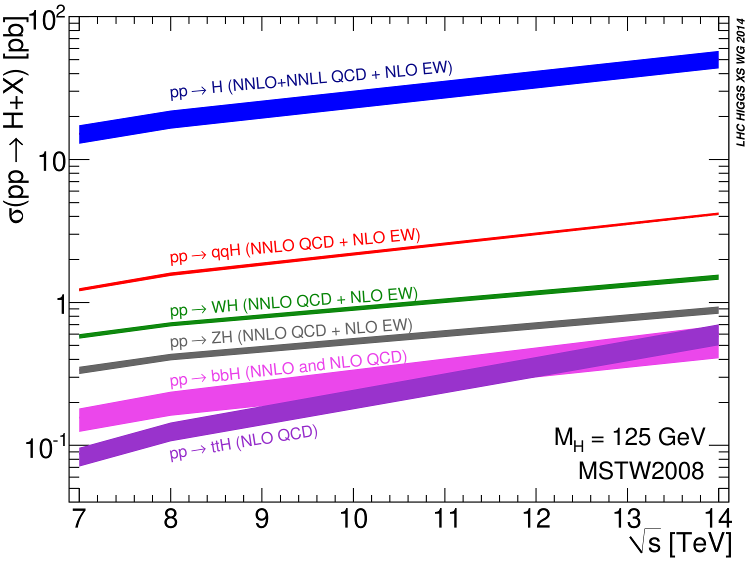

Figure 2.2.3.: Higgs boson production cross sections for $m_H = 125$ GeV as a function of the centre-of-mass energy $\sqrt{s}$. Image from Ref. [12].

Table 2.2.1 summarises the coupling constant g, which describes the Higgs boson coupling to the fermions/bosons/itself. The coupling strength is proportional to the mass of fermions, and to the square of the mass of bosons or itself.

Vertex	Coupling Constant g	Representation
Higgs−Fermions	m_f/v	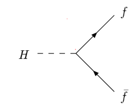
Higgs−Vector Bosons	$2m_V^2/v$	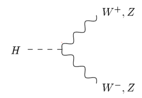
Two Higgs bosons−Vector Bosons	$2m_V^2/v^2$	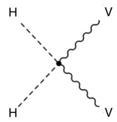
HHH	$3m_H^2/v$	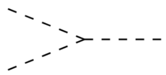
HHHH	$3m_H^2/v^2$	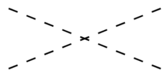

Table 2.2.1.: The couplings of the Higgs boson to fermions $g_{Hf\bar{f}}$, gauge bosons g_{HVV}, g_{HHVV}. Trilinear coupling g_{HHH}, and quartic coupling g_{HHHH} are shown, as well.

The SM predictions for the Higgs boson decay modes and their corresponding branching ratios are laid out in Table 2.2.2 for a Higgs boson mass of 125 GeV.

In the following a discussion of the different Higgs boson decay channels is presented:

- $H \to b\bar{b}$:
    - largest branching ratio in the SM
    - large multi jet background when targeting the ggF and VBF production
    - discovery of this decay channel driven by VH production
    - probes the Higgs boson couplings to fermions
    - excellent channel to measure VH production
- $H \to \tau^+\tau^-$:
    - challenging mass reconstruction: The identification of hadronically decaying τ and the neutrinos in the final state deteriorate the resolution of $m_{\tau\tau}$.
    - probes the Higgs boson couplings to fermions and excellent channel to measure VBF production: has higher p_{T} Higgs boson recoiling against jets. A high-p_{T} Higgs boson typically has larger $E_{\mathrm{T}}^{\mathrm{miss}}$ and benefits from an improved resolution on $E_{\mathrm{T}}^{\mathrm{miss}}$, and thus on $m_{\tau\tau}$.

Decay channel	Branching ratio[%]
$H \to bb$	58.2
$H \to WW$	21.4
$H \to gg$	8.19
$H \to \tau\tau$	6.27
$H \to cc$	2.89
$H \to ZZ$	2.62
$H \to \gamma\gamma$	0.227
$H \to Z\gamma$	0.153
$H \to \mu\mu$	0.022

Table 2.2.2.: The branching ratios for the SM Higgs boson for $m_H = 125$ GeV with $\Gamma_H \sim 4.1 \pm 0.09$ MeV.

- $H \to WW \to \ell^+\nu\ell^-\bar{\nu}$:
  - $H \to WW$ has largest branching ratio of bosonic decay channels
  - complex and relatively large backgrounds
  - neutrinos in the final state make it challenging to reconstruct m_H
  - powerful channel to measure VBF and VH production
- $H \to \gamma\gamma$:
  - important channel for the Higgs boson discovery
  - small branching ratio, but relatively good signal/background ratio
  - background estimates under control
  - fully reconstructible final state with very good resolution
  - important for precision property measurements, including the Higgs boson mass
- $H \to ZZ \to \ell\ell\ell\ell$:
  - important channel for the Higgs boson discovery
  - golden channel: very small branching ratio due to requirement of Z decaying into electrons or muons, but best signal/background ratio of all channels
  - fully reconstructible final state with very good resolution
  - important for precision property measurements, including the Higgs boson mass (still statistics limited for rarer production modes)

2.3. Open Questions and Beyond the Standard Model

The scalar mass term $2\lambda v^2$ as shown in Equation 2.1.24 is associated with the Higgs boson:

$$m_H = \sqrt{2\lambda v^2} \approx \sqrt{\lambda} \times 350 \text{ [GeV]}, \tag{2.3.1}$$

where the Higgs potential parameter v (vacuum expectation value) using Eq 2.1.30 and the weak mixing angle in Eq. 2.1.31:

$$v = \frac{2m_W}{g} \approx 250 \text{ [GeV]} \tag{2.3.2}$$

is measured at the LEP collider given the fine structure constant α (1/128), the Fermi constant G_F ($1.11637(1) \times 10^{-5}$ [GeV^{-2}]), m_Z(91.1875(21) [GeV]), m_W(80.426(34)) [GeV]) and $\sin^2\theta_W$ [13]. Theoretically speaking, $m_H \geq 350$ [GeV] indicates that the Higgs self-coupling is a strong coupling with $\lambda \geq 1$, while $m_H \leq 190$ [GeV] means the constant is relatively weak $\lambda \leq 1$. The discovered Higgs boson has a mass of about 125 GeV indicating that a light Higgs is phenomenologically preferred.

A light boson raises the question of why the electroweak scale ($\mathcal{O}$(100 GeV)) is so much lower than the Planck scale which is around 10^{19} GeV. This is also known as the hierarchy problem of the SM. Looking at it from a different angle, the Higgs boson mass should actually be much larger due to quantum corrections, unless there are fine-tuned cancellations. Moreover, although the SM in principle fulfils Sakharov conditions [14] that generate a matter-antimatter asymmetry, the phase transition is not sufficient to create enough baryon asymmetry within the SM. Besides, questions like candidates for dark matter, and the explanation for dark energy can not be answered within the SM. The SM does not explain gravity, either.

There are many theoretical solutions beyond the SM that have been proposed to solve these theoretical questions. One solution comes from the idea of two complex scalars which can provide additional sources of CP violation, and help solve other problems of the SM in the context of supersymmetric models. One of the well known solutions to the Planck-weak hierarchy problem is provided by the Randall–Sundrum (RS) Model.

2.4. Extensions to the Standard Model: 2HDM

All postulated fermions and gauge bosons have been extremely well verified phenomenologically. On the contrary, the scalar sector has not been fully explored yet. Any phenomenologically viable extended Higgs sector must be compatible with the observed electroweak parameter $\rho = M_W^2/(M_Z^2 cos^2\theta_W) = \frac{\frac{1}{2}g^2v^2}{\frac{1}{4}(g^2+g'^2)v^2\frac{g^2}{g^2+g'^2}} = 1$. More generally, for n (n $\geq$ 1) scalar fields ϕ_i, the ρ parameter is given by [15]:

$$\rho = \frac{\Sigma_{i=1}^n [I_i(I_i+1) - \frac{1}{4}Y_i^2]v_i}{\Sigma_{i=1}^n \frac{1}{2}Y_i^2 v_i}, \tag{2.4.1}$$

where I_i is the weak isospin, Y_i is the weak hypercharge, v_i is the VEV. Both SU(2) singlets with Y $= 0$ and SU(2) doublets with Y$=\pm1$ give $\rho = 1$, and other scalars with larger SU(2) multiplets are compatible with $\rho = 1$.

One of the simplest extensions is the two-Higgs-doublet model (2HDM), which contains two CP even scalars (h and H), one CP odd scalar (or pseudoscalar) A and two charged

Higgs bosons $H^{\pm}$. There are three fields which are 'eaten' to give mass to the $W^{\pm}$ and Z^0 gauge bosons. With two involved scalar fields, the structure of 2HDMs is very rich; scalar potential for two doublets can have CP-conserving (Higgs self-couplings are real), CP-violating (Higgs self-couplings contain complex term), and charge-violating minima. The larger presence of complex phases may have consequences for theoretical models of leptogenesis [16] which is a process of generating the matter-antimatter disparity. Moreover, in the supersymmetric models, the second Higgs field has to be introduced to give mass to up and down type quarks.

The scalar potential for two doublets Φ_1 and Φ_2 with hypercharge +1 is [15]:

$$\begin{aligned} V = & m_{11}^2\Phi_1^\dagger\Phi_1 + m_{22}^2\Phi_2^\dagger\Phi_2 - m_{12}^2(\Phi_1^\dagger\Phi_2 + \Phi_2^\dagger\Phi_1) + \frac{\lambda_1}{2}(\Phi_1^\dagger\Phi_1)^2 + \frac{\lambda_2}{2}(\Phi_2^\dagger\Phi_2)^2 \\ & + \lambda_3\Phi_1^\dagger\Phi_1 + \Phi_2^\dagger\Phi_2 + \lambda_4\Phi_1^\dagger\Phi_2 + \Phi_2^\dagger\Phi_1 + \frac{\lambda_5}{2}\left[(\Phi_1^\dagger\Phi_2)^2 + (\Phi_2^\dagger\Phi_1)^2\right], \end{aligned} \tag{2.4.2}$$

where m_{11}, m_{22}, and m_{12} denote the mass matrix parameters, and $\lambda_1 ... \lambda_5$ represent the scalar Higgs self-couplings.

There are eight field components for each of the scalar SU(2) doublets:

$$\Phi = \begin{pmatrix} \phi_a^+ \\ (v_a + \rho_a + i\eta_a)/\sqrt{2} \end{pmatrix}, a = 1, 2, \tag{2.4.3}$$

where v_a (a = 1, 2) are the VEVs of the $\phi_{1,2}$ fields. The ratio of the two vacuum expectation values is defined as $tan\beta = \frac{v2}{v1}$. The physical scalars are a lighter h and a heavier H, which are orthogonal combinations of ρ_1 and ρ_2:

$$h = \rho_1 \sin\alpha - \rho_2 \cos\alpha, \tag{2.4.4}$$

$$H = -\rho_1 \cos\alpha - \rho_2 \sin\alpha, \tag{2.4.5}$$

where α is the mixing angle between the two CP-even scalars. The physical pseudoscalar is defined by:

$$A = \eta_1 \sin\beta - \eta_2 \cos\beta. \tag{2.4.6}$$

In general, 2HDMs allow leading order diagrams with flavour changing neutral currents (FCNC), which have not been observed in nature. The Paschos-Glashow–Weinberg theorem [17, 18] addresses the FCNC issue. Fermions with the same quantum numbers coupling to the same scalar (Φ) allow avoiding FCNC which leads to several possible configurations: Type I, Type II, Type X (lepton specific) and Type Y (flipped model). Table 2.4.1 summarises the classification of which type of fermions couples to which Higgs doublet. In Type I 2HDM, the charged fermions only couple to the second doublet. In the Type II model, up- and down-type quarks couple to separate doublets. The Type I 2HDM in the quark sector is identical to the lepton-specific model.

One can find a Z_2 symmetry to realize one of these four modes. At tree level, the Yukawa coupling can be determined as follows [15]:

$$\begin{aligned} \mathcal{L}_{Yukawa}^{2HDM} = & -\Sigma_{f=u,d,l}\frac{m_f}{v}\left(\xi_h^f \bar{f} f h + \xi_H^f \bar{f} f H - i\xi_A^f \bar{f}\gamma_5 f A\right) \\ & - \frac{\sqrt{2}V_{ud}}{v}\bar{u}(m_u\xi_A^u P_L + m_d\xi_A^d P_R)dH^+ + \frac{\sqrt{2}m_l\xi_A^l}{v}\nu_L l_R H^+ + H.c.. \end{aligned} \tag{2.4.7}$$

Model	u_R^i	d_R^i	e_R^i
Type I	Φ_2	Φ_2	Φ_2
Type II	Φ_2	Φ_1	Φ_1
Lepton specific	Φ_2	Φ_2	Φ_1
Flipped	Φ_2	Φ_1	Φ_2

Table 2.4.1.: Models which lead to natural flavour conservation. The superscript i is a generation index.

The coupling of the fermion f to the Higgs boson is m_f/v. The parameters ξ_h^f, ξ_H^f, and ξ_A^f are the couplings of up-type quarks (u), down-type quarks (d), charged leptons (l) to the h, H, and A, which are summarised for the four different models in Table 2.4.2. $P_{L/R}$ are projection operators for left-/right-handed fermions. Regardless of the 2HDM type, the coupling of the Higgs bosons to the W and Z are the same: the coupling of the light Higgs (h) is $\kappa_h^V = \sin(\beta - \alpha)$, the coupling of the heavier Higgs (H) is $\kappa_H^V = \cos(\beta - \alpha)$, and the coupling of the derivative of pseudoscalar (A) to vector bosons vanishes due to the conservation of parity, $\kappa_A^V = 0$. As noted in the case of the alignment limit, when $\cos(\beta - \alpha) \to 0$, the lighter CP even Higgs boson h has exactly the same couplings as the SM-Higgs boson. In a similar fashion, when $\sin(\beta - \alpha) \to 0$, the heavier CP even boson (H) becomes SM-like, making the H boson state which can be identified as the observed $h(125)$ Higgs state.

	Type I	Type II	Lepton specific	Flipped
ξ_h^u	$\cos\alpha/\sin\beta$	$\cos\alpha/\sin\beta$	$\cos\alpha/\sin\beta$	$\cos\alpha/\sin\beta$
ξ_h^d	$\cos\alpha/\sin\beta$	-$\sin\alpha/\cos\beta$	$\cos\alpha/\sin\beta$	-$\sin\alpha/\cos\beta$
ξ_h^l	$\cos\alpha/\sin\beta$	-$\sin\alpha/\cos\beta$	-$\sin\alpha/\cos\beta$	$\cos\alpha/\sin\beta$
ξ_H^u	$\sin\alpha/\sin\beta$	$\sin\alpha/\sin\beta$	$\sin\alpha/\sin\beta$	$\sin\alpha/\sin\beta$
ξ_H^d	$\sin\alpha/\sin\beta$	$\cos\alpha/\cos\beta$	$\sin\alpha/\sin\beta$	$\cos\alpha/\cos\beta$
ξ_H^l	$\sin\alpha/sin\beta$	$\cos\alpha/\cos\beta$	$\cos\alpha/\cos\beta$	$\sin\alpha/\sin\beta$
ξ_A^u	$\cot\beta$	$\cot\beta$	$\cot\beta$	$\cot\beta$
ξ_A^d	-$\cot\beta$	$\tan\beta$	-$\cot\beta$	$\tan\beta$
ξ_A^l	-$\cot\beta$	$\tan\beta$	$\tan\beta$	-$\cot\beta$

Table 2.4.2.: Yukawa couplings of u, d, l to the neutral Higgs bosons h, H, A in the four different models [15].

Higgs Decays

The model has seven free parameters: the Higgs boson masses (m_h, m_H, m_A, $m_{H^\pm}$), the ratio of the vacuum expectation values of the two doublets (tanβ), the mixing angle between the CP-even Higgs bosons (α), and the potential parameter m_{12}^2 that mixes the two Higgs doublets. The branching ratios of heavy Higgs bosons decaying into lighter ones will not depend exclusively on the masses but also on α and β for each (pseudo)scalar (h, H, A), which are more complex.

In Type I 2HDM, the coupling of the light neutral Higgs (h) to fermions is the same as in the SM but multiplied by a ξ_h^f (which is $\cos\alpha/\sin\beta$), while its couplings to WW and ZZ are multiplied by $\sin(\beta-\alpha)$. For tan$\beta = 1$, the branching ratios of the light Higgs have been plotted in Figure 2.4.1. It indicates that $\alpha = \pm\, \pi/2$ is the fermiophobic limit (the branching ratio to fermions vanishes), and that $\alpha = \beta$ is the gauge-phobic limit (the branching ratios to WW and to ZZ vanish). The branching ratio to $\gamma\gamma$ at the gauge-phobic point is still there since there is a small contribution from top-quark loops. For larger values of tanβ, the coupling structure looks very similar, with slightly different slopes. Due to the coupling relations discussed above and neglecting additional decay modes, Figure 2.4.1 can also be used to describe the decays of the heavy Higgs boson H (with the given masses) if the graph is shifted to the left by $\pi/2$. The decay branching ratios of the pseudoscalar will be independent of α and β because there are no couplings to a pair of vector bosons, and all fermion couplings are scaled by the same factor cot(β).

In Type II 2HDM, the coupling of the light neutral Higgs (h) to fermions depends on the fermion charge. For example, the coupling of the up type quarks is the SM coupling times ξ_h^u, which is the same as in the Type I 2HDM, while the coupling of the down type quarks and of the leptons is the SM coupling times -sinα/cosβ. This means that the couplings of the down types quarks and of the leptons are larger in the Type II 2HDM when tanβ goes higher. The Type II 2HDM has the same couplings to gauge bosons as the Type I 2HDM. Figure 2.4.2 (a) shows the branching ratios of the light neutral Higgs for tanβ= 1, which is very similar to those of Type I 2HDM. However the branching ratio is strongly dependent on tanβ in the type II 2HDM case as shown in Figure 2.4.2 (b). Again, the couplings of the heavier scalar (H) are identical to those of the h after a $\pi/2$ shift.

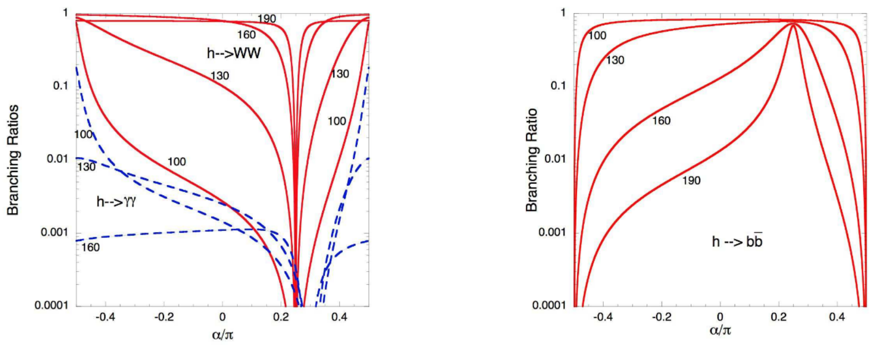

Figure 2.4.1.: The Type-I 2HDM light-Higgs branching ratios into W pairs, diphotons and $b\bar{b}$ are plotted as a function of α for tanβ= 1 and for various values of the Higgs mass [GeV]. In the left figure, the solid lines correspond to $h \to WW$ and the dashed lines to $h \to \gamma\gamma$. The branching ratio into Z pairs has the same ratio to the one into W pairs as in the SM. Image from Ref. [15].

Higgs Production

In 2HDM Type I or lepton-specific, the production cross section of a light Higgs (h) through gluon fusion would be calculated by multiplying the SM cross section by the factor $(\cos\alpha/sin\beta)^2$. Similarly in the Type 2HDM II or flipped, the contribution of the top quark is multiplied by the same factor, while the contribution of the b-quark is multiplied by a factor of -tanαtanβ since bottom Yukawa loop coupling becomes large at large tanβ.

The heavy neutral Higgs (H) has a similar production process. In the Type I or lepton-specific 2HDM, the cross section would be calculated by multiplying the SM production by the factor $(\sin\alpha/\sin\beta)^2$. In the Type II or flipped 2HDM, the factor is cotαtanβ.

When calculating the limits at a given choice of cos(β - α) and tanβ, the relative rates of ggF and VBF production in the fit are set to the prediction of the 2HDM for that

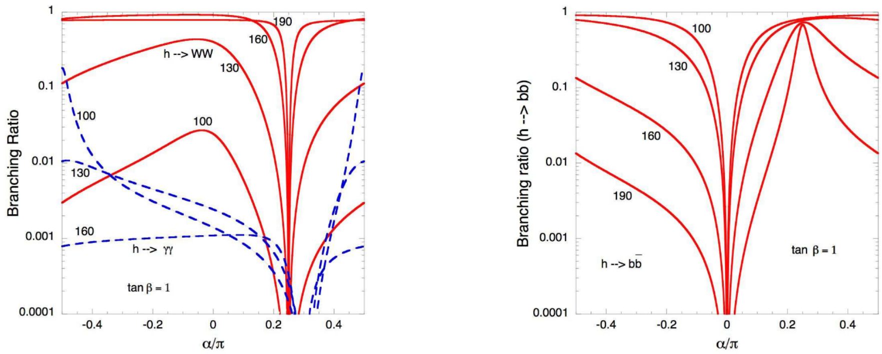

(a)

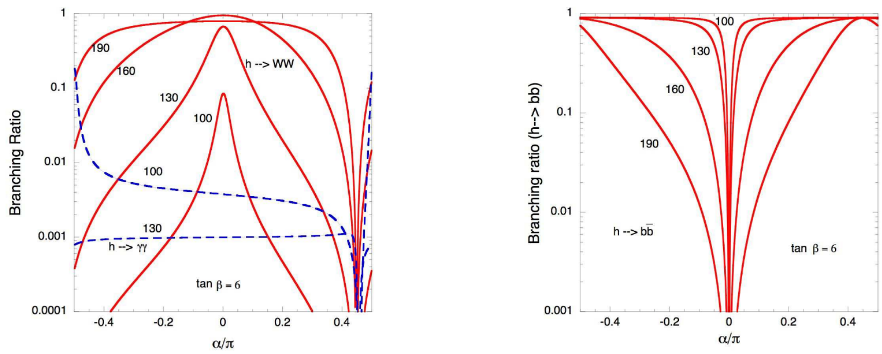

(b)

Figure 2.4.2.: The Type-II 2HDM light-Higgs branching ratios into W pairs, diphotons and $b\bar{b}$ are plotted as a function of α for tanβ= 1 (a) and for tanβ= 6 (b) and for various values of the Higgs mass [GeV]. In the left figure, the solid lines correspond to $h \to WW$ and the dashed lines to $h \to \gamma\gamma$. The branching ratio into Z pairs has the same ratio to the one into W pairs as in the SM. Image from Ref. [15].

parameter choice. The cross-section times branching ratio depending on the values of α and β for $H \rightarrow ZZ$ with $m_H = 200$ GeV varies from 2.4 fb to 10 pb for Type-I and from 0.5 fb to 9.4 pb for Type-II [19]. (The analysis discussed in this thesis only considers 2HDM Type-I and Type-II because the couplings to leptons do not matter in the context of $H \rightarrow ZZ$ process.)

2.5. Extra Dimensions and the Graviton: Randall-Sundrum Model

The answer to the question of the hierarchy between the electroweak scale (∼100 GeV) and the Planck scale ($M_{Pl} \sim 10^{19}$ GeV) is still open. A plausible explanation to the hierarchy problem comes from the existence of one or more extra dimensions. In 1687, Sir Isaac Newton published his law of gravity, which describes that the gravitational field strength decreases inversely with the square of the distance from the source. The surface of a sphere is $4\pi \times r^2$ (r = the radius of the surface. It is the same as Newton's radius). The sphere is a 3 dimensional object, meaning the gravity goes into three dimensions. However, Newton's law of gravity has been only tested to a precision of 10^{-4}, while the fine structure constant α_F is known to a precision of 10^{-10}. It is then conceived that gravity might behave differently at small distances, and an extra dimension with its size below the current experimental constraint can exist. This extra dimension can either have a flat space-time geometry (such as the so-called Large Extra Dimension model [20]) or a 'warped' geometry. This section will address the hierarchy problem by the warped space-time geometry in the Randall-Sundrum (RS) model [21].

The RS Model provides a slice of the warped geometry, AdS_5, connecting the Planck scale and the TeV scale. The 5d space-time interval is given by the following metric:

$$ds^2 = e^{-2kr_c\phi}\eta_{\mu\nu}dx^\mu dx^\nu + r_c^2 d\phi^2, \tag{2.5.1}$$

where k is the curvature scale of order the Planck scale, x^μ are space-time coordinates in 4-dim, which are related to the five-dimensional input, $r_c^2 d\phi^2$ refers to the fifth dimension, r_c indicates the size of the compactified radius, $0 \leq \phi \leq \pi$ is the coordinate for an extra dimension. Two branes are located at the endpoints ($\phi = 0$, π).

The SM fields are assumed to be confined to the TeV brane but they are phenomenologically allowed to propagate in the bulk if the extra dimensions are small enough, and this allows to address the fermion mass hierarchy. The scale of the hierarchy can be generated through the radius (r_c) of the fifth dimension: TeV/$M_{Pl} \sim e^{-k\pi r_c}$; $kr_c \approx 11$. The localization mechanism is responsible for the observed mass hierarchies. It also suppresses FCNCs [22].

The discussed model is based on the Randall-Sundrum (RS1) framework with the scenario that the graviton (zero-mode, $m_{graviton} = 0$) is localized near the UV/Planck brane, and the Higgs sector is localized near the IR/TeV brane where the energy is warped-down to the order TeV. The Kaluza-Klein (KK) particles are the excitation modes of the fields in the bulk. The masses of the fermions generated by Yukawa couplings interactions with the Higgs are on the IR brane. One can localize the light fermions close to the UV brane to make their effective Yukawa couplings hierarchically small. Hence, in this scenario, couplings of KK gravitons to light fermions are highly suppressed resulting in the fact that the $q\bar{q}$ production of gravitons at the LHC is negligible [21]. In contrast, the SM gluons have no such constraints. The gg coupling to KK graviton is suppressed only by the warp factor, which rescales gluon fields localised on the TeV brane. Thus, gg fusion is the non-negligible KK graviton production mode at the LHC.

One feature of the model is that KK gravitons have a mass ~TeV and are localized near the TeV brane so that KK graviton coupling to W, Z, top quark and Higgs is only ~TeV suppressed (instead of Planck scale suppressed). The KK gravitons (spin-2 resonances) can be reconstructed from their decay products. The graviton decays into longitudinal gauge bosons W/Z are dominant compared to those of the transverse W/Z channels as W_L/Z_L are effectively the *unphysical* Goldstone bosons. The partial decay width given the assumption of the Higgs localized on the TeV brane is:

$$\Gamma(G \to Z_L Z_L) \approx \frac{(cx_n^G)^2 m_n^G}{480\pi}, \tag{2.5.2}$$

where c $\equiv k/\bar{M}_{PI}$, x_n^G is a parameter that gives the masses of the KK graviton: $m_n^G = ke^{-k\pi R} x_n^G$.

Couplings of KK Graviton

A general formula for couplings of the bulk fields (denoted by F) to the KK gravitons (denoted by G) is:

$$\mathcal{L}_G = \Sigma_{m,n,q} C_{m,n,q}^{F,F,G} \frac{1}{M_P} \eta^{\eta\alpha} \eta^{\nu\beta} h_{\alpha\beta}^{(q)}(x) T_{\mu\nu}^{(m,n)}(x), \tag{2.5.3}$$

where $h_{\alpha\beta}^{(q)}$ corresponds to the q^{th} mode KK graviton interacting with the m^{th} and n^{th} modes of the guage field. $M_P \sim 2.4 \times 10^{18}$ GeV is the reduced 4-dim Planck scale, η is the 4-dim Minkowski metric, $T_{\mu\nu}^{(m,n)}$ is the 4-dim energy-momentum tensor that includes the contribution from the gluon and W/Z bosons. $C_{m,n,q}^{F,F,G}$ comes from the overlapping of particles' wave functions in the 5^{th} dimension. By keeping the 5-dim dependence in $C_{m,n,q}^{F,F,G}$, the $T_{\mu\nu}$ represents as the usual 4-dim couplings. The production is dominated by gluon fusion due to Yukawa-suppressed $q\bar{q}$ annihilation to KK graviton.

The relevant matrix elements for the process $gg \to$ VV, with V = W, Z via KK graviton are [21]:

$$\mathcal{M}_{\lambda_1\lambda_2\lambda_3\lambda_4}^{G}(g^a g^b \to VV) = -C_{00n}^{AAG} e^{-k\pi R} (\frac{x_n^G c}{m_n^G})^2 \times \Sigma_n \frac{\delta_{ab}[\mathcal{A}_{\lambda_1\lambda_2\lambda_3\lambda_4}]}{\hat{s} - m_n^2 + i\Gamma_G m_n}, \tag{2.5.4}$$

where λ_i refer to initial and final state polarizations. a, b are colour factors. Γ_G is the total decay width of KK graviton, which is $13(cx_n^G)^2 m_n^G/960\pi$. $\mathcal{A}$ is the amplitude of the production.

Theoretical predictions of the graviton production cross-section times ZZ branching ratio for the model used in the $\ell\ell + E_{\mathrm{T}}^{\mathrm{miss}}$ search (assuming $k/\bar{M}_{PI} = 1$) [1] are in the range from around 1.3 pb to 1 fb for a graviton mass range of 600−2000 GeV [21].

Chapter 3

The ATLAS Experiment at the LHC

The Large Hadron Collider (LHC) [23] is a particle accelerator, 27 kilometres in circumference, located on the border of France and Switzerland near Geneva. In the LHC, two beams move in opposite directions and are accelerated to near the speed of light. The beams contain protons which are bundled in bunches, and each bunch contains around 100 billion protons. At four collision points, the beams cross and protons collide with each other. To capture their collisions, there are four detectors which provide information about the resultant particles including their trajectory, electrical charge, and energy. The four detectors are called A Large Ion Collider Experiment (ALICE), A Toroidal LHC ApparatuS (ATLAS), Compact Muon Solenoid (CMS) and LHCb which stands for LHC beauty. However, in most collisions, the two protons beams pass through each other without any significant outcome. To produce enough events of a certain process, one needs either a large enough hadronic cross-section (by increasing the centre of mass energy), a large luminosity, or both. To make a new heavy particle, highly energetic colliding particles are required according to Einstein's equation, $\mathrm{E} = \mathrm{mc}^2$. The strategy in terms of increasing energy is described in Section 3.1 and luminosity is described in Section 3.2, followed by the ATLAS detector including different detecting subsystems in Section 3.3. The trigger which selects the interesting collision events, and the data acquisition system which is responsible for collecting the data recorded by the detectors is given in Section 3.4.

3.1. Accelerator

The LHC is a synchrotron designed to produce pp collisions at an energy of 7 TeV per proton. The hydrogen atoms are first ionized in an electric field and pre-accelerated through a series of accelerators: the linear accelerator (Linac 2), the Proton Synchrotron Booster (PSB), Proton Synchrotron (PS), and the Super Proton Synchrotron (SPS). The proton energy is increased to 450 GeV in the SPS and the beam is passed into the LHC main ring as shown in Figure 3.1.1. The LHC's radio-frequency (RF) cavities bring the energy of the protons up to 6.5 TeV. The LHC was designed for a collision energy of 14 TeV, but it has only reached 13 TeV, due to magnet limitations.

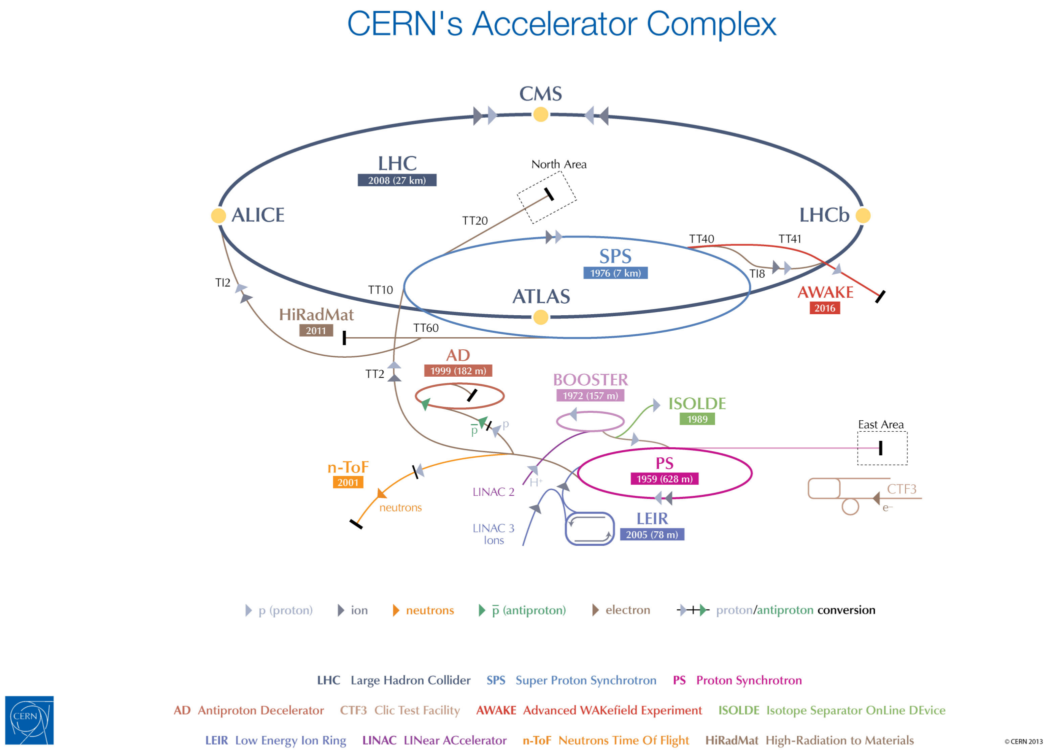

Figure 3.1.1.: The LHC accelerator system. Image from Ref. [24].

Radiofrequency (RF) cavities take radio waves of all frequencies and amplify them into one resonant frequency producing a strong electric field. This amplification is based on the shape of the cavity. In the LHC, per round, each proton experiences a maximum voltage of 16 mega-volts (MV) given eight cavities of 2 MV voltage each at a radio frequency of 400 MHz (f_{RF}). A particle synchronised with the RF is called a synchronous particle. All the other particles in the accelerator will oscillate around this synchronous point. This means the particles will 'clumped' around the synchronous particle in a bunch. The spacing between proton bunches in the LHC is 25 ns, determined at the PS and SPS pre-acceleration stages before injection into the LHC ring.

As the energy of the beam increases, the strength of the magnetic fields also has to increase to make the beam travel in a circle. The main dipole magnets with 8.3 Tesla magnetic field are used to bend the paths of the particles, and quadrupoles help focus the proton beam with the aim of increasing the chance of proton-proton collisions. Figure 3.1.2 illustrates a quadrupole magnet focusing in one plane and defocussing in the other. Pairs of quadrupole magnets work together around the beam pipe to squeeze the beam both vertically and horizontally.

3.2. Luminosity

The luminosity is used to describe the number of particles per meter squared per second in a beam. The LHC instantaneous luminosity ($\mathcal{L}$) can approximately be given by assuming that the colliding beams follow Gaussian distributions in the x and y components. The instantaneous luminosity depends on the number of protons in respective bunches (N_1 and

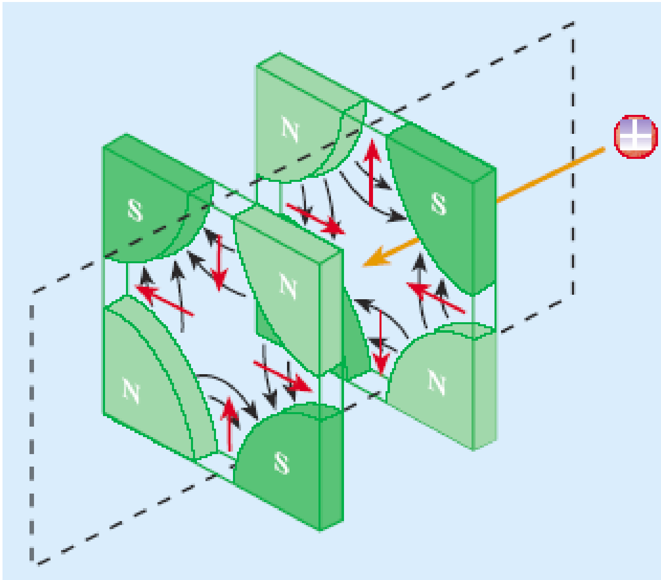

(a)

Figure 3.1.2.: Quadrupole magnets. The positive particles (protons in LHC) come from the right. The first quadrupole takes control of the beam width while the second one does the same with the beam height [25].

N_2 as there can be a different number of protons per crossing bunch), the cross-sectional size of the bunch (σ) and the revolution frequency (f_{rev}):

$$\mathcal{L} \approx \frac{N_1 N_2 f_{rev}}{4\pi\sigma_x\sigma_y} \tag{3.2.1}$$

One of the beam properties used to describe the average spread of particles in position-and-momentum phase space is called beam emittance (ε) with units of length (or length $\times$ angle). Figure 3.2.1 shows the emittance as the area of an ellipse where each particle corresponds to a pair of (x, x') values on the phase-space plot where x describes the position and x' describes its angle w.r.t the central path of the proton. The beam dimension projected onto the x-axis is $2\sqrt{\varepsilon\beta}$. The bunch cross-section is therefore determined by squaring the beam dimension, $4\varepsilon\beta$. The amplitude function, β, is determined by the accelerator magnet configuration (the β minima are at the collision point, and the β is increased with the distance depending on the quadrupole magnet arrangement). By comparing the bunch cross-section, $4\pi\sigma^2$ and $4\varepsilon\beta$, β can be expressed in terms of σ and ε:

$$\beta = \frac{\pi\sigma^2}{\varepsilon} \tag{3.2.2}$$

Apart from making high population bunches (N) of low emittance collide at high frequency, squeezing the beam as much as possible before the interaction point will help increasing the number of collisions. The value of the amplitude function at the interaction point (β^*) can be used to describe the LHC luminosity:

$$\mathcal{L} = \frac{N_b^2 n_b f_{rev}\gamma_r}{4\pi\varepsilon_n\beta^*}F \tag{3.2.3}$$

where N_b is the number of particles per bunch, n_b is the number of bunches per beam, f_{rev} is the revolution frequency of the proton, γ_r is the relativistic gamma factor, ε_n is the normalized transverse beam emittance, β^* is the beta function at the collision point, and F is the geometric luminosity reduction fraction due to the crossing angle at the interaction point.

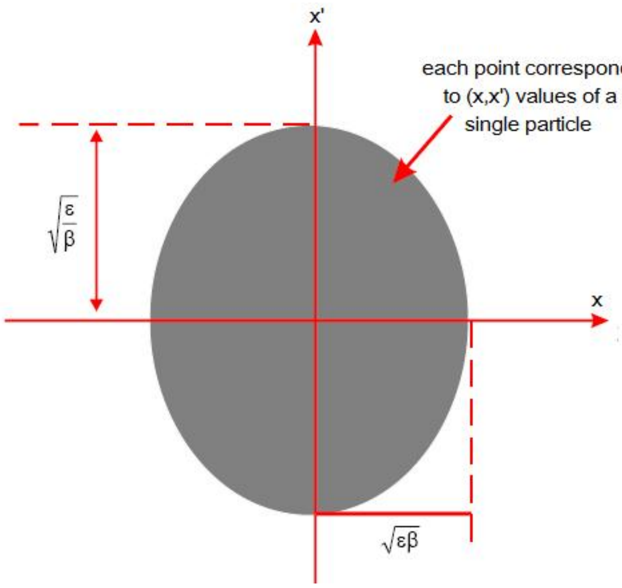

(a)

Figure 3.2.1.: The emittance is the area (length x $\times$ angle x') of the ellipse [26].

The LHC design peak luminosity is 10^{34} cm^{-2}s^{-1}. This number corresponds to $\beta^* = 0.55$ m, $\varepsilon_n = 3.75$ μm, $f_{rev} = 11.2$ kHz, 2808 bunches per proton beam and 10^{11} protons per bunch. The actual instantaneous luminosity that can be reached is larger, and it decreases with time for each LHC fill. For example, the LHC reached a peak luminosity of 1.5×10^{34} in 2017 and 2×10^{34} cm^{-2}s^{-1} in 2018.

The integrated luminosity (L), which is directly related to the number of observed events associated with a certain process over the sensitive time, i.e., excluding dead-time and operational problems of a machine, is defined by integrating the instantaneous luminosity over time:

$$L = \int_0^t \mathcal{L} dt \tag{3.2.4}$$

The integrated luminosity is shown in Figure 3.2.2. A total of 156 fb^{-1} of data was delivered to the ATLAS and CMS detectors for the full Run-2 (2015−2018). Of this, a total of 147 fb^{-1} of data was recorded by ATLAS.

A large luminosity comes with a price as multiple pp interactions may occur simultaneously per bunch crossing, this is called pile-up. The methods to mitigate pile-up effects are described in Section 5.4.2.

The High-Luminosity Large Hadron Collider

The HL-LHC aims to increase the instantaneous luminosity and to produce ∼3000 fb^{-1} of data between 2027 and 2037, increasing the potential for precision measurements of the SM, including the Higgs boson and to find rare new processes. In order to do so, parts of the LHC will have to be upgraded. To achieve the desired higher luminosity, one will

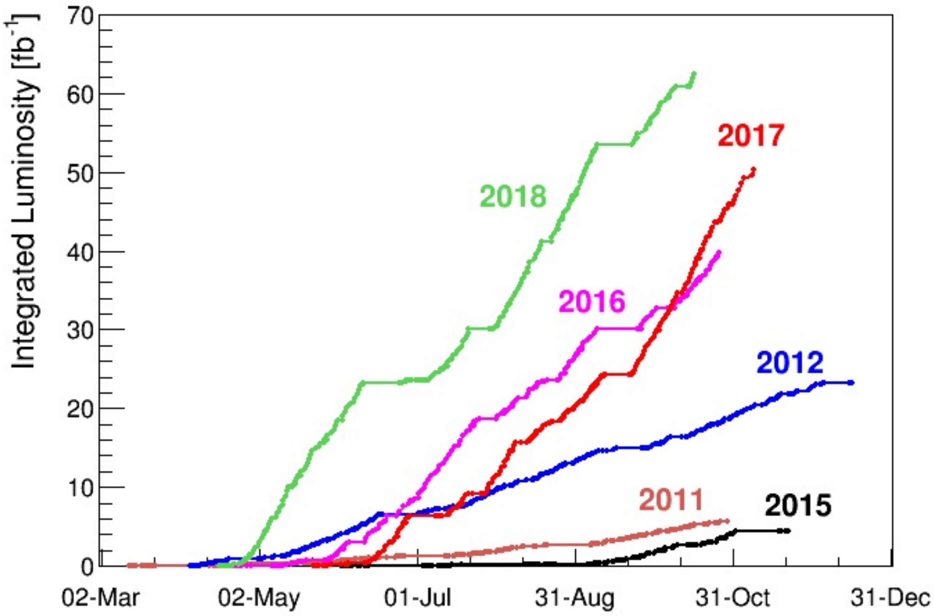

Figure 3.2.2.: Integrated luminosity delivered by the LHC machine to the ATLAS and CMS detectors experiments during the 2011 to 2018 runs [27].

for example require a series of focusing magnets that are more powerful than the existing LHC magnets. Improving the technology in the accelerator is not enough, the detectors which were designed for the original LHC must also be upgraded. The original detectors are not able to handle the increase in luminosity, therefore, the tracking system will have to be replaced entirely, using different detector techniques to deal with the issues of high occupancy and radiation damage.

3.3. The ATLAS Detector

The ATLAS detector (Figure 3.3.1) has a forward-backward symmetric, cylindrical geometry around the interaction point. The detector is 44 meters long and 25 meters high and was designed to probe particles produced at the centre of the detector. ATLAS uses a standard right-handed coordinate system. The coordinate system is defined with the positive x-axis pointing inward to the centre of the LHC, the y-axis is defined as pointing upwards, and so the z-axis is along the beam direction. The polar angle θ is measured from the z-axis ($0 \leq \theta \leq \pi$) while the azimuthal angle ϕ is measured from the x-axis in the x-y plane ($0 \leq \phi \leq 2\pi$). Instead of the angle θ, usually the rapidity (or pseudo-rapidity) of an object is used. This is because the shape of the rapidity (or pseudo-rapidity) distribution remains unchanged under a longitudinal Lorentz boost. The definition of the rapidity is:

$$\begin{aligned} y &= \frac{1}{2}\ln\left(\frac{E+p_z}{E-p_z}\right), \\ &= \frac{1}{2}\ln\left[\frac{\sqrt{m^2+p^2}+p\cos\theta}{\sqrt{m^2+p^2}-p\cos\theta}\right]. \end{aligned} \tag{3.3.1}$$

At very high energy (p $\gg$ m), the rapidity can be approximated as the pseudo-rapidity,

$\eta \equiv -ln\left[tan(\frac{\theta}{2})\right]$. The tangent is defined by a transverse distance over a longitudinal distance where the longitudinal distance gets a factor γ under a Lorentz boost:

$$tan\theta \sim \frac{\Delta x_T}{\Delta x_L} \to tan\theta' \sim \frac{\Delta x_T}{\Delta x_L/\gamma} = \gamma tan\theta. \tag{3.3.2}$$

The γ factor will be cancelled out when taking the difference of pseudorapidity of two particles, $\eta_1 - \eta_2 = \eta_1^{'} - \eta_2^{'}$.

The angular distance ΔR between two particles is defined as $\Delta R \equiv \sqrt{(\Delta\eta)^2 + (\Delta\phi)^2}$. The transverse momentum is the component of the particle momentum vector in the x-y plane. The vector sum of the transverse momenta is zero both initially and after collisions, so any imbalance in p_{T} is accounted as the missing transverse momentum.

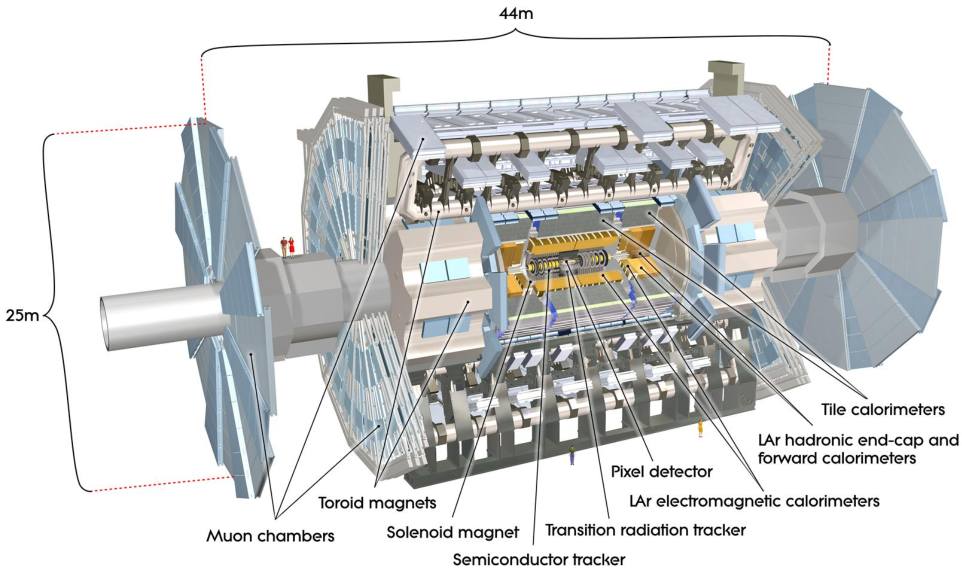

(a)

Figure 3.3.1.: ATLAS detector. Image from Ref. [28].

The magnet configuration shapes the design of the detector consisting of a central solenoid, two end-cap toroids, and a barrel toroid. The 2.6 T solenoidal magnet surrounds the ATLAS tracking detector with the capability to bend the tracks of the charged particles such that the momentum can be measured from their trajectories. The eight-fold toroidal magnets generate approximately 0.5 and 1 T magnetic fields [29] for the muon detector in the barrel ($|\eta| < 1.05$) and end-cap ($1.4 < |\eta| < 2.7$) regions, respectively. These magnets are assembled around the calorimeters.

The ATLAS detector is designed in order to exploit two features. Charged particles ionize the tracking system, and both neutral and charged particles interact with calorimeters generating more particles in the form of particle showers. Figure 3.3.2 shows that electrons, muons, and charged hadrons leave a track in the tracking system while photons, neutrinos and neutral hadrons do not interact in this way. The tracking system will be explained in Section 3.3.1. Electrons and photons induce particle showers over shorter distances while hadrons penetrate deeply into the detector. The calorimeter system will be detailed in Section 3.3.2. Muons ionize but they do not produce showers. The design of the muon spectrometer is described in Section 3.3.3. Neutrinos neither ionize nor shower.

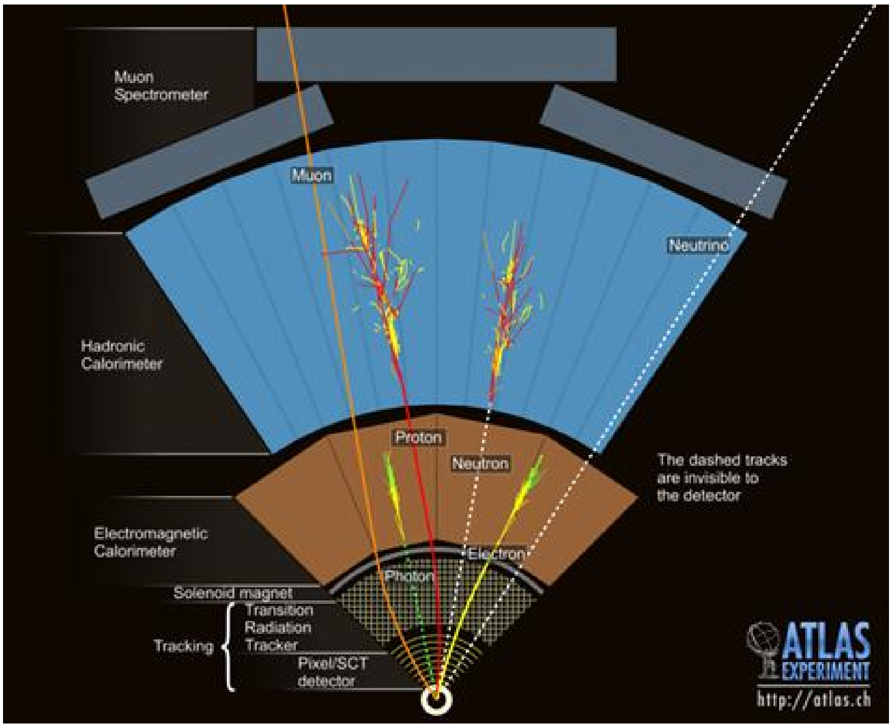

Figure 3.3.2.: ATLAS detector with particle tracks and showers. Image from Ref. [30].

3.3.1. Tracking System

The ATLAS Inner Detector (ID) [31, 32] consists of the Pixel Detector (the Insertable B-Layer (IBL) is part of it) which is the closest detector to the interaction point, the silicon strip (SCT) detector which surrounds the Pixel Detector, and the transition radiation tracker (TRT) which is outside the silicon detector as illustrated in Figure 3.3.3 with the various radii for each layer. The ID provides charged particle tracking coverage in the range of $|\eta| < 2.5$.

The binary (or ternary in some cases) signals, hits, in each detector are used to reconstruct the tracks of charged particles. For clear pattern recognition, one wants either low detector occupancy by having a highly granular detector, or large hit redundancy by giving a large number of detecting layers.

Pixel Detector

The high granularity and fast response of the Pixel Detector are required in order to have a precise and efficient measurement of the trajectories originating from the interaction region. Moreover, radiation hard technologies and an efficient cooling system for high power density are needed to handle the estimated charged particle fluxes.

The Pixel Detector is subdivided into three barrel layers at radii 50.8, 88.5 and 122.5 mm (the IBL is placed at 33.25 mm), and three disks on either side for the forward direction at a distance of 49.5, 58, and 65 cm.

The Pixel Detector is designed to provide three measurement points per track in the pseudo-rapidity region $|\eta| < 2$. The pixel principle is to segment a diode in two dimensions instead of strips measuring in one dimension. This allows for better pattern recognition. A cross-sectional view of a pixel module is shown in Figure 3.3.4. The sensor is subdivided

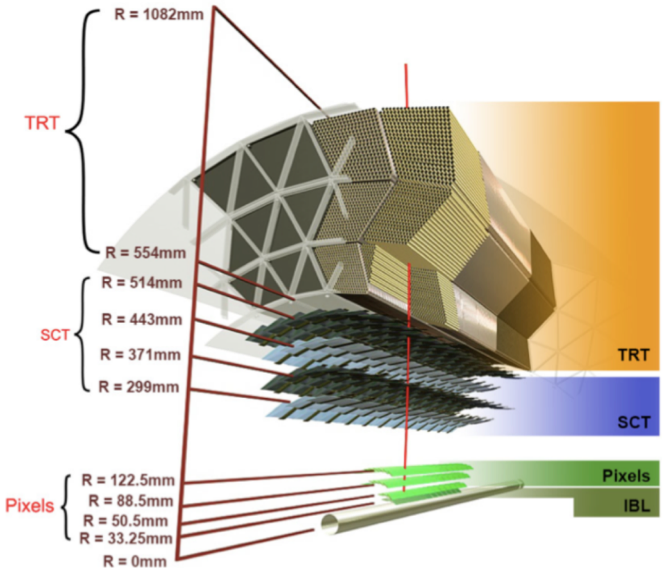

(a)

Figure 3.3.3.: The beam pipe, the IBL, three Pixel layers, four cylindrical layers of the SCT and the TRT are shown for the ID in the barrel region. Image from Ref. [33].

into 47,232 (328 × 144) pixels which are connected individually to 16 front-end (FE) chips using bump bonding. The typical pixel size is ∼50 × 400 μm^2 (50 × 600 μm^2 pixels in gaps between FE chips). The maximum occupancy is expected in the innermost barrel layer, making pixel segmentation in this radial range mandatory. The achieved occupancy is $\sim 5 \times 10^{-4}$ per pixel.

The area of a single silicon sensor is approximately 2 × 6 cm^2. The sensors are 250 μm thick, using oxygenated n-type bulk material to enhance the radiation hardness combined with readout pixels on the n^+-implanted side of the detector to improve position resolution. The advantage of the $n^+ - in - n$ sensors is that after irradiation with high particle fluxes (the n-doped silicon becomes effectively p doped), the sensor's depletion region grows from the pixel electrode side into the sensor such that the drifting charge carriers are still seen by the electrodes, which is not necessarily the case for $p^+ - in - n$ sensor types (it depends on the applied depletion voltage).

Each FE chip is connected to 2880 pixels with a data transfer rate at about 40 - 160 MHz depending on the layer. The 80 million readout channels are arranged into 67 million pixels in three cylindrical barrel layers and 13 million in its end-cap disk layers.

Silicon Strip Tracker

The Semiconductor Tracker (SCT) is the middle layer of the ID. The SCT is made of four barrel layers and nine end-cap disks on each side. The barrel layers are placed at radii between 299 mm and 514 mm while the end-cap discs cover a tracking volume in the range from 854 mm to 2720 mm in the $|z|$ direction. The SCT modules use segmented 80 μm pitch strips in the barrel and 70-90 μm pitch strips in the end-cap disks. To provide two-dimensional hit information, the silicon modules consist of pairs of micro-strip sensors. The sensors are glued back-to-back at a 40 mrad stereo angle to build space-points. Typically there are eight strip measurements corresponding to four space-points in the SCT to provide the information of particles originating in the beam-interaction region.

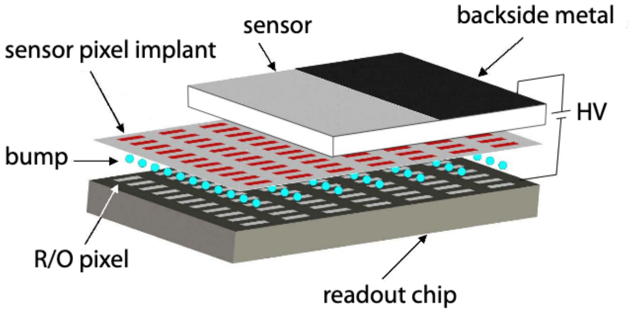

(a)

Figure 3.3.4.: The sensor and electronics chip (readout chip) have pixels of the same size, bonded to each other by means of bump contacts. Each read-out pixel corresponds to a front-end channel. Image from Ref. [34].

Transition Radiation Tracker

At larger radii, the TRT comprises many layers of proportional drift tubes (‘straws’) with a diameter of 4 mm interleaved with transition radiation material made from polypropylene foils (end-cap) or fibres (barrel). A charged particle passing through the straw ionizes the gas creating ionization clusters, and free electrons drift towards a wire at the centre of the tube and cascade in the electric field, producing a signal that is used for tracking. The space between the straws is filled with a material that can cause a charged relativistic particle to radiate a photon. The photons can ionize the Xe in the gas mixture, resulting in a larger signal. Lighter, more relativistic particles such as electrons radiate more energy in the foil than heavier particles such as pions, allowing for electron-pion discrimination. To exploit this effect, the readout defines both a low-level and high-level threshold in order to identify the presence of more transition radiation in a straw.

3.3.2. Calorimeter System

The ATLAS calorimeter system is designed to measure the energy of produced particles including both charged and neutral particles. The produced particle interacts with dense matter and produces a cascade of secondary particles with lower energies, which further can produce more particles. Depending on the particle, the cascade processes form electromagnetic and hadronic showers.

To fully stop these particles, the ATLAS calorimeters are built with large sampling, which consists of alternating layers of absorbers and active materials with full ϕ symmetry and coverage around the beam axis. The layout of the sampling calorimeters is shown in Figure 3.3.5. The electromagnetic calorimeter (EMCal) surrounds the ID and covers the region $|\eta| < 1.475$ and $1.375 < |\eta| < 3.2$ for the electromagnetic interaction. The hadronic calorimeter (HCal) is placed outside the EMCal. The HCal for measuring hadrons through their strong interactions includes the tile calorimeter [35] in the central regions and extended barrels. It also includes two liquid-argon (LAr) [36] hadronic end-cap calorimeters (HEC) and the liquid-argon (LAr) forward calorimeter (FCal) in the end-caps. The information on the particles’ direction can also be derived from the segmented structure of the calorimeters.

The generic parametrisation of relative energy resolution is given by (for both sampling

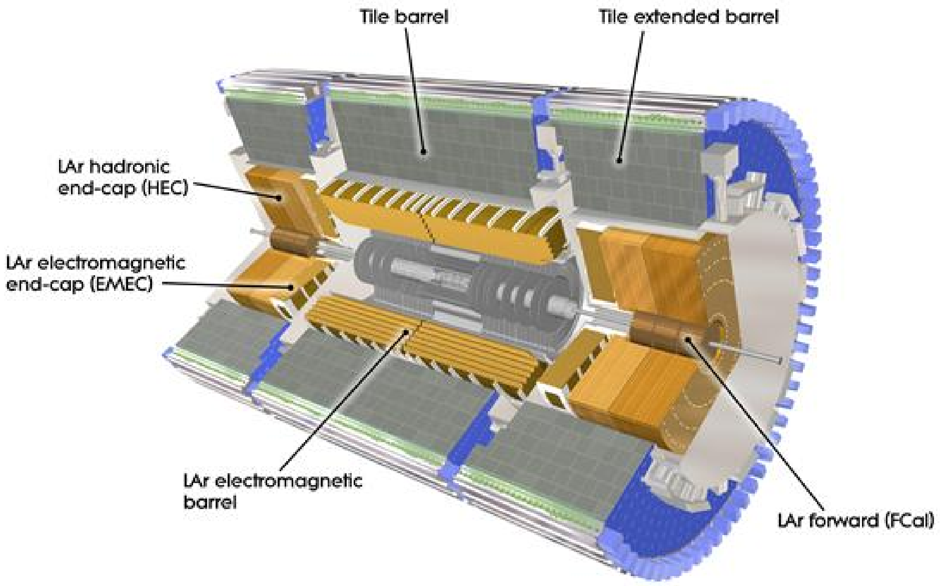

(a)

Figure 3.3.5.: A view of the ATLAS calorimeter system [37].

and homogeneous calorimeters [1]):

$$\frac{\sigma(E_0)}{E_0} = \frac{a}{\sqrt{E_0}} \oplus \frac{b}{E_0} \oplus c \tag{3.3.3}$$

where a, b and c represent the stochastic, noise and constant terms of the energy resolution, respectively. It is assumed that the interaction with the active material ($E_0 \propto N_{tot}$) follows a Poisson distribution with the relation of $\sigma(E_0) \propto N_{tot} \propto \sqrt{N_{tot}}$.

Eq. 3.3.3 shows that the higher the particle's energy, the better the energy resolution.

Electromagnetic Calorimeter

The main goal of an EMCal is to identify electromagnetic showers initiated by electrons or photons and to measure their energy. There are two main types of interactions produced via the electromagnetic force in the EMCal: pair production and bremsstrahlung.

For photons, the pair production is the dominant radiative process at high energy (above $\mathcal{O}$(10 MeV) in lead) [38] . If the photon interacts with an atomic nucleus, the remaining energy of the photon can be converted into an electron-positron pair. Photons can also lose their energy through Compton Scattering (γ + e $\rightarrow \gamma'$ + e') or the photo-electric effect (γ + Z $\rightarrow Z^+ + e^-$). Below $\mathcal{O}$(1 MeV), the photo-electric effect is the dominant form of interaction.

For electrons there are two dominant effects through which electrons lose energy in the interaction with matter: ionization/excitation of atoms (Compton Scattering) or

[1]Homogeneous calorimeters are full absorption detectors, one single active medium for both energy degradation and signal generation. Usually, sampling calorimeters are more compact and cost-effective than homogeneous calorimeters.

Bremsstrahlung. If an electron encounters an atomic nucleus, and its energy E_e is above some critical energy E_c, it will be deflected and produce electromagnetic radiation, which is called Bremsstrahlung. On the other hand, electrons lose energy via ionization if $E_e < E_c$. The critical energy E_c for the electrons is approximated as:

$$E_c = \frac{800\ \text{MeV}}{Z + 1.2}, \tag{3.3.4}$$

where Z is the atomic number of the interacting material. In the ATLAS EMCal the high energy electrons and photons pass through several layers of active material creating large showers before they are eventually stopped. The energy of electrons and photons decreases exponentially:

$$E(x) = E_0 e^{-x/X_0}, \tag{3.3.5}$$

where X_0 is defined to quantify the radiation length where the number of particles double and the energy half (if only pair production and bremsstrahlung are considered), x is the distance that the particle travels and E_0 is the particle's original energy. An electron loses about 2/3 of its original energy on average when emitting photons and photons have a probability of 7/9 for pair production in one radiation length (X_0). For Z > 4, X_0 can be approximated using the following expression:

$$\frac{1}{X_0} = 4\left(\frac{\hbar}{m_e c}\right)^2 Z(Z+1)\alpha^3 n_a log(\frac{183}{Z^{1/3}}), \tag{3.3.6}$$

where Z is the atomic number, n_a is the number density of the nucleus, $\hbar$ is the reduced Planck constant, m_e is the electron rest mass, c the speed of light, and α is the fine structure constant. In principle, photons and electrons are completely stopped in 20 X_0 within the EMCal.

Electrons and photons primarily interact in the lead absorber and the outgoing charged particles ionize the LAr. Electrons then drift in the LAr gap and produce the signal on the readout electrodes. To get a fast charge collection, the EMCal is designed in an accordion-shape with the additional advantage of full coverage in ϕ without any cracks. The central EMCal is made of two half-barrels, each half-barrel is made of 1024 accordion shaped absorbers interleaved with readout electrodes. The total thickness is 24 radiation lengths X_0 in the barrel and 26 X_0 in the end-caps.

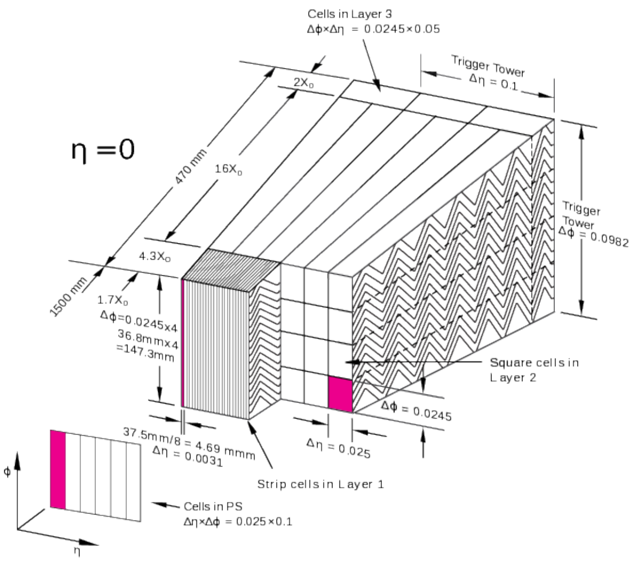

(a)

Figure 3.3.6.: A view of the EMCal module located at $\eta = 0$ in the barrel. Image from Ref. [33].

The energy resolution (Equation 3.3.3) in the barrel has been studied as a function of energy in the range from 10 to 245 GeV at $\eta = 0.687$. The values of a and c, after noise subtraction (the noise term b is around 200 MeV), are obtained from the CERN SPS H8 and H6 beam lines, using electrons and positrons, and the results are in agreement with the Monte-Carlo simulations of the test-beam set-up [29]:

$$\frac{\sigma(E_0)}{E_0} = \frac{10\%}{\sqrt{E_0}} \oplus 0.2\% \tag{3.3.7}$$

The EMCal is segmented in the (η, ϕ) direction. The first layer is finely segmented in η as shown in Figure 3.3.6 in the $0 < \eta < 1.5$ region, which can help to distinguish single photons from pions decaying into two photons.

Hadronic Calorimeter

Hadronic showers are initiated by the hadrons (e.g., p, n, π, K...) through various processes, which make them more complex than electromagnetic cascades. The resulting showers contain hadronic particles, nucleus fragments, secondary particles, such as electromagnetic components generated from neutral pions, and invisible energy (neutrinos). The hadronic shower development is parametrised in terms of nuclear interaction length, λ (analogous to X_0), which is given by:

$$\lambda = \frac{A}{n_a \sigma_{inel}} \tag{3.3.8}$$

where $\sigma_{inel} \approx \sigma_0 A^{0.7}$ indicates that the cross-section is independent of the energy of the incident hadrons (e.g., n, π, K...). $\sigma_0 \approx 35$ mb. A is the mass number of the nucleus. n_a is the number density of the nucleus.

Due to long interaction lengths ($10\lambda_{int} \sim 1-2$ m), hadronic calorimeters are always sampling, otherwise the absorber would be too heavy. The sampling tile calorimeter is one of the HCal sub-detectors. It covers the region $|\eta| < 1.7$ and is located behind the LAr EMCal. The tile calorimeter is divided into a central barrel region, 5.8 m in length, and two extended barrels, each 2.6 m in length. The HEC sits in the pseudo-rapidity range of $1.5 < |\eta| < 3.2$ and the FCal is located in the range of $3.1 < |\eta| < 4.9$ as shown in Figure 3.3.5.

The barrel calorimeter uses steel as the absorber and a scintillator as the active material. The HEC consists of two wheels in each end-cap, HEC1 and HEC2, and is a copper/LAr sampling calorimeter. The FCal is segmented into three 45 cm radiation length modules, FCal1, FCal2, and FCal3. FCal1 uses copper (A = 63.55) as the absorber while FCal2 and FCal3 mainly use tungsten (A = 183.85). The FCal is important for detecting physics processes with forward 'jets' (see Section 5.4) such as in VBF Higgs production. The HCal has a coarser granularity than the EMCal.

It is important to have good pion measurements in the calorimeters for jets. The performance of the fractional energy resolution expressed in Equation 3.3.3 for the combined barrel LAr electromagnetic and tile calorimeter with electronic noise is [29]:

$$\frac{\sigma(E_0)}{E_0} = \frac{52\%}{\sqrt{E_0}} \oplus \frac{1.6}{E_0} \oplus 3\% \tag{3.3.9}$$

The stochastic and constant terms, after noise subtraction, for the HEC are [29]:

$$\frac{\sigma(E_0)}{E_0} = \frac{70.6\%}{\sqrt{E_0}} \oplus 5.8\% \tag{3.3.10}$$

For the FCal using a more sophisticated technique, the stochastic term and constant term can be reduced to [29]:

$$\frac{\sigma(E_0)}{E_0} = \frac{70\%}{\sqrt{E_0}} \oplus 3\% \tag{3.3.11}$$

The expression of the resolution in Eq. 3.3.10 and 3.3.11 are based on test beam measurements after noise subtraction.

3.3.3. Muon Spectrometer

Muons lose energy mainly via ionization (they do not produce showers) which is well-described by the Bethe-Bloch equation [39]. Muons interact electromagnetically but they only radiate a small fraction of their energy when passing through matter due to their high mass. They are 200 times heavier and therefore radiate 40,000 times less energy than electrons, which makes muons penetrating particles.

The muon systems [40] are placed in the outer part of the ATLAS detector and are designed to detect tracks in the pseudo-rapidity range $|\eta| < 2.7$ in a magnetic field of around 2 T. The chambers in the barrel are placed at three different radii of approximately 5, 7.5, and 10 m as illustrated in Figure 3.3.7. Muon chambers form large wheels in the two end-cap regions that are located at distances of $|z| \approx 7.4$, 14, and 21.5 m from the interaction point. The muon detectors trace a muon's path by tracking its position through hits from the passage of a muon in each station. This corresponds to a momentum measurement as muons with more momentum bend less in the magnetic field.

The muon systems consist of two types of systems of precision-tracking chambers:

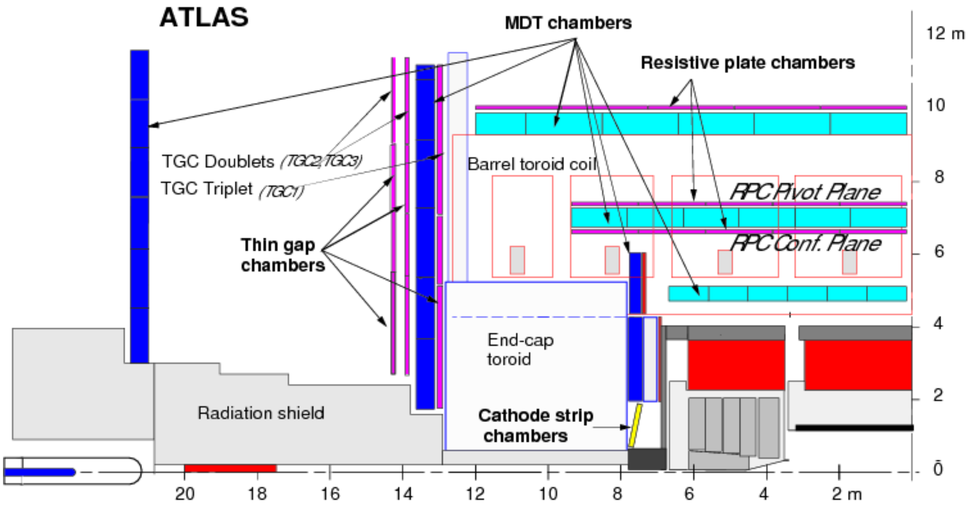

(a)

Figure 3.3.7.: A schematic representation of the muon spectrometer in the z-y projections [41].

- Monitored Drift Tubes (MDTs) consist of multiple layers of aluminium tubes and cover the region $|\eta| < 2.7$. (The coverage is limited up to $|\eta| < 2.0$ in the innermost end-cap tracking layer.)

- Cathode Strip Chambers (CSCs) are multi-wire proportional chambers, which help with resolving multi-track ambiguities and are placed in the forward region of the inner-most tracking layer where the occupancy is relatively high. (The CSC covers the region $2 < |\eta| < 2.7$.)

There also are two types of independent fast trigger chambers which can deliver track information within a few tens of nanoseconds:

- Resistive Plate Chambers (RPCs) are in the barrel, in the region $|\eta| < 1.05$. RPCs are made out of two parallel electrode-plates separated by a spacing of 2 mm which is filled with a gas mixture.

- Thin Gap Chambers (TGCs) are multi-wire proportional chambers which have better resolution than RPCs and are located in the end-caps, in the region $1.05 < |\eta| < 2.4$.

The chamber resolution and the intrinsic time in which the signal is converted into binary numbers are summarised in Table 3.3.1 [33].

		Chamber resolution (RMS) in		
Type	Function	Z/R	ϕ	time
MDT	tracking	35 μm (Z)	–	–
CSC	tracking	40 μm (R)	5 mm	7 ns
RPC	trigger	10 mm (Z)	10 mm	1.5 ns
TGC	trigger	2-6 mm (R)	3-7 mm	4 ns

Table 3.3.1.: Parameters of the four sub-systems of the muon detector.

3.4. Trigger and Data Acquisition

Due to the enormous amount of data taken by the ATLAS detector, it is impossible to archive and then reprocess data offline with a rate of 40 MHz (LHC bunch crossing frequency). Therefore, ATLAS has implemented a trigger and Data Acquisition (TDAQ) system to receive and interpret sensor signals from the detector and convert them at a high rate, together with event filters, into a dataset [42]. This dataset can then be analysed for the diverse physics programs. The trigger system is designed to retain a high efficiency for signals of interest, fast execution time, as well as achieve high rejection rates for pile-up, detector noise, and low-p_{T} QCD processes. Data acquisition systems must be robust against varying data-taking conditions and detector problems while minimizing dead-time. The sources of the dead-time come from computer or detector downtime, or operational dead-time, such as starting/stopping data-taking periods and trigger vetoes.

Figure 3.4.1 shows the principal block diagram for the TDAQ system. The system consists of a hardware-based first-level trigger (L1) and a software-based high-level trigger (HLT). The first level trigger decision uses the L1 calorimeter (L1Calo), and L1 muon (L1Muon) information to decide if the event is interesting enough to be read out. The decision time for an L1 accept is 2.5 μs. If an incoming event passes L1 selection, the event gets transferred to the ReadOut Drivers (RODs) and ReadOut System (ROS). Regions of Interest (ROIs) are also defined at the L1 stage. The maximum L1 output rate of the data associated with the event for all components of the detector is about 100 kHz. The HLT receives information from L1 (either the RoI or the whole event) and it performs a simplified version of the offline reconstruction algorithms, reducing the output rate to $\sim$1 kHz.

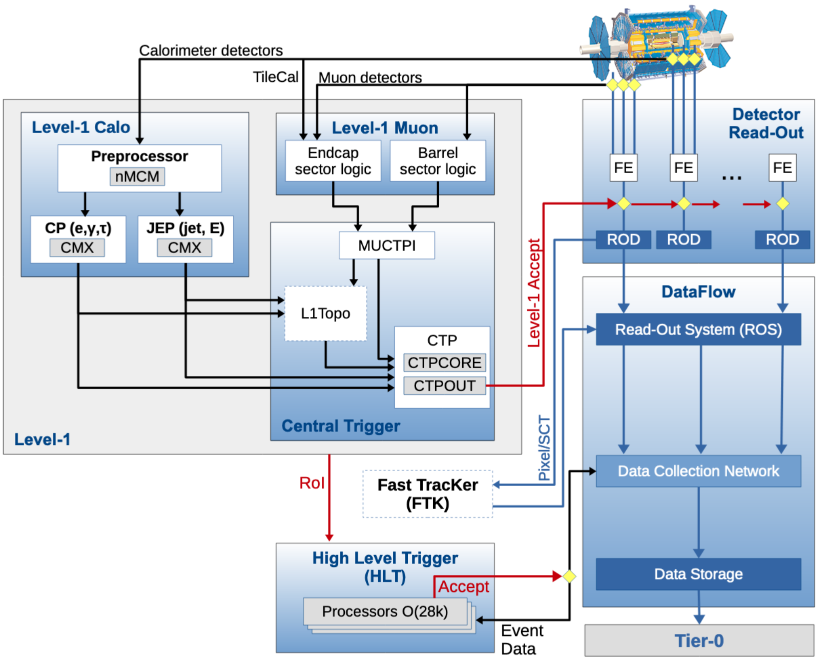

Figure 3.4.1.: Schematic overview of the ATLAS trigger and data acquisition system in Run 2. Image from Ref. [43].

The information from muon detectors and calorimeters is typically used in L1 triggers because they encounter low occupancy and have clear pattern recognition. Tracking detectors, on the other hand, have large collections of hits and complex reconstruction algorithms. Some particle identification can be done in L1; Jet RoIs are required to have the sum of electromagnetic and hadronic energy (trigger towers) in a $\Delta\eta \times \Delta\phi = 0.4 \times 0.4$ area above a given E_T threshold. Electron/photon ROIs use the electromagnetic energy in a core area of $\Delta\eta \times \Delta\phi = 0.2 \times 0.2$. Additionally, to reject hadrons, the energy in a ring around the core can be required to be smaller than a certain value (isolation), and the hadronic energy behind the electromagnetic core can be required to be small. The summed-tower energies are used in the $E_{\mathrm{T}}^{\mathrm{miss}}$ trigger. The Muon trigger uses a subset of the muon spectrometer.

The HLT uses complex algorithms and full-granularity detector data, which results in better energy and position resolutions than in the L1. For many objects, the HLT system only deals with RoI input from the Level 1 trigger, and the reconstruction algorithms are close to the offline ones [42] (see Chapter 5). The HLT processing time is longer than the L1, allowing for more information to be extracted. The processing time for one event is determined by the number of pile-up interactions. The more pile-up an event has, the more processing time is required. The average HLT processing time per event is 230 ms at 5.2×10^{33} cm^{-2}s^{-1}, $<\mu> \sim 15$ [44] (the definition of μ is explained in Section 5.4).

Each physics signature defines a set of trigger chains where the event selections are implemented at the L1 and HLT, i.e.'e24_lhmedium_L1EM20VH' where e stands for an electron from the decision at the HLT, and EM stands for an electromagnetic element formed at the L1. Chains require either full event building (EB) or partial EB with only sub-detector information. An individual prescale factor of N can be given to each chain, meaning 1 out of N passing events would be accepted. The collection of all signatures is called the trigger menu. The menu consists of:

- **Primary physics triggers:** they are used for physics analyses, typically running unprescaled.
- **Support triggers:** they are used for efficiency and performance measurements or monitoring.
- **Calibration and timing triggers:** they are used for detector calibrations.

Recorded events are grouped into categories called data streams. The main physics streams contain all triggers for physics analyses, such as Egamma, Muons, JetTauMET, MinBias (minimal requirements), and B-physics. Figure 3.4.2 shows the HLT trigger rate of the main physics streams as a function of time for a run acquired in 2018 with a peak luminosity of L $= 2.0 \times 10^{34}$ cm^{-2}s^{-1} and a peak average number of interactions per crossing of $<\mu> = 56$. The HLT trigger rates decrease exponentially during a fill due to the luminosity decrease. The dips are caused by dead time and spikes are the effects of detector noise.

The raw data which passed the HLT is sent to the Tier-0 (the CERN Data Centre), and then it is distributed to the Tier-1. The Tier-1 consists of 13 computer centres around the world that store the LHC data.

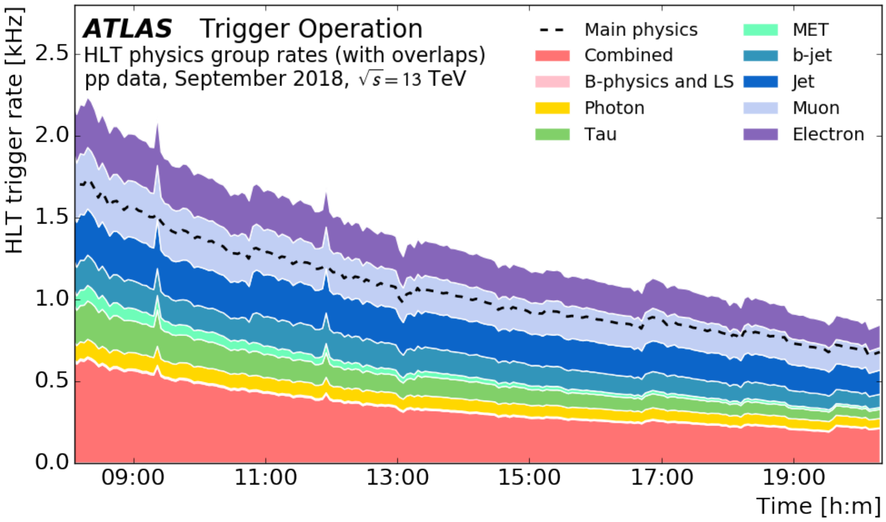

Figure 3.4.2.: HLT physics trigger group rates as a function of time in a fill taken in 2018 [45].

Chapter 4

Monte Carlo Generators

This section discusses the generators that are used to describe the observable characteristics of the physics processes of interest. Monte Carlo event generators give physicists the capability to predict events and topologies, including the rate at which they occur. They are used as a tool to optimize signal-to-background ratios, estimate detector acceptance conditions, interpret the significance of observations, *etc.* Different Monte Carlo generators perform calculations differently. Therefore it is desirable to make use of several generators to simulate a given process. There are a number of different Monte Carlo event generators, such as Pythia [46], Herwig [47], and Sherpa [48].

Monte Carlo methods are used to generate hadronic events according to the relevant probability distributions and obtain a list of all final-state particles. The final-state particles can be passed through the simulation of the detectors [49]; this simulates how particles bend in magnetic fields and interact with the detector if they interact at all. The output of this simulation can be used in the physics analysis and compared to experimental data.

This chapter is organized in three parts: Section 4.1 contains a description of the hadronic event generators. Section 4.2 gives the Monte Carlo samples used in the analysis presented in this thesis. Section 4.3 introduces the computational framework Matrix, and presents the derived theoretical uncertainties for the ZZ and $Z\gamma$ processes.

4.1. Simulation of Hadronic Processes

Events are the different types of physics processes occurring in collisions. Event generators consist of the main components listed below. The models used for the various generators can be different, e.g., for the treatment of the soft and collinear radiation.

- **Hard scattering** The simulation is built around the hard scattering, and partonic events are generated according to their matrix elements and phase space. The programs compute the hard-scattering cross-section at some given order in perturbation theory. For example, the leading order (LO) has the lowest number of couplings for which a process can occur. The calculations nowadays are usually performed at next-to-leading-order (NLO), increasingly also at next-to-NLO (NNLO).

- **Parton Density Function (PDF)** The two incoming partons that enter the hard interaction only carry a fraction of the momenta of the protons and the structure functions are a measure of the probability to find a parton with a given momentum fraction inside a proton probed at a squared energy scale Q^2.
- **Parton showers** The QCD partons entering or exiting the hard scattering can radiate gluons. The subsequent partons cascade because gluons produce quark–antiquark pairs and gluons radiate gluons, generating showers. Programs often model this process with approximate higher-order real-emission corrections to the hard scattering.
- **Fragmentation and decay** As the momentum scale of the event goes lower, to the order of 1 GeV, non-perturbative effects and hadronisation become prominent. Hadronisation is the formation of colourless hadrons out of coloured partons. A rescaling of momenta is required to prevent violations of momentum conservation from independent fragmentations after the hadronisation is completed. These hadrons produced during hadronisation are mostly unstable, and therefore, they sequentially decay into the experimentally observable particles.
- **Underlying event** Each hard interaction only considers two partons colliding head-on from each incoming hadron, but it is possible to have more than one pair of partons interacting with each other in a given hadron-hadron collision. All the other partons acting to produce the beam jets found along the directions of the original incoming hadrons are included in an underlying event.

Running Coupling

A hadron is composed of many point-like constituents, namely quarks and gluons, referred to as partons. The strong interaction between quarks and gluons is described by QCD. However, to make exact calculations in QCD is usually impossible in practice. At a short distance, the effective strong coupling becomes small. Therefore, one can make an expansion in powers of the coupling parameters and approximate it by a finite number of terms, keeping only the dominant terms. A beta function is defined as:

$$\frac{d\alpha_s(Q^2)}{d\ln(Q^2)} \equiv \beta(\alpha_s) = (\beta_0(\alpha_s^2) + \beta_1(\alpha_s^3) + \beta_2(\alpha_s^4) + \cdots). \tag{4.1.1}$$

If one keeps the first contribution term of the beta function (β_0) and integrates from energy scale μ_R^2 to Q^2, the strong coupling can be expressed by an approximate estimation of the beta function:

$$\alpha_s(Q^2) = \frac{\alpha_s(\mu_R^2)}{1 - \frac{\alpha_s(\mu_R^2)}{3\pi}\log\frac{Q^2}{\mu_R^2}}. \tag{4.1.2}$$

A renormalisation μ_R is chosen, and variations (normally by factors of 1/2 or 2) are tried out to probe how sensitive the result is to the choice of the μ_R. The coupling α_s is evaluated at scale Q^2 as shown in Figure 4.1.1. The strong coupling becomes small at short distances (large momentum transfer). This is the regime where the perturbative approach is valid. As the energy goes to infinity, the coupling becomes zero. This is known as *asymptotic freedom*. In contrast, the coupling increases with decreasing energy scale meaning the coupling becomes large at low energies, and one can no longer rely on perturbation theory. As the energy goes to zero, the coupling diverges. This is called *confinement*. There is a cutoff $Q^2 \sim \Lambda^2$, which indicates the boundary between non-perturbative and perturbative energy ranges.

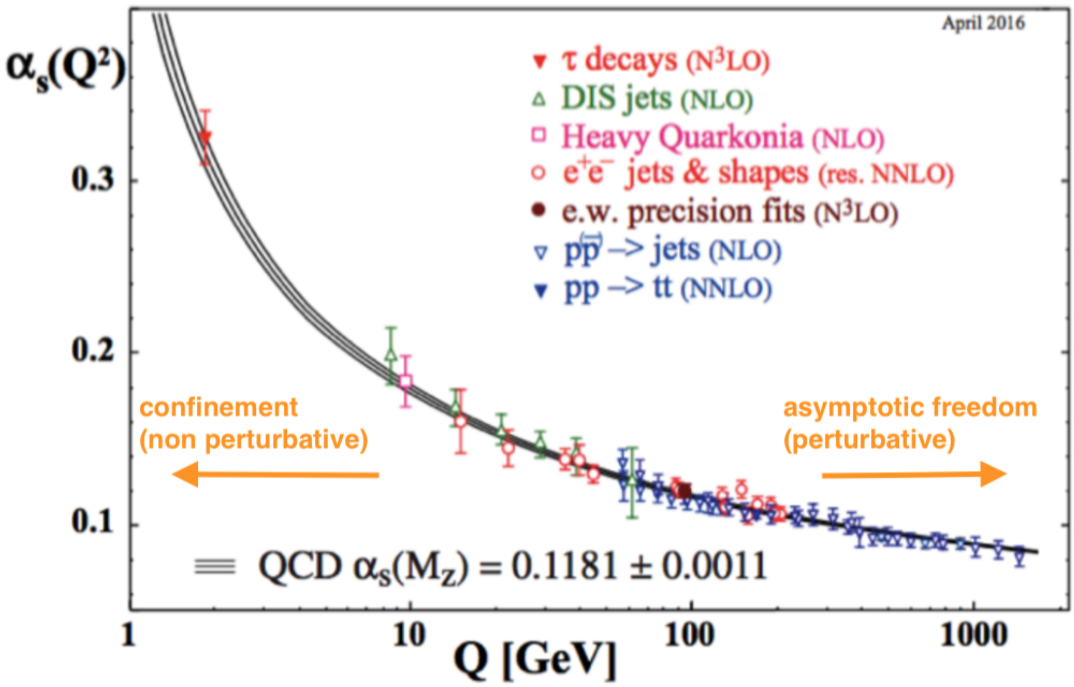

Figure 4.1.1.: The QCD running coupling α_s as a function of the momentum transfer Q. The shown numbers are based on the τ-decays from the ALEPH data using N^{3}LO QCD, a lattice calculation, the QCD interaction between two heavy quarks in quarkonium bound state, e^+e^- hadronic event shape, a global fit to electroweak precision data, and CMS data on the measurement of the jets cross-sections using NLO QCD and the measurement of the $t\bar{t}$ cross-section using NNLO QCD [50].

Parton Distribution Functions and Cross-Sections

The total cross-section for a proton-proton collision is separated into two parts based on the QCD factorization theorem: the universal parton distribution functions (not perturbatively calculable) and the hard scattering cross-section (perturbatively-calculable).

The PDF is the parton distribution as a function of the longitudinal momentum fraction x as illustrated for the proton in Figure 4.1.2. The valence up and down quark distributions peak at $x \sim 0.2$ and sea quark and gluon distributions grow at small x. The typical momentum transfer for Higgs boson production is at energy scale 10^4 GeV^2 with $x \sim 10^{-2}$ at 13 TeV. The kinematic constraint requires that $f_i(x) = 0$ when $x \geq 1$ (i denotes a given quark flavour (or flavour combination) or the gluon). To transform measurements obtained at one scale to a different one, the renormalisation group equations of the PDFs (also called the DGLAP equations) are essential.

Due to the non-perturbative nature of QCD at low energies, parton distribution functions cannot be calculated analytically. PDFs are obtained from fitting observables (cross-sections)

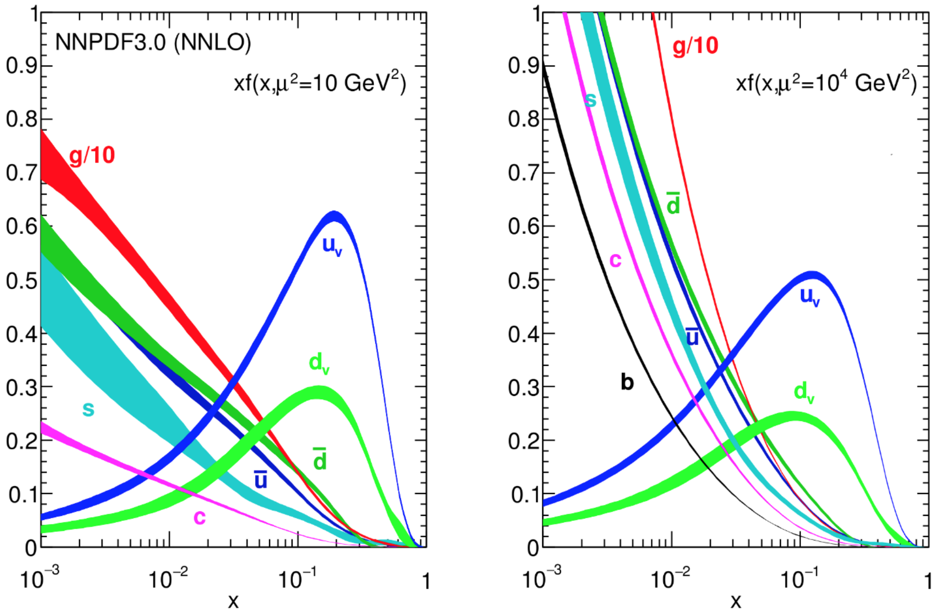

Figure 4.1.2.: The momentum probability densities $xf_i(x)$ are shown at low scale (10 GeV^2) on the left and at high scale (10^4 GeV^2) on the right. Image from Ref. [51].

to experimental data combining information from different processes and scales. PDFs are extracted from various data sets from hadron colliders and deep inelastic scattering experiments, such as the electron-proton HERA collider. The LHAPDF [52] library provides a unified interface to all major PDF sets, including uncertainties.

Considering the Drell-Yan process, one can measure the invariant mass of the final state object (M_X) as an external probe to study the variation of parton densities. The di-lepton final state gets the momentum fractions of the quark and anti-quark in the protons: x_a and x_b at leading order. The partonic centre-of-mass energy ($\hat{s}$) is related to the LHC centre-of-mass energy (s) through the relations:

$$\hat{s} = (p_a + p_b)^2 = p_a^2 + p_b^2 + 2p_a \cdot p_b = 2x_a x_b P_a \cdot P_b = x_a x_b s, \tag{4.1.3}$$

where p_a and p_b are the massless parton momenta.

The observable hadronic cross-sections are a convolution of a partonic cross-section calculated with incoming quarks/gluons carrying the momentum fractions (x_a and x_b) and the renormalisation (μ_R) and factorisation (μ_F) scales times the respective PDFs, which depend on μ_F. Thus the total cross-section is given as:

$$\sigma_{pp\to X} = \Sigma_{a,b} \int dx_a dx_b f_a(x_a, \mu_F^2) f_b(x_b, \mu_F^2) \hat{\sigma}_{ab\to X}(x_a, x_b; \alpha_s, \mu_R^2, \mu_F^2), \tag{4.1.4}$$

where the PDFs f_a and f_b give the probability of finding the partons of type a and b in the two incoming hadrons and $\hat{\sigma}_{ab\to X}$ is the cross-section for the short distance interaction of the partons.

Matrix Element

The cross-section for the production of the final state X through the initial partons a and b can be written as:

$$\hat{\sigma}_{ab\to X} = \int d\Phi \frac{1}{2\hat{s}} |\mathcal{M}_{ab\to X}|^2 (d\Phi_n; \mu_F, \mu_R), \tag{4.1.5}$$

where $\mathcal{M}$ is the 'matrix element' encoding the physics of the processes which can be evaluated in different ways. The parton flux $1/(2\hat{s})$ is $1/(2x_a x_b \mathrm{s})$. $\mathrm{d}\Phi_n$ is the differential Lorentz-invariant phase space element over the n final-state particles, which also depends on initial-state particles a and b:

$$d\Phi_n = \prod_{i=1}^{n} \frac{d^3 p_i}{(2\pi)^3 2E_i} \cdot (2\pi)^4 \delta^{(4)}(p_a + p_b - \Sigma_{i=1}^{n} p_i), \tag{4.1.6}$$

where p_a and p_b are the initial-state momenta given by $x_a P_a$ and $x_b P_b$ from the fixed hadron momenta, respectively. p_i are the final state momenta and the index i goes over the final state partons and the Dirac delta function ensures momentum conservation.

Parton Shower Based Programs v.s. Pure Matrix Element Based Programs

A $2 \to 3$ process might be described either in terms of a basic $2 \to 3$ matrix element, or in the form of a $2 \to 2$ hard scattering followed by final state radiation. This leads to two different approaches in the Monte Carlo program functionality, parton showers (PS) and matrix elements (ME). It is desirable to combine higher order ME and PS. To avoid double-counting when combining the different descriptions is technically challenging.

Parton shower (PS) programs take a fixed-order matrix element and add initial and final state parton radiation to it. For LO and NLO matrix elements, adding a parton shower has been implemented in a general way. For higher-order matrix elements (such as NNLO), this has only been achieved for a few processes so far. The next stage of the PS simulation is to consider that a parton may either split into two partons, or it may not. If two outcoming partons (b and c) are adjacent in colour and collinear, they can be identified to originate from the same parton a with $p_b = z p_a$ and $p_c = (1-z) p_a$. The differential cross-section of n+1 splitting partons is:

$$d\sigma_{n+1} = d\sigma_n \otimes \Sigma_{a\in q,g} \frac{dt}{t} dz \frac{\alpha_s(t,z)}{2\pi} P_{a\to b,c}(z), \tag{4.1.7}$$

where $P_{a\to b,c}$ is the probability of parton splitting for the splitting of partons b and c from the parton a. The splitting partons carry fraction z and (1-z) of the momentum of parton a, respectively.

The PS formalism is approximate, but universal, which means the shower evolution is not allowed to depend on the details of the hard scattering, but only on the energies and flavours of incoming and outgoing partons, and an overall Q^2 scale for the hard scattering. To mimic the events produced in a hadron collider, fragmentation and underlying event can be added.

PS matching to higher order matrix elements is complicated. Therefore, going to predictions with the highest available order, one often needs to rely on pure Matrix Element programs. The matrix elements are at fixed order, which can lead to divergences in certain phase space regions, unless some form of resummation is performed. The PS programs play the role of numerical resummation. There are alternative analytical techniques, e.g., the QCD perturbative prediction can be resummed to all orders in the framework of the so-called leading-log QCD.

Overall, parton shower based programs are fairly easy to use to simulate a new postulated physics process in sufficient detail to establish experimental feasibility. They generate more inclusive event samples and later discard those events that do not satisfy the requirements. On the other hand, the matrix element programs are useful for generating events at highest available accuracy within very specific phase-space regions since selections on kinematic variables can be included from the start.

4.2. Simulated Samples

This section describes the Monte Carlo samples and generators used to model background and signal processes for the $H \to ZZ \to \ell^+\ell^-\nu\bar{\nu}$ search [1]. The $Z\gamma$ samples are used in the $Z\gamma$ method described in Chapter 6. Several processes can produce the same experimental signature of 2-leptons plus missing transverse momentum.

Monte Carlo samples are analysed in a reduced format with respect to the original analysis object data (xAOD), namely the 'derivation' or DxAOD. Derivations are produced centrally. Their purpose is to reduce sample size, add new variables and selections, and apply new or revised combined performance recommendations.

Monte Carlo samples are used to simulate background processes as well as signal processes. All the samples were generated for a centre-of-mass energy of 13 TeV and passed through the full GEANT4 [49] simulation of the ATLAS detector. The same reconstruction algorithms are applied as in the data. All of the samples listed in this section have three datasets, mc16a (for 2015+2016 data), mc16d (for 2017 data), and mc16e (for 2018 data). Each dataset corresponds to different pileup conditions during data-taking.

Monte Carlo samples have been centrally produced by the ATLAS Physics Modelling Group (PMG), which also provides the cross-section value and the filter efficiency (for example, putting a requirement on the lower p_{T} for the partons to avoid generating unimportant events). Whenever a higher-order cross-section computation is available, this is taken into account with a K-factor which is used to adjust the cross-section when normalising the sample to the integrated luminosity of the dataset [53]. Different Monte Carlo generators interfaced with different parton showering programs were used.

Samples for the $\ell^+\ell^-\nu\bar{\nu}$ Analysis

Background Samples

Table 4.2.1 summarises the simulated background Monte Carlo samples used in the analysis [54]. The details on the irreducible backgrounds samples can be found in Table 4.2.2. The $ZZ \to \ell^+\ell^-\nu\bar{\nu}$ process ($l = e$, μ, τ) and EW production of $qq \to \ell^+\ell^-\nu\bar{\nu}jj$ are simulated using the Sherpa [48] event generator with NNPFD3.0NNLO PDF in the case of qq and gg initial state production. The $gg \to ZZ$ processes include a QCD K-factor of 1.7. This factor is calculated by taking the ratio between NLO and LO $gg \to ZZ$ cross-sections at 13 TeV [55]. A factor of 1.5 is taken into account for the neutrino flavours, because the simulation only contains processes where the neutrino flavour is different from the lepton flavour, thus avoiding double counting the $WW(l\nu l\nu)$ contribution. The WW process is modelled with Powheg (qq) and Sherpa (gg).

In the WZ process, two final states are important, $\ell\nu\ell^+\ell^-$ and $qq\ell^+\ell^-$ ($l = e$, μ, τ). The NLO Sherpa samples are used because the jet distributions in control regions agree better with data than in the Powheg [56] simulation.

The production of three vector bosons is suppressed by the request of no more than two leptons in the final state. The expected contribution from these samples is then very minor, compared to that of the di-boson ones. Tri-boson production, VVV, with V = W, Z, is simulated by the Sherpa event generator at NLO.

Events that involve the production of a single Z boson are largely rejected due to the $E_{\mathrm{T}}^{\mathrm{miss}}$ cut. Even though the contribution is small, the Z + jets background has significant systematic uncertainties, as the modelling of the $E_{\mathrm{T}}^{\mathrm{miss}}$ depends on the modelling of pile-up interactions and on the jet energy response. Moreover, the Z + jets background enters in many control regions defined to estimate other backgrounds, so its modelling is crucial in these analyses, in particular that of the $E_{\mathrm{T}}^{\mathrm{miss}}$ and transverse mass distribution. The Z + jets process is simulated using the Sherpa version 2.2.1 event generator. Studies have shown that this version provides good agreement with data. The agreement is better than the previously used MadGraph [57] generator, which does not model the Z p_{T} distribution well and required bin-by-bin reweighting of the Z p_{T} distribution, affecting other variables important for this analysis, like ΔR_{ll}. For this reason, Sherpa was chosen for Z + jets process simulation. The Sherpa samples with 0, 1 or 2 jets at LO and 3 or 4 jets at LO are considered.

Background samples for top-pair production, as well as single top and Wt production, are simulated using Powheg interfaced with Pythia 8 for parton shower. The $t\bar{t}$ sample is filtered at the event generator level requiring at least one lepton originating from a W boson with $p_{\mathrm{T}} > 1$ GeV. Single top production is considered in s-channel and t-channel. For W-boson with single top associated production, inclusive samples have been used.

Background samples for top-pair production in association with one vector boson (W or Z) are simulated with the MadGraph5_aMC@NLO generator [58] interfaced with Pythia 8. Background samples for top-pair production in association with two W bosons are simulated at LO with the MadGraph generator interfaced with Pythia 8. These samples have a minor impact on the total background in the $\ell\ell$ + $E_{\mathrm{T}}^{\mathrm{miss}}$ final state.

Process	Generator	ME Order	PDF Set	PS/UE/MPI
WZ	Sherpa 2.2.2	0,1jNLO + 2,3jLO	NNPDF30NNLO	Sherpa
$q\bar{q} \to WW$	Powheg-Box	NLO	CT10	Pythia
$gg \to WW$	Sherpa 2.2.2	LO + 0,1j	NNPDF20NNLO	Sherpa
Tri-boson	Sherpa 2.2.2	0jNLO + 1,2jLO	NNPDF30NNLO	Sherpa
Z + jets	Sherpa 2.2.1	0,1,2jNLO + 3,4jLO	NNPDF30NNLO	Sherpa
Top-pair and single top	Powheg	NLO	CT10	Pythia
$t\bar{t}$V and $t\bar{t}$VV	MadGraph5_aMC@NLO	NLO	A14NNPDF23	Pythia

Table 4.2.1.: Summary of simulated Monte Carlo event samples used in the analyses. The details are described in the text. PS/UE/MPI mean parton shower, underlying-event and multi-parton interaction, respectively.

Signal Samples

Heavy Higgs boson production through gluon-gluon fusion is modelled with Powheg-Box v2. Gluon–gluon fusion and vector-boson fusion production modes are calculated separately with ME up to NLO in QCD. Powheg-Box v2 is interfaced to Pythia 8 for parton showering and hadronisation and for decaying the heavy Higgs boson into $\ell^+\ell^-\nu\bar{\nu}$. The LO CT10 PDF set is used to for the hard-scattering process. Monte Carlo samples are generated for various Higgs masses ranging from 300 GeV to 2000 GeV.

The graviton samples (Spin-2 Kaluza–Klein gravitons from the bulk Randall–Sundrum model) are produced with the MadGraph5_aMC@NLO generator at LO in QCD with the NNPDF2.3 LO PDF set. It is interfaced to Pythia for parton showering and hadronisation with the A14 set of tuned parameters and for decaying the heavy resonance boson. The dimensionless coupling $k/\bar{M}_{PI}$, where $\bar{M}_{PI} = M_{PI}/\sqrt{8\pi}$ is the reduced Planck scale and k is the curvature scale of the extra dimension, is set to 1. The width of the resonance is correlated with the coupling $k/\bar{M}_{PI}$ and in this configuration is around 6% of its mass. Mass points between 600 GeV and 2 TeV with 200 GeV spacing are generated.

Samples for the $Z\gamma$ Method

Table 4.2.2 summarises the simulated MC samples used in the $Z\gamma$ method where the γ is treated as the $E_{\mathrm{T}}^{\mathrm{miss}}$. The dominant background to the $Z\gamma$ signal is Z + jets, which is estimated using a data-driven method. The background from top-quark production is estimated from a simulated sample of $t\bar{t}\gamma$ events with one or both of the top quarks decaying semileptonically. Other backgrounds, such as $\ell\nu\ell\ell(WZ)$, $\ell\ell\ell\ell(ZZ)$, $WW\gamma$ and $WZ\gamma$ productions contribute a negligible amount when the full analysis selection is applied.

The $Z(\ell\ell)\gamma$ sample is generated with Sherpa 2.2.2 (NLO). For the photons, Frixione isolation (see Eq. 4.3.10) with parameters ϵ as 0.1, δ_0 as 0.1 and n as 2 is used. The $gg \to Z\gamma$ sample has a very small cross section and is not included. In addition to the Sherpa simulation, a ME based Matrix calculation [59] is also performed for the $(qq/gg)\ell^+\ell^-\gamma$ and $(qq/gg)ZZ$ processes and used to calculate the cross-section ratio. This calculation does not include the simulation of the ATLAS detector.

The differences between Sherpa and Matrix are summarised as follows.

Matrix

- fixed order NNLO
- includes NNLO virtual corrections

Sherpa

- NLO0 jet, NLO1 jet, LO2, LO3
- includes parton shower
- processed through full ATLAS simulation

4.3. $ZZ/Z\gamma$ Cross-Section Ratio Using the Matrix Generator

The theoretical cross-section ratio of the ZZ and $Z\gamma$ processes is a crucial ingredient to the data-driven ZZ estimate from $Z\gamma$ events and is presented in this section, as well as the

Process	Generator	ME Order	PDF Set	PS/UE/MPI
$t\bar{t}\gamma$	MADGRAPH5_aMC@NLO 2.2.3	NLO	NNPDF2.3 LO	PYTHIA
(qq)Z$\gamma \to \ell^+\ell^-\gamma$	SHERPA 2.2.2	NLO	NNPDF30NNLO	SHERPA
$(qq/gg)ZZ \to \ell^+\ell^-\nu\bar{\nu}$	SHERPA 2.2.2	gg(LO), qq(NLO)	NNPDF30NNLO	SHERPA
$qq \to llvvjj$	SHERPA 2.2.2	NLO	NNPDF30NNLO	SHERPA
$(qq/gg)Z\gamma \to \ell^+\ell^-\gamma$	MATRIX	gg(LO), qq(NNLO)	NNPDF30_lo_as_0118	-
$(qq/gg)ZZ \to \ell^+\ell^-\nu\bar{\nu}$	MATRIX	gg(LO), qq(NNLO)	NNPDF30_lo_as_0118	-

Table 4.2.2.: List of Monte Carlo samples used for the $Z\gamma$ method: the background process (line 1) and $\ell^+\ell^-\gamma$ signal (line 2). ZZ Monte Carlos (line 3 and line 4) are used for the closure checks in the $Z\gamma$ method. An alternative calculation using the MATRIX generator for the $\ell^+\ell^-\gamma$ and $ZZ \to \ell^+\ell^-\nu\bar{\nu}$ processes is presented. PS/UE/MPI mean parton shower, underlying-event and multi-parton interaction, respectively.

related theoretical uncertainties. Within the MATRIX framework [59], ZZ ($\ell^+\ell^-\nu\bar{\nu}$) and $Z\gamma$ ($\ell^+\ell^-\gamma$) theoretical predictions are fully differential at QCD next-to-next-to-leading order (NNLO) where the boson pairs are produced via quark annihilation [60, 61]. The behaviour of EW corrections was investigated in Ref. [62].

This section presents the $ZZ/Z\gamma$ cross section ratio and its uncertainties in two parts: results with preselection cuts applied are shown in Section 4.3.1, and a study with more additional cuts is shown in 4.3.2. The discussed uncertainties will be included in the $Z\gamma$ method as described in Section 6.3.

Despite similar production mechanisms between the ZZ and $Z\gamma$ at high vector boson p_{T}, care has to be taken due to the Z and γ mass difference. The production ratio of the ZZ and $Z\gamma$ as a function of the $Z(\nu\nu)$ boson and the γ p_{T} will be shown first.

The notation at LO, NLO, and NNLO for the QCD prediction in a generic variable x (x = p_{T}) is:

$$\frac{d}{dx}\sigma_{\mathrm{N^kLO\ QCD}}, \tag{4.3.1}$$

with k = 0,1,2. The nominal predictions are provided at NNLO (k = 2) QCD. And the relative correction factors are defined as

$$\frac{d}{dx}\sigma_{\mathrm{N^kLO\ QCD}}(\mu) = k_{\mathrm{N^kLO}}(x,\mu)\frac{d}{dx}\sigma_{\mathrm{N}^{k_{N-1}}\mathrm{LO\ QCD}}(\mu). \tag{4.3.2}$$

The $\mathrm{k_{NNLO}}$ (or $\mathrm{k_{NLO}}$) factors reflect the ratio of NNLO/NLO (or NLO/LO) QCD predictions, which are used to correct the result obtained from the NLO (or LO) Monte Carlo. [1]

For the $Z\gamma$ method, the K-factors are calculated for the production ratio of the $q\bar{q}$ or $gq \to ZZ/Z\gamma$ processes at NLO and NNLO. Note that the published cross-section of $gg \to ZZ(Z\gamma)$ is only available at NLO (LO) [63]. The $gg \to Z\gamma$ process at NLO is then approximated by applying the $k^{gg}_{\mathrm{NLO/LO}}$ factor from the ZZ process. The notations of the NNLO production for distinguishing between including gg_{LO} and gg_{NLO} are σ_{NNLO} and σ_{nNNLO}, respectively:

$$\begin{aligned} \sigma_{\mathrm{NNLO}} &= \sigma^{qq}_{\mathrm{NNLO}} + \sigma^{gg}_{\mathrm{LO}}, \\ \sigma_{\mathrm{nNNLO}} &= \sigma^{qq}_{\mathrm{NNLO}} + \sigma^{gg}_{\mathrm{NLO}}. \end{aligned} \tag{4.3.3}$$

[1] The k factors depend on the choice of PDFs. Our choice is that all N^{k}LO and LO cross-sections are based on the same set of NNLO PDFs.

Electroweak Corrections

Electroweak corrections cannot be neglected, especially in the tails of the distribution. The current results are LO in EW, but the calculations with high-order diagrams to improve the accuracy of the prediction are needed. The NLO EW contribution to $pp \to \ell^+\ell^-\nu\bar{\nu}$ is at $\mathcal{O}(\alpha^5)$. At this order both the $q\bar{q}$ and $\gamma\gamma$ channels (the latter contributes at higher order in EW) receive EW corrections from two variants [62]:

- **Virtual EW corrections:** coupling to weak bosons (in the $q\bar{q}$ channel) or coupling to a heavy-fermion loop (in the $\gamma\gamma$ channel).
- **Real EW corrections:** real photon emission (in the $q\bar{q}$ channel) or photon bremsstrahlung (in the $\gamma\gamma$ channel).

The impact of NLO EW corrections is calculated by combining the QCD corrections (Δ_{QCD}) and EW higher-order corrections (Δ_{EW}), using both an additive and a multiplicative approach, defined, respectively, as [62]:

$$\begin{aligned} d\sigma_{\mathrm{NNLO\ QCD+EW}} &= d\sigma_{\mathrm{LO}}(1 + \Delta_{\mathrm{QCD}} + \Delta_{\mathrm{EW}}) + d\sigma^{gg}, \\ d\sigma_{\mathrm{NNLO\ QCD\times EW}} &= d\sigma_{\mathrm{LO}}(1 + \Delta_{\mathrm{EW}})(1 + \Delta_{\mathrm{QCD}}) + d\sigma^{gg}, \end{aligned} \tag{4.3.4}$$

where $d\sigma^{gg}$ is the gg production. The prediction with EW corrections is then given by taking the average of the multiplicative and additive corrections. The difference between one of the prescriptions and the average is taken as the EW correction uncertainty in the $Z\gamma$ method.

The event preselection is described in Table 4.3.1. Additionally the photon Frixione isolation is set to $\epsilon_\gamma = 0.075$, $\mathrm{R}_0 = 0.2$, and n=1. The calculation is performed using the MATRIX computational framework at $\sqrt{s} = 13$ TeV with the CT14 PDF set.

Variable	ZZ	$Z\gamma$
N_{lep}	2	
$p_{\mathrm{T}}^{\ell_1}$	> 30 GeV	
$p_{\mathrm{T}}^{\ell_2}$	> 20 GeV	
$p_{\mathrm{T}}^{\nu\nu}$	> 60 GeV	-
p_{T}^{γ}	-	> 60 GeV
$\Delta R(l,\gamma)$	-	> 0.4
$m_{\ell\ell}$	$76 < m_{\ell\ell} < 106$ GeV	

Table 4.3.1.: Event selection for ZZ (left column) and $Z\gamma$ (right column) events.

The resulting distribution of the ratio of the di-boson differential cross-section as a function of the truth p_{T} is shown in Figure 4.3.1. The predictions are calculated with EW corrections as well, and the EW corrections lead to a decrease in the cross-section ratio at high boson p_{T} by $\sim$10%.

4.3.1. Uncertainties on the $ZZ/Z\gamma$ Cross-section Ratio: without applying any cuts beyond the Z mass requirement

Because the cross-sections depend on the choice of PDFs, QCD scales, photon isolation, *etc*, the theoretical uncertainties on the ratio are considered, which will then be propagated

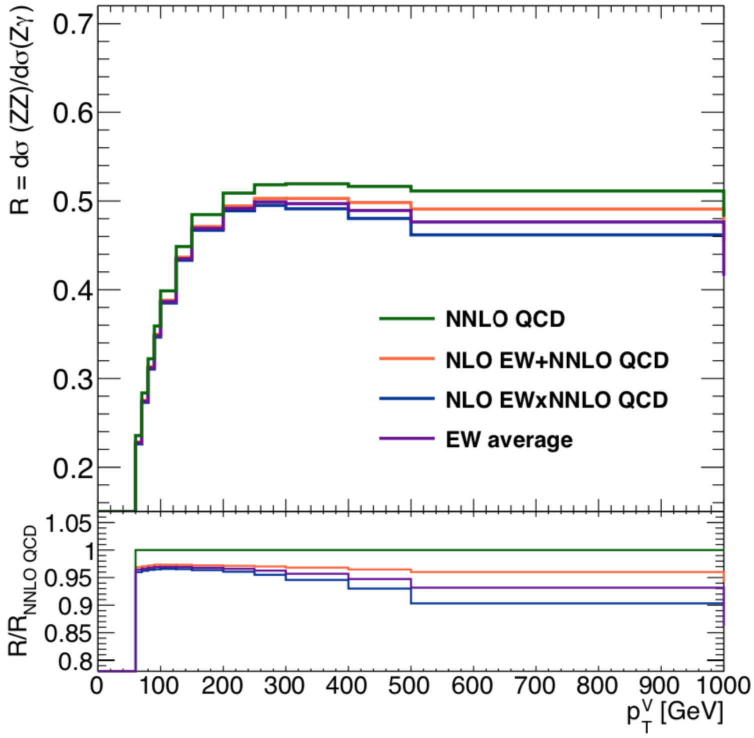

Figure 4.3.1.: The ratio of the ZZ and $Z\gamma$ differential cross-section as a function of the photon or Z $(\nu\nu)$ p_{T}. The NNLO QCD distributions is plotted (in green) along with both the additive (NNLO QCD + EW in red), multiplicative (NNLO QCD $\times$ EW in blue) and the average EW (in violet) prescriptions. The ratio of the distributions with respect to NNLO QCD is presented in the lower panel [64].

through to the overall uncertainty on the $Z\gamma$ method (see Section 6.3). The understanding of the uncertainty of the relationship between the ZZ and $Z\gamma$ processes will be presented in this section.

QCD uncertainties

This paragraph will address the uncertainty, which is caused by uncalculated higher-order (HO) terms in perturbative calculations [65]. The renormalisation and factorisation scales of the ZZ and $Z\gamma$ processes are chosen to be the same with the form $\mu_{R,F} = \sqrt{m_Z^2 + p_{\mathrm{T}}^V}$.

The uncertainties due to missing higher-orders are typically determined by varying factorisation and renormalisation scales, which are called seven-point variations. The nominal prediction is used as the central value and related uncertainties are defined as the half-width of the band resulting from the variations. The variation can be expressed in terms of production cross-section and the ratio:

$$\begin{aligned}\delta^{\text{scale}}\sigma(x) &= \frac{1}{2}\left(\sigma^{V,\max}(x) - \sigma^{V,\min}(x)\right),\\ \delta^{\text{scale}}\mathrm{R}(x) &= \frac{1}{2}\left(\mathrm{R}^{V,\max}(x) - \mathrm{R}^{V,\min}(x)\right).\end{aligned} \tag{4.3.5}$$

where $\sigma^{V,\max}$, $\sigma^{V,\min}$, $\mathrm{R}^{V,\max}$, and $\mathrm{R}^{V,\min}$ correspond to the maximal and minimal values of seven-point variations on the cross-section and the ratio, respectively.

The scale variations tend to underestimate shape uncertainties, thus, for a reasonably conservative estimate of shape uncertainties, an additional variation is introduced:

$$\begin{aligned}\delta^{\text{shape}}\sigma(x) &= \omega_{\text{shape}}(x)\delta^{\text{shape}}\sigma(x),\\ \delta^{\text{shape}}R(x) &= \omega_{\text{shape}}(x)\delta^{\text{shape}}\mathrm{R}(x),\end{aligned} \tag{4.3.6}$$

where δ^{shape}, the standard scale uncertainty, is supplemented by a shape distortion $\omega_{\text{shape}}(x)$. The function ω_{shape} is defined as:

$$\omega_{\text{shape}}(p_{\mathrm{T}}) = tanh\left[ln\frac{p_{\mathrm{T}}}{p_{T0}}\right] = \frac{p_T^2 - p_{T,0}^2}{p_T^2 + p_{T,0}^2}, \tag{4.3.7}$$

where p_{T}^0 is the reference transverse momentum, chosen to be in the middle of the range of interest. For the $Z\gamma$ method, 250 GeV is chosen.

The scale and shape uncertainties assume that the renormalisation and factorisation scales of the $Z\gamma$ and ZZ processes adopt the same behaviour. The scale in Equation 4.3.5 is varied coherently for both processes, causing a partial cancellation, so that the uncertainty on the ratio is smaller than that on either cross-section.

For the non-correlated part of the ZZ and Zγ QCD scale uncertainties, an additional higher order (HO) correction uncertainty is estimated. The difference between the ZZ and Zγ K-factors is considered a conservative value to assess differences between the processes, which is defined as δ^{HO}:

$$\delta^{HO}k_{nNNLO}^{Z\gamma}(x) = k_{nNNLO}^{Z\gamma}(x) - k_{nNNLO}^{ZZ}(x), \tag{4.3.8}$$

where nNNLO indicates that the LO $ggZZ$ and LO $ggZ\gamma$ are replaced by the NLO version to have a more accurate description.

The total uncertainty of the QCD is at the level of 2% in most bins as shown in the ratio panel of Fig 4.3.2. The QCD uncertainty is calculated by adding scale, shape, and higher-order uncertainties in quadrature.

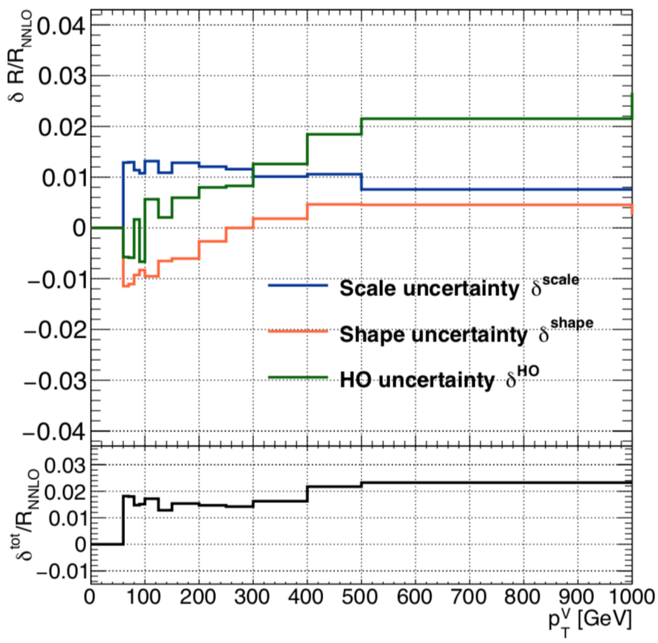

Figure 4.3.2.: Relative scale, shape, and HO uncertainties on the ratio of ZZ and $Z\gamma$ distributions at NNLO QCD. In the ratios panel, three uncertainty sources are combined in quadrature [64].

PDF Uncertainties

The role of PDF uncertainties can be significant especially at high-p_{T}, where PDFs tend to be less precise. The PDFs are estimated using the 30 eigenvectors provided by the PDF4LHC15_30 set [66]. This uncertainty is evaluated using NLO predictions with NNLO PDFs on the cross-section and the ratio in the following way:

$$\begin{aligned} \delta^{\mathrm{PDF}}\sigma &= \sqrt{\Sigma_{k=1}^{\mathrm{N}}(\sigma^k - \sigma^0)^2}, \\ \delta^{\mathrm{PDF}}\mathrm{R} &= \sqrt{\Sigma_{k=1}^{\mathrm{N}}(\mathrm{R}^k - \mathrm{R}^0)^2}, \end{aligned} \tag{4.3.9}$$

where N corresponds to the number of PDF sets (we have tested N=30). The σ^k (R^k) and σ^0 (R^0) are the cross-sections (ratio) evaluated for each set and for the nominal PDF set respectively.

The PDFs [66] uncertainty on the ratio of ZZ and $Z\gamma$ contributes around 1% to 2 % in all p_{T} regions.

The Photon-isolation Prescription and Uncertainties

Due to the presence of $q \to q\gamma$ collinear singularities and the need to suppress them to obtain a finite prediction in perturbation theory, the Frixione isolation approach is adopted which is defined as:

$$\Sigma_{i=partons/hadrons} p_{T,i} \Theta(R - \Delta R_{i\gamma}) \leq \epsilon_0 p_{T,\gamma} \left(\frac{1 - cosR}{1 - cosR_0} \right)^n , \tag{4.3.10}$$

where the sum runs over all quarks/gluons and hadrons within a cone of radius R. The $p_{T,i}$ and $p_{T,\gamma}$ represent the transverse momenta of partons/hadrons and the photon. The p_{T}-fraction ϵ_0, the cone size R_0, and n are free parameters that allow one to control the amount of QCD radiation in the vicinity of the photon.

Varying the Frixione parameters shows that the ratio changes only within ~1%, so $\delta^{\mathrm{iso}} = 1\%$ is assigned as a conservative uncertainty.

In conclusion, the production ratio as a function of the photon or Z $(\nu\nu)$ p_{T} with breakdown of associated uncertainties is shown in Figure 4.3.3. The largest contribution is from EW corrections, which is about 3% for $p_{\mathrm{T}} > 500$ GeV.

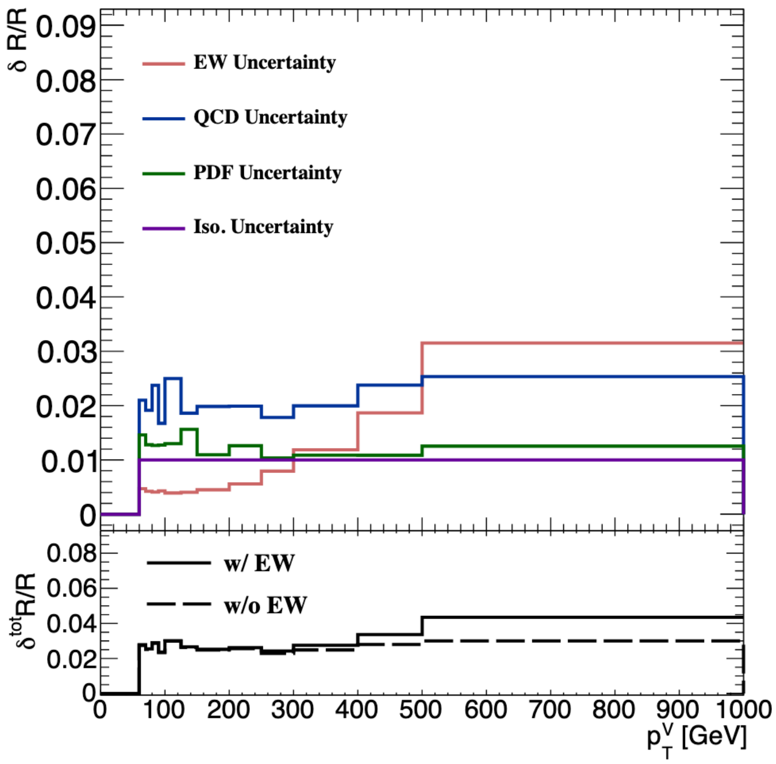

Figure 4.3.3.: Relative EW (red), QCD (blue), PDF (green) and photon isolation (violet) uncertainties on the ratio ZZ and $Z\gamma$ are shown. The bottom panel shows the combined uncertainty with EW corrections (solid) and w/o EW corrections (dashed) [64].

4.3.2. Uncertainties on the $ZZ/Z\gamma$ Cross-section Ratio: additional selection cuts

More event selections cuts are applied in the $\ell\ell + E_{\mathrm{T}}^{\mathrm{miss}}$ searches to suppress backgrounds. For a reliable estimate, these selection cuts need to be applied on the ZZ and $Z\gamma$ events and will affect the cross section ratio as well as its uncertainties. The additional cut list (ΔR, $\Delta\phi$, and truth $E_{\mathrm{T}}^{\mathrm{miss}}$ significance) is shown in Table 6.3.2.

At the time of this thesis, new studies indicate that the QCD uncertainty following the current conservative methodology is significantly larger when selection cuts are applied, while other uncertainties remain very similar. Cuts tend to increase the sensitivity to additional radiation which increases the QCD scale uncertainty.

This section presents how the additional cuts affect the QCD uncertainties, which include scale variations, shape, and higher-order uncertainties. As shown in Figure 4.3.4, the uncertainties are dominated by the higher order uncertainty ($\sim 10\%$ at low p_{T}) (compared to Figure 4.3.2). This HO uncertainty is estimated in a fairly conservative way through the k-factor difference and future studies are needed to understand if it is possible to reduce it.

When the $Z\gamma$ estimate in Chapter 6 was performed, the QCD uncertainty numbers with selection cuts were not available yet, so the preselection numbers were used.

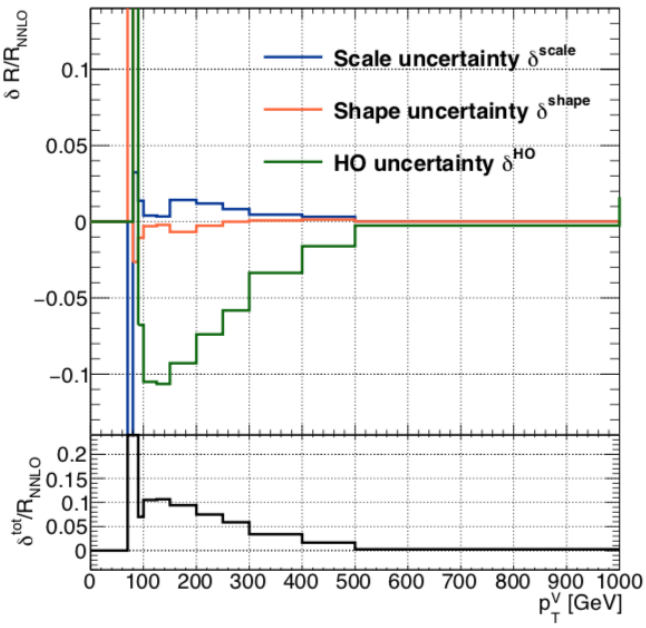

Figure 4.3.4.: The ratio of ZZ and $Z\gamma$ distributions at NNLO QCD with the additional selection cuts for relative scale, shape and HO uncertainties are shown. In the ratio panel, three uncertainty sources are combined in quadrature [64].

Chapter 5

Object Reconstruction

In ATLAS, the electronic signals might be identified as physical objects (electrons, muons, taus, photons) or physical processes such as jets. Moreover one can reconstruct invisible processes, which are the absent signals, based on momentum conservation in an event. The object reconstruction algorithms translate the detector responses into objects. Once the objects are identified, their four-momentum is calibrated to correct for detector effects before they are used in physics analyses. In this chapter, the algorithms for particle reconstruction in the ATLAS detector are discussed.

The final state signature in the described analyses requires two charged leptons that are identified as electrons or muons, as well as missing transverse momentum ($E_{\mathrm{T}}^{\mathrm{miss}}$). The reconstruction algorithms, based on information from the tracking detectors, calorimeters, and muon systems are developed by the ATLAS collaboration. The track and vertex reconstruction for the charged particles in the Inner Detector (ID) is presented in Section 5.1. The algorithms for charged leptons are described in Section 5.2 and 5.3 for electrons and muons, respectively. Reconstructed photons, used in the $Z\gamma$ method for predicting the ZZ background (see Section 6.3), are introduced in Section 5.2. The algorithms for the jet reconstruction and calibration are described in Section 5.4. The $E_{\mathrm{T}}^{\mathrm{miss}}$ reconstruction algorithm and its performance are presented in Section 5.6.

5.1. Track and Vertex Reconstruction

The ATLAS ID provides the position measurements of charged particles along their tracks. The momentum of charged particles can then be determined from their bending radius in the magnetic field. The track reconstruction of the ID consists of several algorithms. This section introduces the pattern recognition and identification of particle tracks from hits. It is a very complex task especially with the rapidly increasing number of interactions per bunch crossing [67]. Vertex reconstruction algorithms used to identify the hard scattering process and suppress the pile-up contribution are described as well.

Tracks are reconstructed from hits in the ID using the *inside-out* algorithm, which is the baseline algorithm, and then are combined with the results of the *outside-in* algorithm which starts looking for tracks in the TRT and extends them inwards to add silicon hits [68].

Track reconstruction with the *inside-out* algorithm starts by finding seeds, which are combinations of three space points. Space points are the output of a clustering algorithm run on the raw hits. Seeds are formed from combinations of three space points in the ID in order of expected purity, with SCT-only combinations considered first, then pixel-only, and finally mixed. Requirements are imposed on the momentum and impact parameter of the seeds, which are calculated assuming a helical trajectory in a uniform magnetic field. A Kalman filter is then used to build track candidates from the seeds that survive. Typically 20k seeds end up with 2k track candidates. Once track candidates are built, a dedicated software module for resolving track overlaps and removing outlier hits from tracks is then inserted as a reward/penalty scheme to find the best candidates. Figure 5.1.1 shows an example, in which three built tracks a, b, and c share several hits. The ambiguity processor is then used to select the best silicon-only tracks using a scoring function, which rewards tracks for the presence of space points, low χ^2, and high momenta, and penalizes them for the presence of holes (locations where hits are expected but not found), high χ^2, and low momenta. The ambiguity processor can also assign hits that are shared between tracks to one track, increasing its score and lowering the score of the others. The final step is the extension of the tracks that survived the ambiguity resolution step in the silicon detector to the outer TRT tracking system. The TRT hits are a pure extension, meaning the silicon tracks are not modified.

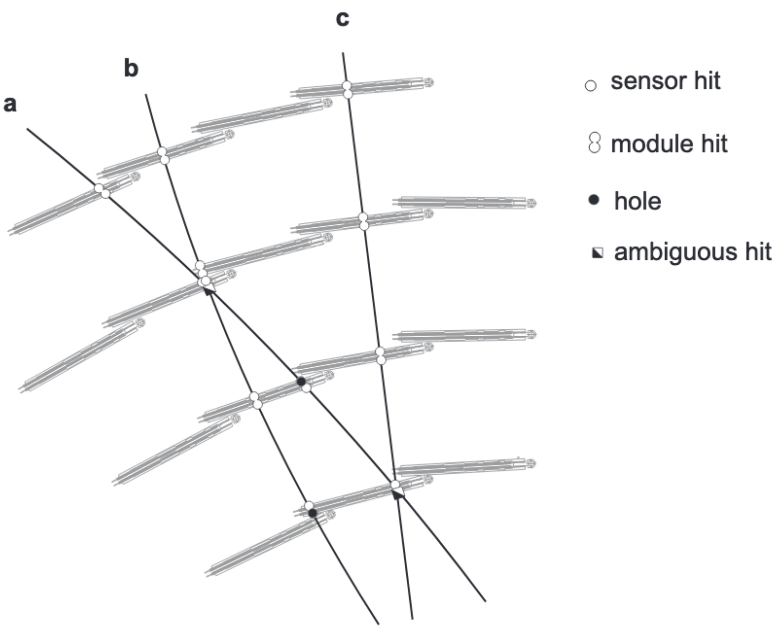

Figure 5.1.1.: Inside-out track reconstruction in the SCT: seeding and track finding with ambiguity solving. Image from Ref. [69].

The descriptions for the track reconstruction so far are mainly for reconstructing charged particles from the interaction point. However, particles like electrons from photon conversions are automatically lost in the procedure of the extension into the TRT if they do not have hits in the silicon detector. The *outside-in* sequence is then followed, which starts at TRT segments and extrapolates back into the silicon detector (backtracking) by associating any hits not already used for existing tracks from the *inside-out* stage.

Tracks are parametrized by five parameters (the geometry of the trajectory parameters is illustrated in Figure 5.1.2):

$$(d_0,\ z_0,\ \phi,\ \theta,\ q/|\overrightarrow{p}|) \tag{5.1.1}$$

where d_0 is defined as the shortest distance between a track and the beam line in the transverse plane. z_0 is defined as the distance in z between the primary vertex and the point on the track used to evaluate d_0. $\sigma(d_0)$ and $\sigma(z_0)$ denote the corresponding uncertainties, ϕ is measured in the transverse plane in (-π, π), and the polar angle θ is measured w.r.t. the z-axis in (0, π). The right-handed coordinate system is used, as described in Section 3.3. $q/|\overrightarrow{p}|$ is the ratio of the charge over momentum.

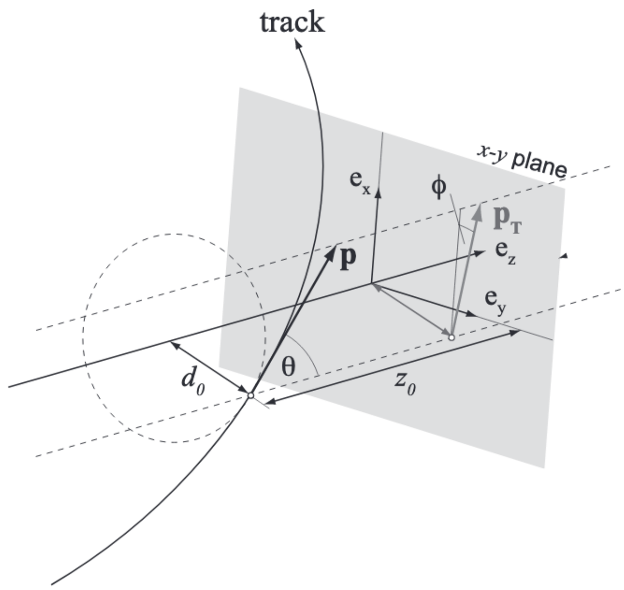

Figure 5.1.2.: Track parameterisation: A trajectory of a charged particle in a magnetic field requires five track parameters. Image from Ref. [70].

The collection of reconstructed tracks are the input of the vertex reconstruction in the ID. For the construction of a vertex, tracks must pass several requirements, such as where the hits are and the maximal number of holes [71]:

- $p_{\mathrm{T}} > 400$ MeV
- $|\eta| < 2.5$
- Number of silicon hit ≥ 9 if $|\eta| \leq 1.65$
- Number of silicon hit ≥ 11 if $|\eta| > 1.65$
- IBL hits + B-layer hits ≥ 1
- A maximum of 1 shared module[1]

[1] Clusters can be shared by no more than two tracks. A track can have no more than two shared clusters.

- Pixel holes = 0
- SCT holes ≤ 1

Different vertex topologies in a typical collision event are shown in Figure 5.1.3. The reconstruction of primary vertices is crucial for pile-up rejection, flavour tagging, long-lived particle searches, reconstruction of conversions, *etc.* Vertex seeds are collected from the track z-positions along the beam-line and the one with the largest scalar p_T sum of tracks among several reconstructed vertexes is selected as the primary vertex. The number of vertices increases with the number of interactions per bunch crossing $<\mu>$. The vertex finding is challenging at high $<\mu>$ once separation distance is less than the resolution on the vertex position.

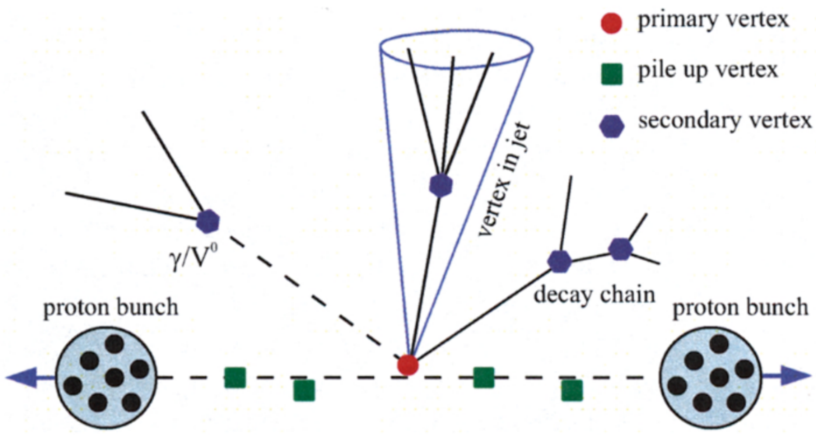

Figure 5.1.3.: The topologies of primary vertex, pile-up vertex and secondary vertex. Image from Ref. [72].

5.2. Electrons and Photons

The electron and photon energies are measured via shower production. As described in Section 3.3.2, the EM showering of electrons and photons are similar processes. Thus, the reconstruction of electron and photon energy deposits within the calorimeter follows the same procedure. Nevertheless, an electron and a photon have a fundamental difference in tracks where electrons are charged, while photons are neutral, leaving no hits except if they convert into e^+e^- leaving curved tracks in the ID. The TRT provides further discriminating power between electrons and charged hadrons, such as $\pi^{\pm}$ mesons, based on transition radiation as described in Section 3.3.1.

The first step in reconstructing an electron or photon is the construction of clusters of calorimeter energy deposits [73]. The algorithm constructs the dynamic clusters, which are called super-clusters, using pre-selected tracks and topo-clusters (see Section 5.4.2). In most regions only the energy from the cells in the EMCal is used, and the energy fraction in the EMCal is required to be larger than 0.5 [74]. These topo-clusters are matched to ID tracks, which are re-fitted accounting for bremsstrahlung. The algorithm also builds conversion vertices and matches them to the topo-clusters.

The super-clusters are built independently for electrons and photons (converted and unconverted photons) as illustrated in Figure 5.2.1. The reconstruction algorithm starts with topo-cluster sorting in the 4-2-0 scheme (see Section 5.4.2) for reducing cell noise from electronics and from pile-up. The super-cluster is composed of seed clusters and satellite cluster candidates, satisfying the selection criteria within a 3 × 5 window ($\delta\eta \times \delta\phi = 0.075 \times 0.125$) around the seed cluster.

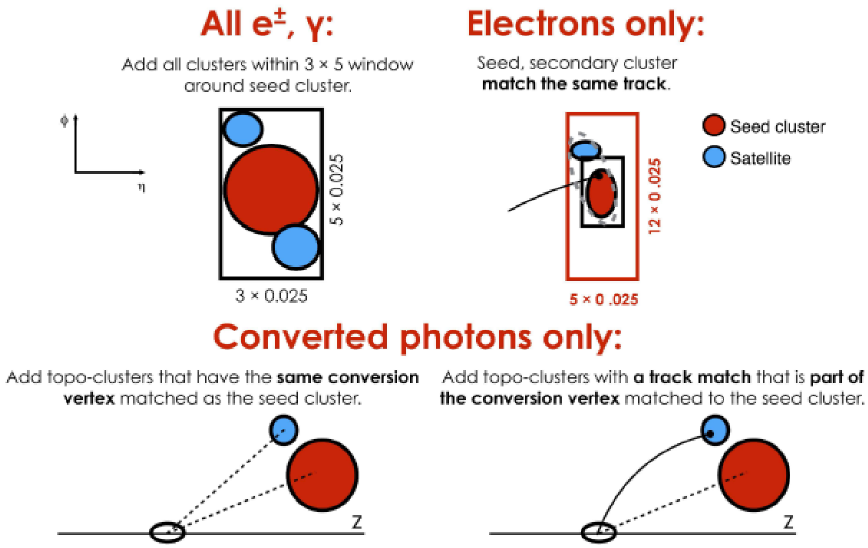

Figure 5.2.1.: Diagram of the super-clustering algorithm for electrons and photons. Seed clusters are shown in red. Satellite clusters in blue. Image from Ref. [73].

The electron super-cluster is built according to the following:

- A topo-cluster is considered as an electron super-cluster seed if it satisfies $E_{\mathrm{T}} > 1$ GeV.
- The seed must also be matched to a track with at least four hits in the ID.
- Clusters within $\delta\eta \times \delta\phi = 0.075 \times 0.125$ of the seed barycentre are considered satellite clusters and added to the super-cluster.
- Clusters within $\delta\eta \times \delta\phi = 0.125 \times 0.3$, whose best-matched track is also the best-matched track of the seed, are also added as satellite clusters.

The unconverted photon super-cluster is constructed in the following way:

- The super-cluster seed has $E_{\mathrm{T}} > 1.5$ GeV and no matching track or conversion vertex.
- Clusters within $\delta\eta \times \delta\phi = 0.075 \times 0.125$ of the seed barycentre are considered satellite clusters and added to the super-cluster.

For converted photons:

- The super-cluster seed has $E_{\mathrm{T}} > 1.5$ GeV and has a matching track or conversion vertex.
- A satellite cluster can be added if it matches to a track coming from the conversion vertex associated to the seed cluster.
- A satellite cluster can be added if the conversion vertex belonging to the seed cluster is matched to the satellite.

Once the electron and photon super-clusters are built, a sequence of calibration and position corrections are applied, and tracks are matched to electron super-clusters and conversion vertices to photon super-clusters. The p_{T} of an electron is calculated using the energy from the cluster and the direction of the track. It is possible that a seed cluster is consistent with both an electron and photon hypothesis. Resolving these ambiguous cases is performed on an analysis-by-analysis basis (if necessary).

The Selection of Electrons in the $\ell\ell + E_{\mathrm{T}}^{\mathrm{miss}}$ Analysis

In the scope of the $Z\gamma$ method (see Section 6.3) and the $\ell\ell + E_{\mathrm{T}}^{\mathrm{miss}}$ selections [1], the baseline electrons are required to have transverse momentum p_{T} larger than 7 GeV and $|\eta| < 2.47$. After overlap removal (see Section 5.5), electrons with $p_{\mathrm{T}} > 20$ GeV are selected.

Identification is performed using a likelihood, which is a discriminator built using one-dimensional pdfs of signal and background distributions. The electron likelihood discriminant is composed of shower shape distributions (e.g., e/γ results in a narrow width in η compared to jets), ratio of E_T in the HCal to E_T in the EMCal, and quantities that combine both tracking and calorimeter information. Additional cuts on some of the track quality distributions, as well as quantities related to whether the reconstructed electron is consistent with a converted photon, are also applied. There are three working points for the likelihood identification of electron candidates corresponding to different efficiencies and fake rejection probabilities: *Loose*, *Medium* and *Tight* selections. The selection is tightened by applying higher thresholds on the likelihood discriminant, in addition to stricter cuts on the additional variables mentioned. The *Medium* working point (WP) is used for selecting electrons in both $Z\gamma$ method and $\ell\ell + E_{\mathrm{T}}^{\mathrm{miss}}$ analyses. For the *Medium* WP operating point, the identification efficiency varies from 80% at $p_{\mathrm{T}} = 20$ GeV to 94% at $p_{\mathrm{T}} = 100$ GeV.

The electron efficiency can be estimated directly from data using a tag-and-probe method. This method exploits di-electron resonances like Z or J/ψ. The tag electron candidate is required to pass a *Tight* WP identification and the probe definition is relaxed to include all reconstructed electrons. The efficiency is then computed from the ratio of the passing probes to the total probes after accounting for residual background contamination. The differences observed between data and simulation arise from detector mismodelling, which for example affects shower shapes in the simulation. For this reason, the scale factors (SF $= \epsilon_{Data}/\epsilon_{MC}$) are calculated, and subsequently applied as a correction weight to MC.

To suppress the contribution from non-prompt electrons, which means electrons that are not from the hard-scatter process, a cut on the impact parameter with respect to the primary vertex is applied to the electron track in the ID. Specifically $|d_0$ significance$| < 5$[2] and $|z_0 \cdot sin(\theta)| < 0.5$ mm are required (see the definition in Section 5.1).

In order to enhance prompt production as much as possible, electrons are required to be isolated with respect to other tracks and calorimeter clusters. The isolation quantity is measuring the amount of activity in the vicinity of the electron by summing the transverse energies of clusters in the calorimeter or the transverse momenta of tracks in a cone of radius ΔR $= 0.2$ or 0.3 (in some cases a varying cone size is used) [75]. Signals with electrons at lower p_{T} may favour tighter isolation requirements, and be willing to sacrifice some signal in order to ensure high background rejection, whereas signals with electrons at higher p_{T} may instead favour looser requirements in order to maintain high signal efficiency. The optimized working points differ in the ratio value of the electron E_{T} and its

[2] the track impact parameter d0 significance is defined as S $= d_0/\sigma(d_0)$, where $\sigma(d_0)$ is the error on the reconstructed d_0.

isolation quantities. In this analysis, a *Loose* working point is used for selecting isolated electrons. The efficiency for electrons with $E_{\mathrm{T}} = 40$ GeV is approximately 90% for the tightest operating points and nearly 99% for *Loose*.

Energy calibration and resolution smearing are calculated from data and simulated samples using multivariate techniques. The calibration scale factor is applied as a correction to the data to cover the calorimeter response affecting the data, while the difference in energy resolution between data and simulation and the corresponding efficiency scale factor are applied to the simulation to ensure that it matches the data.

In 2015+2016 data and the corresponding MC samples only, electrons which are affected by an error in the e/γ reconstruction code in the crack region of the EMCal are removed. This is detailed in Section A.1. Table 5.2.1 gives a summary of the electron selection criteria.

Crack Veto (After OR)	exclude events if electrons are in the crack region for 15/16 data
Identification after OR/baseline	Likelihood Medium ID/Likelihood *Loose* ID
Kinematic cuts after OR/baseline	$p_{\mathrm{T}} > 20$ GeV/$p_{\mathrm{T}} > 7$ GeV and $\|\eta\| < 2.47$
Non-prompt cuts	$\|d_0$ significance$\| < 5$ $\|z_0 \cdot sin(\theta)\| < 0.5$ mm
Isolation	*Loose* Isolation

Table 5.2.1.: Summary of electron selections.

The Selection of Photons in the $\ell\ell + E_{\mathrm{T}}^{\mathrm{miss}}$ Analysis

NOTE: Photons are only used for the $Z\gamma$ method to estimate the ZZ background. The $Z\gamma$ method is described in Chapter 6. The main idea of taking the photon to be a substitute for the Z is that the photon is expected to have similar kinematics as a Z boson in the high p_{T} regions.

The photon selection is based on the EM cluster information. First, the photon is classified as converted or unconverted depending on whether its cluster is associated with a track or a vertex in the ID. The shower shapes and other discriminating variables are used to identify between prompt photons and non-prompt photons originating from the decay of neutral hadrons in jets. Prompt photons typically produce narrow energy deposits in the EMCal and have minimal leakage in the HCal, while background photons from jets ($\pi^0 \to \gamma\gamma$) are characterised by two separate local energy maxima in the finely segmented strips of the EMCal first layer. The optimization of the photon identification process is used to define two sets of cuts, *Loose* and *Tight* selections. The *Tight* working point is used for selecting photons in the $Z\gamma$ method.

To avoid selecting 'fragmentation' photons that are produced from jets during parton showering, photons are required to be isolated with respect to calorimeter clusters and tracks. A p_{T}-dependent cone-based isolation is calculated based on the transverse energy with angular size ΔR around the direction of the photon candidate. A *Loose* WP is adopted, based on both the calorimeter isolation and the track isolation in a cone with $\Delta\mathrm{R} = 0.2$.

The photon identification efficiency is measured to account for the differences between data and MC, due to detector mismodelling in the simulation. There are three methods to measure the efficiency in data in bins of E_{T} and $|\eta|$:

- *Radiative Z decays*: The events required the presence of a photon candidate and an opposite-charge pair of electron or muon candidates. A fit to data using signal and background $m_{ll\gamma}$ templates obtained from simulation and a data control region are used to extract the number of radiative Z events before and after photon identification selections are applied: the efficiency is defined as the ratio $N_{\mathrm{pass}}/N_{\mathrm{all}}$. The computation is performed in the range up to $E_T = 100$ GeV due limited statistics of the $Z\gamma$ events.
- *Electron extrapolation*: A sample of electron candidates are selected from $Z \to ee$ decays by using a tag-and-probe method. Contributions from fake electrons are identified using a template fit to the m_{ee} distribution and subtracted. The distributions of the shower shape variables are modified to match the expected photon profiles separately for converted and unconverted photons. The photon identification selection cuts are then applied to the transformed electron shower shapes as if they were photon candidates. The efficiency is then measured based on the number of the transformed electron candidates that pass the selections.
- *Inclusive photons*: An inclusive photon sample is collected using single-photon triggers over a wide kinematic range. A tight track isolation cut is used to select prompt photons in the full sample and also in the sub-sample of photon candidates that pass the tight identification selection. The efficiency is defined as the ratio of the latter to the former; these terms, as well as the background contamination in the regions, are determined using a matrix method.

The efficiency of the *Tight* identification criteria is measured using the three methods outlined above. All measurements are performed for photons satisfying the loose isolation selection. The identification efficiency reaches about 95-98% for $E_T > 70$ GeV.

Table 5.2.2 summarises the photon selection for the $Z\gamma$ method.

Identification	*Tight* ID
Kinematic cuts	$p_{\mathrm{T}} > 60$ GeV (> 10 GeV for baseline) $\lvert\eta\rvert < 1.37$ or $1.52 < \lvert\eta\rvert < 2.37$
Isolation	*Loose*

Table 5.2.2.: Summary of photon selections.

5.3. Muons

The information used in the muon reconstruction comes mainly from the ID and the muon spectrometer (MS). Tracks from muons are initially reconstructed in the ID and MS independently. An *inside-out* reconstruction algorithm, in which ID tracks are matched to MS hits and then a combined fit is performed to reconstruct the so-called combined muons (CB). Other muon reconstruction algorithms require different identification criteria depending on which sub-detectors are used.

The Selection of Muons in the $\ell\ell + E_{\mathrm{T}}^{\mathrm{miss}}$ Analysis

Several working points for muon identification are available, with different efficiencies and fake rejection probabilities. In this analysis, the *Loose* WP is used as a baseline and the *Medium* WP as nominal. The *Medium* identification is based on requirements on the number of hits in the different ID and muon spectrometer sub-systems, and on the compatibility between ID and muon spectrometer p_{T} measurement to suppress the contamination due to hadrons which are misidentified as muons. The *Loose* identification has a high reconstruction efficiency (there is also *VeryLoose* with a maximal efficiency, but there would be far too many fakes), while the *Tight* identification maximizes the purity of muons with low muon reconstruction efficiency.

The baseline muons are required to have transverse momentum p_{T} larger than 7 GeV. After overlap removal, muons with p_{T} greater than 20 GeV are used as signal muons.

To suppress the contribution from cosmic muons and non-prompt muons, a cut on the impact parameters with respect to the primary vertex is applied to the muon track in the ID, specifically d_0 significance < 3 and $|z_0 \cdot sin(\theta)| < 0.5$ mm are required (see the definition in Section 5.1). In order to avoid muons associated with jets and to additionally suppress semi-leptonic decays of b hadrons, the candidates are required to be isolated. Isolation is based on the activity observed in the calorimeter and in the ID both within a cone of radius $\Delta\mathrm{R} = 0.2$ or 0.3 (in some cases a varying cone size is used) around the muon object. A loose isolation selection is used for muons, which corresponds to an isolation efficiency of $\geq 99\%$ for $p_{\mathrm{T}} > 20$ GeV muons.

Finally, to account for effects of detector resolution that are not well reproduced in MC samples, the transverse momentum of the muons is smeared and weights are applied to account for the difference in efficiency.

The muon selection is summarised in Table 5.3.1.

Identification after OR/baseline	Combined muons with *Medium*/*Loose* quality
Kinematic cuts after OR/baseline	$p_{\mathrm{T}} > 20$ GeV/$p_{\mathrm{T}} > 7$ GeV
Cosmic cuts	$\lvert d_0$ significance$\rvert < 3$ $\lvert z_0 \cdot sin(\theta)\rvert < 0.5$ mm
Isolation	*Loose*

Table 5.3.1.: Summary of muon selections.

5.4. Jets

The ensemble of quarks and gluons produced from inelastic proton-proton collisions cannot be isolated due to colour confinement, so they are measured as jets after they undergo hadronisation in the ATLAS detector. In other words, reconstructed jets are a piece of information of the detector response to represent the dynamics of the underlying process formed by a hard-scatter parton.

Dealing with pile-up is a major challenge during jet reconstruction. These additional low p_T pp collisions are differentiated between *in-time* and *out-of-time* pile-up. *In-time* pile-up refers to the additional pp interactions in the same bunch-crossing. An *out-of-time* pile-up corresponds to the deposited energy in the calorimeter from the earlier or following bunch crossing. *In-time* effects are related to the number of primary vertices in the bunch crossing, N_{PV}. Similarly, the *out-of-time* effects are parametrized in the average number of inelastic pp interactions per bunch crossing $<\mu>$ [76]. The μ is the bunch pile-up parameter, which is directly related to the instantaneous luminosity. The effect of *out-of-time* pile-up is reduced in the calorimeters by a technique called *optimal filter coefficients* [77] based on the different shaped signals of the detector pulse with respect to time [ns].

There exist many variants of jet algorithms that define a deterministic set of rules on how final-state particles are combined into jets, meaning which particles belong to a jet depends on the algorithm. Jet clustering algorithms will be discussed in Section 5.4.1. Specific to ATLAS, topological-cluster (EMTopo) jets and particle-flow (PFlow) jets with jet energy corrections are presented in Section 5.4.2. The details of jet energy calibration are described in Section 5.4.3. Additionally, the algorithm developed to reduce pile-up in the event is summarised in Section 5.4.6.

5.4.1. Reconstruction Algorithms

The definition of a jet is not unique, and there are several approaches in use for reconstructing jets. Different types of sequential cone algorithms, including *anti-*k_t and k_t are described in the following. These algorithms are specified by the definition of the distance measures:

$$d_{ij} = min(k_{ti}^{2p}, k_{tj}^{2p})\frac{\Delta y_{ij}^2 + \Delta\phi_{ij}^2}{R^2}, \quad d_{iB} = k_{ti}^{2p}, \tag{5.4.1}$$

where d_{ij} is the distance between two particles i and j with $\Delta y_{ij}^2 = (y_i - y_j)^2$ and $\Delta\phi_{ij}^2 = (\phi_i - \phi_j)^2$; k_{ti}, y_i, and ϕ_i are the transverse momentum, rapidity, and azimuth of particle i, respectively; and R is the jet radius parameter that determines the jet size. The free parameter p sets the power of the transverse momentum scale. The *anti-*k_t, k_t, and Cambridge/Aachen algorithms correspond to p = -1, 1, and 0, respectively. The variable d_{iB} calculates the distance from the particle i to the beam.

In the *anti-*k_t algorithm, high-p_T particles are clustered first, while the k_t algorithm clusters soft particles first. The clustering algorithm works by iterative recombinations until all particles are part of a jet within the radius R: merging particles i and j by combining two four-vectors if $d_{ij} < d_{iB}$, otherwise if $d_{ij} > d_{iB}$, then particle i is considered a complete jet and removed from the list of particles. The algorithm repeats this procedure of all combinations of d_{ij} and d_{iB} until no objects remain. Figure 5.4.1 illustrates the *anti-*k_t and k_t algorithm with the same radius, R = 1. Larger-R is a preference for boosted topologies while smaller-R is mostly used for QCD jets containing quarks/gluons.

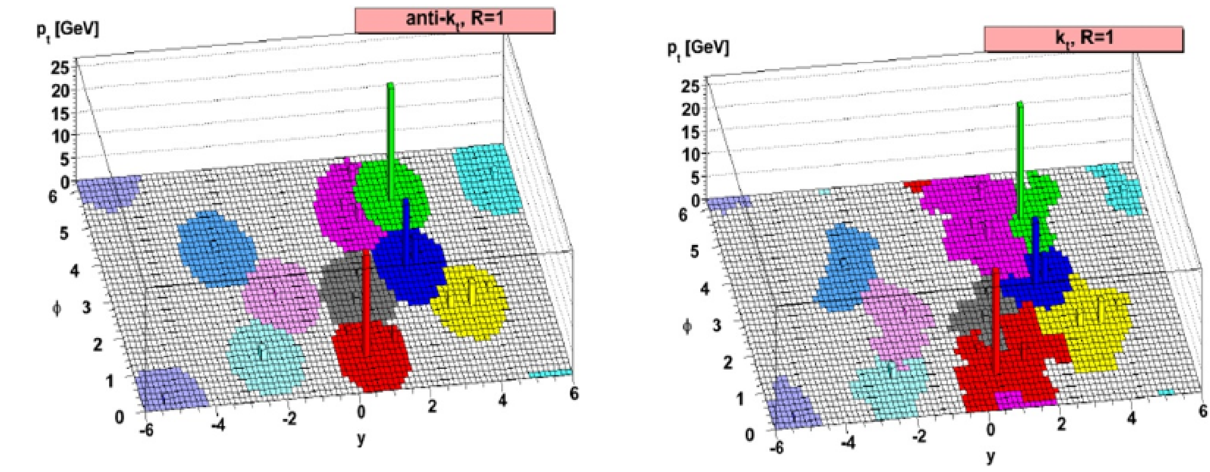

(a) (b)

Figure 5.4.1.: Coloured areas represent clustered jets. An illustration of the *anti-k_t* jet reconstruction is shown on the left and k_t algorithm is shown on the right. The preference for hard radiation can be seen in the features of *anti-k_t* jets [78].

The algorithms are also required to be infrared and collinear (IRC) safe. Collinear safety means a collinear splitting does not affect the jet boundaries. Figure 5.4.2 (a) gives an example of an algorithm that is not collinear safe. It shows a jet containing all three partons while the splitting of the highest p_{T} parton leads to a different jet clustering. Infrared safety means the soft emission particle does not affect the clustering result drastically. The soft emission should not change the jet multiplicity. Figure 5.4.2 (b) shows an infrared unsafe case where the algorithm is sensitive to the soft particle resulting in the two jets to be merged into one jet. Changing the jet multiplicity means changing the observed physics. It is thus important to find a set of algorithms that ensure the jet boundaries are insensitive to both IR and splitting particles in hadronic showers.

All Cambridge/Aachen, *anti-k_t* and k_t algorithms are IRC safe. The k_t algorithm can better approximate the stochastic evolution of hadronic showers, while the *anti-k_t* algorithm starting from the hardest particles is expected to miss some of the deposited energy. However, the *anti-k_t* algorithm has more benefits (fast, and IRC safe) than drawbacks (missing energy) in collider environments. The missed energy can be fixed through jet calibrations. Therefore, the *anti-k_t* algorithm is the preferred one in studies involving jets performed at the LHC.

5.4.2. EMTopo Jets and Particle Flow Jets

EMTopo Jets

ATLAS primarily uses topological cell clustering (topo-clustering) as the inputs to jet reconstruction, which are designed to suppress noise effects by grouping cells in a 4-2-0 topo-cluster scheme:

- **Seed cells:** the energy deposits with $\xi > 4$. (see Figure 5.4.3 (a))
- **Secondary cells:** all neighbor cells or secondary cells with $\xi > 2$. (see Figure 5.4.3 (b))

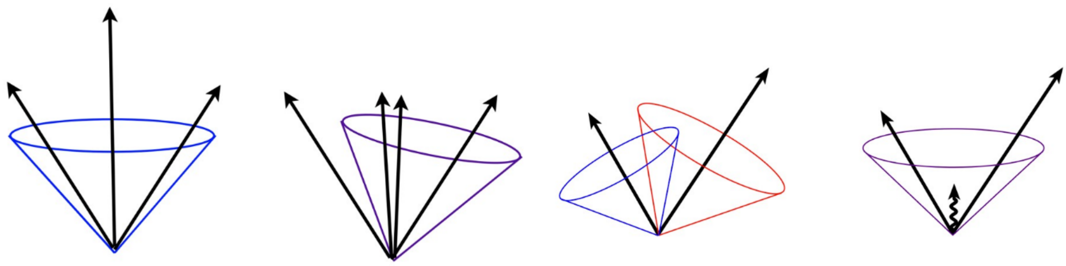

(a) (b)

Figure 5.4.2.: (a) Example of collinear unsafety. The jet is changed due to a collinear splitting. (b) Example of infrared unsafety. Jets are merged after the emission of a soft particle [79].

- **Basic threshold:** adding all calorimeter cells adjacent to the topo-cluster. (see Figure 5.4.3 (c))

where ξ is the ratio of measured energy divided by the average amount of noise (electronic and pile-up) expected in the cell:

$$\begin{aligned} \xi^{EM}_{cell} &= \frac{E^{EM}_{cell}}{\sigma^{EM}_{noise,cell}}, \\ \sigma &= \sqrt{(\sigma_{electronic\ noise})^2 + (\sigma_{pile-up\ noise})^2}. \end{aligned} \tag{5.4.2}$$

Topo-clusters are grouped in three dimensions meaning adjacent cells can be in the same layer of the same calorimeter, different layers of the same calorimeter, or a different calorimeter. Topo-clusters can be calibrated at one of two scales: Electromagnetic (EM) scale which corrects the calorimeter level energies to the electromagnetic scale and Local cell weighted (LCW) scale which applies different weights to electromagnetic and hadronic interactions in the calorimeters. The jet energy scale will be detailed in Section 5.4.4.

Origin Correction

The default 4-vector of topo-clusters points toward the centre of the detector. However, a significant improvement in jet η resolution was seen after applying *origin corrections*. This is achieved by modifying the jet 4-vector based on the assumption that jets are from the position of the hard scattering (see Figure 5.4.4). The correction is done event-by-event to every topo-cluster. The jet energy is unchanged but the jet's direction is changed.

Particle Flow Jets

Formation of topo-clusters already suppresses some pile-up (primary goal of topo-clusters is to reject noise). Pile-up suppression can be done not only at the level of an average topo-cluster but also event-by-event. Several techniques have been developed (see Section 5.4.3, Section 5.4.6) as well as the alternative particle flow (PFlow) jet.

The PFlow approach uses measurements from the tracking system and calorimeters. The advantage of each measurement is listed below:

Tracking detector:

- Pile-up suppression by requesting the tracks to come from the hard-scatter vertex.

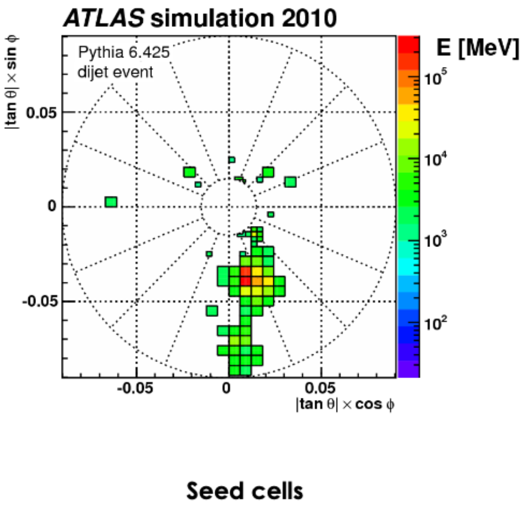

(a)

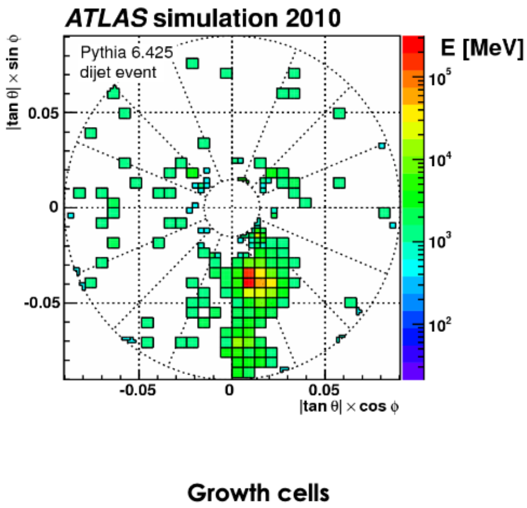

(b)

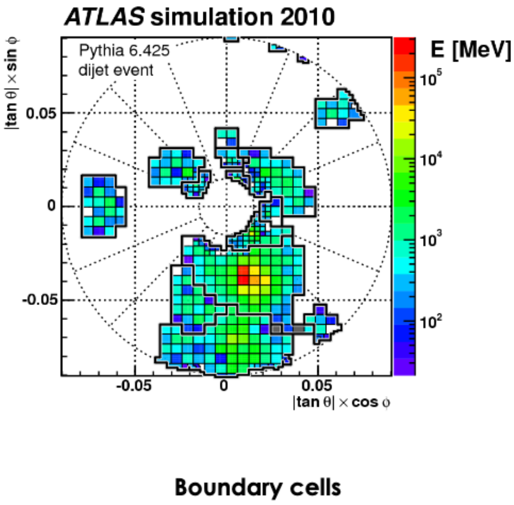

(c)

Figure 5.4.3.: Building a 4-2-0 topo-cluster. Figure (a) shows the individual calorimeter cells that are chosen if cells have $\xi > 4$. Figure (b) shows the adjacent cells to the seed when $\xi > 2$ are added. Figure (c) shows the tertiary cells with $\xi > 0$ [80].

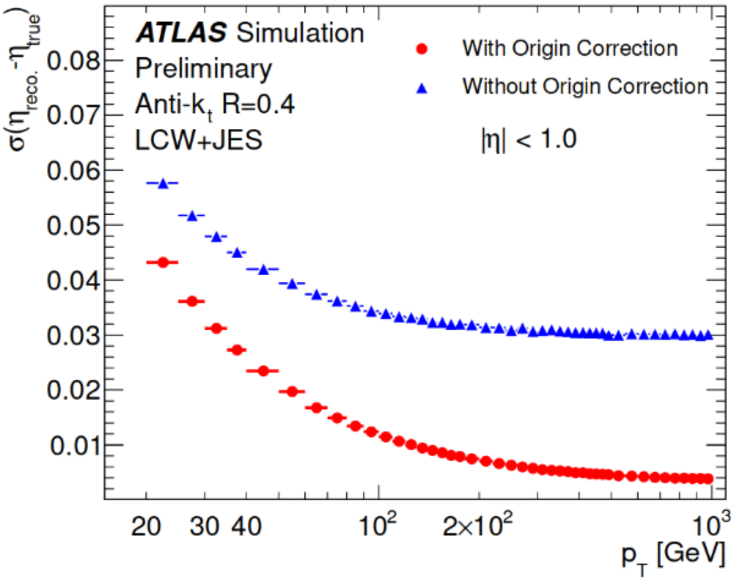

Figure 5.4.4.: The effect of the origin correction on the η resolution for R = 0.4 jets with LCW scale. Image from Ref. [81].

- Better reconstruction efficiency and momentum resolution at low p_{T}.

Calorimeters:

- Sensitive to both neutral and charged particles.
- Better energy resolution at high p_{T}.

For a single charged pion in the centre of the detector, the design calorimeter energy resolution is [82]:

$$\frac{\sigma(E_0)}{E_0} = \frac{50\%}{\sqrt{E}} \oplus \frac{1\%}{E} \oplus 3.4\% \tag{5.4.3}$$

The equation of the design track resolution shows that the momentum resolution of the tracker is better than the energy resolution of the calorimeter for low-energy charged particles [82]:

$$\sigma(\frac{1}{p_{\mathrm{T}}}) \cdot p_{\mathrm{T}} = 0.036\% \cdot p_{\mathrm{T}} \oplus 1.3\% \tag{5.4.4}$$

The PFlow algorithm subtracts the calorimeter cluster matching an extrapolated track. Because about two-thirds of visible jet energy consist of charged pions, depositing energy in the tracking detector, the PFlow algorithm uses the pion mass hypothesis for all tracks to reconstruct jets. The subtraction flow is described in Figure 5.4.5, which can be summarised into the following steps:

- **Matching tracks to topo-clusters.** The tracks matched to candidate electrons or muons (with medium quality criteria, but no isolation requirements) are not selected.
- **Evaluation of the expected deposited particle energy** A particle with measured momentum p^{trk} on average is given as: p^{trk} $\times$ the mean response estimated

using single pion samples. The mean response is calculated by summing the energies of topo-clusters (extrapolated to the second layer of the EMCal) around the track position over the momentum.

- **Recovering split showers.** Each track can be matched to one topo-cluster or more. The charged hadron particles, such as $\pi^{\pm}$ have shower development and leave most of their energy in the calorimeter detector. In Figure 5.4.6 (a), the track/topo-cluster matching is shown on the left-hand side where the charged pion is matched to one topo-cluster, and split shower recovery is shown on the right-hand side where the charged pion is matched to two topo-clusters. The determination uses the information from the second item.

- **The subtraction procedure.** The subtraction does cell-by-cell removal to avoid taking off contributions from neutral hadrons as shown in Figure 5.4.6 (b). The remnant energy from shower fluctuations is also removed (Figure 5.4.6 (c)).

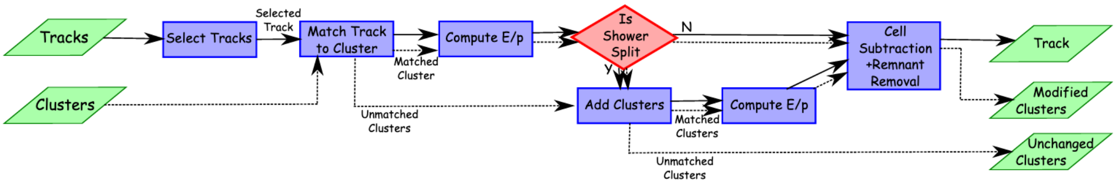

Figure 5.4.5.: A flow chart shows how the neutral particle flow (nPFOs) and charge particle flow (cPFOs) objects proceed. Image from Ref. [83].

The performance of EMTopo jets and PFlow jets used in the $E_{\mathrm{T}}^{\mathrm{miss}}$ algorithm is shown in Section 5.6.5.

5.4.3. Jet Calibration

Particles pass through the sampling calorimeters and deposit their energy until they are fully stopped. However, not all of the layers are active materials, and so some energy is deposited in the passive layers, resulting in energy loss that is not recorded. The sampling fraction of the electromagnetic barrel calorimeter in ATLAS is 18%, which is defined as:

$$f_{sample} = \frac{E_{active}}{E_{active} + E_{passive}}. \tag{5.4.5}$$

About 1/3 of hadronic processes result in neutral pions. Neutral pions decay almost immediately into two photons, producing an electromagnetic component to the hadronic shower. The remaining 2/3 include the production of charged hadrons (20%), fragments of nuclei (30%), neutrons (10%), and invisible, mostly nuclear, processes (40%) [84]. In other words, a significant fraction of the hadronic shower energy is undetectable. These effects cause the reconstructed jet momentum to not be the same as the reconstruction at the truth level. The way to include the missing energy is to calibrate the jets after reconstruction.

The reconstructed jets are calibrated through a series of sequential steps to make their energy and mass match the truth jet: area-based pile-up correction (jet ghost-area subtraction method) with residual pile-up correction, absolute MC-based calibration, a *global sequential calibration* (GSC), and *in-situ* calibration [85].

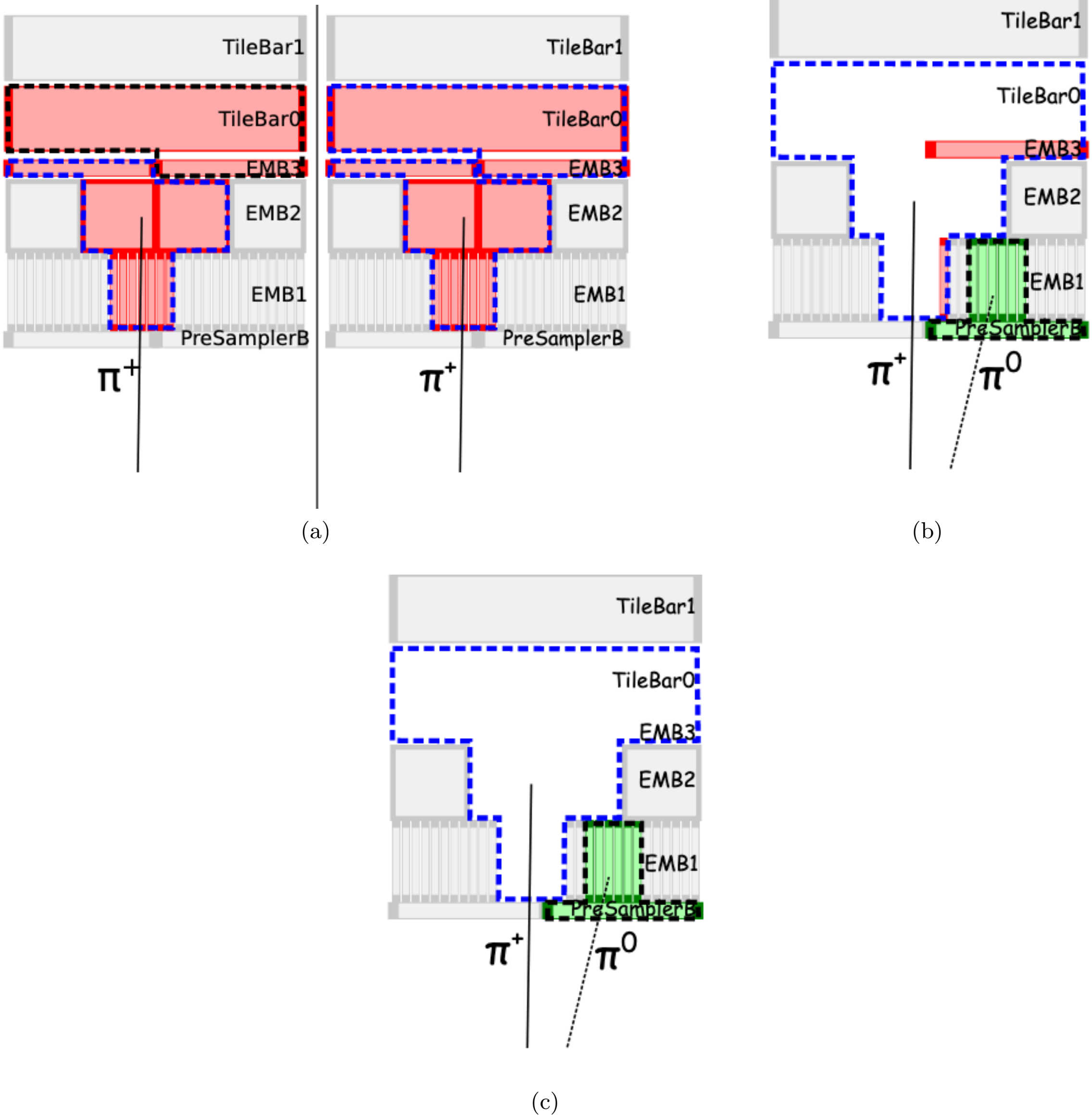

Figure 5.4.6.: The shower subtraction procedure in PFlow algorithm dealing with different cases as discussed in the text. The red cells associated to tracks represent charged hadrons, while green cells without a track close by are recognized as a neutral hadron or the photons. The dotted line means the boundaries of the selected cells by the algorithm. Three electromagnetic calorimeter layers and two tile calorimeter layers are shown. Image from Ref. [83].

Area-based Pile-up Correction and Residual Pile-up Correction

The pile-up suppression is the first step of the calibration chain. The jet p_{T} has a dependency on N_{PV} and μ as the multiplicity is increased from both hard-scatter interaction and pile-up sources. To remove the dependence of the jet p_{T} on the pile-up, using the number of primary vertices N_{PV} and the average number of interactions per crossing $<\mu>$, p_T^{corr} is defined as the following equation correcting the p_{T} of an individual jet:

$$p_T^{corr} = p_T^{reco} - \rho \times A - \alpha \times (N_{PV} - 1) - \beta \times \mu \tag{5.4.6}$$

where jet area A is a measure of how much pile-up will be clustered into the jet (per jet). The "ghosts" (infinitesimal energy that does not change the energy of the jet) are added evenly throughout an event with p_{T} density equal to ρ, which is the median of the jet p_{T} of R $= 0.4$ k_t jets with $|\eta| < 2$ in an event:

$$\rho = median\left(\frac{p_{\mathrm{T}}}{A}\right). \tag{5.4.7}$$

The "ghosts" are determined by using k_t jets because the k_t algorithm is sensitive to the soft radiation. The $\rho \times$ A term is supposed to subtract the per-event pile-up contribution to the p_{T} of each jet according to its area. The third and the fourth terms are event specific *in-time* pile-up corrections and subtract *out-of-time* pile-up dependence, respectively. The coefficients α ($\frac{\partial p_{\mathrm{T}}}{\partial N_{PV}}$) and β ($\frac{\partial p_{\mathrm{T}}}{\partial \mu}$) in Equation 5.4.6 are determined from simulation in bins of $|\eta|$ as shown in Figure 5.4.7 (a) and (b) respectively, and the factors are determined by linear fits as a function of η. The subtraction for each jet brings the jet energy scale closer to the scale without pile-up.

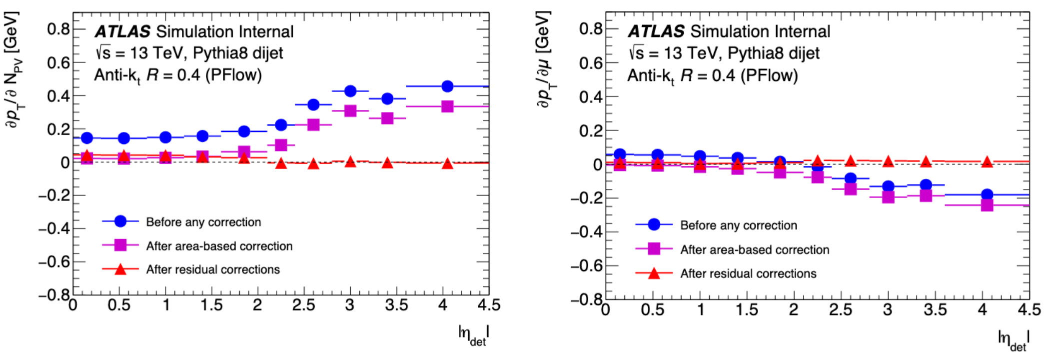

(a) (b)

Figure 5.4.7.: (a) In-time pile-up dependence. (b) Out-of-time pile-up dependence. Image from Ref. [86].

Absolute MC-based Calibration

The absolute MC-based calibration is applied after pile-up corrections for non-compensating calorimeter response, energy losses in dead material, leakage, truth/reconstructed jet migration, and biases in the jet η reconstruction. The procedure corrects the reconstructed jet to the particle level by calculating the average jet energy response (R) and the η response. Isolated reconstructed jets are used and matched to truth jets within ΔR $= 0.3$ in the calibration.

The inverse of the ratio $< \frac{E^{reco}}{E^{truth}} >$ is applied as an energy correction. The ratio is measured in bins of E^{truth} and η_{det} (the jet η pointing away from the geometric centre of the detector). Additional correction is applied for the geometric differences in the pseudo-rapidity of the jet, which is caused by the detector's transition regions or cracks as shown in Figure 5.4.8. The barrel-endcap ($|\eta_{det}| \sim 1.4$) and endcap-forward ($|\eta_{det}| \sim 3.1$) regions get higher corrections. This step is able to bring the jet energy closer to the truth scale, often referred to as the EM+JES.

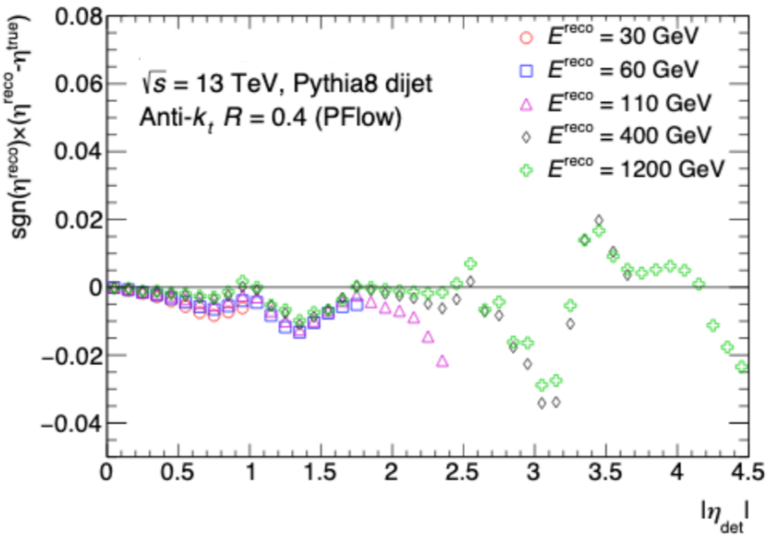

Figure 5.4.8.: The signed difference between the reconstructed and truth jet η, η^{reco} and η^{true}. Each value is obtained from the corresponding parametrized function derived with the Pythia MC sample, and only jets satisfying $p_{\mathrm{T}} > 20$ GeV are shown. Image from Ref. [86].

Global Sequential Calibration

Global sequential calibration (GSC) mainly accounts for the jet energy scale (JES) flavour dependence. For quark-initiated jets, they penetrate deeply into the calorimeter, while for gluon-initiated jets, they consist of softer components that would lead to non-Gaussian distribution of tails.

Residual in-situ Calibration

The final stage of the chain accounts for differences between data and MC. The correction is applied to data to consider detector effects which are not captured by simulation. The procedures are done by comparing data and MC in several well-known topologies and consist of three steps in order :

- **The η inter-calibration:** using back-to-back dijet events to calibrate forward jets ($0.8 < |\eta| < 4.5$) to the same energy scale as the central jets ($|\eta| < 0.8$).
- **The V+jet calibration:** Balancing the p_{T} of a jet within $|\eta|$<0.8 against a Z or a γ boson in the p_{T} range 20−800 GeV. One can balance between the full hadronic recoil in an event and the reference boson, that would be less sensitive to the jet definition, radius parameter, pile-up and underlying activity.

- **The multi-jet calibration:** jets can be calibrated in multijet events in the p_{T} range 300 GeV$-$2 TeV for large-R jets. A leading large-R jet is balanced against a system that consists of multiple lower-p_{T} jets (obtained from calibrated small-R *anti-k_t* jets).

The remaining differences between data and MC after *in-situ* correction are taken as uncertainties.

5.4.4. Jet Energy Scale Uncertainties

The JES calibration scheme is discussed in Section 5.4.3 including pile-up correction, Monte Carlo jet energy scale calibration, flavour dependency, and different response in data and MC. Thus the associated JES uncertainty sources include a set of 80 JES systematic uncertainty terms. The majority (67) of uncertainties come from the $Z\gamma$ + jet and multi-jet balance (MJB) *in-situ* calibrations and account for assumptions made in the event topology, MC simulation, sample statistics, and propagated uncertainties of the electron, muon, and photon energy scales. The remaining 13 uncertainties are derived from other sources: four pile-up uncertainties (N_{PV}, μ, ρ, and p_{T} dependence), three η inter-calibration uncertainties (potential physics mismodelling, statistical uncertainties, and the method non closure), three jet response uncertainties (quarks-gluons, b-quark, and gluon-initiated), GSC punch-through correction, a high-pT jet uncertainty, and AFII [3] modelling uncertainty. AFII non-closure is applied only to AFII MC samples [85].

When constructing the full set of uncertainty sources, each component is generally treated uncorrelated. But there are some exceptions, such as the electron and photon energy scale measurement. The full combination of all uncertainties is shown in Figure 5.4.9 where the JES uncertainty varies between 1$-$4.5% in the central region with $\eta = 0$ and the uncertainty is quite independent on η and the largest value is about 2.5% for forward jets with $p_{\mathrm{T}} = 80$ GeV.

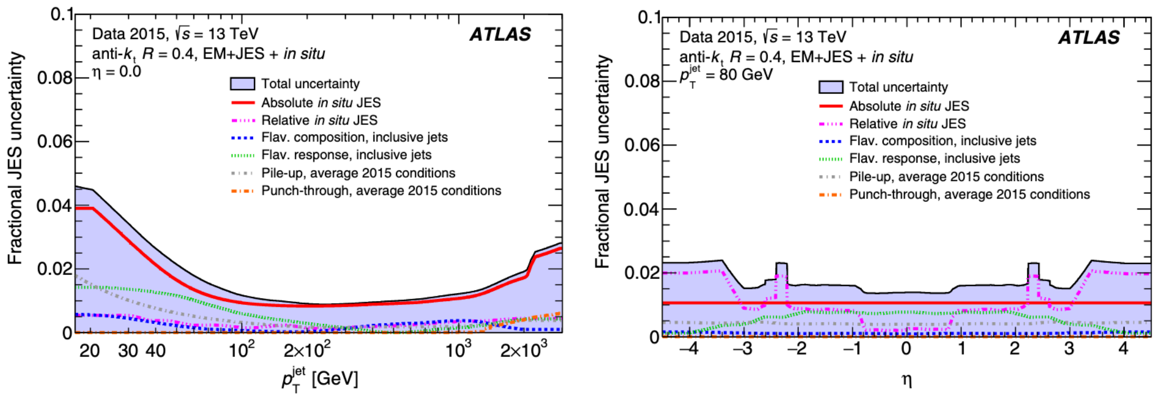

(a) (b)

Figure 5.4.9.: Combined uncertainty in the JES of fully calibrated jets as a function of (a) jet p_{T} at $\eta = 0$. (b) η at $p_{\mathrm{T}} = 80$ GeV. Image from Ref. [85].

5.4.5. Jet Energy Resolution

The Jet Energy Resolution (JER) is an important quantity giving the peak width of the Gaussian jet response distributions as a function of energy. The energy and momentum

[3] AFII (Atlfast2) and AFIIF (Atlfast2F) are fast simulations. Some ways that can speed up simulation: approximate geometry (only keep sensitive modules identical), approximate models, etc.

of the jets are calibrated to the electromagnetic scale by applying the mean of the ratio of reconstructed energy and the truth distribution in bins of p_{T} and $|\eta|$ as described in the JES calibration Section 5.4.3. The width quantifies how much of a spread remains; a narrow jet energy width means the jet is being calibrated to the correct scale.

The jet energy resolution is parametrized as shown in Equation 3.3.3 including the noise term (N), stochastic term (S), and a constant term (C). The noise term comes from pile-up and electronics noise, the stochastic term arises from the sampling nature of the calorimeters, and the constant term is a p_{T}-independent term.

Techniques to determine the JER can be exploited by the p_{T} balance in γ + jet and Z + jet, dijet, and multijet event. Using dijet events, one can calibrate the different response to jets in different calorimeter regions as the two jets are expected to have the same p_{T}. A quantity for the momentum balance is defined by:

$$\mathcal{A} = \frac{p_T^{prob} - p_T^{ref}}{p_T^{avg}}, \tag{5.4.8}$$

where p_T^{ref} is the transverse momentum of a jet in a well-calibrated reference region (i.e. $0.2 \leq |\eta| \leq 0.7$), p_T^{prob} is the p_{T} of the jet in the calorimeter region under investigation (i.e. $0.7 \leq |\eta| \leq 2.0$), and $p_T^{avg} = (p_T^{prob} + p_T^{ref})/2$.

The standard deviation of the probe jet p_{T} is derived by:

$$\left\langle \frac{\sigma_{p_{\mathrm{T}}}}{p_{\mathrm{T}}} \right\rangle_{prob} = \sigma_{\mathcal{A}}^{prob} \ominus \left\langle \frac{\sigma_{p_{\mathrm{T}}}}{p_{\mathrm{T}}} \right\rangle_{ref}. \tag{5.4.9}$$

The relative jet p_{T} resolution of the reference region is defined by:

$$\left\langle \frac{\sigma_{p_{\mathrm{T}}}}{p_{\mathrm{T}}} \right\rangle_{ref} = \frac{\sigma_{\mathcal{A}}^{det}}{\sqrt{2}}. \tag{5.4.10}$$

$\sigma_{\mathcal{A}}^{det}$ is measured by subtracting in quadrature the asymmetry width of truth-particle quantity from that of observed quantity: $\sigma_{\mathcal{A}}^{reco} \ominus \sigma_{\mathcal{A}}^{truth}$. The standard deviation of the asymmetry distribution can be expressed as:

$$\sigma_{\mathcal{A}}^{prob} = \frac{\sigma_{p_{\mathrm{T}}}^{probe} \oplus \sigma_{p_{\mathrm{T}}}^{ref}}{p_T^{avg}}, \tag{5.4.11}$$

where $\sigma_{p_{\mathrm{T}}}^{probe}$ and $\sigma_{p_{\mathrm{T}}}^{ref}$ are the standard deviations of p_T^{probe} and p_T^{ref}, respectively. The *in-situ* techniques are introduced to derive a data-to-MC ratio as systematic uncertainties. The JER combined dijet results are fitted with an N, S and C parametrization as shown in Figure 5.4.10. Particle flow jets show lower JER and smaller uncertainties at low p_{T} than EMTopo jets.

The total uncertainty and the sources of systematic uncertainty are shown in Figure 5.4.11. The noise term uncertainties are important at low p_{T}.

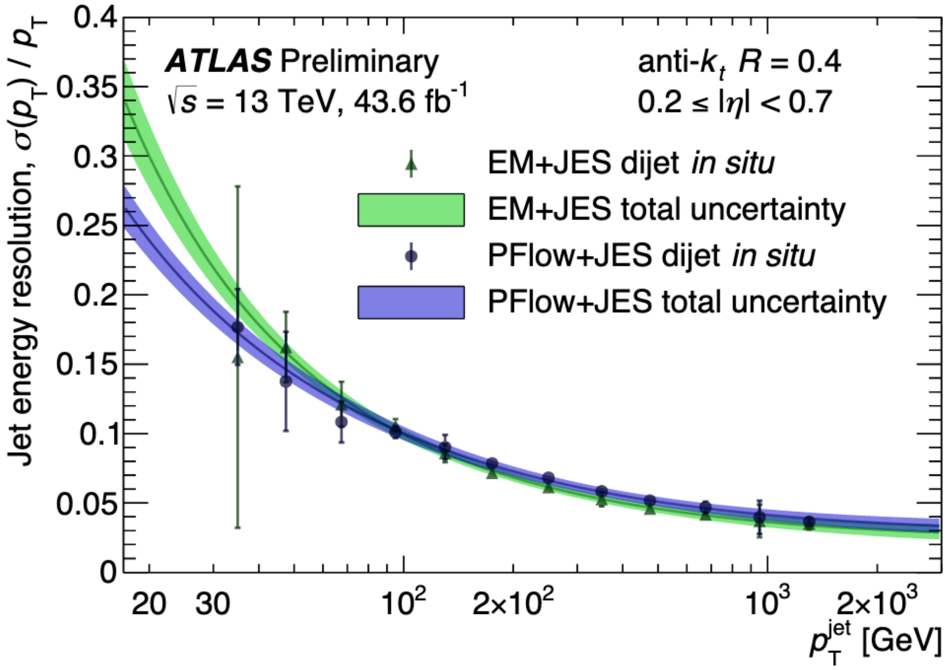

(a)

Figure 5.4.10.: Jet energy resolution as a function of jet p_{T}. Image from Ref. [87].

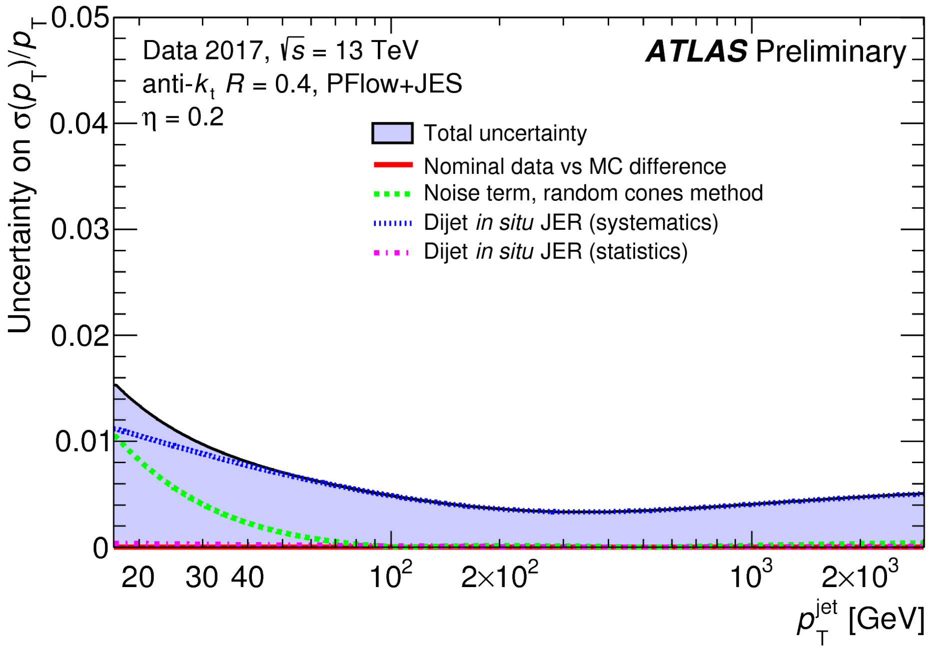

(a)

Figure 5.4.11.: The uncertainty on the relative jet energy resolution as a function of p_{T} for *anti-*k_t R = 0.4 PFlow jets. The uncertainty sources include the difference between data and simulation when the nominal data resolution is superior (red), the noise term (green), systematics (blue) and statistical (pink) uncertainty of the method in dijet events. Image from Ref. [87].

5.4.6. (forward)Jet Vertex Tagger

Applying a jet p_{T} threshold was found to substantially reduce the multiplicity of pile-up jets. However, it does not remove pile-up overlapping with a jet from a primary vertex. A Vertex Tagger (JVT) is developed for the local fluctuations in the pile-up activity. For the central jets ($|\eta| < 2.4$) where the track system is located, a JVT is applied to separate hard-scatter (HS) from pile-up. A JVT is built out of the combination of two quantities by 2-dimensional JVT likelihood fitting [88]; corrJVF (Equation 5.4.12) and $R^0_{p_{\mathrm{T}}}$ (Equation 5.4.13).

$$\mathrm{corrJVF} = \frac{\Sigma_k p_{\mathrm{T}}^{\mathrm{trk}_k}(PV_0)}{\Sigma_l p_{\mathrm{T}}^{\mathrm{trk}_l}(PV_0) + \frac{\Sigma_{n\geq 1}\Sigma_l p_{\mathrm{T}}^{\mathrm{trk}_l}(PV_n)}{k \cdot n_{\mathrm{trk}}^{PU}}}, \tag{5.4.12}$$

where $\Sigma_k p_{\mathrm{T}}^{\mathrm{trk}_k}(PV_0)$ is the scalar p_{T} sum of the tracks that are associated with the jet originating from a primary vertex. The term $\Sigma_{n\geq 1}\Sigma_l p_T^{\mathrm{trk}_l}(PV_n)$ is considered the scalar p_{T} of tracks associated to any of the pile-up interactions, and it is divided by a correction of the total number of pile-up tracks per event ($n_{\mathrm{trk}}^{\mathrm{PU}}$). k in the formula is set to be 0.01. The higher corrJVF, the higher chance of jet candidates coming from a hard-scatter as shown in Figure 5.4.12 (a).

$$R^0_{p_{\mathrm{T}}} = \frac{\Sigma_k p_{\mathrm{T}}^{\mathrm{trk}_k}(PV_0)}{p_{\mathrm{T}}^{jet}}, \tag{5.4.13}$$

where p_{T}^{jet} is the fully-calibrated jet p_{T}. $R^0_{p_{\mathrm{T}}}$ at small values indicates jets with no or little p_{T} from hard-scatter tracks. The spread of the charged p_{T} fraction ($R^0_{p_{\mathrm{T}}}$) for hard-scatter jets is larger than for pile-up jets as seen in Figure 5.4.12 (b).

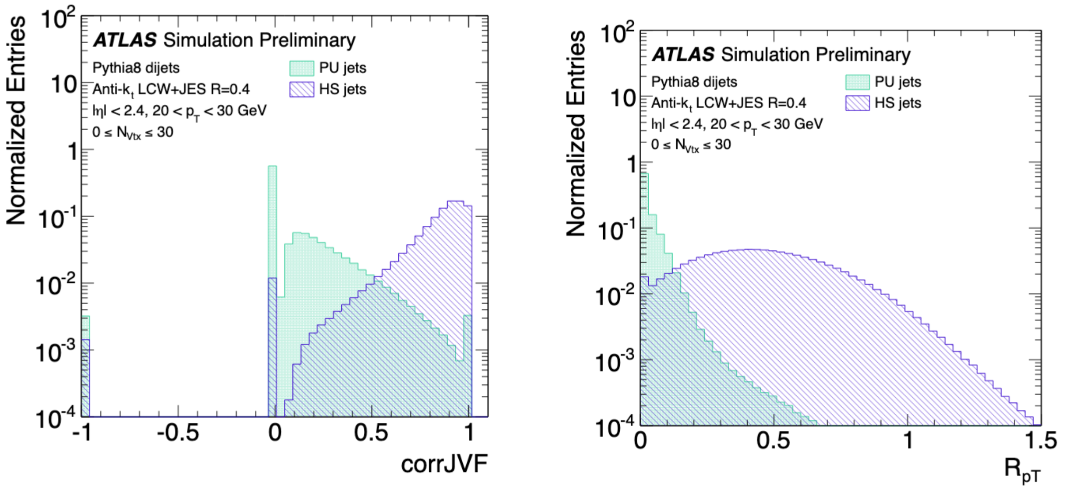

(a) (b)

Figure 5.4.12.: (a) Distribution of corrJVF. (b) Distribution of $R^0_{p_{\mathrm{T}}}$. Image from Ref. [88].

Another discriminating variable $R^i_{p_{\mathrm{T}}}$ is calculated with respect to any vertex as an extension of the $R^0_{p_{\mathrm{T}}}$:

$$R^i_{p_{\mathrm{T}}} = \Sigma_{\mathrm{trk}} \frac{P_T^{\mathrm{trk}}(PV_i)}{p_{\mathrm{T}}^{jet}}. \tag{5.4.14}$$

QCD pile-up jets are expected to have a single pile-up vertex ending up with a larger $\Delta R_{p_{\mathrm{T}}}$ (the difference between the highest and second highest values of $R_{p_{\mathrm{T}}}$ computed w.r.t any vertex i). Stochastic pile-up jets are from a random combination, and $\Delta R_{p_{\mathrm{T}}}$ turns out smaller. Pile-up jets in the forward region can be reduced by applying an fJVT cut. The fJVT algorithm computes the sum of QCD pile-up jets in the central region for each vertex:

$$\overrightarrow{p}^{\mathrm{miss}}_{\mathrm{T},i} = \Sigma_{\substack{\mathrm{jet}\in PV_i \\ p_{\mathrm{T}}^{\mathrm{jet}}>20\mathrm{GeV}}} \overrightarrow{p}^{\mathrm{jet}}_{\mathrm{T}} + \Sigma_{\substack{\mathrm{tracks}\in PV_i \\ p_{\mathrm{T}}^{\mathrm{jet}}<20\mathrm{GeV}}} \overrightarrow{p}^{\mathrm{track}}_{\mathrm{T}} + \Sigma_{\mathrm{tracks,\ jets\ fail}\ R^i_{p_{\mathrm{T}}}\ \mathrm{cut}} \overrightarrow{p}^{\mathrm{track}}_{\mathrm{T}}, \tag{5.4.15}$$

where the first two components compute the vector sum of jet p_{T} not coming from HS central jets and the third term calculates the vector sum of QCD pile-up jet p_{T} in the central region discriminated by the $\Delta R_{p_{\mathrm{T}}}$ cut. The energy of a forward QCD pile-up jet is expected to be balanced by the central QCD pile-up jet leading to fJVT $\rightarrow$ 1:

$$\mathrm{fJVT_i} = \frac{\overrightarrow{p}^{\mathrm{miss}}_{T,i} \cdot \overrightarrow{p}^{fj}_{T,i}}{|\overrightarrow{p}^{fj}_{T}|^2}, \ \mathrm{fJVT} = \mathrm{max_i}(\mathrm{fJVT_i}). \tag{5.4.16}$$

The recommended lower threshold of 0.5 on the JVT is used in the analyses to reject jets with $p_{\mathrm{T}} < 60$ GeV and $|\eta| < 2.4$, which correspond to an efficiency of 92% and to an observed fake rate of 2%. If such a jet passes the JVT cut, but is "bad" (not associated to real energy deposits, such as an electrical spike, cosmic-ray shower, *etc*), then the whole event is rejected. The forward jet is tagged as pile-up if its fJVT value is above 0.4 (0.5), for the *Tight* (*Loose*) working point, in a jet p_{T} range of 20 to 60 GeV.

Lastly, jets are retained in the analyses only if they pass the Loose selection criteria for the Jet Cleaning [89], which is designed to provide an efficiency of selecting jets from proton-proton collisions above 99.5% for $p_{\mathrm{T}} > 20$ GeV.

A veto on b-tagged jets with $p_{\mathrm{T}} > 30$ GeV and $|\eta| < 2.5$ is applied for the analyses in Chapter 6 to reject the contributions from $t\bar{t}$ events. Jets are b-tagged as likely to contain b-hadrons using the MV2c10 algorithm [90]. It utilizes jet properties and variables based on the reconstructed charged particle tracks. Together with the new reconstruction algorithm, b-tagging performances in Run-2 benefit from the insertion of the Pixel Insertable B-Layer, the IBL, which has significantly improved impact parameter resolution and the reconstruction of secondary vertices. For the considered analyses, a jet is b-tagged if the MV2c10 weight is larger than a cut value corresponding to approximately 85% b-tagging efficiency for b-jets in $t\bar{t}$ events.

Table 5.4.1 summarises the jets selection used in the analyses in Chapter 6.

Identification	AntiKt4EMPFlow jets
Kinematic cuts	$p_{\mathrm{T}} > 30$ GeV $\lvert\eta\rvert < 4.5$
Pile-up removal	JVT > 0.5 for $p_{\mathrm{T}} < 60$ GeV, $\lvert\eta\rvert < 2.4$ jets
Cleaning	*Loose* jets accepted
b-tagging	MV2c10 > 0.1758

Table 5.4.1.: Summary of jet selections.

5.5. Overlap Removals

An overlap removal procedure is carried out to resolve ambiguities and to avoid double counting. Possible overlaps among the various objects are resolved following recommendations from the ATLAS harmonisation group [91]. Table 5.5.1 summarises the standard overlap removal strategy used in the analyses. The steps are performed in listed order where only surviving objects participate in subsequent steps. Nearby objects can be removed based on criteria of angular distance ΔR, the number of tracks, or p_{T} ratio requirements.

	Reference objects	Criteria
Remove jets	electrons	$\Delta \mathrm{R}_{\mathrm{e-jet}} < 0.2$
	muons	$\Delta \mathrm{R}_{\mu\mathrm{-jet}} < 0.2$ if $N_{\mathrm{Trk}}(\mathrm{jet}) < 3$ OR $p_T^{jet}/p_T^{\mu} < 2$ and $p_T^{\mu}/\Sigma_{\mathrm{Trk}p_{\mathrm{T}}} > 0.7$)
	photons	$\Delta \mathrm{R}_{\gamma\mathrm{-jet}} < 0.4$ (used in the $Z\gamma$ method)
Remove electrons	jets	$0.2 < \Delta \mathrm{R}_{\mathrm{jet-e}} < 0.4$
	muons	share the same ID track
	electrons	shared track, p_{T} 1 < p_{T} 2
Remove muons	jets	$0.2 < \Delta \mathrm{R}_{\mathrm{jet}-\mu} < 0.4$
	electrons	is calo-muon and shared ID track
Remove Photons	electrons	$\Delta \mathrm{R}_{\mathrm{e}-\gamma} < 0.4$
	muons	$\Delta \mathrm{R}_{\mu-\gamma} < 0.4$

Table 5.5.1.: Overlap removal criteria adopted in the $\ell\ell + E_{\mathrm{T}}^{\mathrm{miss}}$ analyses.

5.6. Missing Transverse Momentum

The Missing Transverse Momentum ($E_{\mathrm{T}}^{\mathrm{miss}}$) signature [92] is key for many analyses with neutrino final states as well as BSM, such as dark matter searches. There is no transverse momentum to the beam-line in the initial state of the pp collision, so the $E_{\mathrm{T}}^{\mathrm{miss}}$ is reconstructed based on the momentum conservation law. The missing transverse momentum is inferred from the existence of particles that cannot be measured using those that can be measured. The $E_{\mathrm{T}}^{\mathrm{miss}}$ is therefore defined as the negative vector sum of the p_{T} of all objects:

$$E_{\mathrm{T}}^{\mathrm{miss}} = -(\Sigma \overrightarrow{p_{\mathrm{T}}}^{e} + \Sigma \overrightarrow{p_{\mathrm{T}}}^{\gamma} + \Sigma \overrightarrow{p_{\mathrm{T}}}^{\tau} + \Sigma \overrightarrow{p_{\mathrm{T}}}^{jet} + \Sigma \overrightarrow{p_{\mathrm{T}}}^{\mu} + \Sigma \overrightarrow{p_{\mathrm{T}}}^{soft}). \tag{5.6.1}$$

In the $E_{\mathrm{T}}^{\mathrm{miss}}$ calculation, the objects are further categorized into the hard and soft term. The hard term is computed from high p_{T} physics objects, such as leptons and photons. They are analysis dependent (see brief descriptions for each term below). For the jets the $E_{\mathrm{T}}^{\mathrm{miss}}$ algorithm has its own selections based on a no-double-counting principle. The algorithms for the soft term are presented in Section 5.6.1. One of the sources of fake $E_{\mathrm{T}}^{\mathrm{miss}}$ is overlapping objects, which will be described in Section 5.6.2, specifically jets and e/γ ambiguity resolution. The $E_{\mathrm{T}}^{\mathrm{miss}}$ significance is a powerful tool, which can help to understand the impact on the $E_{\mathrm{T}}^{\mathrm{miss}}$ coming from reconstruction resolution and inefficiencies. More details about the $E_{\mathrm{T}}^{\mathrm{miss}}$ significance will be presented in Section 5.6.3. Systematic uncertainties of the soft term are shown in Section 5.6.4. The $E_{\mathrm{T}}^{\mathrm{miss}}$ performance, which helps to understand how well the $E_{\mathrm{T}}^{\mathrm{miss}}$ is reconstructed including EMTopo $E_{\mathrm{T}}^{\mathrm{miss}}$ and PFlow $E_{\mathrm{T}}^{\mathrm{miss}}$, is shown in Section 5.6.5.

Electron/Photon Term

In the current ATLAS software release 21, the electron/photon reconstruction algorithms use super-clusters, as described in Section 5.2. In the older software release 20.7, which was the version used for the electron-jet overlap removal study in Section 5.6.2, the electrons were reconstructed using a *sliding-window* [93] cluster. This is a different type of calorimeter cluster compared to the ones used in jets (topo-cluster). In release 20.7, the $E_{\mathrm{T}}^{\mathrm{miss}}$ algorithm considered the full amount of energy from the sliding window cluster for electrons. The same treatment of overlap removal (OR) is used in both release 20.7 and release 21.

Muon Term

Muon candidates are identified by the selections described in Section 5.3. The muon in the $E_{\mathrm{T}}^{\mathrm{miss}}$ algorithm only undergoes track-based overlap removal in the context of the order preference as shown in Figure 5.6.1. In general, the muon does not remove anything else and it is not removed either. However, there are very rare exceptions. For example, the muon deposits small amounts of energy when it enters the calorimeter, and the e-loss can be misreconstructed as a jet which leads to double counting of the energy. In this case, the $E_{\mathrm{T}}^{\mathrm{miss}}$ has its specific treatment to remove jets overlapping with muons. The muon can lose its energy by radiating hard photons at small angles, and they are not reconstructed as photons. To address this, the $E_{\mathrm{T}}^{\mathrm{miss}}$ algorithm treats the photon as a jet (the $E_{\mathrm{T}}^{\mathrm{miss}}$ uses the EM scale of the jet because the energy is thought coming from an FSR photon from the muon) if it passes some requirements and then puts it to the jet term of the $E_{\mathrm{T}}^{\mathrm{miss}}$.

Jet Term

Jets used in the $E_{\mathrm{T}}^{\mathrm{miss}}$ have their selections depending on which working points is required by the respective analysis. There are two common types of jets in ATLAS, EMTopo jets and PFlow jets (see Section 5.4.2). Using EMTopo jets as input jets in the $E_{\mathrm{T}}^{\mathrm{miss}}$ is called EMTopo $E_{\mathrm{T}}^{\mathrm{miss}}$, likewise using PFlow jets as input jets in the $E_{\mathrm{T}}^{\mathrm{miss}}$ is called PFlow $E_{\mathrm{T}}^{\mathrm{miss}}$. Several $E_{\mathrm{T}}^{\mathrm{miss}}$ working points are developed to deal with pile-up depending on the topology. For example, the $\ell\ell + E_{\mathrm{T}}^{\mathrm{miss}}$ analysis uses the *Tight* PFlow working point which imposes additional JVT > 0.5 on 20 GeV $< p_{\mathrm{T}} < 60$ GeV central jets ($|\eta| < 2.4$) and requires $p_{\mathrm{T}} > 30$ GeV for the forward jets ($|\eta| > 2.4$).

Soft Term

The soft term is composed of hard scatter tracks or energy deposits not associated with any hard objects. The current recommended soft term reconstruction algorithm is track-based, and is called TST in ATLAS. The TST algorithm was found to be less dependent on pile-up in the $E_{\mathrm{T}}^{\mathrm{miss}}$ resolution than the calorimeter based algorithm, but it misses soft neutral particles. The algorithms are described in Section 5.6.1.

Fake $E_{\mathrm{T}}^{\mathrm{miss}}$ Sources

The contribution of fake $E_{\mathrm{T}}^{\mathrm{miss}}$ can come from miscalibration or mismeasurement of the physics objects. Moreover, the contamination with pile-up jets would lead to miscalibration. Because of the importance of pile-up suppression, the (f)JVT tool (detailed in Section 5.4.6) has been implemented in the jet reconstruction. A number of new pile-up mitigation techniques have been developed, such as Voronoi Soft-killer (SK) [94] and Constituent Subtraction (CS) [95], which would help to remove calorimeter clusters contaminated by pile-up jets.

The cases where electrons, photons, or hadronically-decaying τs have a jet close-by can give rise to a large source of fake $E_{\mathrm{T}}^{\mathrm{miss}}$. The most common scenario is the overlap of electrons and jets. The study of jets and electrons ambiguity resolution will be shown in Section 5.6.2.

5.6.1. MET Soft Term Algorithms

There are several algorithms to reconstruct the soft term. The calorimeter-based algorithm (CST) was used in most analyses in the past [96, 97], while a track-based term (TST) is used in most analyses these days, including everywhere in this thesis. A calorimeter-based soft term is reconstructed mainly using energy deposits in the calorimeter, which are not matched to the high p_{T} objects. The CST keeps neutral particles, but there is no pile-up suppression. On the other hand, the TST is purely reconstructed from the tracks, and it allows good vertex matching which removes the pile-up contribution. However, it misses the contribution from soft neutral particles. The selections for the tracks and vertex are listed below [98]:

- $p_{\mathrm{T}} > 0.5$ GeV (0.4 GeV for vertex reconstruction and the calorimeter soft term)
- $|\eta| < 2.5$
- Minimum number of hits in the ID.

These tracks are then matched to the PV by applying the following selections:

- $|d_0| < 1.5$ mm (no requirement on d_0 for PFlow TST)
- $|z_0 \sin(\theta)| < 3.0$ mm.

Additionally, tracks are excluded from the soft term if they are associated with the high-p_T object to avoid double counting particles. The TST does not include the forward region where $|\eta|$ is larger than 2.4. It has a more stable resolution with increasing number of reconstructed vertices than the CST.

5.6.2. Overlap Removal

There is a significant fraction of hadronic jets depositing part of their energy in the electromagnetic calorimeter from processes like $\pi^0 \to \gamma\gamma$. As explained in Section 5.4.2, both electromagnetic and hadronic calorimeters information are used to estimate the jet four-momentum as precisely as possible. Therefore, jets can include electron energy and photon energy. Care must be taken that clusters are not counted twice as duplicated energy leads to fake $E_{\mathrm{T}}^{\mathrm{miss}}$ and results in large $E_{\mathrm{T}}^{\mathrm{miss}}$ tails.

Figure 5.6.1 shows the general idea of overlap handling in the calculation of $E_{\mathrm{T}}^{\mathrm{miss}}$. Once objects have been identified, any jet close enough to the high-priority object is removed from the event by using a ΔR matching. There is no outright order recommendation. Changing the order of anything will result in differences.

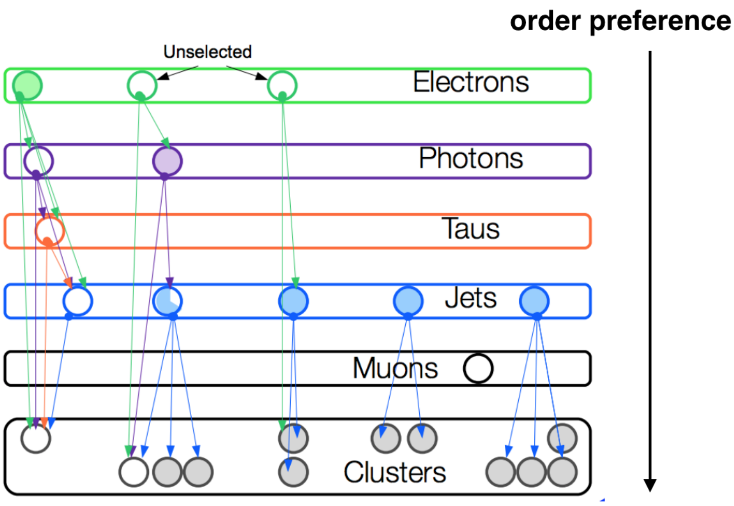

Figure 5.6.1.: Matching procedures used in the $E_{\mathrm{T}}^{\mathrm{miss}}$ map to avoid double counting. Each circle stands for a cluster. The solid circle in green, purple, and red means the cluster is matched with the object. The cluster is then removed if it is associated with an object, otherwise the cluster is recognized as a jet in blue. The lines link between clusters and objects through a ΔR matching [99].

However, the hard objects produced in the detector can deposit their energy in the same clusters or have overlapping energy deposits with the close-by object. Figure 5.6.2 provides the example of scenarios of electrons with close-by jets: keep the electron and the jet if they both are real and overlapping, pile-up jets and fake electrons might lead to miscalibration and double counting, the case of electrons creating jets in the calorimeter might lead to double counting.

The treatments of assigning energy deposits to the electron or the jet that generated them to identify the scenarios mentioned above will be discussed in this section. The old treatment

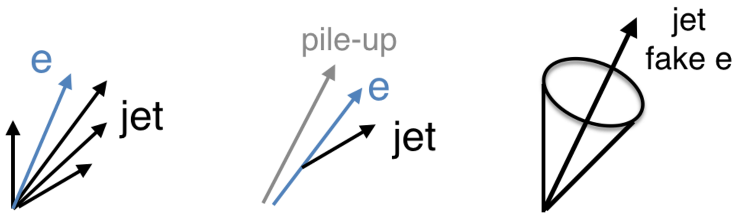

Figure 5.6.2.: Overlapping leptons and jets. (a) Real jet close to real electron. (b) Jets from pile-up or electrons faking jets in the calorimeter. (c) Real jet and fake electron.

and its problems will be discussed first and the developed discriminating variables that could be used to understand the signal ambiguity will be shown later on. The studies were done with topo-cluster jets in ATLAS release 20.7 software and the optimized parameters are used in release 21 reconstruction as well. The updated treatment also has been tested for PFlow jets.

Monte Carlo Samples

A sample list is given in Table 5.6.1 that is used for the jet-electron overlap removal studies.

Sample	$Z \rightarrow \ell\ell$	$t\bar{t}$	$ZZ \rightarrow \ell\ell\nu\nu$
Generator	Sherpa 2.2.1	Powheg-Box v2	Powheg-Box v2 + Pythia 8
ME PDF set	NNPDF3.0NNLO	CT10	CT10NLO
PS and Hadronization	Sherpa 2.2.1	Pythia 6.428	Pythia 8.186
UE Model TUNE	Default	P2012[100]	AZNLO[101]

Table 5.6.1.: Generators, PDF sets, and MC tunes used in the OR (electron, jet) analysis for the $E_{\mathrm{T}}^{\mathrm{miss}}$.

The Old Overlap Removal and Issues

A variable called *frac* was used in the $E_{\mathrm{T}}^{\mathrm{miss}}$ algorithm to determine the unique jet p_{T} fraction:

$$frac = \frac{jet\_const\_p_{\mathrm{T}} - electron\_p_{\mathrm{T}}}{jet\_const\_p_{\mathrm{T}}}, \tag{5.6.2}$$

where *jet_const_pt* is the calorimeter jet p_{T} at the EM scale. Figure 5.6.3 illustrates the old treatment. The simplest case is shown in Figure 5.6.3(b) with only one electron without jets. The $E_{\mathrm{T}}^{\mathrm{miss}}$ algorithm removes the electron track. Figure (c) shows one event with one electron and one jet without any jet tracks. (The jet energy is the sum of all two hadronic clusters and an EM cluster.) The $E_{\mathrm{T}}^{\mathrm{miss}}$ algorithm removes the electron track and hadronic clusters if $frac < 0.5$. If $frac \geq 0.5$, the jet and the electron are considered to be real in the $E_{\mathrm{T}}^{\mathrm{miss}}$ algorithm, and only the electron track is removed. (d) The event has one electron and one jet with jet tracks, the $E_{\mathrm{T}}^{\mathrm{miss}}$ algorithm removes the electron track and hadronic clusters if $frac < 0.5$ or removes the electron track and jet tracks if $frac \geq 0.5$. Jet tracks are ghosts associated to the jet and roughly have ΔR(e, track) > 0.05. ("Ghost" means adding the tracks to the calorimeter cluster during the jet reconstruction, not changing the calorimeter E_{T} measurement.)

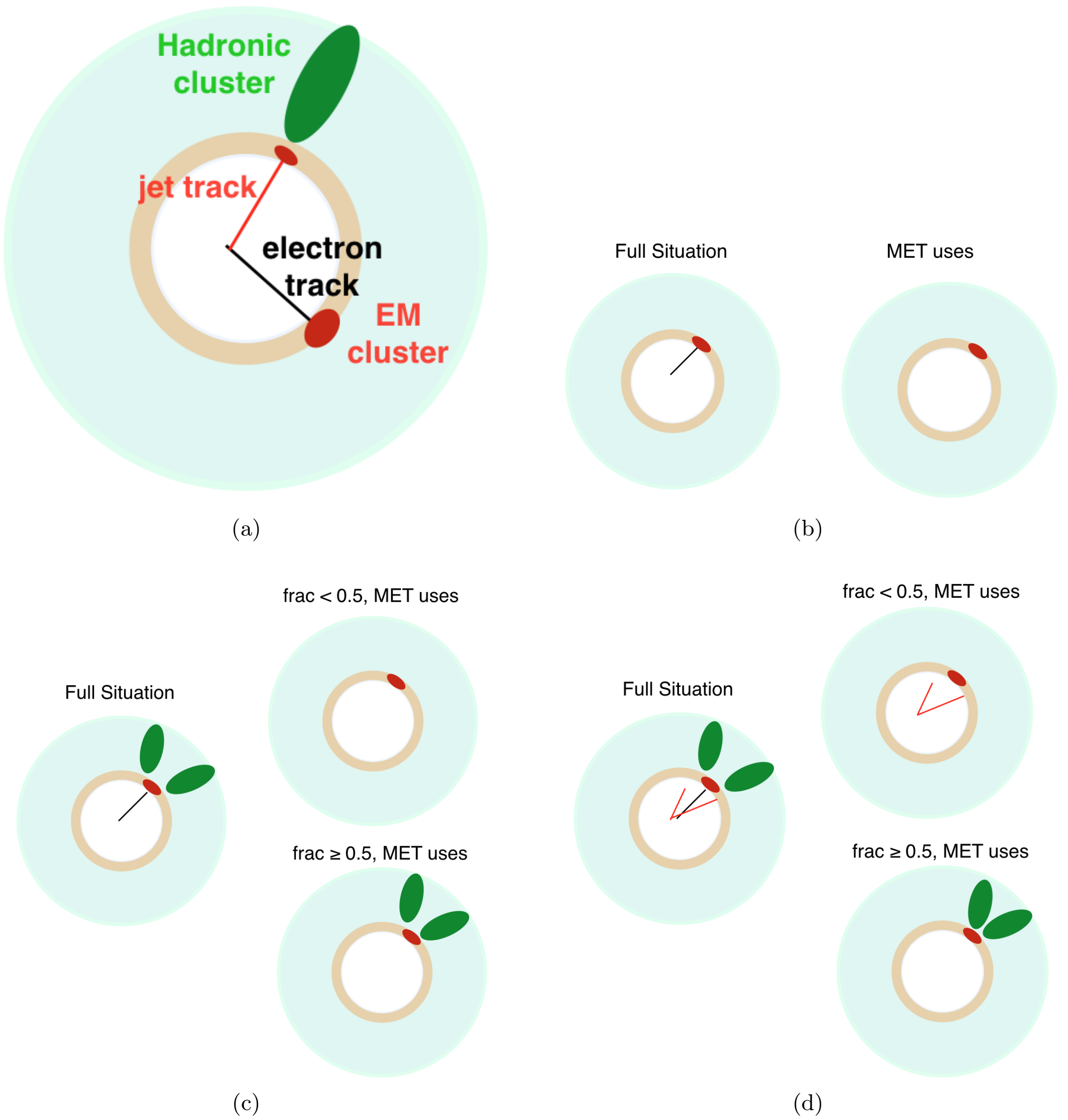

Figure 5.6.3.: Illustration of the old treatments used for the overlap removal in the E_T^{miss} calculation. (a) Legend. (b) Only one electron and no jet. (c) Only one electron and one jet without jet tracks. (d) Only one electron and one jet with jet tracks.

A problem arises, if the jet is real, but the hadronic clusters are moved to the soft term, and they are not built by the soft term algorithm (track based algorithm). This means $E_{\mathrm{T}}^{\mathrm{miss}}$ would completely miss the neutral components of this jet, which can lead to large tails of fake $E_{\mathrm{T}}^{\mathrm{miss}}$. Therefore, adding back the real neutral jet that was being wrongly removed is crucial.

The studies were done for electrons and jets with ΔR(e, jet) < 0.4 using $Z \to ee$ event topology, where no significant real $E_{\mathrm{T}}^{\mathrm{miss}}$ is expected. The $Z \to ee$ event selection criteria are:

- The events are required to have two same-flavour opposite-sign electrons passing “Medium” identification.
- No isolation cut is applied in release 20.7 reconstruction. (A *Loose* isolation cut is applied in release 21.)
- The leading and sub-leading electrons in the pair are required to have $p_{\mathrm{T}} > 25$ GeV.
- The invariant mass of the selected two electrons is required to be within the range of 75 GeV $\leq M_{ll} \leq$ 116 GeV.

Figure 5.6.4 shows the $E_{\mathrm{T}}^{\mathrm{miss}}$ tails above 100 GeV are dominated by jets with *frac* < 0.5 indicating jet energy is being missed in the $E_{\mathrm{T}}^{\mathrm{miss}}$ reconstruction. *frac* $= 1$ is the case where MET code does not think that the jet and the electron share any clusters and it is not particularly dominant in the tails.

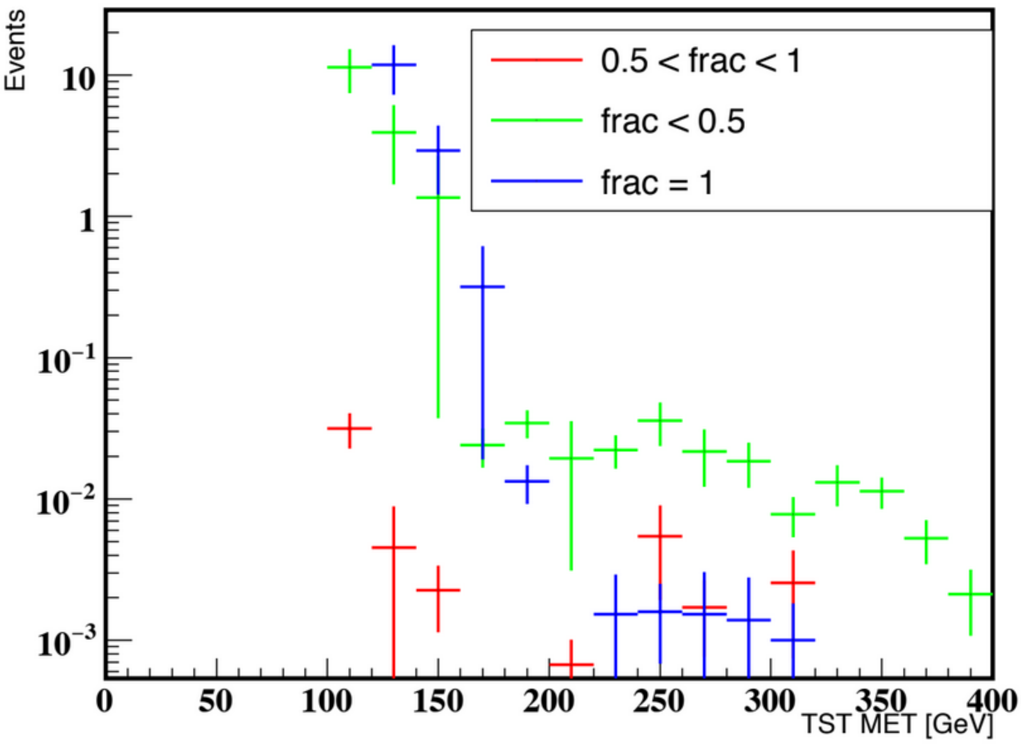

Figure 5.6.4.: Comparison of the $E_{\mathrm{T}}^{\mathrm{miss}}$ (TST MET = track-based algorithm is used for the soft term) with 3 different *frac* ranges where the events are required to have $E_{\mathrm{T}}^{\mathrm{miss}} > 100$ GeV, $N_{jet} = 1$, and ΔR(e, jet) < 0.4.

Kinematics

The kinematics for the case of the jet with a close-by electron are studied by requiring an angular distance (ΔR(e, jet) < 0.4). The plots are categorized into different *frac*, which was the quantity used to decide the amount of a jet's unique energy. Figure 5.6.5 (a) shows jets are mostly at around 0.2 away from the electrons, which means jet clusters are just next to the electron clusters, in case of $0.5 < frac < 1$. Figure 5.6.5 (b) shows that for *frac* <0.5, jets tend to be closer to ΔR(e, jet) $\sim$ 0.4 rather than 0, which means the jets are probably real and should be included. Figure 5.6.5 (c) and Figure 5.6.5 (d) indicate real electrons are inside jets in both cases. As stated above, in the old treatment, in case of $frac \geq 0.5$, the jet was included in the $E_{\mathrm{T}}^{\mathrm{miss}}$ reconstruction, and its energy was scaled by the *frac*. In case of $frac < 0.5$, the jet was assigned to the soft term, and only the tracks associated with the jet were included in the $E_{\mathrm{T}}^{\mathrm{miss}}$ calculation.

As larger tails were seen in the $frac < 0.5$ cases, we introduced an alternative cut on the absolute difference in the jet and electron p_{T}: $p_{\mathrm{T}}\ diff$ = jet_const_pt - ele_pt. The studies were done by scanning jet p_{T} *frac* from 0.0 (no frac criteria), 0.1, 0.15, 0.2, 0.25, 0.3, 0.4, and 0.5 and then combining with jet_const_pt - ele_pt > 10, 20, and 30 GeV. For example, the jet is assigned to the soft term if it satisfies the discriminating combination of *frac* < 0.5 criteria and jet_const_pt - ele_pt < 10 GeV. The scan of p_{T} differences of the jet with no frac criteria is shown in Table 5.6.2, including the mean and RMS of the $E_{\mathrm{T}}^{\mathrm{miss}}$ and the $E_{\mathrm{T}}^{\mathrm{miss}}$ tails (the integral of $E_{\mathrm{T}}^{\mathrm{miss}} > 200$ GeV). For comparison, the scan with jet p_{T} *frac* > 0.5 is shown in Table 5.6.3. The $E_{\mathrm{T}}^{\mathrm{miss}}$ tails are smaller in the no frac criteria treatment. The study is performed with data (6 fb^{-1}) as well.

The recommended treatment in release 20.7, dropping the frac criteria and defining a jet as real if jet_const_pt - ele_pt > 20 GeV, improved the $E_{\mathrm{T}}^{\mathrm{miss}}$ calculation in the tails by 30% as shown in Figure 5.6.6. In other words, if jets with a close-by electron meet the criteria of jet_const_pt - ele_pt > 20 GeV, the jets go into the jet term. Interestingly, the new treatment and the old treatment performed similarly in release 21.

5.6.3. MET Significance

The $E_{\mathrm{T}}^{\mathrm{miss}}$ Significance (METSig) is another useful variable, which is basically calculated by dividing the reconstructed $E_{\mathrm{T}}^{\mathrm{miss}}$ by the resolution of all objects. The ideal momentum distribution of each object is Gaussian. The width of the momentum measurement is deteriorated by the pile-up and detector effects, e.g., the sampling of the calorimeter. The METSig is useful for signal-background discrimination because measured $E_{\mathrm{T}}^{\mathrm{miss}}$ coming from a resolution effect has small METSig.

METSig is defined by the log-likelihood function with a p_T^{inv} parameter (representing invisible particles' momentum) and has a form as [102]:

$$S^2 = 2ln\left(\frac{max_{p_T^{inv}\neq 0}\mathcal{L}(\overrightarrow{E}_T^{miss}|\overrightarrow{p}_T^{inv})}{max_{p_T^{inv}=0}\mathcal{L}(\overrightarrow{E}_T^{miss}|\overrightarrow{p}_T^{inv})}\right) = (\overrightarrow{E}_T^{miss})^T(\Sigma_i V_i)^{-1}\overrightarrow{E}_T^{miss}, \tag{5.6.3}$$

where $\overrightarrow{E}_T^{miss}$ is the reconstructed $E_{\mathrm{T}}^{\mathrm{miss}}$ measured event by event. V_i is the covariance matrix per object given the measurements of the p_{Ti} and the azimuthal angle ϕ_i, which is:

$$V_i = \begin{pmatrix} \sigma_{p_{Ti}}^2 & 0 \\ 0 & p_{Ti}^2\sigma_{\phi_i}^2 \end{pmatrix}. \tag{5.6.4}$$

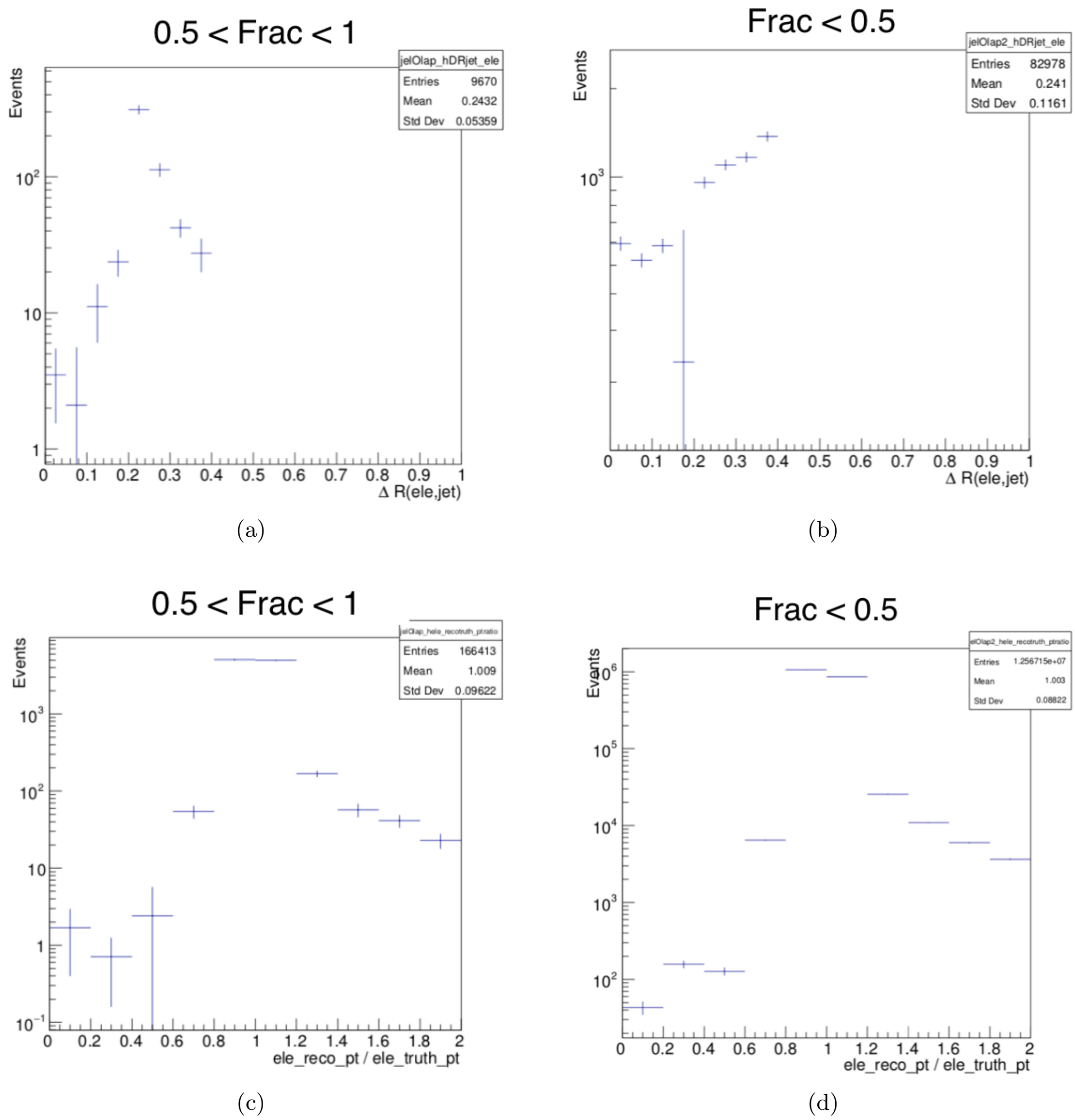

Figure 5.6.5.: The angular distance between the electron and the jet with (a) $0.5 < frac < 1$ and (b) $frac < 0.5$ for $Z \rightarrow ee$ MC events. ΔR(e, jet) < 0.4 is required. The ratio of reconstructed electrons and the truth electrons within ΔR(e, jet) < 0.4 in the case of (c) $0.5 < frac < 1$ and (d) $frac < 0.5$. The reconstructed electron is matched with the truth electron requiring ΔR < 0.2.

$Z \to ee$	MET	p_T *diff* > 10 GeV	p_T *diff* > 20 GeV	p_T *diff* > 30 GeV
Mean MET (GeV)	17.55	17.85	17.57	17.55
RMS MET (GeV)	13.47	13.57	13.47	13.46
Integral MET > 200 GeV	5.35	3.69	3.62	3.64
$Z \to \mu\mu$	MET	p_T *diff* > 10 GeV	p_T *diff* > 20 GeV	p_T *diff* > 30 GeV
Mean MET (GeV)	18.29	18.29	18.29	18.30
RMS MET (GeV)	14.09	14.08	14.08	14.09
Integral MET > 200 GeV	2.51	2.12	2.12	2.14
$t\bar{t}$	MET	p_T *diff* > 10 GeV	p_T *diff* > 20 GeV	p_T *diff* > 30 GeV
Mean MET (GeV)	5.49	5.37	5.40	5.47
RMS MET (GeV)	24.38	23.81	24.03	24.31
Integral |MET-truth MET| > 100 GeV	360.36	269.93	275.25	286.51
$ZZ \to \ell\ell\nu\nu$	MET	p_T *diff* > 10 GeV	p_T *diff* > 20 GeV	p_T *diff* > 30 GeV
Mean MET (GeV)	2.85	3.40	2.92	2.83
RMS MET (GeV)	18.63	18.62	18.50	18.51
Integral |MET-truth MET| > 100 GeV	0.56	0.49	0.49	0.46
data	MET	p_T *diff* > 10 GeV	p_T *diff* > 20 GeV	p_T *diff* > 30 GeV
Mean MET (GeV)	38.15	35.06	35.82	36.67
RMS MET (GeV)	39.67	36.58	36.78	37.11
Integral MET > 200 GeV	88.0	76.0	75.0	75.0

Table 5.6.2.: E_T^{miss} tails studies with no criteria on *frac*. The jet is treated as a real jet if p_T *diff* is larger than a threshold. About 30% and 24% reduction in the E_T^{miss} tails for $Z \to ee$ and $t\bar{t}$ when requiring jet_const_pt - ele_pt > 20 GeV. The mean and RMS are relatively unaffected.

$Z \to ee$	MET	p_T *diff* > 10 GeV	p_T *diff* > 20 GeV	p_T *diff* > 30 GeV
Mean MET (GeV)	17.55	17.55	17.55	17.55
RMS MET (GeV)	13.47	13.47	13.48	13.48
Integral MET > 200 GeV	5.35	5.35	5.35	5.36
$Z \to \mu\mu$	MET	p_T *diff* > 10 GeV	p_T *diff* > 20 GeV	p_T *diff* > 30 GeV
Mean MET (GeV)	18.29	18.30	18.30	18.30
RMS MET (GeV)	14.09	14.09	14.10	14.10
Integral MET > 200 GeV	2.51	2.52	2.51	2.54
$t\bar{t}$	MET	p_T *diff* > 10 GeV	p_T *diff* > 20 GeV	p_T *diff* > 30 GeV
Mean MET (GeV)	5.49	5.49	5.52	5.57
RMS MET (GeV)	24.38	24.39	24.50	24.67
Integral |MET-truth MET| > 100 GeV	360.36	360.42	363.17	369.45
$ZZ \to \ell\ell\nu\nu$	MET	p_T *diff* > 10 GeV	p_T *diff* > 20 GeV	p_T *diff* > 30 GeV
Mean MET (GeV)	2.85	2.84	2.81	2.80
RMS MET (GeV)	18.63	18.63	18.63	18.63
Integral |MET-truth MET| > 100 GeV	0.56	0.56	0.55	0.55
data	MET	p_T *diff* > 10 GeV	p_T *diff* > 20 GeV	p_T *diff* > 30 GeV
Mean MET (GeV)	38.15	38.18	38.46	38.77
RMS MET (GeV)	39.67	39.66	39.70	39.82
Integral MET > 200 GeV	88.0	89.0	87.0	86.0

Table 5.6.3.: E_T^{miss} tails studies. The scan was performed using selection criteria on *frac* > 0.5 (the old treatment) with three different p_T *diff*. The jet is treated as a real jet and put into the jet term if *frac* > 0.5 or p_T *diff* is larger than a threshold.

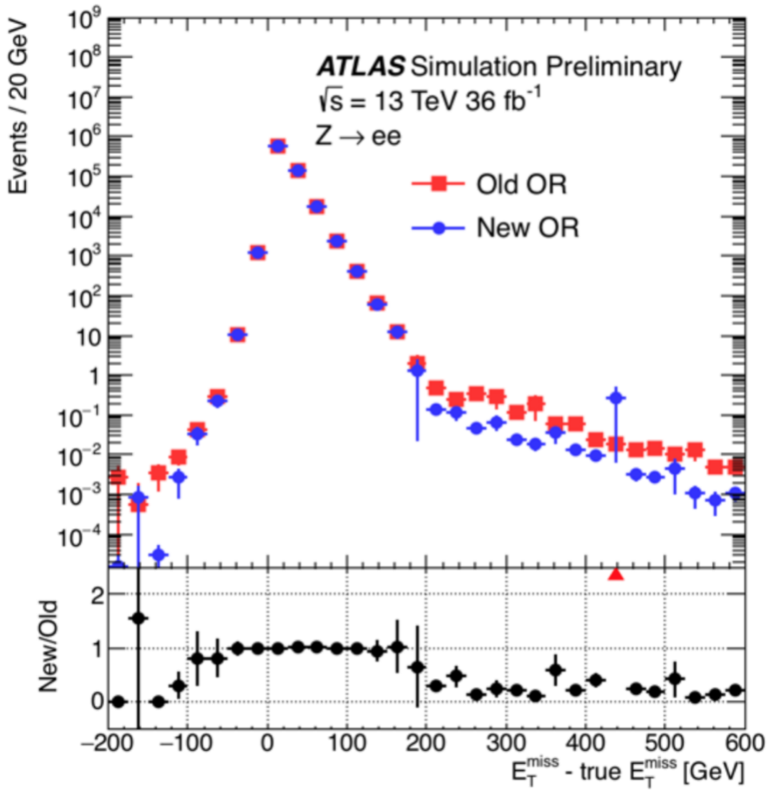

Figure 5.6.6.: Comparison of the $E_{\mathrm{T}}^{\mathrm{miss}}$ performance between old (red) and new (blue) jet and electron/photon/hadronically decaying τ-lepton overlap removal (OR) procedure in $Z \to ee$ simulation. The $E_{\mathrm{T}}^{\mathrm{miss}}$ tails are diminished with the new technique, indicating fake $E_{\mathrm{T}}^{\mathrm{miss}}$ has been reduced. The studies were performed in release 20.7 [92].

The resolution of each object ($\sigma_{p_{Ti}}$) is assumed to have a Gaussian shape. σ_{ϕ_i} is the variance in ϕ per object. The $\sigma_{p_{Ti}}$ and σ_{ϕ_i} are considered uncorrelated. After a ϕ_i rotation to make each object have the same direction in the basis of (x, y), the covariance becomes:

$$V_{xy} = \Sigma_i V_i = \begin{pmatrix} \sigma_x^2 & \sigma_{xy}^2 \\ \sigma_{xy}^2 & \sigma_y^2 \end{pmatrix}. \tag{5.6.5}$$

One can then rotate the (x,y) system to the longitudinal and transverse (L,T) system by rotating such that the total p_{T} resolution is split into components parallel and transverse to the $E_{\mathrm{T}}^{\mathrm{miss}}$. The covariance matrix is given by the rotation in the angle of the total reconstructed $E_{\mathrm{T}}^{\mathrm{miss}}$:

$$V_{LT} = R^{-1}(\phi) V_{xy} R(\phi),\ R(\phi) = \begin{pmatrix} cos(\phi) & sin(\phi) \\ -sin(\phi) & cos(\phi) \end{pmatrix}. \tag{5.6.6}$$

The METSig is rewritten in the (L,T) system as:

$$S^2 = (E_T^{miss}, 0) \begin{pmatrix} \sigma_L^2 & \sigma_{LT}^2 \\ \sigma_{LT}^2 & \sigma_T^2 \end{pmatrix}^{-1} \begin{pmatrix} E_T^{miss} \\ 0 \end{pmatrix}. \tag{5.6.7}$$

where the calculation of the covariance is:

$$\begin{aligned} V_{LT}^{-1} &= \frac{1}{detV_{LT}} \begin{pmatrix} \sigma_T^2 & -\sigma_{LT}^2 \\ -\sigma_{LT}^2 & \sigma_L^2 \end{pmatrix}, \\ &= \frac{1}{\sigma_T^2 \sigma_L^2 - \sigma_{LT}^4} \begin{pmatrix} \sigma_T^2 & -\sigma_{LT}^2 \\ -\sigma_{LT}^2 & \sigma_L^2 \end{pmatrix}. \end{aligned} \tag{5.6.8}$$

With the above calculations, the object-based METSig can be cast in the form:

$$\begin{aligned} S^2 &= \frac{1}{\sigma_T^2 \sigma_L^2 - \sigma_{LT}^4} (E_T^{miss}, 0) \begin{pmatrix} \sigma_T^2 & -\sigma_{LT}^2 \\ -\sigma_{LT}^2 & \sigma_L^2 \end{pmatrix} \begin{pmatrix} E_T^{miss} \\ 0 \end{pmatrix}, \\ &= \frac{\sigma_T^2 (E_T^{miss})^2}{\sigma_T^2 \sigma_L^2 - \sigma_{LT}^4}, \\ &= \frac{\sigma_T^2 (E_T^{miss})^2}{\sigma_T^2 \sigma_L^2 - \rho_{LT}^2 \sigma_L^2 \sigma_T^2}, \\ &= \frac{(E_T^{miss})^2}{\sigma_L^2 (1 - \rho_{LT}^2)}, \end{aligned} \tag{5.6.9}$$

where $\sigma_{LT}^2 = \rho_{LT} \sigma_L \sigma_T$. σ_L and σ_T are the variances in the longitudinal and transverse directions to the $E_{\mathrm{T}}^{\mathrm{miss}}$, respectively. ρ_{LT} is the correlation factor of the longitudinal L and the transverse T measurement. The object-based METSig provides good discriminating power against fake $E_{\mathrm{T}}^{\mathrm{miss}}$ in many analyses.

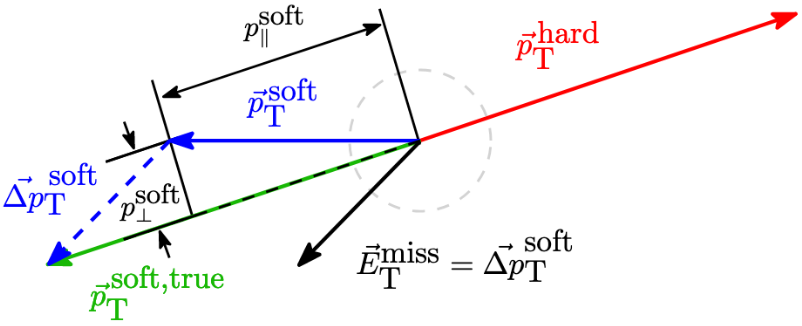

Figure 5.6.7.: Sketch of the track-based soft term projection with respect to p_T^{hard}. Image from Ref. [92].

5.6.4. Soft Term Systematic Uncertainty

For the $E_{\text{T}}^{\text{miss}}$ systematics, the uncertainties on the hard term come from the recommendations of the object (p.ex. muon) groups, which are propagated to the $E_{\text{T}}^{\text{miss}}$. The MET group evaluates the modelling uncertainties of the soft term in events by measuring the degree of balance between the soft term and the hard term in the transverse plane. This is measured in $Z \to ee$ or $Z \to \mu\mu$ events, which ideally have no truth $E_{\text{T}}^{\text{miss}}$. Figure 5.6.7 illustrates the projections of p_T^{soft} along p_T^{hard}.

Three projected quantities are studied, and the largest disagreement between simulation and data is used as the systematic uncertainty in the soft term:

- Mean of the soft $E_{T\|}^{miss}$. This is the scale of the soft $E_{\mathrm{T}}^{\mathrm{miss}}$ that is parallel to the hard term
- Resolution of the soft $E_{\mathrm{T}}^{\mathrm{miss}}$ that is parallel to the hard term
- Resolution of the soft $E_{\mathrm{T}}^{\mathrm{miss}}$ that is transverse to the hard term

To account for the effect on different topologies, the systematic is additionally split into jet inclusive and 0-jet selections. The maximal data/MC discrepancy is derived from these two cases as the systematic envelope.

5.6.5. MET Performance

The $E_{\mathrm{T}}^{\mathrm{miss}}$ algorithm can be tested, e.g. with $W \to l\nu$ events to reveal how well the algorithm reconstructs intrinsic $E_{\mathrm{T}}^{\mathrm{miss}}$ and with $Z \to \ell\ell$ events to reveal how much fake $E_{\mathrm{T}}^{\mathrm{miss}}$ the algorithm reconstructs. A set of variables are constructed in order to understand if the $E_{\mathrm{T}}^{\mathrm{miss}}$ algorithm is performing well: resolution, scale, tails, Data/MC..., *etc.*

Resolution

Due to non-Gaussian tails of the $E_{\mathrm{T}}^{\mathrm{miss}}$, the resolution is calculated by taking the root-mean-square (RMS) of the $E_{\mathrm{T}}^{\mathrm{miss}}$ in the x and y directions. The information of the tails would get lost if the resolution is only taken from a Gaussian fit over the core of the distribution. The width is measured:

$$\mathrm{RMS}(E_{x(y)}^{miss}) = \begin{cases} \mathrm{RMS}(E_{x(y)}^{miss} - E_{x(y)}^{miss,true}) \; W \to e\nu \text{ or } t\bar{t} \text{ sample.} \\ \mathrm{RMS}(E_{x(y)}^{miss}) \; Z \to \ell\ell \text{ sample.} \end{cases} \tag{5.6.10}$$

Figure 5.6.8 shows the $E_{\mathrm{T}}^{\mathrm{miss}}$ resolution in 2017 data. The resolution gets worse with more pile-up. Increasing the jet p_{T} threshold from 20 GeV (*Loose* operating point) to 30 GeV (*Tight* operating point) in the forward region produces a smaller dependence on pile-up as shown in 5.6.8 (a). Figure 5.6.8 (b) indicates most of the pile-up dependence comes from forward jets. The improved PFlow $E_{\mathrm{T}}^{\mathrm{miss}}$ performance compared with EMTopo $E_{\mathrm{T}}^{\mathrm{miss}}$ in terms of resolution is shown in 5.6.8 (c). Figure 5.6.8 (d) shows data 2017 and MCs (Sherpa and Powheg) agree in the $E_{\mathrm{T}}^{\mathrm{miss}}$ resolution with respect to the average number of interactions per bunch crossing $<\mu>$ (similar results for EMTopo and PFlow).

Tails

The $E_{\mathrm{T}}^{\mathrm{miss}}$ tail is defined as:

$$f(x) = \frac{\int_x^{\infty} dE_{\mathrm{T}}^{\mathrm{miss}} \frac{dN}{dE_{\mathrm{T}}^{\mathrm{miss}}}}{\int_0^{\infty} dE_{\mathrm{T}}^{\mathrm{miss}} \frac{dN}{dE_{\mathrm{T}}^{\mathrm{miss}}}}, \tag{5.6.11}$$

where x refers to a certain $E_{\mathrm{T}}^{\mathrm{miss}}$ threshold, normally taking 150 GeV or 200 GeV. The fraction of the $E_{\mathrm{T}}^{\mathrm{miss}}$ in tails represents an important quantity of event-by-event fluctuations in terms of detection of overlapping objects in the $E_{\mathrm{T}}^{\mathrm{miss}}$ reconstruction. Appendix A.1 is a good example of how incorrect overlap removal affects the $E_{\mathrm{T}}^{\mathrm{miss}}$ calculation resulting in larger $E_{\mathrm{T}}^{\mathrm{miss}}$ in tails.

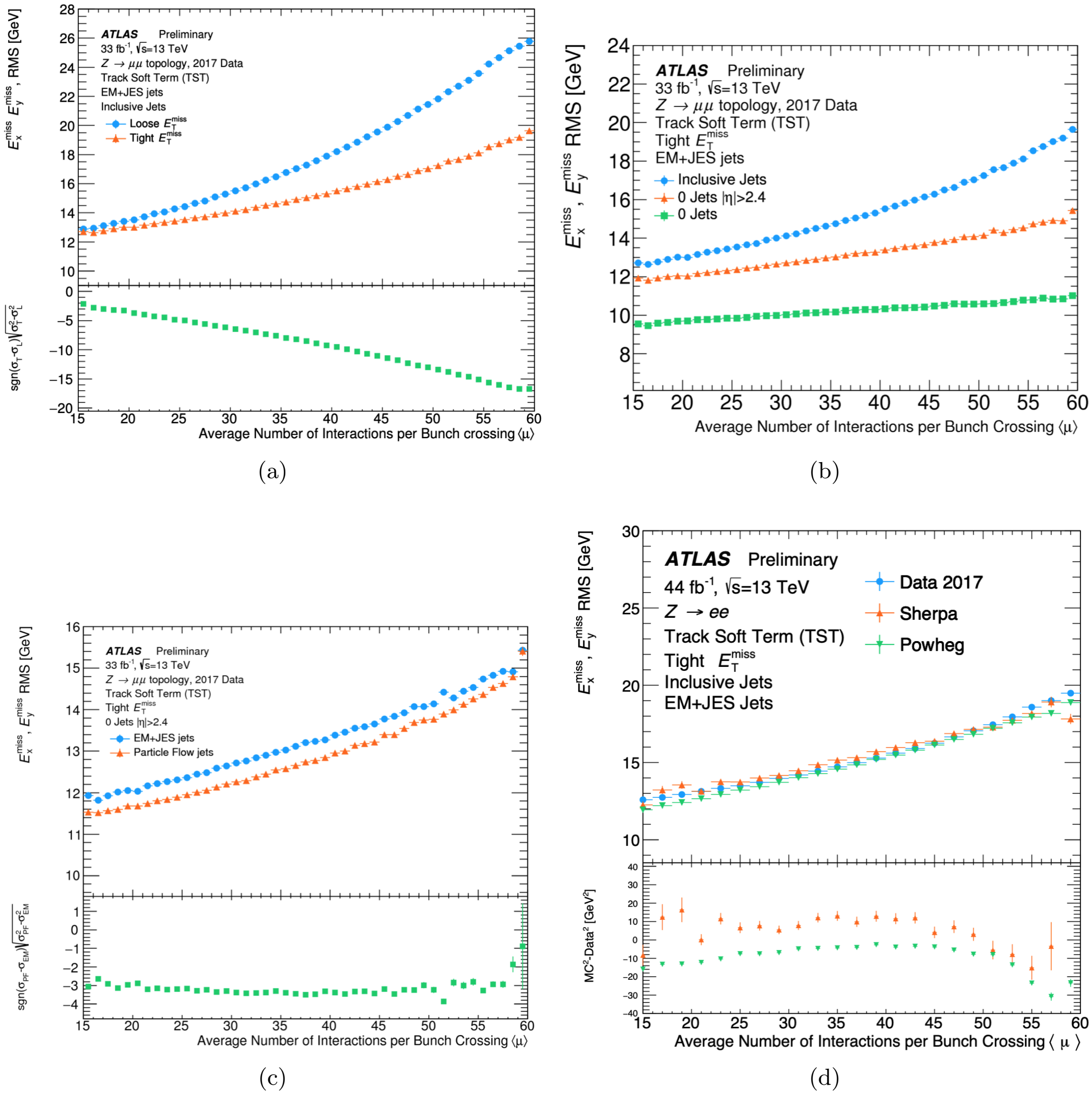

Figure 5.6.8.: The $E_{\mathrm{T}}^{\mathrm{miss}}$ resolution determined in 2017 data for (a) EMTopo Jets with inclusive jets for *Loose* and *Tight* working points with respect to $<\mu>$. (b) EMTopo jets with inclusive jets and exclusive jets with $p_{\mathrm{T}} > 20$ GeV ($N_{jet} = 0$) in the forward region ($|\eta| > 2.4$) and the whole η region. (c) *Tight* working point with EMTopo v.s. PFlow. (d) Data v.s. Sherpa and Powheg comparison for EMTopo jets.

Scale

For events without intrinsic $E_{\mathrm{T}}^{\mathrm{miss}}$ ($Z \to \ell\ell$ decays), ideally the calibrated $E_{\mathrm{T}}^{\mathrm{miss}}$ is 0, and the degree of balance is estimated by projecting $E_{\mathrm{T}}^{\mathrm{miss}}$ onto the Z boson direction:

$$< \overrightarrow{E}_T^{miss} \cdot \hat{A_Z} >, \tag{5.6.12}$$

where $\hat{A_Z}$ is defined as:

$$\hat{A_Z} = \frac{\overrightarrow{p_{\mathrm{T}}}^{\ell+} + \overrightarrow{p_{\mathrm{T}}}^{\ell-}}{|\overrightarrow{p_{\mathrm{T}}}^{\ell+} + \overrightarrow{p_{\mathrm{T}}}^{\ell-}|}. \tag{5.6.13}$$

The projection being close to 0 is preferred, which means the recoil is well reconstructed. Figure 5.6.9 displays the scale comparison between full Run-2 data and MCs with PFlow jets in the $Z \to \mu\mu$ events. he scale ends up being different from 0 mostly because the soft term misses the neutral components. One can also compare events with and without jets which allows distinction between the jet and soft term responses.

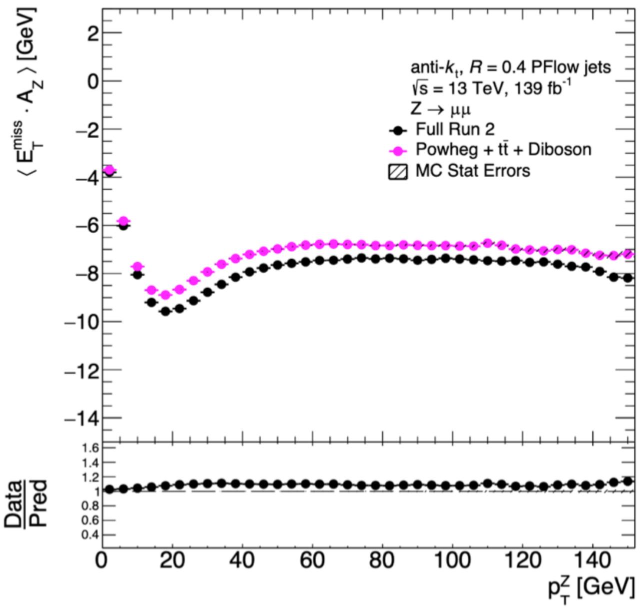

(a)

Figure 5.6.9.: $E_{\mathrm{T}}^{\mathrm{miss}}$ projection. The $E_{\mathrm{T}}^{\mathrm{miss}}$ scale as a function of the p_{T} of the Z boson. Image from Ref. [103].

In events that have intrinsic $E_{\mathrm{T}}^{\mathrm{miss}}$ ($W \to \mu\nu$) the scale is measured using *linearity*:

$$linearity = \left\langle \frac{\overrightarrow{E}_T^{miss} - \overrightarrow{E}_T^{miss,truth}}{\overrightarrow{E}_T^{miss,truth}} \right\rangle. \tag{5.6.14}$$

The ideal *linearity* is expected to be toward zero if the calibrated $E_{\mathrm{T}}^{\mathrm{miss}}$ is equal to the truth $E_{\mathrm{T}}^{\mathrm{miss}}$.

Data/MC

The modelling of the $E_{\mathrm{T}}^{\mathrm{miss}}$ distributions in a $Z \rightarrow ee$ selection with full Run-2 data is shown in Figure 5.6.10. Data is well described by the low-$E_{\mathrm{T}}^{\mathrm{miss}}$ and high-$E_{\mathrm{T}}^{\mathrm{miss}}$ samples, especially below 400 GeV.

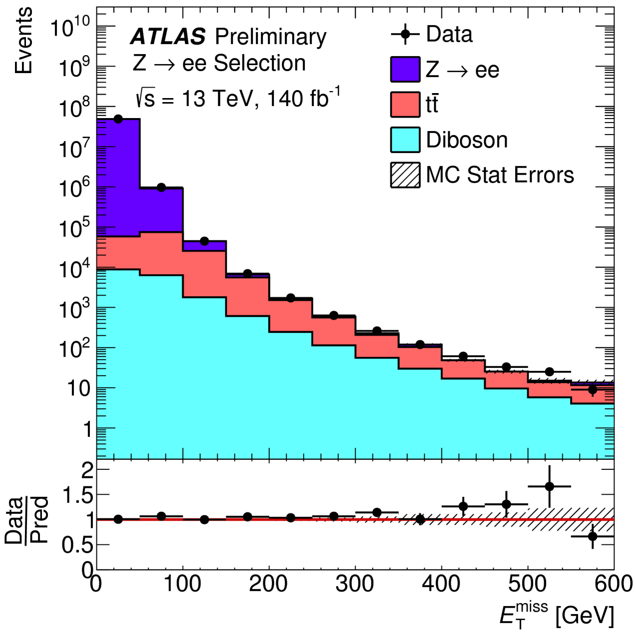

Figure 5.6.10.: Modelling of PFlow $E_{\mathrm{T}}^{\mathrm{miss}}$. The $Z \rightarrow ee$ sample is produced with Powheg. Diboson samples include: $WW \rightarrow l\nu l\nu$, $WZ \rightarrow l\nu ll$, and $ZZ \rightarrow \ell\ell\nu\nu$. Image from: Ref. [103].

Chapter 6

Heavy Higgs Search

A search is performed for an additional heavy Higgs boson in the $H \to ZZ \to \ell^+\ell^-\nu\bar{\nu}$ final state using the Run-2 data-set taken in 2015−2018 in 13 TeV pp collisions [1]. The $\ell^+\ell^-\nu\bar{\nu}$ signal region is split into VBF and ggF categories targeting the Higgs production processes as shown in Figure 6.0.1. The SM ZZ process is the dominant background and the largest source of systematic uncertainty in this search. A novel method to estimate the ZZ background based on boson substitution using $Z\gamma$ events in data, aiming to reduce significant systematic uncertainties, is developed and presented in this chapter. The $Z\gamma$ method can also be used to measure the (dominant) SM ZZ background in other searches: a single Z boson recoiling against missing transverse momentum (mono-Z) including the specific case of SM Higgs bosons (h) decaying into invisible particles, produced in association with a leptonically decaying Z boson ($\ell\ell + E_{\mathrm{T}}^{\mathrm{miss}}$). The mono-$Z$ and Zh(inv) channels are only discussed in this chapter in the context of the $Z\gamma$ to ZZ estimate. For the $Z\gamma$ to ZZ estimate for these analyses, $E_{\mathrm{T}}^{\mathrm{miss}}$ is assumed as the discriminating variable, but since the analyses are not finalised yet, no details or results are given.

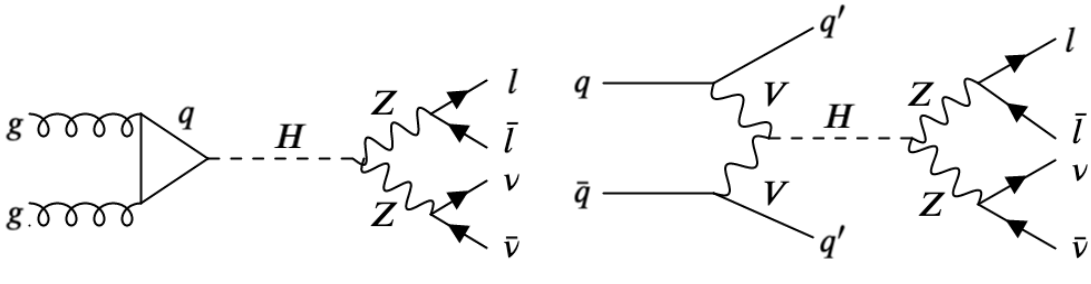

(a) (b)

Figure 6.0.1.: Feynman diagrams for the leading production modes ggF (a), and VBF (b), where the heavy Higgs decays to $Z(\ell\ell)Z(\nu\nu)$.

The studied experimental signature of the heavy Higgs boson production is a pair of leptons and the $E_{\mathrm{T}}^{\mathrm{miss}}$. This final state contributes complementary sensitivity to other channels such as $H \to ZZ \to \ell\ell\ell\ell$, $H \to ZZ \to \ell\ell qq$ and $H \to ZZ \to \nu\nu qq$. The $\ell\ell\ell\ell$ channel dominates the sensitivity at low m_H ($<$ 500 GeV) due to its better mass resolution and smaller background yields. Despite the larger backgrounds of the $ZZ \to \ell^+\ell^-\nu\bar{\nu}$, $\ell\ell qq$, and $\nu\nu qq$ decay modes compared to the $ZZ \to \ell^+\ell^-\ell'^+\ell'^-$ final state, the larger branching ratios for these channels allow them to improve the sensitivity at high m_H. Because the neutrinos in the final state are not experimentally accessible, it is not possible to use the conservation of four-momentum to fully reconstruct the invariant mass of the two Z bosons. The transverse mass, m_{T}, is then used to discriminate between the high mass Higgs boson and the background expectation from SM processes. The m_{T} is defined as:

$$m_{\mathrm{T}}^2 \equiv \left[\sqrt{m_Z^2 + |\overrightarrow{p}_T^{\ell\ell}|^2} + \sqrt{m_Z^2 + |\overrightarrow{p}_T^{miss}|^2}\right]^2 - \left[\overrightarrow{p}_T^{\ell\ell} + \overrightarrow{p}_T^{miss}\right]^2. \tag{6.0.1}$$

95% C.L. upper limits on the production cross-section of an additional heavy Higgs boson are determined in the case that no significant deviation from the SM is observed. The results of the analysis are also interpreted in terms of 2HDM and Randall-Sundrum graviton models (the theoretical motivation is given in Sections 2.4 and 2.5). The data and MC samples used in this analysis are described in Chapter 4. The object selections are detailed in Chapter 5. This chapter is organized as follows: Section 6.1 introduces the event selections for the $\ell\ell$ $+E_{\mathrm{T}}^{\mathrm{miss}}$ final state. Section 6.2 gives an overview of the background contributions in the analysis. Section 6.3 details the ZZ estimation method using $Z\gamma$ events and its associated systematic uncertainties. The kinematic distributions in the signal region showing data and the comparison with the predicted SM background can be found in Section 6.4. In Section 6.5, the limit setting and signal scans are discussed, and the results are presented.

6.1. Event Selection

The event selections for the $\ell\ell$ $+E_{\mathrm{T}}^{\mathrm{miss}}$ final state for the separate analyses are given in this section: the search for the heavy Higgs with $\ell\ell$ $+E_{\mathrm{T}}^{\mathrm{miss}}$ final state (high mass (HM) search) and the search for a Higgs boson through associated production $Zh(\to\mathrm{inv})$ with $\ell\ell$ $+E_{\mathrm{T}}^{\mathrm{miss}}$ final state (low mass (LM) search). While both analyses differ in their optimization studies and the interpretation of their results, the common experimental signature of two charged leptons from a Z boson plus some appreciable $E_{\mathrm{T}}^{\mathrm{miss}}$ allows for a common baseline event selection and the same strategy for background estimation. The optimal thresholds are determined based on a standard Poisson counting experiment with and without background uncertainties. The expected significance without taking into account background uncertainties is estimated with:

$$Z = \sqrt{2\left(S + B\ ln[1 + \frac{S}{B}] - S\right)}, \tag{6.1.1}$$

where S and B are the signal and background yields, respectively. This number is degraded in the presence of a systematic uncertainty on the background. The expected significance including background uncertainties is calculated with [104, 105]:

$$
\begin{aligned}
Z &= \sqrt{2} erf^{-1}(1-2p), \\
p &= A \int_0^\infty db\, G(b; N_b; \delta N_b) \Sigma_{i=N_{data}}^\infty \frac{e^{-N_b} N_b^i}{i!}, \\
A &= \left[\int_0^\infty db\, G(b; N_b; \delta N_b) \Sigma_{i=0}^\infty \frac{e^{-N_b} N_b^i}{i!} \right]^{-1}.
\end{aligned}
\tag{6.1.2}
$$

The summation term from data (N_{data} = the number of background events N_b + the number of signal events N_s) to infinity is the probability of observing i data events taken from a Poisson distribution with an expected N_b. The *p-value* (p) is the probability that the background fluctuates up to give as many or more than i data events. The symbol A is a normalisation factor. The δN_b is the size of the systematic uncertainty of the background, and G is a Gaussian function. The *p-value* is converted into a sensitivity, Z, where *erf(x)* is the error function. The selection criteria are chosen such that the highest expected significance is achieved [106].

The data used in the analyses are collected with single lepton triggers (electron or muon). The trigger menu used is reported in Table 6.1.1.

	Trigger selection
Single Muon	mu20_iloose_L1MU15 OR mu50 (2015)
	mu26_ivarmedium OR mu50 (2016,2017,2018)
Single Electron	e24_lhmedium_L1EM20VH OR e60_lhmedium OR e120_lhloose (2015)
	e26_lhtight_nod0_ivarloose OR e60_lhmedium_nod0 OR e140_lhloose_nod0 (2016, 2017, 2018)

Table 6.1.1.: Trigger requirement in $\ell\ell + E_{\mathrm{T}}^{\mathrm{miss}}$ analyses in 2015−2018 data periods. The single lepton triggers are all un-prescaled in the 2015−2018 data taking period, and require that low p_{T} electrons/muons pass isolation requirements.

A high trigger efficiency with a sharp turn-on curve for the electron p_{T} is shown in Figure 6.1.1. The performance of the single electron triggers is evaluated exploiting a tag-and-probe method using $Z \to ee$ events. HLT efficiencies for p_{T} thresholds of 140 GeV, 60 GeV, and 26 GeV with an additional tight isolation requirement are measured. Above a certain p_{T} threshold, meaning above the turn-on curve, the HLT efficiency is about 90−95%. The agreement is within 2−4% above 30 GeV in p_{T} between data and MC. The residual differences are corrected with a data/MC scale factor.

Since the triggers are operating in LHC collisions with increasing instantaneous luminosity, the trigger selections are adjusted according to the year. The trigger selections attain high signal efficiency for the full Run-2 data taking period. Due to the sharp turn-on curve of single lepton trigger efficiencies, a $p_{\mathrm{T}} > 30$ GeV selection on the leading lepton is applied.

All data events are required to pass the Good Runs List (GRL) to exclude events in problematic conditions. A set of quality checks on data events are applied, following the recommendations of the data preparation group. In particular, events affected by detector/read-out problems are removed [108].

This analysis uses a set of data events collected by the ATLAS detector in *pp* collisions based on the full 2015−2018 (Run-2) dataset, which corresponds to 139 fb^{-1} at a centre-of-mass

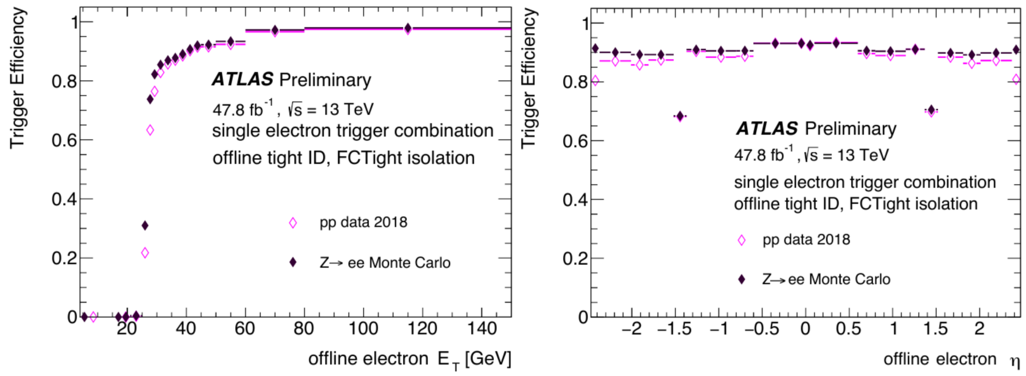

(a) (b)

Figure 6.1.1.: Efficiency of the lowest un-prescaled single electron trigger combination (logical OR of HLT_e26_lhtight_nod0_ivarloose, HLT_e60_lhmedium_nod0 and HLT_e140_lhloose_nod0) in 2018 data, compared to $Z \to ee$ POWHEG +PYTHIA Monte Carlo (a) as a function of the offline electron transverse energy, (b) as a function of the offline electron pseudorapidity. The offline electron fulfills a tight offline identification requirement. Image from Ref. [107].

energy of 13 TeV. The uncertainty on the combined 2015−2018 integrated luminosity is 1.7% [109], obtained from the LUCID-2 detector [110] for the primary luminosity measurements.

A set of *Jet Cleaning* criteria is applied to remove jets originating from non-collision events, such as hardware problems, cosmic-ray showers or beam related backgrounds. These jets can give rise to fake missing transverse momentum that results in an increased tail of the $E_{\mathrm{T}}^{\mathrm{miss}}$ distribution. Events with poor quality jets, defined as $p_{\mathrm{T}} > 20$ GeV jets not passing the *Loose* selection criteria for the *Jet Cleaning* [89], are rejected.

The event selection is summarised in Table 6.1.2. Events are required to contain exactly two same flavour and oppositely charged electrons or muons that pass the object selections described in Sections 5.2 and 5.3. Certain backgrounds are reduced by the event selections, which are shown in the table as well. For example:

- Events with a third lepton are vetoed to reduce background from $ZZ \to \ell\ell\ell\ell$ (with two unidentified leptons) and $WZ \to \ell\nu\ell^+\ell^-$ events. The p_{T} thresholds and selection criteria for the third lepton are shown in Tables 5.2.1 and 5.3.1. The p_{T} threshold is set to be 7 GeV as baseline selection with a looser lepton quality.

- The invariant mass of the selected two leptons is required to be within the range of 76 GeV $\leq \mathrm{M}_{\ell\ell} \leq$ 106 GeV. This requirement significantly reduces events which don't include a Z boson, for example $t\bar{t}$, $WW \to \ell^+\nu\ell^-\bar{\nu}$, *etc.*

- Other common selections are applied, which exploit the topology and kinematics of the signal events. In both analyses, a lower threshold is set on the $E_{\mathrm{T}}^{\mathrm{miss}}$ variable, which helps selecting signal events while rejecting the inclusive Z production. Due to different signal topologies for HM and LM searches, the $E_{\mathrm{T}}^{\mathrm{miss}}$ threshold requirements differ accordingly.

- A heavy Higgs boson decays into a pair of boosted Z bosons, which implies the two decay leptons are close in the space. An upper threshold on the distance $\Delta R_{\ell\ell}$ is therefore applied.

- As the heavy Higgs is expected to be produced at rest, the two Zs are expected to be back-to-back, and so the $E_{\mathrm{T}}^{\mathrm{miss}}$ should be back-to-back with the observed Z boson. Therefore, $\Delta\ \phi(Z,\ E_{\mathrm{T}}^{\mathrm{miss}})$ is required to be above a certain threshold.

- High m_T Drell-Yan events that pass the above selection criteria usually have high p_{T} jets, a boosted Z boson, and large $E_{\mathrm{T}}^{\mathrm{miss}}$, which originates from the mismeasurement of high p_{T} jets. To reduce this background, the minimum azimuthal angular separation between the $E_{\mathrm{T}}^{\mathrm{miss}}$ and all jets with $p_{\mathrm{T}} > 100$ GeV in the event ($\Delta\phi(\text{jet},\ E_{\mathrm{T}}^{\mathrm{miss}})$) must be larger than a certain value. Background sources arising from fake $E_{\mathrm{T}}^{\mathrm{miss}}$ are further reduced by requiring a $E_{\mathrm{T}}^{\mathrm{miss}}$ significance cut.

- A veto on any b-tagged jets is applied to reduce heavy flavour background, such as events including top quarks.

Due to its non-negligible production cross-section and unique signature, the vector boson fusion process is also considered. The vector boson fusion topology in the heavy Higgs search is targeted by applying stringent requirements on the invariant mass (M_{jj}) and separation ($|\Delta\eta_{jj}|$) of the two leading jets (both are required to have p_{T} of at least 30 GeV, which allows reducing pile-up effects) in the event. These selections reduce ggF contamination in the VBF signal region and reduce backgrounds. (The description of the VBF topology can be found in Section 2.2.) All events that do not fulfil the VBF criteria are collected in the ggF category.

Event Pre-Selection		
All_Good GRL events		
Vertex with ≥ 2 tracks with $p_{\mathrm{T}} > 1$ GeV		
Single lepton trigger as in Table 6.1.1		
Event Selection		**Targeted background**
High mass	**Low mass**	—
Two same flavour opposite-sign leptons (e^+e^- OR $\mu^+\mu^-$)		
Veto of any additional lepton with Loose ID and $p_{\mathrm{T}} > 7$ GeV		$ZZ \to \ell\ell\ell\ell$, WZ
$76 < M_{\ell\ell} < 106$ GeV		Non-resonant $\ell^+\ell^-$
$E_{\mathrm{T}}^{\mathrm{miss}} > 120$ GeV	$E_{\mathrm{T}}^{\mathrm{miss}} > 90$ GeV	Z + jets
$\Delta R_{\ell\ell} < 1.8$		Z + jets, Non-resonant $\ell^+\ell^-$
$\Delta\phi(Z,\ E_{\mathrm{T}}^{\mathrm{miss}}) > 2.5$	$\Delta\phi(Z,\ E_{\mathrm{T}}^{\mathrm{miss}}) > 2.7$	Z + jets, Non-resonant $\ell^+\ell^-$
b-jet Veto		Single top, $t\bar{t}$
$E_{\mathrm{T}}^{\mathrm{miss}}$ significance > 10	$E_{\mathrm{T}}^{\mathrm{miss}}$ significance > 9	fake $E_{\mathrm{T}}^{\mathrm{miss}}$ sources
$\Delta\phi(\text{jet}(p_{\mathrm{T}} > 100\ \text{GeV}),\ E_{\mathrm{T}}^{\mathrm{miss}}) > 0.4$	—	Z + jets
High Mass VBF	—	
At least 2 jets with $p_{\mathrm{T}} > 30$ GeV	—	
$M_{jj} > 550$ GeV	—	
$\lvert\Delta\eta_{jj}\rvert > 4.4$	—	

Table 6.1.2.: List of selections applied at the event selection level for high mass (heavy Higgs) and low mass (mono-Z, Zh(inv)) analyses. For the Zh(inv) analysis, a boosted decision tree (BDT) is currently studied which could replace the current discriminating variable $E_{\mathrm{T}}^{\mathrm{miss}}$.

6.2. Background Estimates

This section describes how the main backgrounds in the $\ell\ell + E_{\mathrm{T}}^{\mathrm{miss}}$ final state are estimated. The backgrounds are divided into two main categories:

- **Irreducible Backgrounds:** processes with a true $\ell\ell + E_{\mathrm{T}}^{\mathrm{miss}}$ final state.
- **Reducible Backgrounds:** processes with an $\ell\ell + E_{\mathrm{T}}^{\mathrm{miss}}$ final state arising from fake or missing leptons, and/or fake $E_{\mathrm{T}}^{\mathrm{miss}}$.

Some backgrounds remain even after applying event selections. The dominant irreducible background in the $\ell\ell + E_{\mathrm{T}}^{\mathrm{miss}}$ final state is the Standard Model $ZZ \to \ell^+\ell^-\nu\bar{\nu}$ process ($\sim 60\%$), since it has two genuine leptons from a Z-boson plus two neutrinos giving missing transverse momentum. Due to its similarity to the signal events, the signal region selections are unable to significantly reduce this background, and it remains the dominant analysis background. The second leading background is $WZ \to \ell\nu\ell^+\ell^-$ ($\sim 30\%$), despite the higher cross-section w.r.t the $ZZ \to \ell^+\ell^-\nu\bar{\nu}$ process, as it can be reduced by vetoing the presence of a third lepton in the event. Other reducible backgrounds include the non-resonant $\ell\ell$ production ($\sim 5\%$), Z + jets ($\sim 4\%$), and the remaining contribution from VVV and $t\bar{t}V$ ($\sim 1\%$).

Control regions (CR) are defined to be orthogonal to the signal region (SR) by inverting one or more of the SR selections. Each CR aims to preferentially select specific categories of background events. Whenever possible, the estimation of each background is extracted directly from the data sample. Otherwise, MC based estimates verified in data are used and scaled accordingly.

Background Estimation Methods and Uncertainties

- $ZZ \to \ell^+\ell^-\nu\bar{\nu}$ is the leading background in the $\ell\ell + E_{\mathrm{T}}^{\mathrm{miss}}$ analyses. It consists of contributions from three production modes, the $qq \to ZZ$, $gg \to ZZ$, and EW $q\bar{q} \to ZZ$ processes. The shape of the m_{T}^{ZZ} distribution is provided by the MC simulation. MC sample production for the ZZ background is discussed in Section 4.1. The ZZ MC uncertainties consider both the theoretical uncertainties and the experimental uncertainties. The experimental uncertainties are provided by the Combined Performance (CP) groups and include efficiency uncertainties for triggering, the reconstruction and identification of physics objects, as well as the energy scale and resolution of leptons, jets and $E_{\mathrm{T}}^{\mathrm{miss}}$. The theoretical uncertainties from parton-density-functions (PDFs), missing higher-order QCD scales, and parton showers (PS) are estimated. The PDF uncertainty is deduced from the envelope of bands of different PDF choices and its internal PDF error sets. The largest variation of varying the factorization and renormalisation scales by half or double is taken as the QCD uncertainty. More explanations of these uncertainties can be found in Section 4.1. Additionally, the parton shower uncertainty is obtained by varying shower-related parameters in Sherpa. Matrix element matching scale (CKKW), resummation scale (QSF), and parton shower recoil scheme (CSSKIN) are varied using truth samples. The CKKW scale is used to resolve the overlap between jets from the matrix element and the parton shower. The QSF scale is used for the resummation of soft gluon emissions. The CSSKIN scale is used for the subtraction scheme that covers soft limits, and collinear limits, *etc.* For illustration, the theoretical uncertainties are propagated to the MC-based estimation on the total yield. The size of each uncertainty is summarised in Table 6.2.1. The large value of the QCD

Percentage(%)		Inclusive		
		PDF	QCD	PS
qqZZ	ggH	1.7	5.3	3.8
	VBF	1.7	16.0	16.3
ggZZ	ggH	1.8	40.7	3.8
	VBF	2.0	45.2	11.2
qqZZjj	ggH	1.9	5.3	
	VBF	2.7	9.7	

Table 6.2.1.: Theory uncertainties on the total yield of the different ZZ processes in the ggF and the VBF categories, due to PDF, QCD, and PS variations.

uncertainty on the $ggZZ$ process is due to the fact that the simulation is only leading order in QCD.

Moreover, NLO EW corrections have been considered [62], which are calculated in two schemes, additive and multiplicative with NLO QCD, and the central value of the corrections is the average. Above 1 TeV, the EW corrections reduce the expected event yield by about 20%. The uncertainty on the EW correction (less than 1% in low mass region and $\sim$ 10% in the high mass region) is taken from the difference of the average w.r.t the additive/multiplicative schemes.

In the $H \to ZZ \to \ell^+\ell^-\nu\bar{\nu}$ analysis, the shape of the m_{T} distribution is estimated using the MC simulation, but the predicted ZZ yield is scaled by a floating normalization factor, which is derived in a simultaneous likelihood fit to the signal-region data. Therefore, the normalisation uncertainties only enter the relative yield of $qqZZ$ and $ggZZ$ processes.

An alternative estimation method, the $Z\gamma$ method, will be discussed in Section 6.3 and it is used as a cross-check especially of the shape.

- $WZ \to \ell\nu\ell^+\ell^-$ is the subleading background. The shapes of m_{T}^{ZZ} distributions are estimated using NLO QCD MC samples. The normalization factor with respect to NLO is obtained by comparing the MC and data in a three-lepton CR, which is dominated by $WZ \to l\nu\ell\ell$ events. The selections are based on the transverse mass of the W boson and the $E_{\mathrm{T}}^{\mathrm{miss}}$ significance. The m_{T}^{W} is reconstructed by the $E_{\mathrm{T}}^{\mathrm{miss}}$, the transverse momentum of the third lepton p_{T}^{l}, and the azimuthal opening angle between the two leptons:

$$m_{\mathrm{T}}^{W} = \sqrt{2p_{\mathrm{T}}^{l}E_{\mathrm{T}}^{\mathrm{miss}}(1 - cos\Delta\phi)}. \tag{6.2.1}$$

The CR selection is shown in Table 6.2.2.

m_{T} $(W) > 60$ GeV
$E_{\mathrm{T}}^{\mathrm{miss}}$ significance > 3
b-jet Veto

Table 6.2.2.: $3l$ CR selection, which is applied on top of the modified pre-selections (purity $> 90\%$).

The WZ yield in data in the SR ($\mathrm{N}^{2l\mathrm{SR}}_{WZ,\mathrm{data}}$) is derived by the number of data events in the $3l$ CR ($\mathrm{N}^{3l\mathrm{CR}}_{WZ,\mathrm{data}}$) times the MC ratio of $2l$ SR ($\mathrm{N}^{2l\mathrm{SR}}_{WZ,\mathrm{MC}}$) and $3l$ CR ($N^{3l\mathrm{CR}}_{WZ,\mathrm{MC}}$):

$$\mathrm{N}^{2l\mathrm{SR}}_{WZ,\mathrm{data}} = \mathrm{N}^{3l\mathrm{CR}}_{WZ,\mathrm{data}} \times \frac{\mathrm{N}^{2l\mathrm{SR}}_{WZ,\mathrm{MC}}}{N^{3l\mathrm{CR}}_{WZ,\mathrm{MC}}}. \tag{6.2.2}$$

The uncertainties considered are experimental systematics measured by CP recommendations and PDF and QCD scale uncertainties from theory. The total uncertainty from all sources is about 4% in ggF and 25% in VBF. The dominant experimental uncertainties come from the jet energy scale and jet energy resolution.

- The non-resonant-$\ell\ell$ contributions include top, Wt, WW, and $Z \to \tau\tau$ events. They are estimated by studying $e\mu$ + $E_{\mathrm{T}}^{\mathrm{miss}}$ events from data. A CR is defined with the standard event selection except for the requirement of an opposite sign $e\mu$ pair. The final background contribution is estimated in both yield and shape by using the ratio between di-lepton final states, ee : $\mu\mu$: $e\mu = 1 : 1 : 2$, and the differences in reconstruction efficiencies of electrons and muons:

$$\begin{aligned} \mathrm{N}^{\mathrm{SR}_{ee}}_{ee} &= \frac{1}{2} \times \epsilon \times \mathrm{N}^{\mathrm{data,sub}}_{e\mu}, \\ \mathrm{N}^{\mathrm{SR}_{\mu\mu}}_{\mu\mu} &= \frac{1}{2} \times \frac{1}{\epsilon} \times \mathrm{N}^{\mathrm{data,sub}}_{e\mu}, \end{aligned} \tag{6.2.3}$$

where ϵ ($\epsilon^2 = \frac{\mathrm{N}_{ee}}{\mathrm{N}_{\mu\mu}}$) is a p_{T} and η dependent efficiency for the number of electrons (e) and muons (μ), and it is calculated as:

$$\epsilon^2(p_{\mathrm{T}}, \eta) = \frac{\mathrm{N}_{e^1_{(p_{\mathrm{T}},\eta)} e^2_{(p_{\mathrm{T}},\eta)}}}{\mathrm{N}_{\mu^1_{(p_{\mathrm{T}},\eta)} \mu^2_{(p_{\mathrm{T}},\eta)}}}. \tag{6.2.4}$$

$\mathrm{N}^{\mathrm{data,sub}}_{e\mu}$ is the number of eμ data events after non-$e\mu$ MC has been subtracted off in the CR, $\mathrm{N}^{\mathrm{data,sub}}_{e\mu} = \mathrm{N}^{\mathrm{data}}_{e\mu}$ - $\mathrm{N}^{\mathrm{MC}}_{\mathrm{non}-e\mu}$.

The estimation of the non-resonant-$\ell\ell$ in the VBF-enriched signal region is obtained by a CR with a looser selection on the jets compared to the SR due to the limited size of the data sample. The estimate is then scaled by a MC-based transfer factor to extrapolate to the SR.

The total systematic uncertainty on the estimated WZ yield in the ggF category is about 4%, and in the VBF category is about 40%. The total statistical uncertainty in the ggF category is about 10%, and in the VBF category is about 30%.

- The Z + jets background is estimated by a sideband technique. This method defines a CR with a single reversed cut to enhance the background. The $E_{\mathrm{T}}^{\mathrm{miss}}$ significance variable is used because it provides good separation between Z + jets events and events with intrinsic $E_{\mathrm{T}}^{\mathrm{miss}}$. The $\Delta\phi$(jet, $E_{\mathrm{T}}^{\mathrm{miss}}$) selection is removed to increase statistics in the CR. The 1D sideband estimate is calculated as

$$\mathrm{N}^{\mathrm{est}}_{\mathrm{SR}} = \mathrm{N}^{\mathrm{data,sub}}_{\mathrm{CR}} \times \frac{\mathrm{N}^{\mathrm{MC}}_{\mathrm{SR}}}{\mathrm{N}^{\mathrm{MC}}_{\mathrm{CR}}}, \tag{6.2.5}$$

where the CR selection is defined in Table 6.2.3. The Z + jets prediction uses both the corrected yield and the shape from the sideband. The systematic uncertainty is $\sim$ 40 % for the ggF category and $\sim$ 80 % for the VBF category. Dominant uncertainties come from jet related uncertainties (38% for ee and 30% for $\mu\mu$).

without $\Delta\phi(\text{jet}(p_{\text{T}} > 100\,\text{GeV}), E_{\text{T}}^{\text{miss}})$
$E_{\text{T}}^{\text{miss}}$ significance < 9

Table 6.2.3.: Z + jets CR selection (purity $\sim$ 70-80%)

An alternative method using $\gamma+$ jets is performed and serves as a cross-check of the sideband technique. This method relies on the similarity between Z + jet and $\gamma+$ jets event topologies to estimate the SR Z + jets background from single-photon events.

6.3. Introduction to the $Z\gamma$ Method

The $Z\gamma$ method is a way to estimate the $ZZ \rightarrow \ell^+\ell^-\nu\bar{\nu}$ background from data, using events with a Z and a photon. $Z(\ell\ell)\gamma$ production is very similar to $ZZ \rightarrow \ell^+\ell^-\nu\bar{\nu}$ as shown in Figure 6.3.1, but occurs at a higher rate, which reduces the statistical uncertainties. The processes of γ and $Z(\rightarrow \nu\nu)$ are kinematically similar especially at high p_{T}, where the mass difference between the photon and the Z boson becomes insignificant, so many of the uncertainties on the cross-section will cancel in the ratio, reducing the theoretical uncertainties.

The basic idea of the method is to correct the measured m_{T} distribution in $Z\gamma$ events with the calculated cross-section ratio. This cross-section ratio is calculated as a function of Z or photon truth p_{T}. The $Z\gamma$ events are additionally corrected for the photon reconstruction efficiency ϵ_γ, again as a function of photon p_{T}. These two factors are applied on an event-by-event basis to the m_{T} distribution in data $Z\gamma$ events where the photon p_{T} is added to the missing transverse momentum of the event to mimic the production of $ZZ \rightarrow \ell^+\ell^-\nu\bar{\nu}$ background as illustrated by the following formula:

$$ZZ = Z\gamma^{\text{reco}}_{\gamma\rightarrow E_{\text{T}}^{\text{miss}}} \times \frac{1}{\epsilon_\gamma^{\text{reco/truth}}} \times R(\frac{\sigma_{ZZ}}{\sigma_{Z\gamma}})^{\text{truth}}_{\gamma_{p_{\text{T}}}}. \tag{6.3.1}$$

The $Z\gamma$ method is not fully a data-driven method, as the formula shows that it still depends on the theory calculations of the ratio and the MC simulation for the efficiency term. No attempt is currently made in the $Z\gamma$ method to split the signal region into ggF and VBF parts, instead an inclusive signal region is considered. The discussion of each ingredient in the formula is organized as follows: the $E_{\text{T}}^{\text{miss}}$ calculation, where the photon is treated as $E_{\text{T}}^{\text{miss}}$ (in data events), the photon efficiency calculation, where the photon is extrapolated from the truth to the reconstructed level (in MC events), and the determination of the cross-section ratio of ZZ and $Z\gamma$ events at the truth level are shown in Subsection 6.3.1, 6.3.2 and 6.3.3, respectively. The validation of the method using a closure test on ZZ MC is presented in Subsection 6.3.4. To use $Z\gamma$ events in data, one must think about what other backgrounds are going to fall into the $Z\gamma$ CR. The calculation for these backgrounds is described in Subsection 6.3.5. The data/MC agreement in the $Z\gamma$ CR is shown in

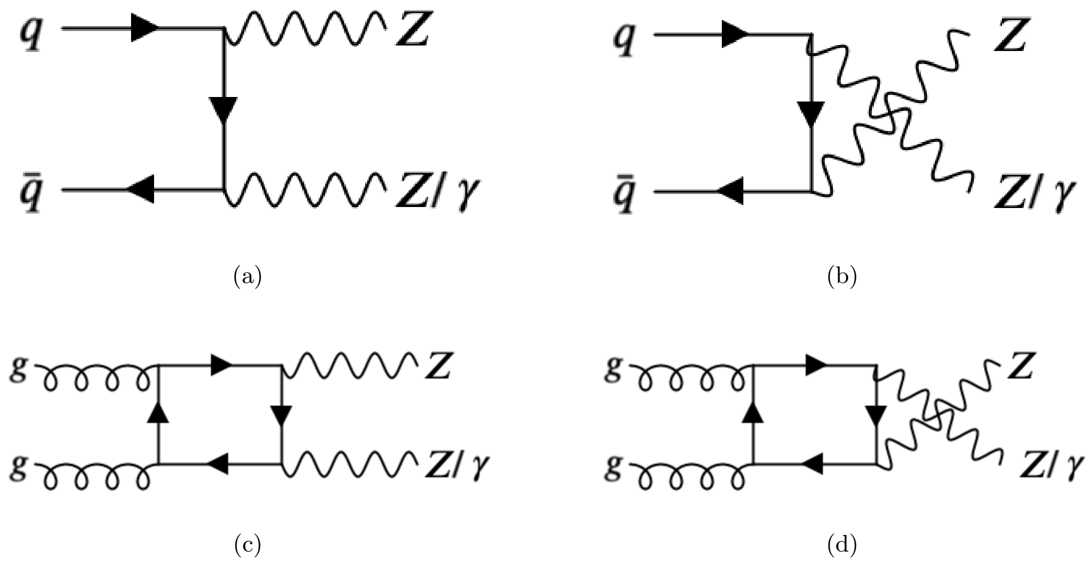

Figure 6.3.1.: Leading order Feynman diagrams for $ZZ/Z\gamma$ production through the $q\bar{q}$ and gg initial state.

Subsection 6.3.6. The sources of systematic uncertainty that affect the ZZ prediction are investigated in Subsection 6.3.7. The comparison between the finalized prediction of the ZZ distribution using the $Z\gamma$ method and the ZZ prediction from MC is given in Subsection 6.3.8.

6.3.1. Ingredient Discussion: $E_{\mathrm{T}}^{\mathrm{miss}}$ Reconstruction

$Z\gamma$ events have no intrinsic $E_{\mathrm{T}}^{\mathrm{miss}}$ at LO in QCD. One ingredient in the $Z\gamma$ method is treating the highest p_{T} photon as invisible, thus contributing to the existing $E_{\mathrm{T}}^{\mathrm{miss}}$, which is dominantly caused by reconstruction effects and referred to as fake $E_{\mathrm{T}}^{\mathrm{miss}}$ in the following. The photon is treated as an invisible particle by using a tool in the $E_{\mathrm{T}}^{\mathrm{miss}}$ software, which corresponds to the $E_{\mathrm{T}}^{\mathrm{miss}}$ obtained by calculating the sum of the photon and missing energy 4-vectors, as shown in Figure 6.3.2.

6.3.2. Ingredient Discussion: Photon Efficiency

The baseline selections for photons are found in Table 5.2.2. Additional requirements are placed on the separation of photons from other objects in the event. Photons are rejected if they have $\Delta R < 0.4$ with any electrons or muons in the event, and jets are removed if they have $\Delta R < 0.4$ with a photon. Each event is required to have at least one photon with $p_{\mathrm{T}} > 70$ GeV. The truth photon used to calculate the photon efficiency must be the same as the truth photon in the ratio R to allow the extrapolation from reconstruction to truth level. The truth photon selections are shown in Table 6.3.1.

Events are rejected if the photon comes from hadron decays or the final state radiation (FSR). The selection criteria on reconstructed photons are the same as those used in the ATLAS $Z\gamma$ production cross-section measurement [111]. The photon efficiency for truth photons to pass identification and isolation selection criteria is computed as a function of transverse energy using Sherpa samples at NLO. The efficiency is obtained by applying

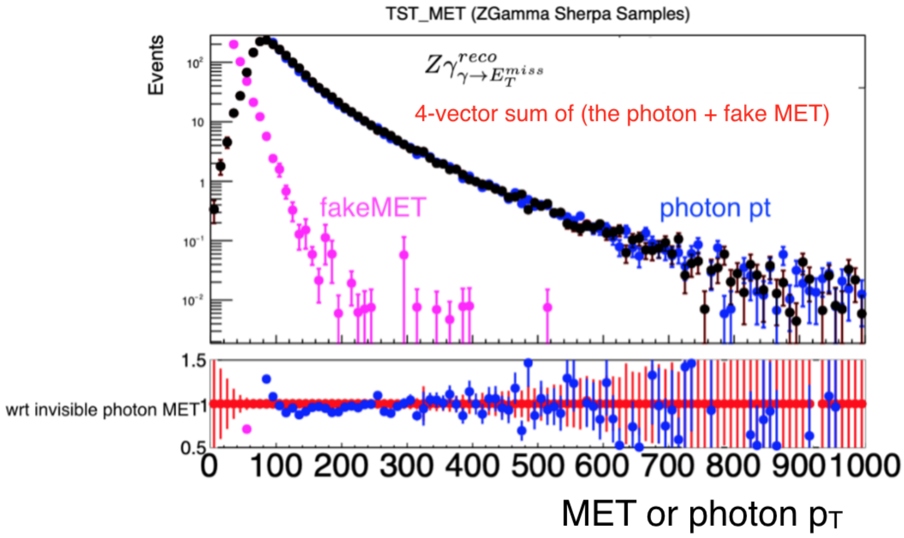

(a)

Figure 6.3.2.: Sanity check for the $E_{\mathrm{T}}^{\mathrm{miss}}$ calculation in the $Z\gamma$ events. The black $E_{\mathrm{T}}^{\mathrm{miss}}$ distribution shows the $E_{\mathrm{T}}^{\mathrm{miss}}$ calculation treating the photon as an invisible particle using the $E_{\mathrm{T}}^{\mathrm{miss}}$ tool, which is exactly the same as the vector sum of the fake $E_{\mathrm{T}}^{\mathrm{miss}}$ and the photon p_{T}, shown in red.

Table 6.3.1.: Truth photon selections used to calculate the cross section ratio R and the photon efficiency.

Stable particles (lifetime $ct_0 > 10$ mm)
Prompt or lepton-associated photons (pdgID=22, not from hadrons or τs)
$p_{\mathrm{T}} > 70$ GeV
$\lvert\eta\rvert < 2.5$

all the event selections up to the $\Delta\mathrm{R}(\ell\ell) < 1.8$ selection. The efficiency curves compared to case without the $\Delta\mathrm{R}(\ell\ell) < 1.8$ cut are shown in Figure 6.3.3. A dependence is seen on this cut, especially at lower photon p_{T}. The efficiency is similar at high p_{T} with and without the $\Delta\mathrm{R}(\ell\ell)$ cut. More cuts were not applied, because no statistically significant difference was seen, and it would reduce the available MC statistics. The efficiencies for high p_{T} photons go up to about 80% as shown in Figure 6.3.4. The increasing trend is because boosted photons are more likely to pass the shower shape criteria, which are part of the photon identification, as they have narrower energy deposits.

6.3.3. Ingredient Discussion: Production Ratio of the ZZ and $Z\gamma$ Processes

The different production rate between the $Z\gamma$ and ZZ processes is taken into account with p_{T} dependent ratios. The cross-sections are calculated at NNLO using the Matrix program. The ratio R has also been calculated for closure checks with Sherpa samples at NLO. The event selection used in the calculation of the ratio R can be found in Table 6.3.2.

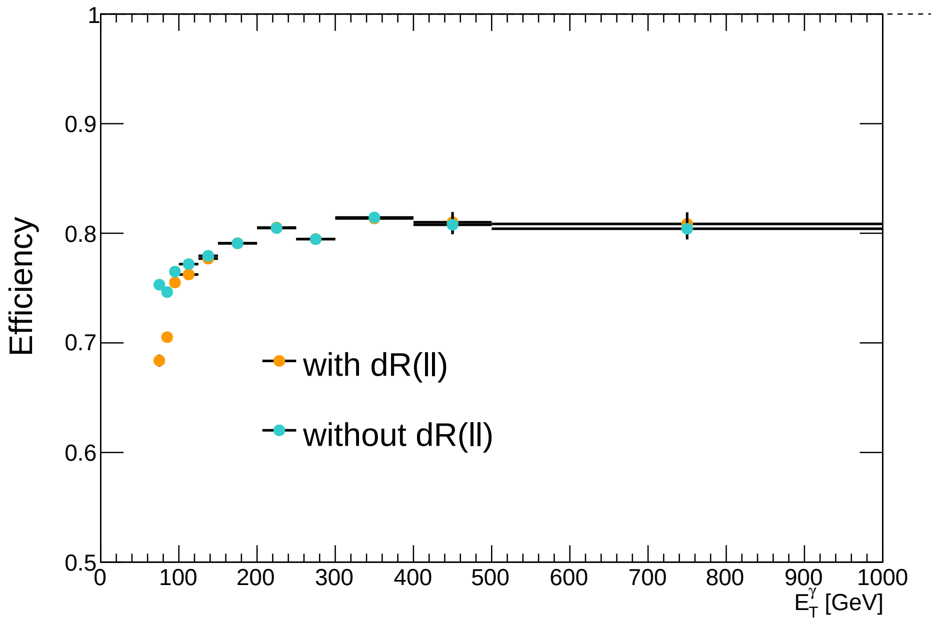

Figure 6.3.3.: The efficiency for a truth photon to pass the reconstruction selection criteria is shown as a function of the reconstructed photon transverse energy. The photon is required to pass tight identification criteria and the loose isolation selection. The simulated samples were produced using SHERPA generator, and MC campaigns correspond to the full Run-2 dataset.

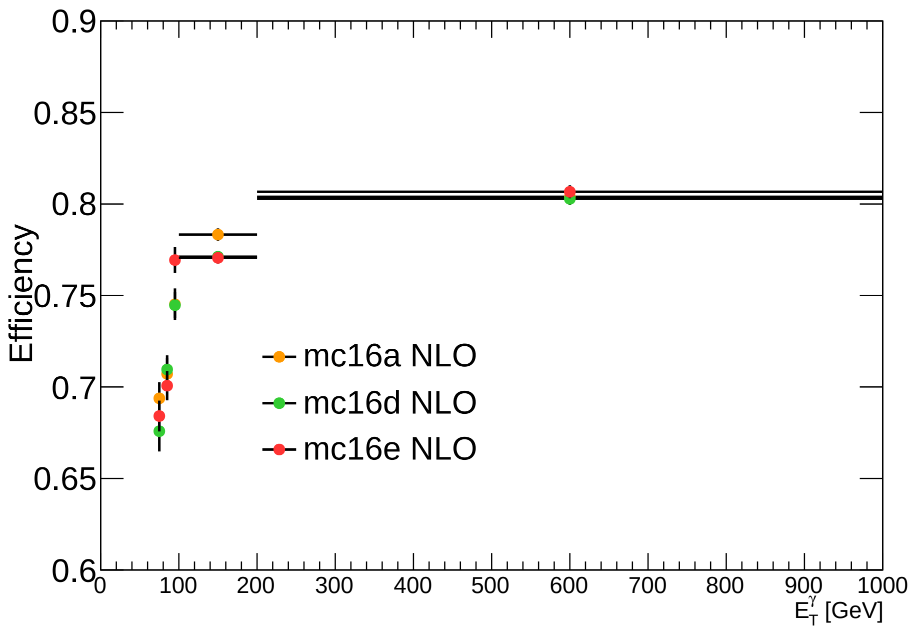

Figure 6.3.4.: Efficiency of the tight identification and loose isolation criteria as a function of the reconstructed photon transverse energy. The comparison is shown between years where mc16a, mc16d, and mc16e corresponding to the dataset in 2015/2016, 2017 and 2018, respectively.

Table 6.3.2.: Event selection at truth-level for $ZZ \to \ell^+\ell^-\nu\bar{\nu}$ and $Z\gamma \to \ell^+\ell^-\gamma$ used to calculate the cross section ratio R.

Variable	ZZ	$Z\gamma$
N_{lep}	$= 2$	
$p_T^{\ell_1}$	> 30 GeV	
$p_T^{\ell_2}$	> 20 GeV	
$m_{\ell\ell}$	$76 < m_{\ell\ell} < 106$ GeV	
$p_T^{\nu\nu}$	> 60 GeV	-
p_T^{γ}	-	> 60 GeV
$\lvert\eta^{\gamma}\rvert$	-	< 2.5
$\Delta R(\ell_1, \ell_2)$	< 1.8	
$\Delta\phi(Z, \gamma)$	-	> 2.5(HM) or $>$2.7(LM)
$\Delta\phi(Z, E_{\mathrm{T}}^{\mathrm{miss}})$	> 2.5(HM) or $>$2.7(LM)	-
truth $E_{\mathrm{T}}^{\mathrm{miss}}$ significance	$>$9(HM) or $>$8(LM)	

It was found to be important to mimic the analysis cuts as closely as possible when calculating the cross-section ratio as shown in Figure 6.3.5. The $E_{\mathrm{T}}^{\mathrm{miss}}$ significance cut, in particular, affects ZZ and $Z\gamma$ events differently, as $Z\gamma$ has more jet activity at low γ p_{T} than ZZ. Since the $E_{\mathrm{T}}^{\mathrm{miss}}$ significance variable is a reconstruction-level variable, a truth level variable which can mimic the $E_{\mathrm{T}}^{\mathrm{miss}}$ significance is therefore defined, and a selection on it is applied for the calculation of the truth production ratio R. The truth $E_{\mathrm{T}}^{\mathrm{miss}}$ significance for ZZ events is defined as:

$$\text{truth } E_{\mathrm{T}}^{\mathrm{miss}} \text{ significance} = \frac{p_{\mathrm{T}}\nu\nu}{\sqrt{p_{\mathrm{T}}^{\ell_1} + p_{\mathrm{T}}^{\ell_2} + \sum_l p_{\mathrm{T}}^{\mathrm{jet}_l}}}, \tag{6.3.2}$$

where the truth jet selection is summarised in Table 6.3.3. For the $Z\gamma$ events, the numerator in Eq. 6.3.2 would be replaced by photon p_{T}.

Identification	AntiKt4TruthWZ jets[1]
Kinematic cuts	$p_{\mathrm{T}} > 20$ GeV $\lvert\eta\rvert < 4.5$
dR(jet, $\ell_1/\ell_2/\gamma$)	> 0.4

Table 6.3.3.: Summary of truth jet selections.

Figure 6.3.6 shows the correlation between the truth-level and reco-level $E_{\mathrm{T}}^{\mathrm{miss}}$ significance obtained from SHERPA MC samples. The reco $E_{\mathrm{T}}^{\mathrm{miss}}$ significance cut is mapped to the truth $E_{\mathrm{T}}^{\mathrm{miss}}$ significance cut, which is then applied when calculating the ratio R in the $Z\gamma$ method. The truth $E_{\mathrm{T}}^{\mathrm{miss}}$ significance cut value is obtained by taking the peak value of the truth $E_{\mathrm{T}}^{\mathrm{miss}}$ significance distribution corresponding to a range of reco $E_{\mathrm{T}}^{\mathrm{miss}}$ significance values around the target value, as illustrated in Figure 6.3.7. Applying the truth $E_{\mathrm{T}}^{\mathrm{miss}}$ significance cut changes the production ratio R up to 30% in low p_{T} regions as shown in Figure 6.3.5. An uncertainty is applied to account for the slight miscorrelation between the

[1] anti-k_t jet with radius 0.4. Muons and electrons from $W/Z/H/\tau$ are not included.

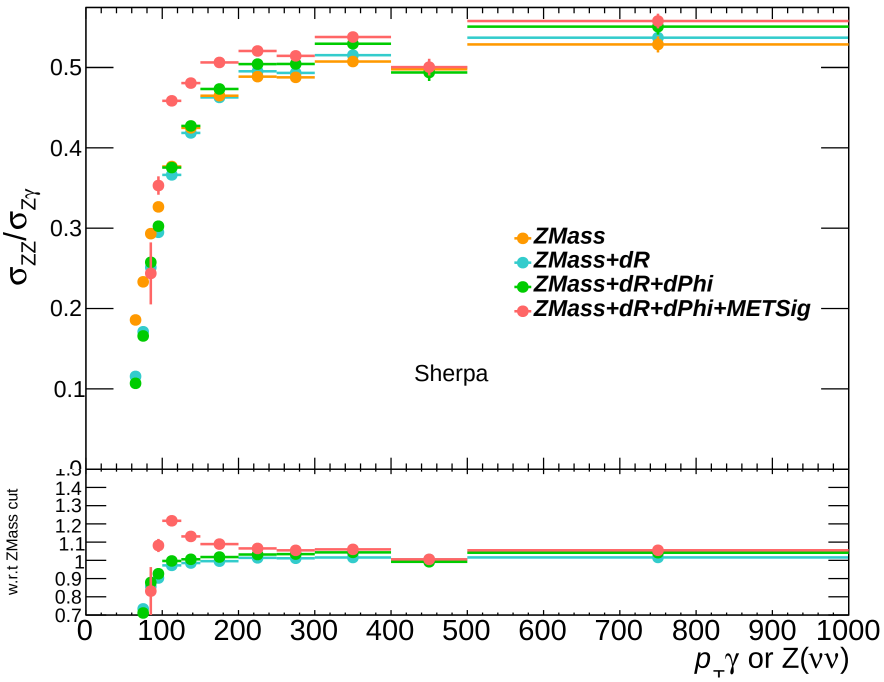

(a)

Figure 6.3.5.: Production ratio R as a function of the truth photon (or neutrinos) transverse energy with different analysis cuts applied (without EW corrections). The simulated samples were produced using the Sherpa generator.

truth $E_{\mathrm{T}}^{\mathrm{miss}}$ significance and reco $E_{\mathrm{T}}^{\mathrm{miss}}$ significance variables (more detailed calculations are shown in Section 6.3.7).

Two generators are used to investigate the production ratio. The Matrix R is calculated as the fraction of $(gg{+}qq)ZZ$ and $(gg{+}qq)Z\gamma$, which is the one chosen as the central value for the data-driven method. The precision of the Matrix calculation was chosen to be at permille level. There is no $ggZ\gamma$ Sherpa sample, but the impact is expected to be small from Matrix studies. Figures 6.3.8 (a) and (b) show the agreement between the R obtained from Sherpa in red and Matrix in cyan ($ggZ\gamma$ is included in the denominator, which gives a complete calculation). The differences are due to differences in Matrix and Sherpa calculations (see details in Section 4.2).

Figure 6.3.9 shows R with EW corrections is in general lower, which is expected. (The EW corrections were produced by the authors of Ref. [62] for both ZZ and $Z\gamma$.)

6.3.4. Closure Checks

Closure checks are done using $Z\gamma$ MC as input instead of data and trying to reproduce the ZZ MC. Reco closure checks using Sherpa NLO samples also for the production ratio R have been performed with and without EW corrections applied to the truth R, ZZ MC, and $Z\gamma$ MC. Figure 6.3.10 shows closure within a couple of percent reproducing the m_{T} distribution using the HM selections with the exception of one bin, which is likely a statistical outlier. We have also checked the closure without applying the $\Delta\mathrm{R}(\ell\ell)$, $\Delta\phi$, b-jet veto, and $E_{\mathrm{T}}^{\mathrm{miss}}$ significance cuts, which can be found in Appendix B. Closure checks on the $E_{\mathrm{T}}^{\mathrm{miss}}$ distribution, used in the LM analysis, are shown in Figure 6.3.11. The

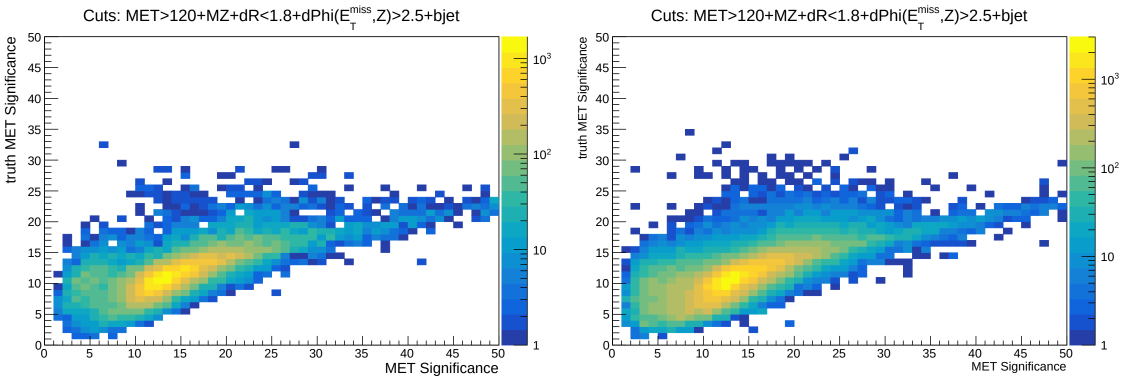

Figure 6.3.6.: Truth $E_{\mathrm{T}}^{\mathrm{miss}}$ significance v.s. reco $E_{\mathrm{T}}^{\mathrm{miss}}$ significance on ZZ events (left) and $Z\gamma$ events (right). Z mass window, $\Delta\mathrm{R}(\ell\ell)$, $\Delta\phi$ and b-jet veto cuts are applied.

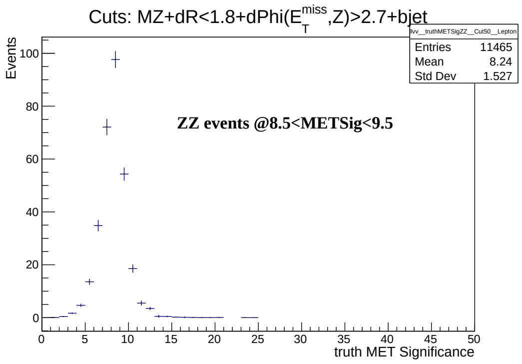

(a)

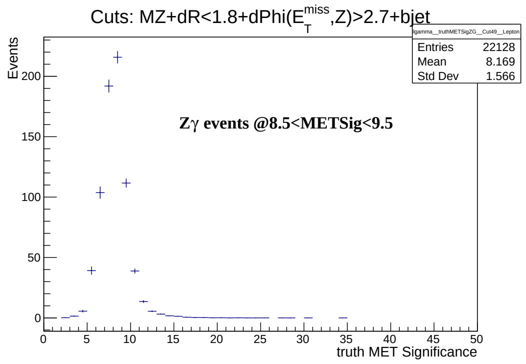

(b)

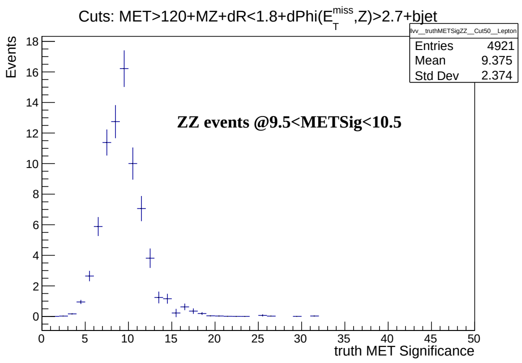

(c)

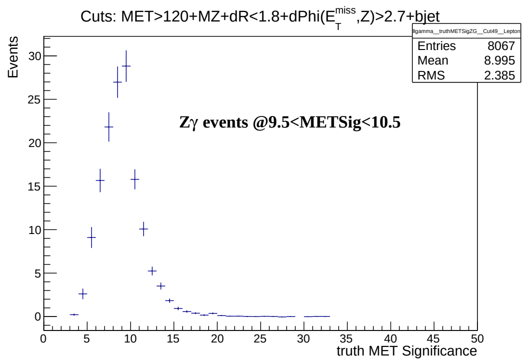

(d)

Figure 6.3.7.: Truth $E_{\mathrm{T}}^{\mathrm{miss}}$ significance distributions in a range of 8.5 to 9.5 of reco $E_{\mathrm{T}}^{\mathrm{miss}}$ significance for (a) ZZ events and (b) $Z\gamma$ events for the LM search, which uses a reco $E_{\mathrm{T}}^{\mathrm{miss}}$ significance threshold of 9. Truth $E_{\mathrm{T}}^{\mathrm{miss}}$ significance distributions in a range of 9.5 to 10.5 of reco $E_{\mathrm{T}}^{\mathrm{miss}}$ significance for (c) ZZ events and (d) $Z\gamma$ events for the HM search, which uses a reco $E_{\mathrm{T}}^{\mathrm{miss}}$ significance threshold of 10. Z mass window, $\Delta\mathrm{R}(\ell\ell)$, $\Delta\phi$ and b-jet veto cuts are applied. The chosen truth $E_{\mathrm{T}}^{\mathrm{miss}}$ significance cut values are 8 for the LM search and 9 for the HM search.

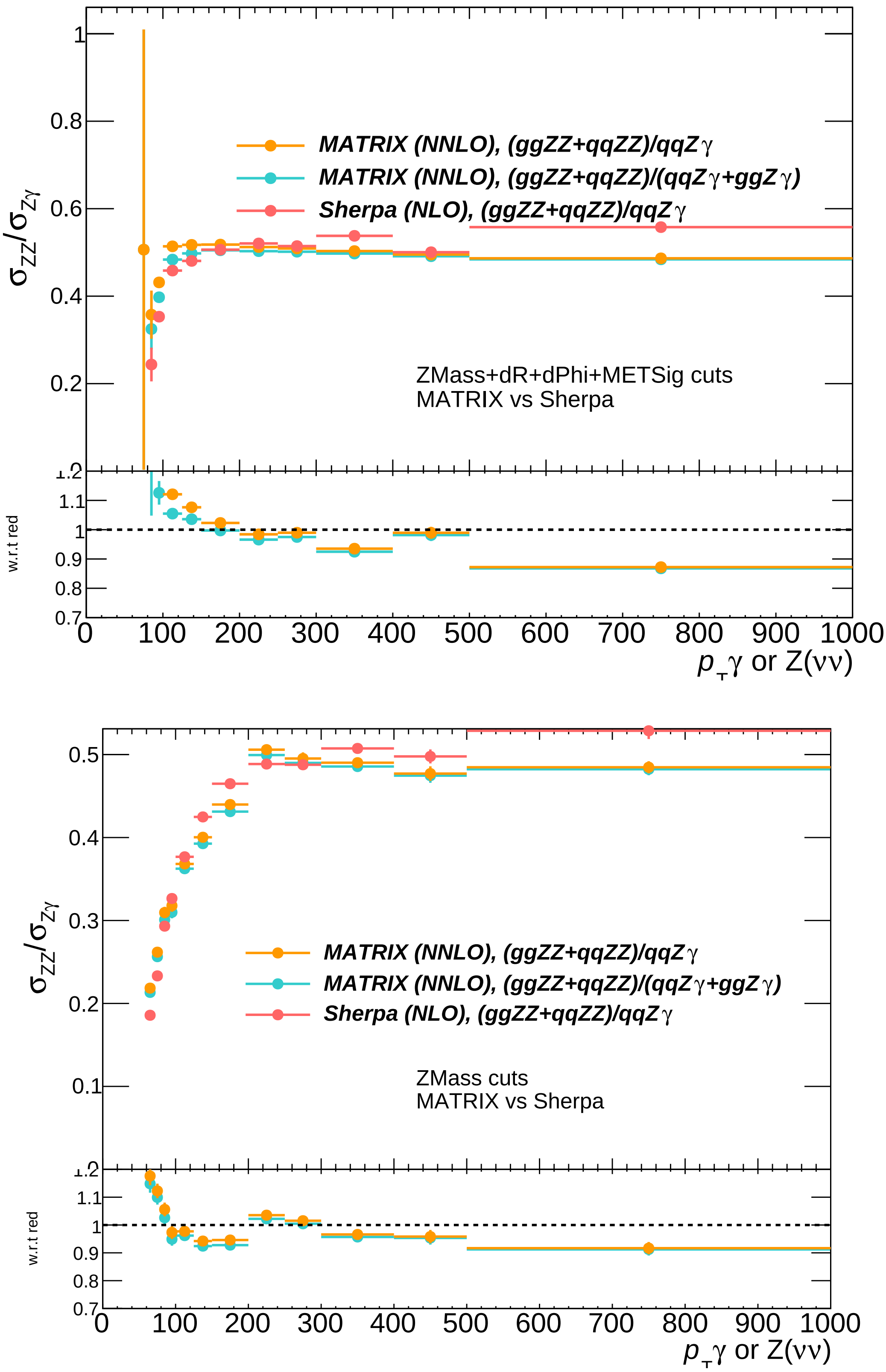

Figure 6.3.8.: Production ratio R as a function of the truth photon (or $Z \to \nu\nu$) transverse energy with full analysis cuts and without EW corrections. The Ratio calculated by Sherpa is in red, Matrix with $ggZ\gamma$ is in cyan, and Matrix without $ggZ\gamma$ is in yellow. (a) Full analysis selections are applied. (b) Selections are applied up to the Z mass window cut.

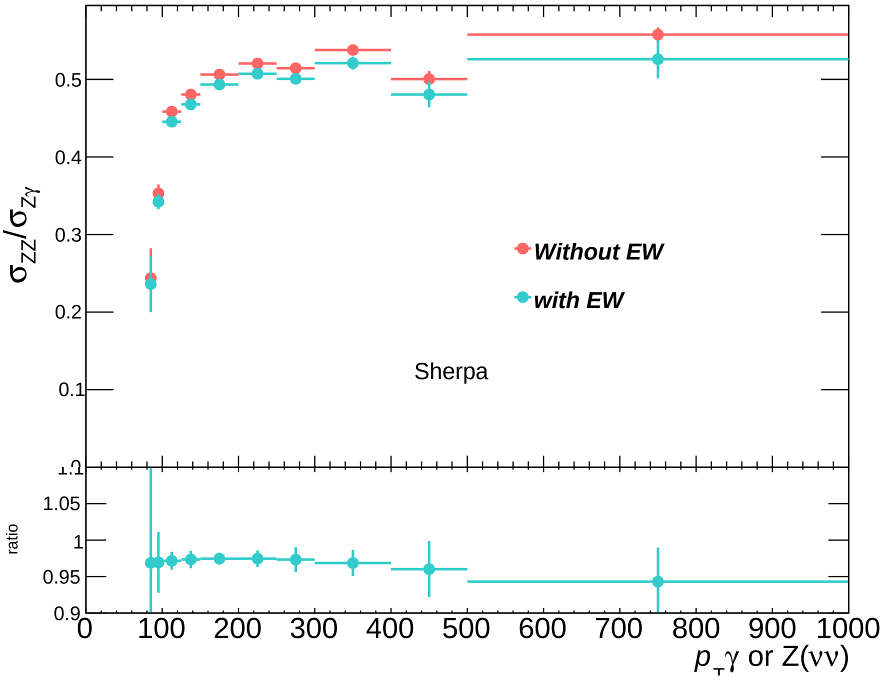

Figure 6.3.9.: Production ratio R as a function of the truth photon (or neutrinos) transverse energy with full analysis cuts applied with and w/o EW corrections. The Rs are made using SHERPA NLO MC.

remaining differences between ZZ MC and ZZ predictions are taken into account as a closure uncertainty described in Section 6.3.7.

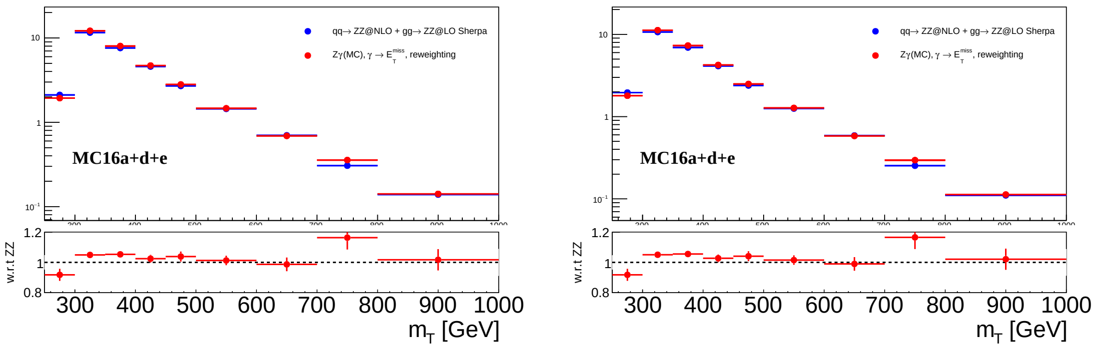

Figure 6.3.10.: Transverse mass closure checks without EW corrections (left) and with EW corrections (right). The ZZ estimate and the ZZ MC have correlated statistical uncertainties, as the same sample is used both for the prediction and the production ratio. The HM selections are used here.

6.3.5. Z + Jets Background Estimate

To use the $Z\gamma$ method in data, one must consider backgrounds. The Standard Model backgrounds that contribute to the $Z\gamma$ spectrum can be divided into three distinct categories:

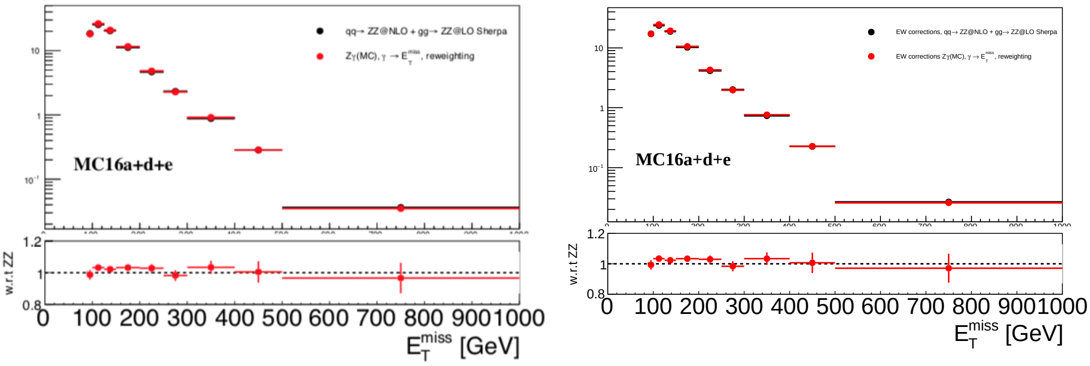

Figure 6.3.11.: $E_{\mathrm{T}}^{\mathrm{miss}}$ closure checks without EW corrections (left) and with EW corrections (right). The ZZ estimate and the ZZ MC have correlated statistical uncertainties, as the same sample is used both for the prediction and the production ratio. The LM selections are used here.

- Z + jets - this is the main background that contributes to the $Z\gamma$ spectrum, where the jet is misidentified as a photon. This background is estimated using the data-driven method developed in the context of the SM $Z\gamma$ cross-section measurement [111]. This category contributes 6% of the events with photon transverse energy above 90 GeV.
- $tt\gamma$, $Z\gamma \to \tau\tau\gamma$, and $WW\gamma$ - these processes contain genuine prompt photons. $tt\gamma$ events account for about 1% of the total background at the Z mass cut level, and it is negligible with the full analysis applied. The $tt\gamma$ contribution is estimated using MC simulation.
- $WZ \to \ell\nu\ell^+\ell^-$ and $H \to ZZ \to \ell\ell\ell\ell$- if one electron is misidentified as a photon. The background contribution in this category is also negligible (less than 1%).

In the SM $Z\gamma$ cross-section measurement, the photon purity is evaluated using an ABCD method. The method relies on two discriminating variables: the photon isolation and the photon identification based on shower shape variables. Four ABCD[2] regions are defined in which the signal photon selections are relaxed, forming three background-enriched regions. Assuming that there is no correlation between the four regions for background photon candidates, the predicted Z + jets background in the signal region is derived by:

$$\frac{N_A^{Z+jets}}{N_B^{Z+jets}} = \frac{N_C^{Z+jets}}{N_D^{Z+jets}}. \tag{6.3.3}$$

In each region, the number of Z + jets events can be defined as N_{data} - $N_{background}$ - $N_{Z\gamma}$, where N_{data} is the total number of events in data and $N_{background}$ is the number of events from processes that are not Z + jets or $Z\gamma$, taken from MC. The signal leakage in each CR is also obtained from MC, allowing to solve for the number of signal events in signal region (A). The leakage parameters are defined as the ratio of the N_{sig} in each CR to the N_{sig} in the SR.

The final result can be expressed in terms of the photon purity in the signal region, which is defined as:

[2]The four ABCD regions are the signal region, A, and three background-enriched regions in which one or both of the signal photon selections are reversed.

$$\text{photon purity} = \frac{N_{Z\gamma}}{N_{data} - N_{background}}. \tag{6.3.4}$$

The correlation between the four regions is considered when calculating the purity, and three signal leakage parameters are taken into account for the case of signal leakage into the CR. The purity in bins of the photon transverse energy is shown in Figure 6.3.12 where the photon purity is up to 94% in the region above 70 GeV. The photon purity results are taken directly from Ref. [111], which is possible because the photon selection was chosen to be exactly the same in the $Z\gamma$ method. In the $Z\gamma$ method, only the $tt\gamma$ background is non-negligible. Therefore, the number of Z + jets background events is determined by subtracting the $tt\gamma$ events from data, and multiplying this number by (1 - purity = 0.06). This number of Z +jets background events per bin is associated with a systematic error of 4%, which is propagated to the $Z\gamma$ uncertainty. Details are presented in Section 6.3.7.

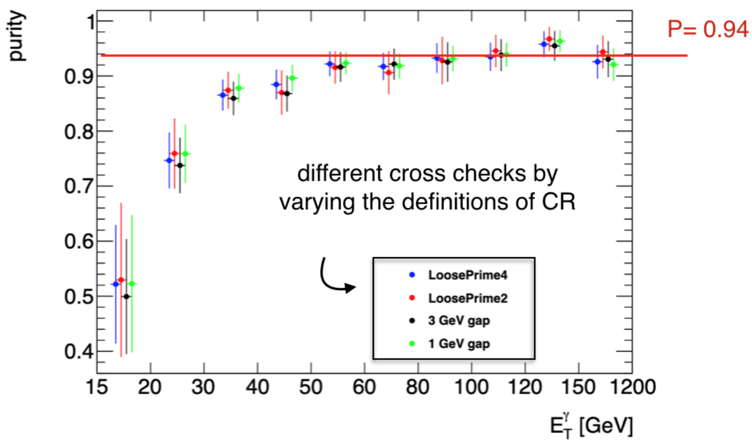

Figure 6.3.12.: Signal purity measured as a function of the photon transverse momentum. Different cross checks from varying the definitions of the ABCD CR are shown in different colour curves. Figure from Ref. [112].

6.3.6. Data/MC in the $Z\gamma$ Control Region

The photon p_{T} distribution measured in $Z\gamma$ events in data is one of the ingredients used in the $Z\gamma$ method. The nominal $Z\gamma$ event samples are produced using Sherpa (2.2.2) at NLO generator with the NNPDF3.0 NNLO PDF set. The $t\bar{t}\gamma$ event samples are produced using MadGraph5_aMC@NLO with the NNPDF23 PDF set at LO. The $t\bar{t}\gamma$ distribution includes the systematic uncertainty, which is calculated by taking a 30% of the $t\bar{t}\gamma$ cross-section [112]. A NLO K-factor of 1.44 is applied on the $t\bar{t}\gamma$ samples [113]. The Z + jets distributions are estimated as described in Section 6.3.5.

Photon p_{T} distributions with the analysis selection criteria applied cumulatively are shown in Figure 6.3.13 (no EW corrections are applied for these figures).

Comparison for $E_{\mathrm{T}}^{\mathrm{miss}}$ in data and simulation with and without EW corrections are shown in Figures 6.3.14. As discussed above, the photon p_{T} is added to the intrinsic $E_{\mathrm{T}}^{\mathrm{miss}}$ of the $Z\gamma$ events. It can be seen that EW corrections on the $Z\gamma$ MC decrease the data/MC differences in the $E_{\mathrm{T}}^{\mathrm{miss}} > 200$ GeV region when full analysis cuts are applied. However the agreement is worse at the Z mass cut level. It appears as if QCD mismodelling affecting

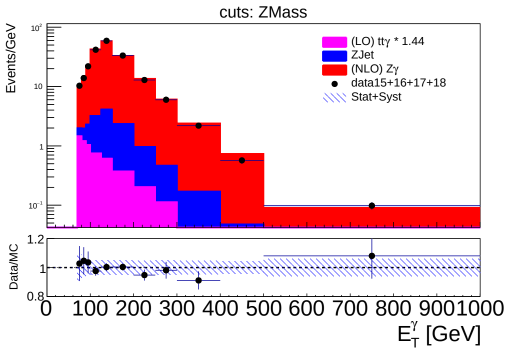

(a)

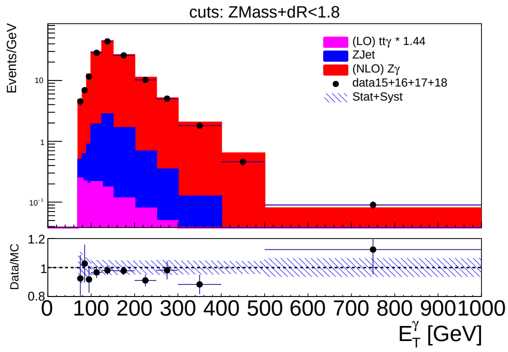

(b)

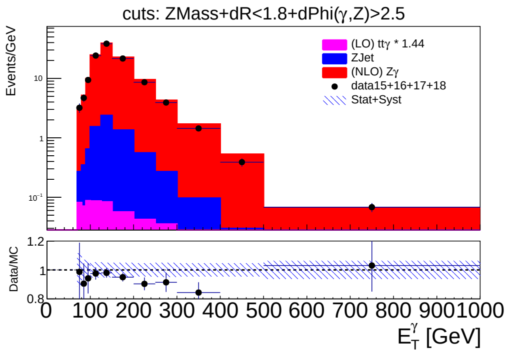

(c)

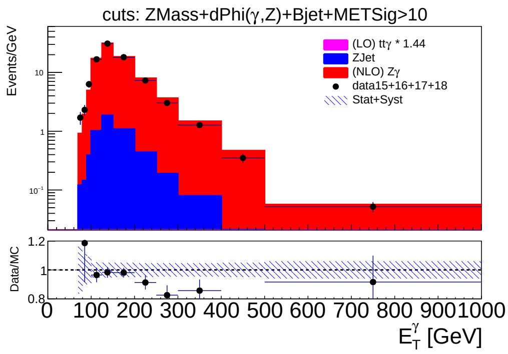

(d)

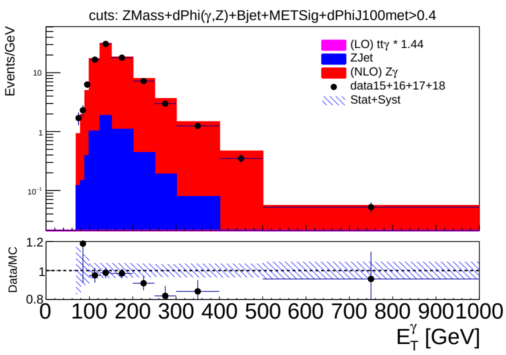

(e)

Figure 6.3.13.: The photon p_{T} distribution as measured in the $Z\gamma$ CR. Data points represent collected data from 2015−2018 and are compared with the predicted Standard Model background contributions in stacked histograms. The $Z\gamma$ process is measured from Sherpa at NLO (without EW corrections). (a) with Z mass window cut applied, (b) with Z mass and ΔR cuts applied, (c) with Z mass, ΔR, and $\Delta\phi$ cuts applied, (d) with Z mass, ΔR, $\Delta\phi$, and b-jet veto cuts applied, (e) with full analysis cuts applied. The Stat+Syst band includes the statistical and systematic uncertainties of both Z + jets and $t\bar{t}\gamma$, and statistical uncertainty from the $Z\gamma$ MC. The HM selections are used here.

the analysis selection efficiencies and EW mismodelling cancel each other for the high $E_{\mathrm{T}}^{\mathrm{miss}}$ range. The discrepancy in the region of 90−120 GeV stays similar w.r.t the $E_{\mathrm{T}}^{\mathrm{miss}}$ without EW corrections.

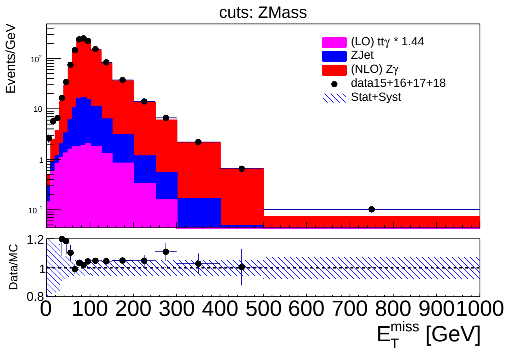

(a)

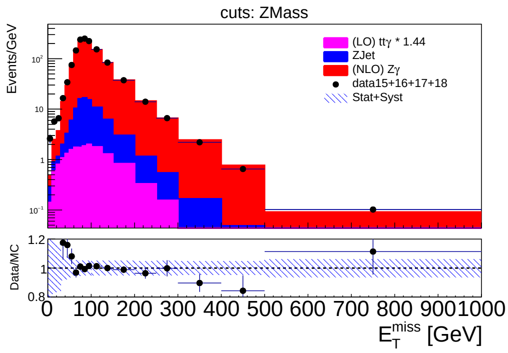

(b)

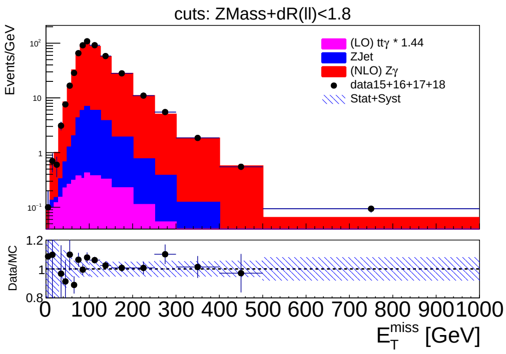

(c)

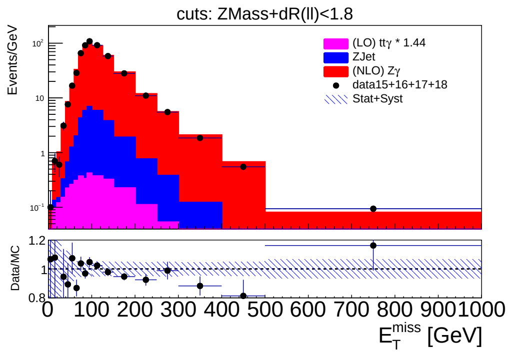

(d)

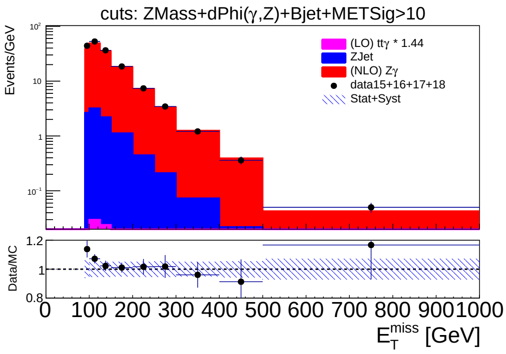

(e)

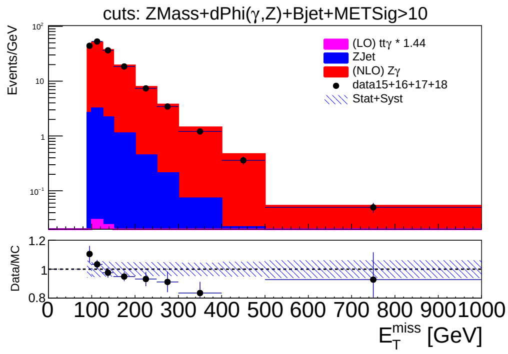

(f)

Figure 6.3.14.: The $E_{\mathrm{T}}^{\mathrm{miss}}$ distribution as measured in the $Z\gamma$ CR. The photon p_{T} is added to the intrinsic $E_{\mathrm{T}}^{\mathrm{miss}}$ of the $Z\gamma$ events. Data points represent collected data from 2015−2018 and are compared with the predicted Standard Model background contributions in stacked histograms. The $Z\gamma$ process is predicted by Sherpa at NLO, with EW corrections (a, c, e) and without EW corrections (b, d, f) applied. (a) and (b) show the distributions with the Z mass window cut applied, (c) and (d) with Z mass, ΔR cuts applied, (e) and (f) with full analysis cuts applied. The Stat+Syst band includes the statistical and systematic uncertainties of both Z + jets and $t\bar{t}\gamma$, and statistical uncertainty from the $Z\gamma$ MC. The LM selections are used here.

Comparison for m_{T} distributions in data and simulation with and without EW corrections are shown in Figure 6.3.15. Because there is an $E_{\mathrm{T}}^{\mathrm{miss}}$ cut of 120 GeV applied in the HM analysis, the region with the worst data/MC agreement from Figure 6.3.14 is cut out, and a better data/MC agreement is seen in this case, especially after full selection cuts are applied.

6.3.7. Systematic Uncertainties on the Zγ Method

Sources of systematic uncertainty taken into account in the $Z\gamma$ method arise from uncertainties in the ratio R (including the difference in R between Sherpa and Matrix), photon reconstruction, closure, truth $E_{\mathrm{T}}^{\mathrm{miss}}$ significance, backgrounds in the $Z\gamma$ CR.

The cross-section ratio R is estimated from Matrix NNLO [59, 65] and it is currently assigned a systematic uncertainty of 2.5% (plus EW uncertainties), which is obtained without applying any cuts beyond the Z Mass requirement. Detailed studies are shown in Section 4.3.1. The following uncertainties are considered:

- Uncertainties due to higher order QCD corrections, δ^{QCD}. These are estimated by varying the renormalisation and factorisation scales (δ^{scale}), by an additional shape-factor (δ^{shape}) and by comparing the NNLO/NLO K-factors of the two processes (δ^{HO}). The quadratic sum of these three components gives the QCD uncertainty, δ_{QCD}.
- Uncertainties due to photon isolation treatment (δ^{iso}).
- Uncertainties on the parton distribution functions (δ^{PDF}).
- Uncertainties due to higher order electroweak corrections (δ^{EWK}).

The total uncertainty on $R(p_{\mathrm{T}})$ is the quadratic sum of these individual uncertainties:

$$\delta R(p_{\mathrm{T}}) = \delta^{\mathrm{HO}} \oplus \delta^{\mathrm{scale}} \oplus \delta^{\mathrm{shape}} \oplus \delta^{\mathrm{iso}} \oplus \delta^{\mathrm{PDF}} \oplus \delta^{\mathrm{EWK}}. \tag{6.3.5}$$

The background uncertainty to the $Z\gamma$ is assigned a conservative number, 4% (94% purity $\times$ 0.04 relative uncertainty for photon $p_{\mathrm{T}} > 70$ GeV). The number is estimated based on a study from the $Z\gamma$ cross-measurement [111]. The estimation from the SM $Z\gamma$ analysis is summarised in Figure 6.3.16 showing the uncertainties on the three signal leakage fractions (blue), event yields in the ABCD regions (pink) and the total (black). The relative total uncertainties on the purity in bins of photon p_{T} are calculated by varying each source ± 1 σ independently and adding the deviations in the nominal purity value in quadrature:

$$\begin{aligned} \sigma_P &= \sqrt{\Sigma \sigma_{P_i}^2}, \\ \sigma_{P_i} &= \mathrm{Max}\left[P(x_i \pm \sigma_{x_i} - P(x_i))\right]. \end{aligned} \tag{6.3.6}$$

The truth $E_{\mathrm{T}}^{\mathrm{miss}}$ significance uncertainty is shown in Figure 6.3.17 (a). The transverse mass distribution is produced using the nominal truth $E_{\mathrm{T}}^{\mathrm{miss}}$ significance cut and a cut that is varied by 0.5, and the largest difference w.r.t the nominal distribution (truth $E_{\mathrm{T}}^{\mathrm{miss}}$ significance cut applied at 9 as the nominal in HM search) is taken as the truth $E_{\mathrm{T}}^{\mathrm{miss}}$ significance uncertainty. The truth $E_{\mathrm{T}}^{\mathrm{miss}}$ significance uncertainty is correlated with the closure uncertainty as the closure result depends on the choice of the truth $E_{\mathrm{T}}^{\mathrm{miss}}$ significance. Therefore, the uncertainty is determined by the largest one out of the two sources. The

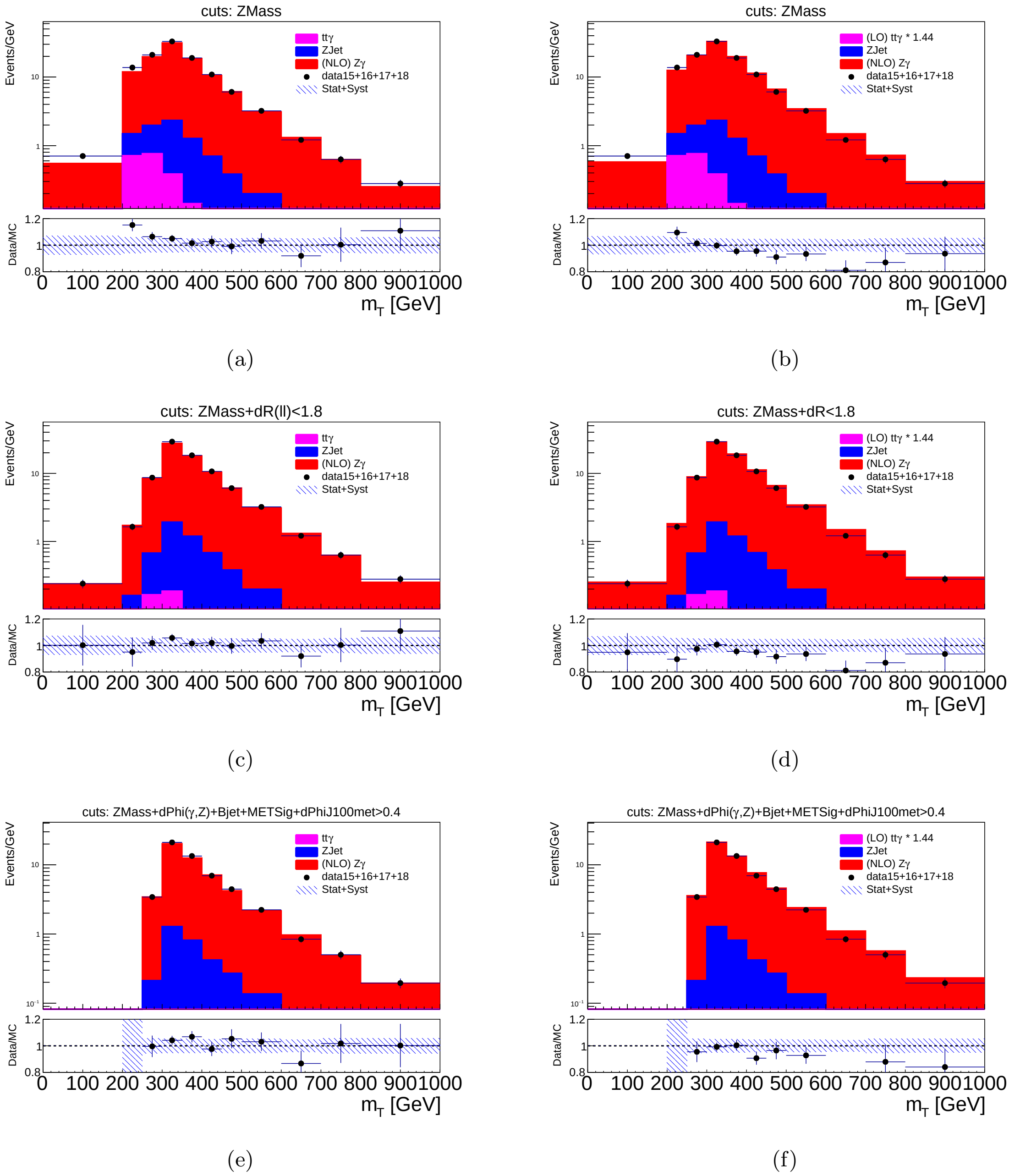

Figure 6.3.15.: The m_{T} distribution as measured in the $Z\gamma$ CR. The photon p_{T} is added to the intrinsic $E_{\mathrm{T}}^{\mathrm{miss}}$ of the $Z\gamma$ events. Data points represent collected data from 2015−2018 and are compared with the predicted Standard Model background contributions in stacked histograms. The $Z\gamma$ process is predicted by SHERPA at NLO, with EW corrections (a, c, e) and without EW corrections (b, d, f) applied. (a) and (b) show the distributions with the Z mass window cut applied, (c) and (d) with Z mass, ΔR cuts applied, (e) and (f) with full analysis cuts applied. The Stat+Syst band includes the statistical and systematic uncertainties of both Z + jets and $t\bar{t}\gamma$, and statistical uncertainty from the $Z\gamma$ MC. The HM selections are used here, including $E_{\mathrm{T}}^{\mathrm{miss}} > 120$ GeV.

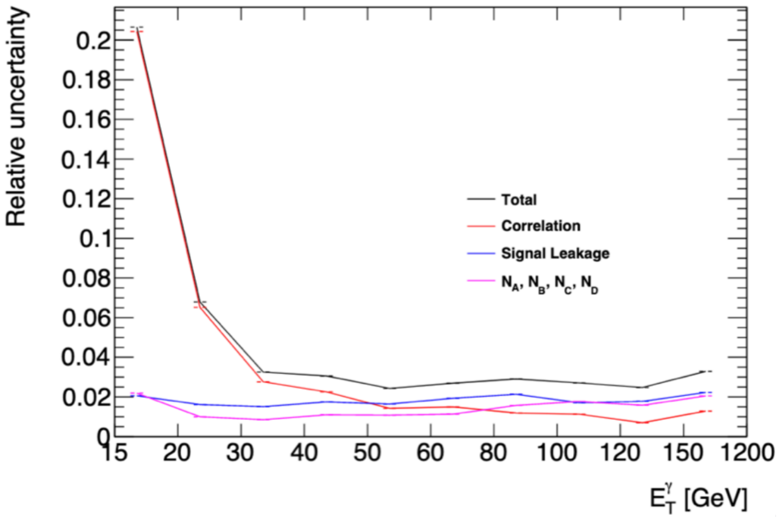

Figure 6.3.16.: Relative uncertainties on the purity as a function of photon p_{T}. Figure from Ref. [112].

transverse mass distribution with the photon efficiency varied up and down based on CP recommendations for photons is shown in Figure 6.3.17 (b), and the largest difference with respect to the nominal is taken.

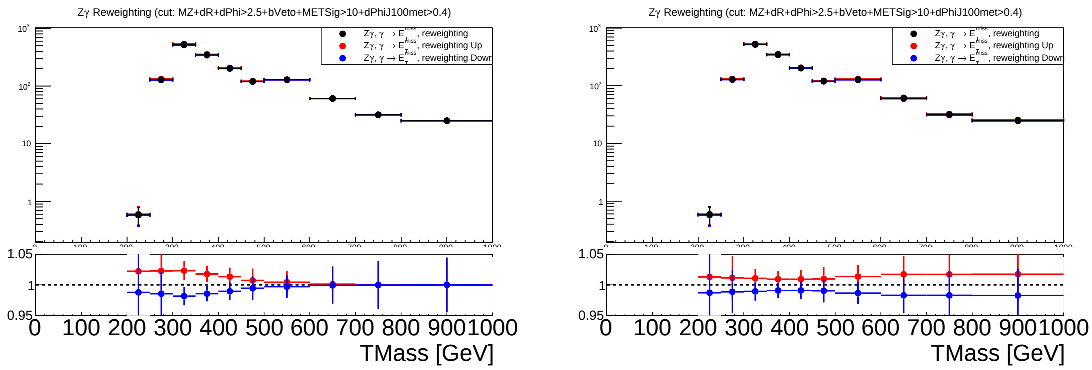

(a) (b)

Figure 6.3.17.: (a) The m_{T} distribution with truth $E_{\mathrm{T}}^{\mathrm{miss}}$ significance cut in the R applied at 9.5 in red, at 8.5 in blue, at 9 (the nominal cut) in black. (b) The m_{T} distribution with the photon efficiency varied up is in red, with the down variation is in blue, and the nominal one is in black.

The uncertainty based on the difference between Sherpa and Matrix (detailed in Section 4.2) is calculated by taking the differences of the ZZ prediction using the Sherpa R and using the Matrix R.

The total uncertainty on the $Z\gamma$ method is the sum of all sources in quadrature. The results for $E_{\mathrm{T}}^{\mathrm{miss}}$ and m_{T} are shown with EW corrections in Figure 6.3.18 and Figure 6.3.19, respectively. These uncertainties are compared to the total experimental and theory uncertainties of the ZZ MC estimate (yields and shape), and they are of a similar magnitude for the medium m_{T} range. In most bins, the data statistical uncertainty is the dominant uncertainty (about 3% to 16% in total). To reach 10% statistic uncertainty for the largest uncertainty bin (compared to 16% now), the luminosity needs to be increased to about 2.5 times the luminosity of Run-2.

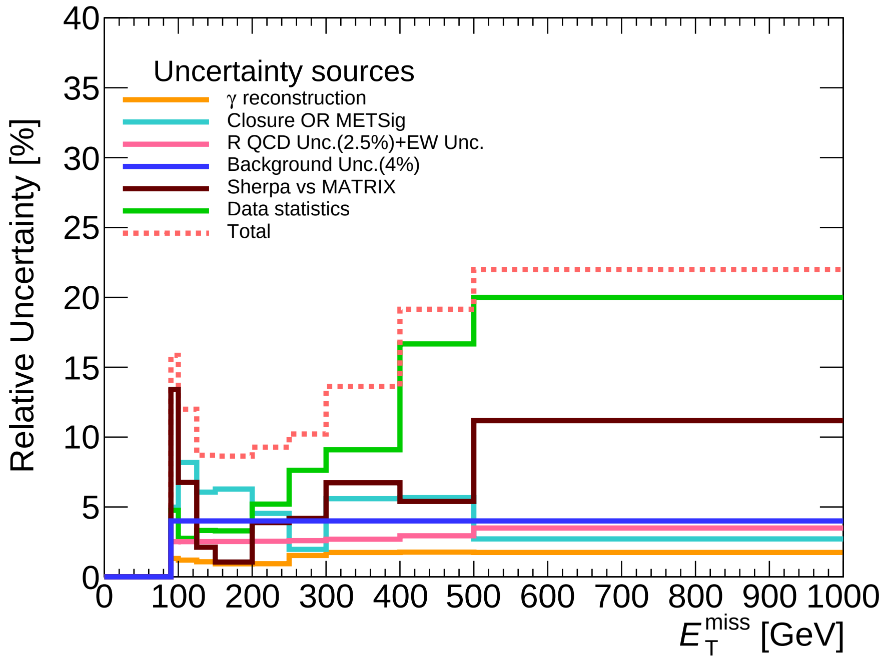

Figure 6.3.18.: The total uncertainty in bins of the $E_{\mathrm{T}}^{\mathrm{miss}}$ with EW corrections. The theoretical uncertainty on the ratio is obtained without applying any cuts beyond the Z mass requirement. New studies indicate that theoretical uncertainty is underestimated for the case where more analysis cuts are applied (detailed in Section 4.3).

However, the statistical uncertainty depends on the chosen binning. Table 6.3.4 shows the relative data statistical uncertainty using the binning chosen for the presented estimate, which is coarser than the HM analysis binning. This choice was made to keep the statistical uncertainties under control, and still allows to validate the shape.

6.3.8. Resulting ZZ Prediction and Comparison

The nominal data-driven ZZ estimate is performed using the Matrix R. Figure 6.3.20 shows the comparison of this estimate with the Sherpa ZZ simulation, which is used in the analysis currently with EW corrections/uncertainties. Figure 6.3.21 shows the results of the data-driven ZZ estimate using Matrix R without EW corrections applied on R or the Sherpa ZZ simulation. It also shows the results using the Sherpa R with and w/o EW corrections. The transverse mass distributions agree with the MC prediction within the total uncertainties. The biggest deviation is in the bins of 300−400 GeV and the corresponding pull is ∼2.29 σ. This good agreement constitutes an important cross-check of the MC-based ZZ estimate currently used in the heavy Higgs search, especially the shape of the distribution.

Comparing the data-driven estimate with Matrix R in bins of $E_{\mathrm{T}}^{\mathrm{miss}}$ is shown in Figure 6.3.22. The differences between the distributions are covered by the systematics except in the low $E_{\mathrm{T}}^{\mathrm{miss}}$ regions. If no EW corrections are applied on the Matrix R or the Sherpa ZZ simulation, the ratio between the data-driven and the MC estimate drops more

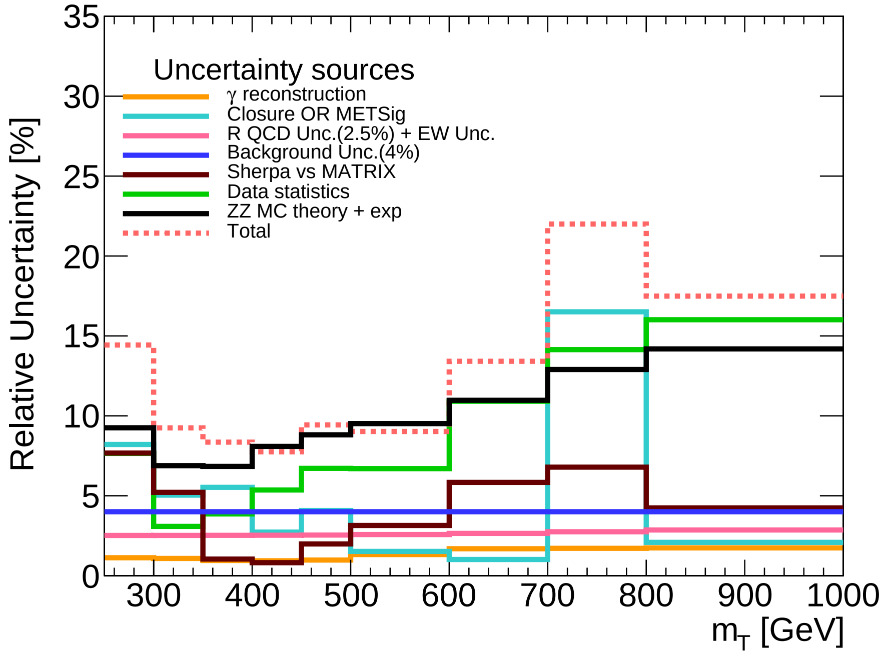

Figure 6.3.19.: The total uncertainty in bins of the transverse mass with EW corrections. The theoretical uncertainty on the ratio is obtained without applying any cuts beyond the Z mass requirement. New studies indicate that theoretical uncertainty is underestimated for the case where more analysis cuts are applied (detailed in Section 4.3). The total experimental and theoretical uncertainty for MC ZZ production is shown in black (including shape and yield uncertainties).

m_T range [GeV]	relative uncertainty [%]	N_{events}
250 - 300	7.67	171
300 - 350	3.08	1054
350 - 400	3.8	670
400 - 450	5.3	348
450 - 500	6.71	222
500 - 600	6.69	223
600 - 700	10.9	84
700 - 800	14.1	50
800 - 1000	16	39

Table 6.3.4.: Data statistical uncertainty in the $Z\gamma$ CR using the binning chosen for the presented estimate.

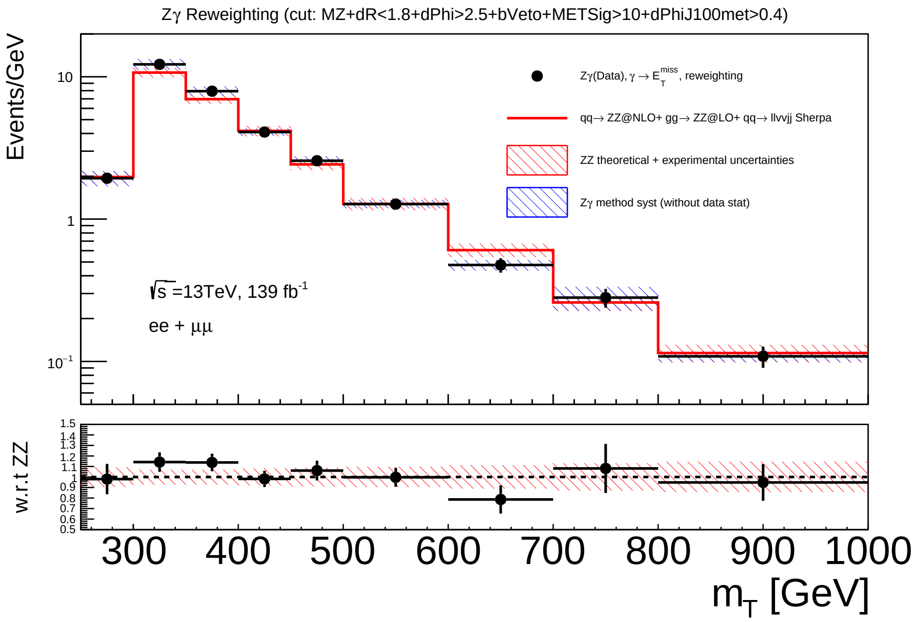

Figure 6.3.20.: Comparison of the data-driven estimate with Matrix R and ZZ MC prediction in the m_{T} distribution for electron and muon channel combined with EW corrections. The uncertainty in the red band shows the theoretical and experimental uncertainties on the ZZ MC-based estimate (including shape and yield uncertainties). The black error bar in the top panel include all systematic uncertainties except the data statistics. The blue band includes all the uncertainties sources from the $Z\gamma$ method except data statistics. The lower panel shows the ratio of the data-driven method to the ZZ MC prediction, the error bars in black show the statistical and systematic uncertainties on the data-driven method, and the band shows the systematic uncertainty on the ZZ MC prediction.

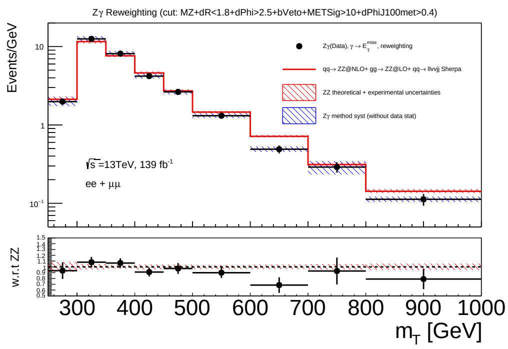

(a)

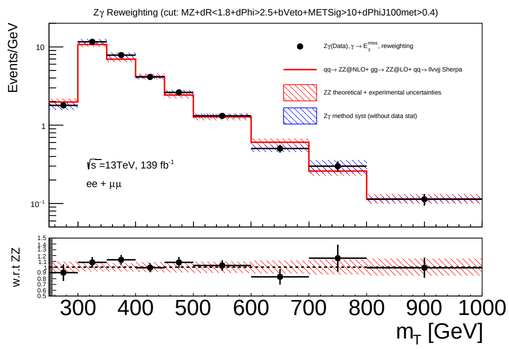

(b)

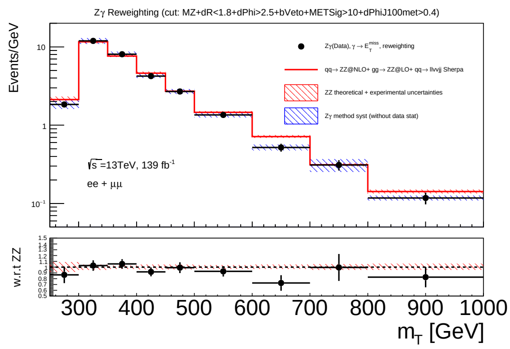

(c)

Figure 6.3.21.: Comparison of the data-driven estimate with MATRIX R and ZZ MC prediction in the m_{T} distribution (a) without EW corrections for electron and muon channel combined. Comparison of the data-driven estimate with SHERPA R and ZZ MC prediction in the m_{T} distribution (b) with EW corrections, (c) without EW corrections for electron and muon channel combined. The uncertainty in the red band shows the theoretical and experimental uncertainties on the ZZ MC-based estimate (including shape and yield uncertainties). The black error bar in the top panel include all systematic uncertainties except the data statistics. The blue band includes all the uncertainties sources from the $Z\gamma$ method except data statistics. The lower panel shows the ratio of the data-driven method to the ZZ MC prediction, the error bars in black show the statistical and systematic uncertainties on the data-driven method, and the band shows the systematic uncertainty on the ZZ MC prediction.

strongly with higher $E_{\mathrm{T}}^{\mathrm{miss}}$ as shown in Figure 6.3.23 (a). This is seen in the $Z\gamma$ data/MC comparison in Figure 6.3.14 as well. Likewise, the data-driven estimates with SHERPA R with EW corrections and without EW corrections are shown in Figure 6.3.23 (b) and (c), respectively. The data-driven background estimate using the MATRIX R is higher than the MC prediction in the low $E_{\mathrm{T}}^{\mathrm{miss}}$ region. This arises partially because MATRIX's truth production ratio R is higher than SHERPA as shown in Figure 6.3.8.

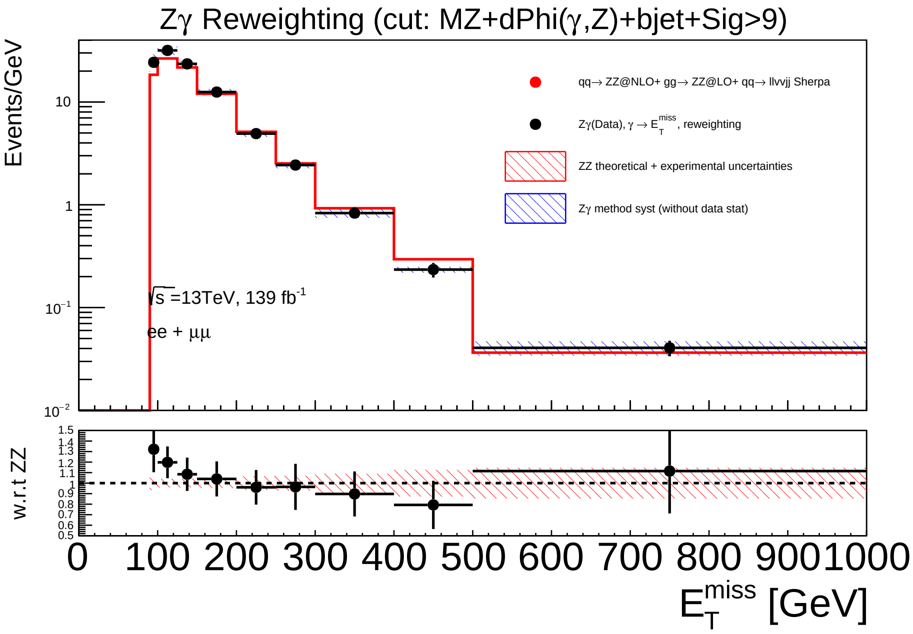

Figure 6.3.22.: Comparison of the data-driven estimate with MATRIX R and ZZ MC prediction in the $E_{\mathrm{T}}^{\mathrm{miss}}$ distribution for electron and muon channel combined with EW corrections. The uncertainty in the red band shows the theoretical and experimental uncertainties on the ZZ MC-based estimate (including shape and yield uncertainties). The blue band includes all the uncertainties sources from the $Z\gamma$ method except data statistics. The lower panel shows the ratio of the data-driven method to the ZZ MC prediction ratios, the error bars in black show the statistical and systematic uncertainties on the data-driven method, and the band shows the systematic uncertainty on the ZZ MC prediction.

As stated above, EW corrections improve the agreement in the tails between the MC and the data-driven estimate. Figure 6.3.24 shows the ratio between the data-driven and the MC-based estimate is flatter if EW corrections are applied. This seems to indicate that applying EW corrections is a better way to go when using the MC-based estimate.

The total uncertainty (yields and shape) in the MC ZZ prediction with EW corrections is similar to the total uncertainty in the $Z\gamma$ method's prediction in the chosen binning. However, as described in Section 6.2, in the $H \to ZZ \to \ell^+\ell^-\nu\bar{\nu}$ search, only the ZZ background shape taken is from SHERPA, while the normalisation is fitted, thus reducing the MC-driven systematic uncertainties from what is shown in this section. Subsection 6.3.7 shows that the largest source of uncertainties in the $Z\gamma$ method comes from the data statistic. The statistical uncertainties arise from random fluctuations described by a Poisson distribution, which might be preferable over other systematic uncertainties.

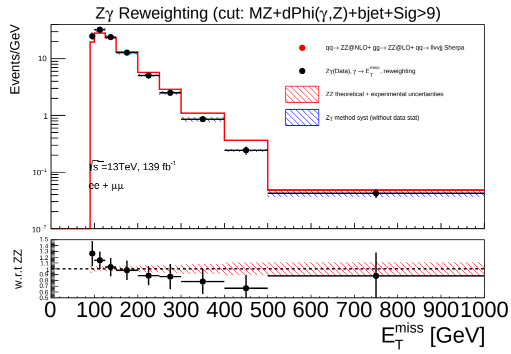

(a)

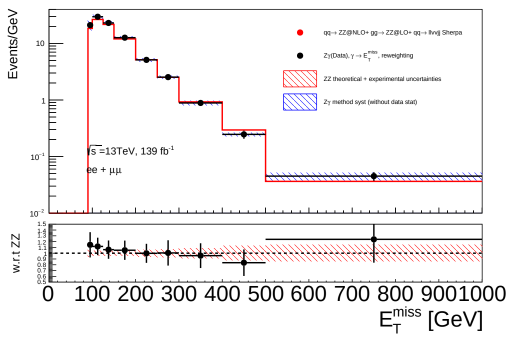

(b)

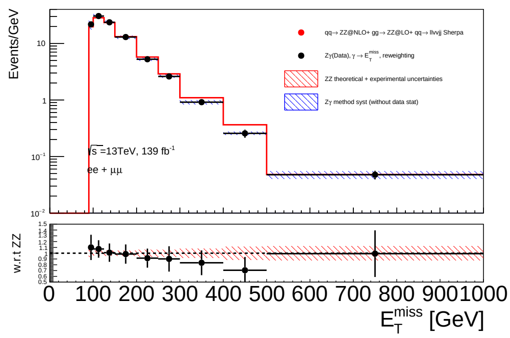

(c)

Figure 6.3.23.: Comparison of the data-driven estimate with Matrix R and ZZ MC prediction in the $E_{\mathrm{T}}^{\mathrm{miss}}$ distribution (a) without EW corrections for electron and muon channel combined. Comparison of the data-driven estimate with Sherpa R and ZZ MC prediction in the $E_{\mathrm{T}}^{\mathrm{miss}}$ distribution (b) with EW corrections and (c) without EW corrections for electron and muon channel combined. The uncertainty in the red band shows the theoretical and experimental uncertainties on the ZZ MC-based estimate (including shape and yield uncertainties). The blue band includes all the uncertainties sources from the $Z\gamma$ method except data statistics. The lower panel shows the ratio of the data-driven method to the ZZ MC prediction ratios, the error bars in black show the statistical and systematic uncertainties on the data-driven method, and the band shows the systematic uncertainty on the ZZ MC prediction.

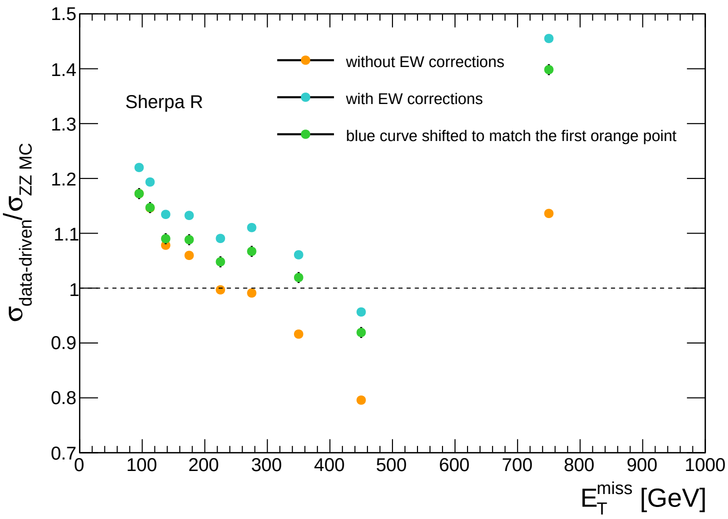

Figure 6.3.24.: The ratio between data-driven estimate and the MC ZZ estimate. The ratio with EW corrections is in cyan, without EW corrections is in orange. For illustration, the ratio with EW corrections is shifted down to match the ratio without EW corrections in the first point, this corresponds to the green points.

6.3.9. Possible Improvements for the Future

The statistical uncertainties on the $Z\gamma$ data sample are still fairly large with the current luminosity. However, more data will help reduce these. One thing to keep in mind is that the statistical uncertainty is dependent on the binning.

The m_{T} distribution estimated with the $Z\gamma$ method agrees quite well with the MC prediction. The largest discrepancy can be found in the bins of 300-400 GeV, and the combined pull of these two bins is ~ 2.29. As a cross-check, it would be interesting to see the results from the $ZZ \to \ell^+\ell^-\ell'^+\ell'^-$ CR where two leptons are treated as the $E_{\mathrm{T}}^{\mathrm{miss}}$. This CR is closer to the $ZZ \to \ell^+\ell^-\nu\bar{\nu}$ process than the $Z\gamma$ CR, but it runs out of statistics at $E_{\mathrm{T}}^{\mathrm{miss}}$ larger than $\mathcal{O}(100\text{ GeV})$, so a combination of the two methods would be beneficial.

It seems like EW corrections allow for a better agreement of the MC shape with the data-driven estimate, but they might be over-correcting in normalization (this is already visible in the $Z\gamma$ control region). Further investigation on the EW corrections and a differential cross-section measurement of the cut variables and other observables in the $Z\gamma$ process, to also better understand the QCD modelling will be helpful. This should also help improve the theory calculation as well.

Further work is needed in terms of the ratio uncertainty when selection cuts are applied, and in terms of the uncertainty correlation between the ZZ and $Z\gamma$ as described in Section 4.3.2.

In the current $Z\gamma$ method, the production ratio of the ZZ and $Z\gamma$ processes is measured from the truth-level information. Although the cuts made at the truth-level are kept as close as possible to the cuts at the reconstruction-level, the correspondence between them is particularly concerning for the truth $E_{\mathrm{T}}^{\mathrm{miss}}$ significance. Figure 6.3.25 presents the measured cross-section as a function of m_{T} in events predicted by the MC, the $Z\gamma$ method prediction reweighted by Sherpa ratio in bins of $p_{\mathrm{T}}\ \gamma$, and the prediction reweighted by the reconstruction ratio of the ZZ and $Z\gamma$ events in bins of m_{T}. The predictions are similar to each other, which is reassuring as it confirms the extrapolation of the phase space. One of the advantages of using reweighing with reconstruction-level distributions is, that it could help with more complicated signal regions and discriminants, such as a BDT. However, one would need to evaluate full experimental uncertainties on the reconstruction ratio and need a strategy for theory uncertainties.

Another strategy is to provide the $Z\gamma$ control region as an input into a simultaneous signal region and control region fit, which helps reduce systematic uncertainty with nuisance parameters constrained by the data. One should consider the extrapolation uncertainty from the $Z\gamma$ phase space to the signal phase space.

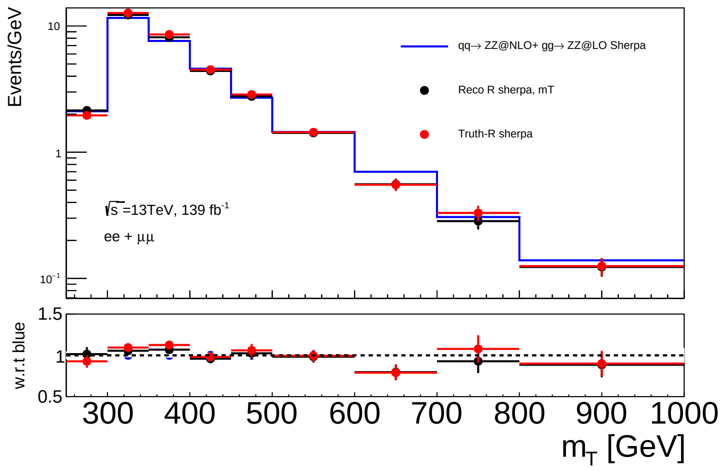

Figure 6.3.25.: Comparison of finalized ZZ prediction as a function of m_{T} without EW corrections. The ZZ MC prediction is shown in blue, the standard $Z\gamma$ method with the truth ratio applied in bins of γ p_{T} is shown in red, and the prediction using a ratio based on reconstruction-level m_{T} distributions is shown in black. The black and red curves include the MC statistical uncertainties only.

6.4. Data/MC

This section shows the comparison of the pre-fit MC predictions to data in the $ZZ \to \ell^+\ell^-\nu\bar{\nu}$ signal region. The background estimation and the corresponding uncertainties are described in Section 6.2. The WZ, Z + jets, and non-resonant backgrounds have yields measured by data-driven methods. The ZZ background ($qqZZ$, $ggZZ$, and ZZ (EW)) is predicted purely from MC in the pre-fit case. The $Z\gamma$ method is not used mainly because the statistical uncertainties on the $Z\gamma$ are still fairly large, but it is important as a cross-check. The expected background events and data are given in Table 6.4.1 for the ggF and VBF productions.

The pre-fit m_{T} distributions in the ggF category after the final selection are shown in Figure 6.4.1 for ee and $\mu\mu$ channels. The pre-fit m_{T} distributions in the VBF category after the final selection are shown in Figure 6.4.2 for ee and $\mu\mu$ channels.

6.4.1. Another View of the Signal Region

The comparison of the data-driven ZZ estimate from $Z\gamma$ and the data after subtracting other backgrounds (WZ, Z + jets, $e\mu$, and Others) is shown in Figure 6.4.3 together with

Process	ggF-enriched categories		VBF-enriched categories	
	e^+e^-*channel*	$\mu^+\mu^-$*channel*	e^+e^-*channel*	$\mu^+\mu^-$*channel*
$q\bar{q} \rightarrow ZZ$	671 $\pm$ 6.1	768 $\pm$ 33	2.7 $\pm$ 0.2	3.2 $\pm$ 0.2
$gg \rightarrow ZZ$	81 $\pm$ 21	90.41 $\pm$ 24	0.9 $\pm$ 1.5	0.8 $\pm$ 1.08
ZZ (EW)	7 $\pm$ 0.2	6.99 $\pm$ 0.20	0.8 $\pm$ 0.2	0.9 $\pm$ 0.2
WZ	413 $\pm$ 23	454.44 $\pm$ 15	2.5 $\pm$ 0.9	2.6 $\pm$ 4.7
Z + jets	40 $\pm$ 9	55.61 $\pm$ 14	0.2 $\pm$ 0.2	0.3 $\pm$ 0.3
non-resonant-$\ell\ell$	66 $\pm$ 6	77 $\pm$ 7	0.3 $\pm$ 0.2	0.3 $\pm$ 0.2
Others	5.88 $\pm$ 0.03	6 $\pm$ 0.08	0.08 $\pm$ 0.04	0.04 $\pm$ 0.02
Data	1323	1542	8	10
Total backgrounds	1284	1459	7	8

Table 6.4.1.: The number of predicted (pre-fit) background and data events (corresponding to 139 fb^{-1}) in ee and $\mu\mu$ signal regions after full ggF and VBF event selections. The errors represent the systematic uncertainty [114].

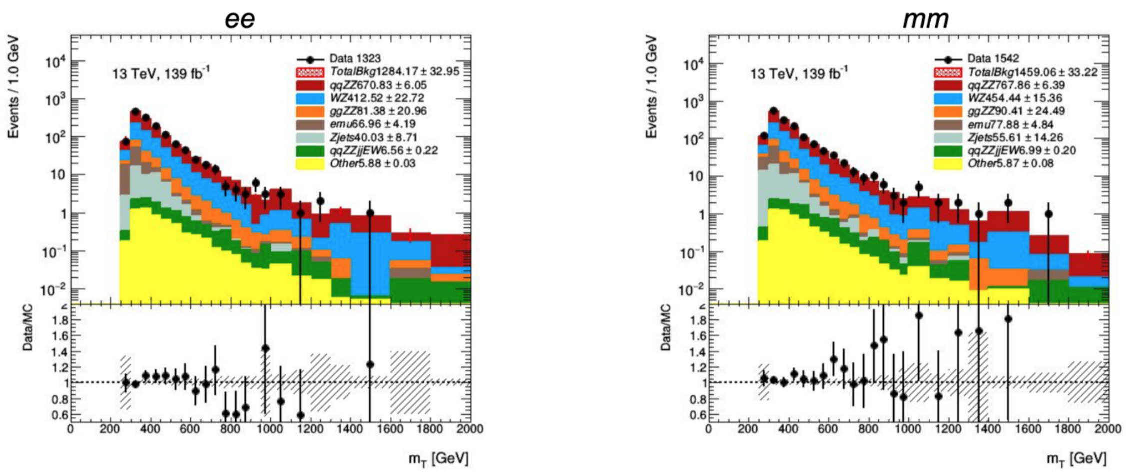

Figure 6.4.1.: Pre-fit m_{T} distributions in the ggF SR. EW corrections are applied to $qqZZ$. The uncertainty includes stat+syst. The small background contribution from VVV and ttV is categorized into Others. The last bin includes overflow [114].

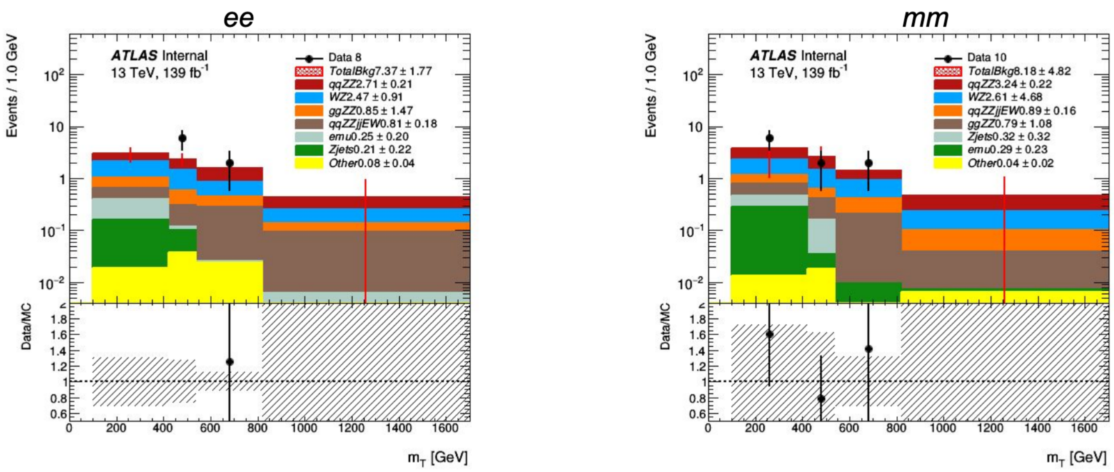

Figure 6.4.2.: Pre-fit m_{T} distributions in the VBF SR. EW corrections applied to $qqZZ$. The uncertainty includes stat+syst. The small background contribution from VVV and ttV is categorized into Others. The last bin includes overflow [114].

the ZZ MC estimate. The m_{T} distributions are made in the inclusive category (ggF and VBF) with combined ee and $\mu\mu$ channels. EW corrections are applied to the $qqZZ$ MC and the $Z\gamma$ method in the ratio. There is good agreement between all distributions above m_{T} $\sim$400 GeV. Interestingly, both the data and the data-driven ZZ estimate favour slightly higher event yields at lower m_{T}.

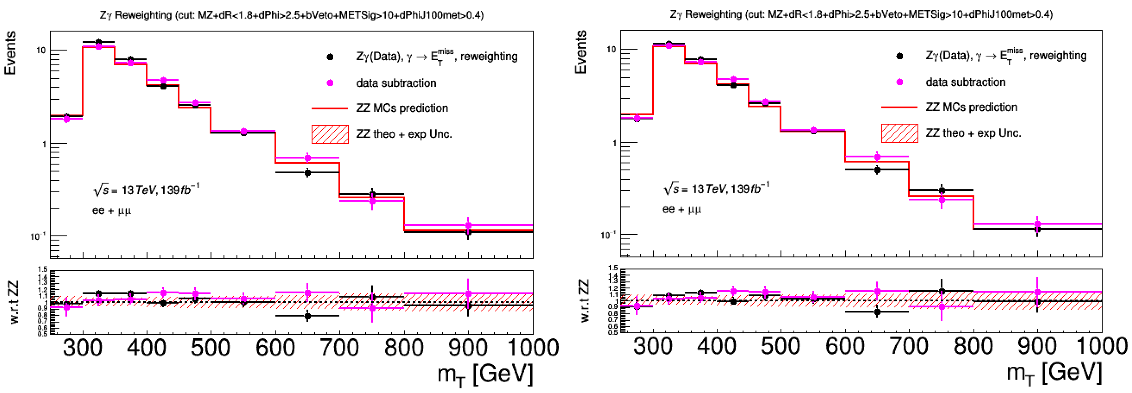

(a) (b)

Figure 6.4.3.: Comparison between the data-driven $Z\gamma$ method in black and the data after subtraction (all the background predictions are subtracted from data except the ZZ MCs) in pink. The ZZ MC prediction is shown in red. The lower panel shows the ratio of each distribution with respect to the ZZ MC prediction. The red band in the ratio panel shows theoretical and experimental uncertainties in the ZZ MC. The black bars in the ratio panel indicate the statistical and systematic uncertainties from the $Z\gamma$ method. (a) The ZZ prediction is estimated using the $Z\gamma$ method with the MATRIX ratio of the ZZ and $Z\gamma$ cross-sections. (b) The ZZ prediction is estimated using the $Z\gamma$ method with the SHERPA ratio of the ZZ and $Z\gamma$ cross-sections.

6.5. Limit Setting

As there is no significant excess seen in the data compared to the background expectation as shown in Figure 6.4.1, limits on the $\sigma \times$ BR of the S $\rightarrow ZZ$ process will be set (S can be interpreted as the heavy Higgs or the graviton). The method for the limit calculation is commonly used in the CMS and ATLAS experiments. A global binned likelihood function [115] is built as:

$$\mathcal{L}(n|\boldsymbol{\mu},\boldsymbol{\theta}) = \prod_{i \in bins} \mathcal{P}(n_i|\boldsymbol{\mu} \cdot S_i(\boldsymbol{\theta}) + B_i(\boldsymbol{\theta})), \tag{6.5.1}$$

where $\mathcal{P}$ is the Poisson distribution. The symbol n_i is the number of observed events, μ is the 'signal strength' parameter. S_i and B_i are the number of predicted signal events and the number of predicted background events in bin i, respectively. The signal and background predictions depend on parameters: parameters of interest (POI) corresponding to the actual quantities that are to be estimated, such as signal strength (μ), and a set of 'nuisance' parameters (NPs) representing potential sources of systematic biases collectively denoted with $\boldsymbol{\theta}$.

The profile likelihood ratio is used to test a hypothesized value of μ. The profile likelihood ratio is defined as:

$$\lambda(\mu) = \frac{\mathcal{L}(\mu,\hat{\hat{\boldsymbol{\theta}}})}{\mathcal{L}(\hat{\mu},\hat{\boldsymbol{\theta}})}, \text{where } 0 \leq \hat{\mu} \leq \mu, \tag{6.5.2}$$

where $\hat{\hat{\boldsymbol{\theta}}}$ is the value of θ maximizing $\mathcal{L}$ for the assumed μ. The parameters $\hat{\mu}$ and $\hat{\theta}$ are the parameters under which the likelihood reaches its global maximum.

A test statistic is defined based on the profile likelihood ratio to compare the compatibility of the data with the background-only and background-plus-signal hypotheses. The data refers to the actual experimental observation or pseudo-data (toys) used to construct sampling distributions. The signal strength $\mu = 0$ corresponds to the background-only hypothesis. This test statistic extracts the information on the signal strength from fitting to the data. In large statistics data samples, the distribution of the test statistic is known as a χ^2 distribution according to Wilks' theorem.

The p-value, p_μ, is defined to quantify the level of disagreement of the data with a particular signal strength hypothesis:

$$p_\mu = \int_{q_\mu^{obs}}^{\infty} f(q_\mu|\mu) dq_\mu, \tag{6.5.3}$$

where q_μ^{obs} is the value of the test statistic observed in data, and $f(q_\mu|\mu)$ is the probability distribution function of q_μ for the given signal strength hypothesis.

The modified frequentist method, CL_s, inspired by the Neyman–Pearson lemma is defined as:

$$CL_s(\mu) = \frac{CL_{s+b}}{CL_b}, \tag{6.5.4}$$

where CL_b is calculated by $\int_{q_\mu^{obs}}^{\infty}$ f$(q_\mu|\mu$=0$)dq_\mu$ in the background-only hypothesis, and CL_{s+b} is calculated by $\int_{q_\mu^{obs}}^{\infty}$ f$(q_\mu|\mu)dq_\mu$. The corresponding μ is excluded if CL_s is less than 5%.

Expected limits will be compared with the results obtained from the fit to the real data. By using the Asimov (pseudo-data) representative data set instead, one can easily derive the median expected limits under a given background-only hypothesis and $\pm 1\sigma$ (68%) and $\pm 2\sigma$ (95%) error bands.

Upon computing the quantity q_μ = -2ln$\lambda(\mu)$ for $\mu = 0$ (null hypothesis) given the actually observed data, a p-value can be determined and then translated into a significance level [3].

The original likelihood is modified to have two different components to deal with nuisance parameters:

$$\mathcal{L}(\mu,\boldsymbol{\theta}) = \mathcal{L}_\mu(\mu,\boldsymbol{\theta})\mathcal{L}_\theta(\tilde{\boldsymbol{\theta}},\boldsymbol{\theta}). \tag{6.5.5}$$

For a fixed value of μ, the likelihood is maximized with respect to the nuisance parameters $\boldsymbol{\theta}$. The $\mathcal{L}_\theta(\tilde{\theta},\theta)$ is constructed from a probability density function, pdf, $\rho(\boldsymbol{\theta})$ and some external measurements, $\tilde{\boldsymbol{\theta}}$:

$$\mathcal{L}_\theta(\tilde{\boldsymbol{\theta}},\boldsymbol{\theta}) = \prod_j \rho_j(\theta|\tilde{\theta}). \tag{6.5.6}$$

The product, $\prod_j$ runs over all sources of the systematic uncertainties. The systematic error pdfs $\rho(\theta|\tilde{\theta})$ reflect the degree of belief on what the true value of θ might be. One can turn the probability around with a prior, $\pi_\theta(\theta)$, as given by Bayes' theorem to compute the posterior $(\rho(\theta|\tilde{\theta}))$:

$$\rho(\theta|\tilde{\theta}) \sim \rho(\tilde{\theta}|\theta) \cdot \pi_\theta(\theta), \tag{6.5.7}$$

where $\rho(\tilde{\theta}|\theta)$ represents the probability density function of the measurements θ given a true θ, and it is usually assumed to be Gaussian:

$$\rho_i(\tilde{\theta}|\theta) = \frac{1}{\sqrt{2\pi\sigma_i^2}} exp\left[-\frac{(\tilde{\theta}-\theta)^2}{2\sigma_i^2}\right]. \tag{6.5.8}$$

Each measurement is given a Gaussian probability that is centred on θ, which is the true value with a width σ_i, and then the multiple measurements are multiplied together into the Likelihood as shown in Eq. 6.5.6. Using this approach, the initial estimate $\tilde{\theta}$ can be used to constrain the likelihood of the main parameter of interest. The prior to the nuisance probability density function is chosen to be flat. The systematic uncertainties on NPs

[3]The p-value can be computed as p = $\int_{q^{obs}}^{+\infty}$ f(q|μ=0)dq. A significance is defined as Z_0=$\phi(x)^{-1}(1-p_0)$ where ϕ is the distribution of the test hypothesis. In case the search is performed without knowing the position of the peak, the formula above gives only a *local p-value* for a given signal hypothesis. The *global p-value* quantifies the probability that a background fluctuation at any mass value gives a value of the test statistic greater than the observed one. A signal with a significance Z of at least 3 (3σ level) is claimed as the *evidence*, which corresponds to a p-value of 1.35×10^{-3} or less. One can claim the *observation* when significance exceeds 5 (5σ level corresponds to the p-value = 2.9×10^{-7}).

affecting the total signal or background are called normalization factors (NFs), and those affecting the corresponding *pdf* are called shape uncertainties. Their respective systematics act as constrained NPs in the fit using Gaussian functions. The limited number of MC events are considered as independent uncertainties (MC stat.) in each bin.

The profile likelihood fit can change the background prediction when the best-fit θ values are different from θ_0. It can reduce the uncertainty on backgrounds through constraints on NPs and correlations between NPs.

The modelling of the m_{T} distribution for signal is based on templates derived from fully-simulated events as given in Section 4.2. Figure 6.5.1 shows the m_{T} distributions of all ggF and VBF signals. The simulated signal events are used to determine the signal acceptance including the respective theoretical and experimental uncertainties as well. Contributions from background sources including systematic uncertainties are described in Section 6.4. The ZZ normalization factor is obtained in the fit, in order to avoid depending on the theory prediction and to reduce systematic uncertainties for the ZZ yields. Three parameters of interest (signal strength of ggF and VBF and the ZZ normalisation factor) are used in the fit.

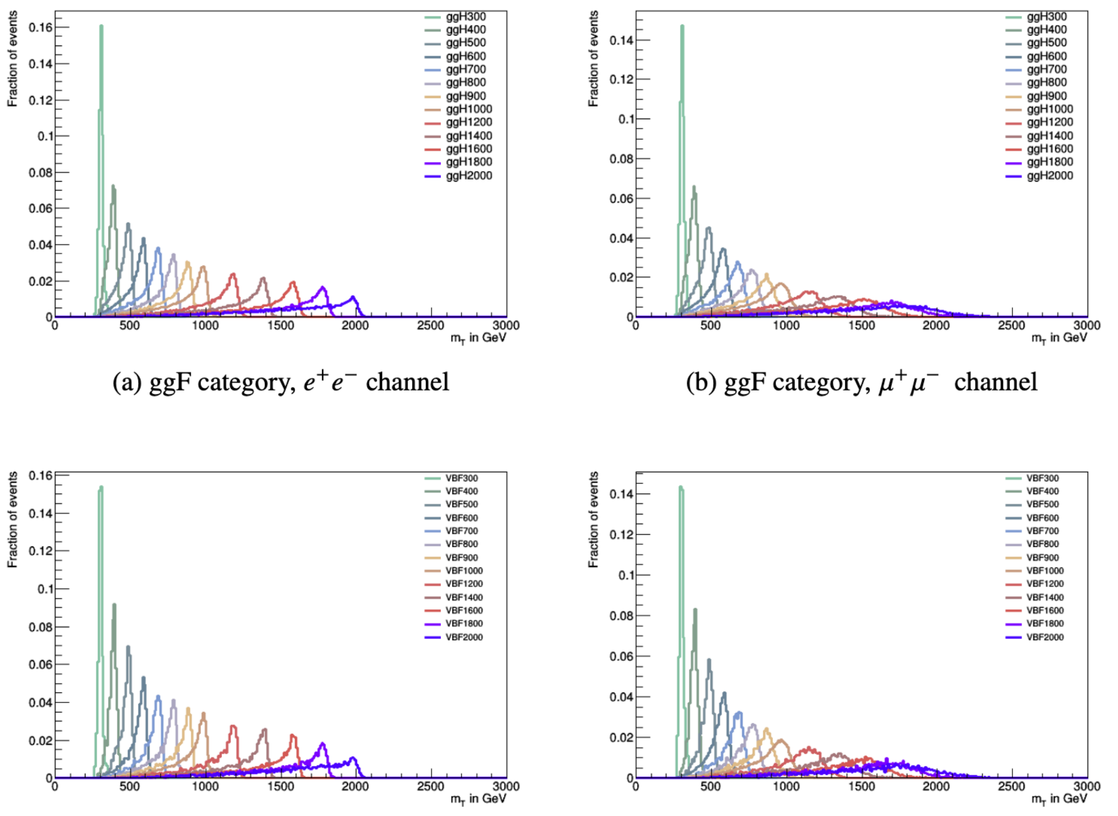

(a) ggF category, e^+e^- channel

(b) ggF category, $\mu^+\mu^-$ channel

(c) VBF category, e^+e^- channel

(d) VBF category, $\mu^+\mu^-$ channel

Figure 6.5.1.: m_{T} distributions from the NWA signal samples in the ggF (top) and VBF SR (bottom) for ee and $\mu\mu$ channels [114].

The post-fit expected and observed numbers of events and their statistical and systematic uncertainties are presented in Table 6.5.1 for both ggF and VBF categories.

Figure 6.5.2 shows the post-fit m_{T} distributions in the ggF SR. The MC ZZ is scaled by

Process	ggF-enriched categories		VBF-enriched categories	
	e^+e^-*channel*	$\mu^+\mu^-$*channel*	e^+e^-*channel*	$\mu^+\mu^-$*channel*
$q\bar{q} \rightarrow ZZ$	714 ± 38	817 ± 44	2.9 ± 0.2	3.5 ± 0.2
$gg \rightarrow ZZ$	94 ± 29	105 ± 32	1 ± 0.5	1 ± 0.4
ZZ (EW)	6.6 ± 0.5	7.0 ± 0.5	0.8 ± 0.1	0.9 ± 0.1
WZ	412 ± 14	455 ± 12	2.5 ± 0.5	3.0 ± 1.5
Z + jets	43 ± 13	60 ± 22	0.3 ± 0.2	0.4 ± 0.3
non-resonant-$\ell\ell$	66 ± 6	77 ± 7	0.2 ± 0.2	0.3 ± 0.2
Others	5.9 ± 0.4	5.9 ± 0.4	0.09 ± 0.02	0.04 ± 0.01
Total backgrounds	1342 ± 52	1527 ± 60	7.8± 0.8	9 ± 1.6
Observed	1323	1542	8	10

Table 6.5.1.: The observed and MC expected yields (corresponding to 139 fb^{-1}) in ee and $\mu\mu$ signal regions after full ggF and VBF event selections. The expected number of events and errors are obtained from a likelihood fit to the data under the background-only hypothesis. The ZZ yields have the post-fit normalization scaling applied. The uncertainty on the ZZ normalisation factor, $\mu_{ZZ} = 1.07 \pm 0.05$ is taken into account [1].

the normalization factor $\mu_{ZZ} = 1.07$ derived from the fit for both ggF and VBF. Likewise, m_{T} distributions in the VBF SR post-fit are shown in Figure 6.5.3.

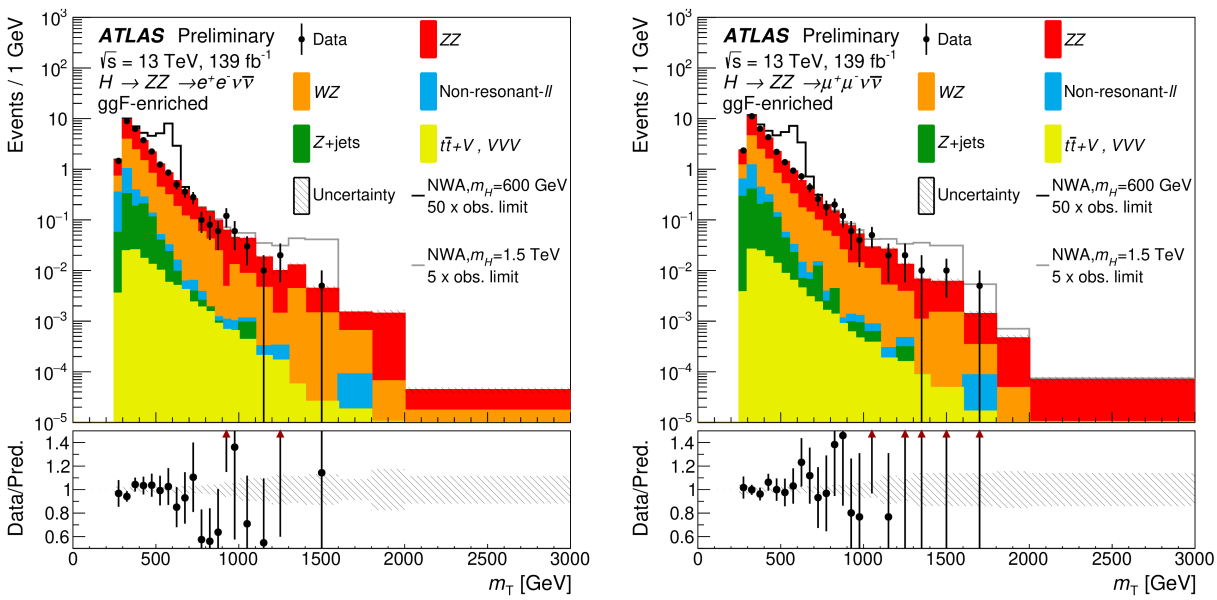

(a) (b)

Figure 6.5.2.: Post-fit m_{T} distributions in the (a) ee (b) $\mu\mu$ channel for the ggF SR. The ZZ is scaled by the floating normalization factor. The uncertainty includes stat+syst. The last bin includes overflow [1].

The number of signal events (N) is translated into cross-section (σ) × Branching Ratio (BR) through the formula, N = σ × BR × Acc × Luminosity. Acc is the signal acceptance, which is defined by the number of events in the signal region over the total number of generated events in the respective sample. Figure 6.5.4 shows the signal acceptances at

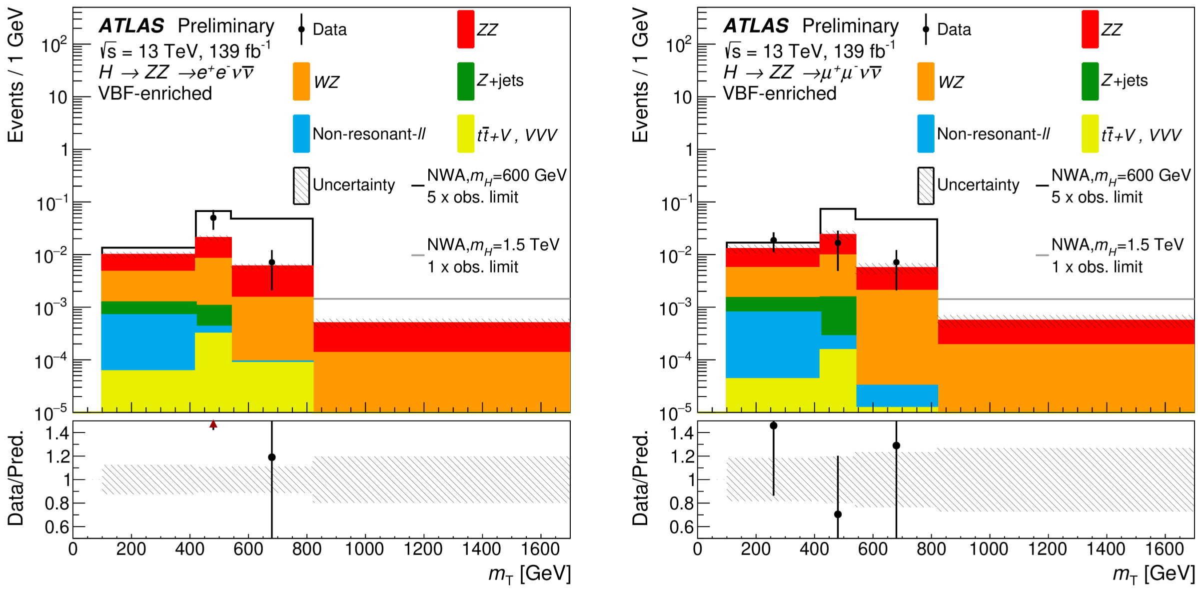

(a) (b)

Figure 6.5.3.: Post-fit m_{T} distributions in the (a) ee (b) $\mu\mu$ channel for the VBF SR. The ZZ is scaled by the floating normalization factor. The uncertainty includes stat+syst. The last bin includes overflow [1].

each mass point.

The signal strength is varied until a 95% confidence level is reached. Figure 6.5.5 (a) presents the expected and observed 95% CL limits on $\sigma \times \mathrm{BR}(H \rightarrow ZZ)$ for an additional heavy Higgs boson (narrow width[4], with mass varying from 300 GeV to 2 TeV in 100 GeV step) produced through gluon fusion using the ee and $\mu\mu$ combined channels. Limit lines between each mass are linearly interpolated based on a logarithmic scale on the y-axis. Similarly, the limits for the VBF category can be found in Figure 6.5.5 (b). In the ggF production mode, the exclusion limits go down a range from around 395 fb (expected) and 305 fb (observed) at a signal mass of 300 GeV to 4-5 fb for signals above 1.4 TeV. In the VBF category, they range from roughly 555 fb (expected) and 400 fb (observed) at 300 GeV to 3-4 fb above 1.4 TeV. There is no significant excess observed.

Understanding each NP and their correlations with each other is important. The NP ranking as shown in Figure 6.5.6 indicates the impact of systematics from individual NP on the parameter of interest (μ) for the $\ell^+\ell^-\nu\bar{\nu}$ channel. The plots are made for $m_H = 1$ TeV. The ranking is derived from a fit to the observed data in which the ZZ yield is floating. The impact of each nuisance parameter, $\Delta\mu$, is computed by comparing the nominal best-fit value of μ with the result of the fit re-done with this NP fixed to its +/- 1 σ value. In spite of the normalisation to data, the theoretical uncertainties on the ZZ background rank very highly, showing the possible advantage of a data-driven estimate. The dominant systematic uncertainty comes from the EW correction uncertainty on the $qqZZ$ prediction for the ggF

[4] The 'narrow-width assumption' (NWA) describes a total width of the resonant particle that is much smaller than their mass. In contrast, the 'large-width approximation' (LWA) study, not shown here, assuming widths of 1%, 5%, 10% and 15% of the resonance mass, considers the interference between the heavy scalar (H) and the SM Higgs boson (h) as well as between the heavy Higgs and the $gg \rightarrow ZZ$ continuum background.

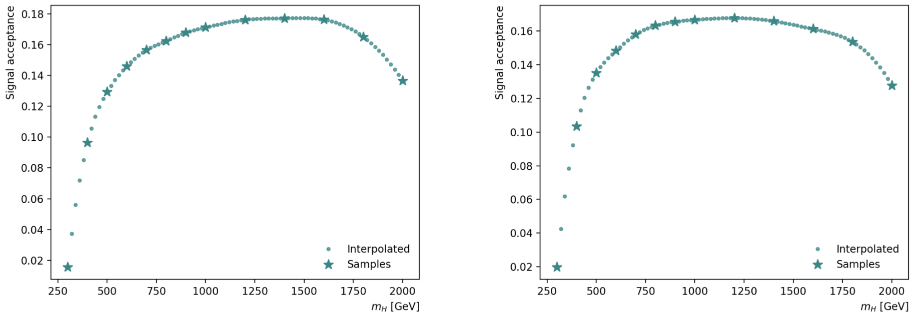

(a)

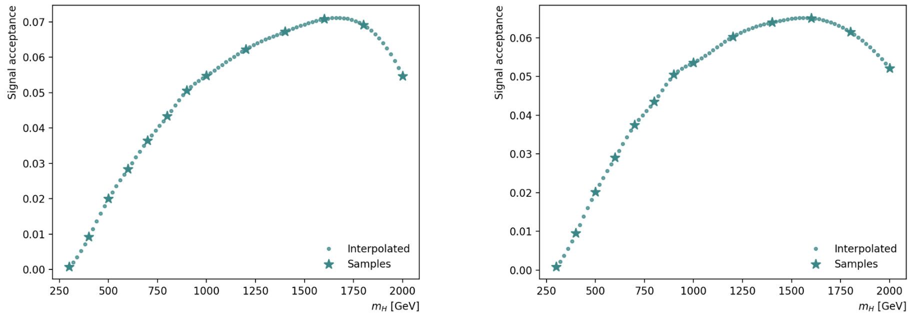

(b)

Figure 6.5.4.: The signal acceptances for the (a) ggF signals in the ggF categories and (b) VBF signals in the VBF categories derived in both ee and $\mu\mu$ channels for a heavy Higgs boson [114].

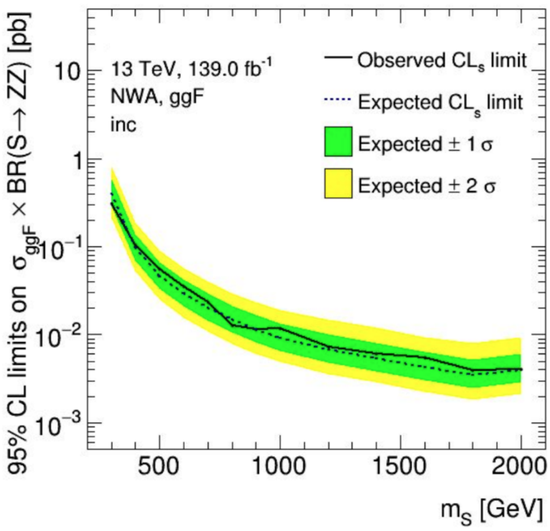

(a)

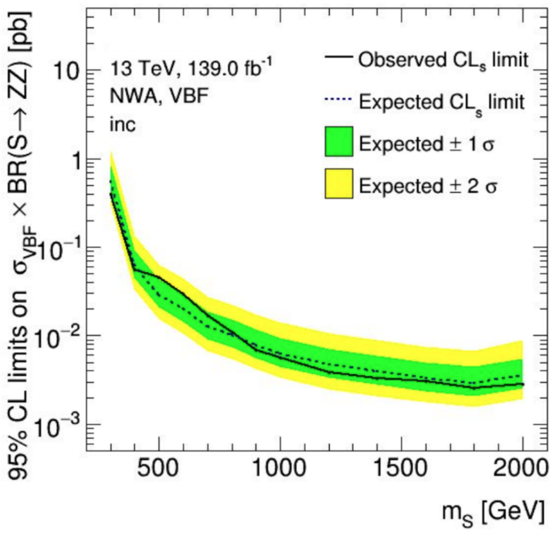

(b)

Figure 6.5.5.: 95% C.L. limits on $\sigma \times \mathrm{BR}(H \rightarrow ZZ)$ for a narrow width heavy Higgs boson produced in (a) ggF and (b) VBF as a function of its mass. The limits are derived using events in both ee and $\mu\mu$ combined channels of the $\ell^+\ell^-\nu\bar{\nu}$ final state [114].

category and VBF category. Figure 6.5.7 shows the correlations between each POI and NP, again for $m_H = 1$ TeV. It can be seen that the correlations between NP are generally very small. The strongest anti-correlation can be found between the fitted mu_{ZZ} and the ZZ QCD scale uncertainty.

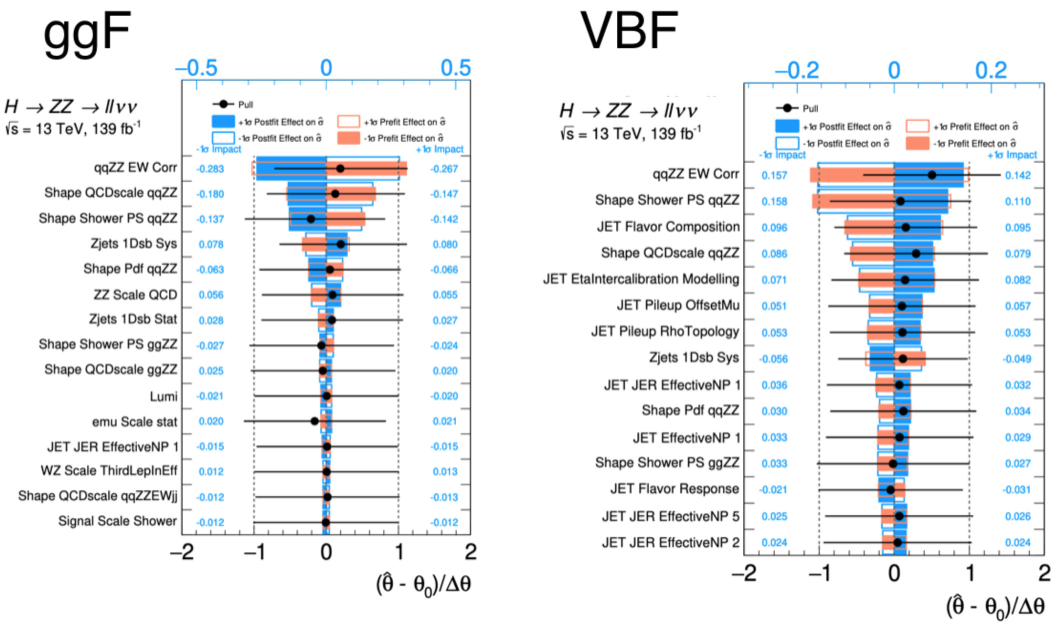

Figure 6.5.6.: Ranking of the nuisance parameters showing the impact of systematic uncertainties on the measured signal strength μ in the $H \to ZZ \to \ell^+\ell^-\nu\bar{\nu}$ search. The mass point $m_H = 1$ TeV is chosen and both the ggF (left) and VBF (right) cases are shown. The 15 most highly ranked parameters are displayed. Nuisance parameters corresponding to MC statistical uncertainties are not included here. The empty blue boxes correspond to the pre-fit impact on μ and the filled blue ones correspond to the post-fit impact on μ. The black points represent $(\hat{\theta} - \theta_0)/\Delta\theta$. The error bars are the post-fit errors of the fit parameter [114].

Nevertheless, one should keep in mind that the dominant uncertainties are due to the limited size of the data sets, and the effects of systematic uncertainties are subdominant in this analysis.

The $\ell^+\ell^-\nu\bar{\nu}$ results are combined with results from the $H \to ZZ \to \ell\ell\ell\ell$ decay channel. Both $\ell^+\ell^-\nu\bar{\nu}$ and $\ell\ell\ell\ell$ channels introduced a floating normalization factor to model the ZZ backgrounds yield by data. Studies showed negligible effects, so the two normalisation factors are treated as uncorrelated [1, 114].

The $\ell^+\ell^-\nu\bar{\nu}$ channel is more sensitive than the $\ell\ell\ell\ell$ channel in the high mass region, due to the higher branching ratio. The $\ell\ell\ell\ell$ channel is more powerful in the low mass region due to better resolution and signal/background, but loses statistics fast for higher masses. For the mass region from 200 GeV to 300 GeV, only the $\ell\ell\ell\ell$ channel is considered, and a 5 GeV scan step is used. For masses above 300 GeV, both $\ell\ell\ell\ell$ and $\ell^+\ell^-\nu\bar{\nu}$ channels are taken into account. A 20 GeV mass step is adopted from 300 GeV to 1 TeV, and a 100 GeV mass step is adopted from masses above 1 TeV.

Limits on the cross-section times branching ratio from the combination of $\ell\ell\ell\ell$ and $\ell^+\ell^-\nu\bar{\nu}$ channels are shown in Figure 6.5.8. In the mass range considered for this search the 95%

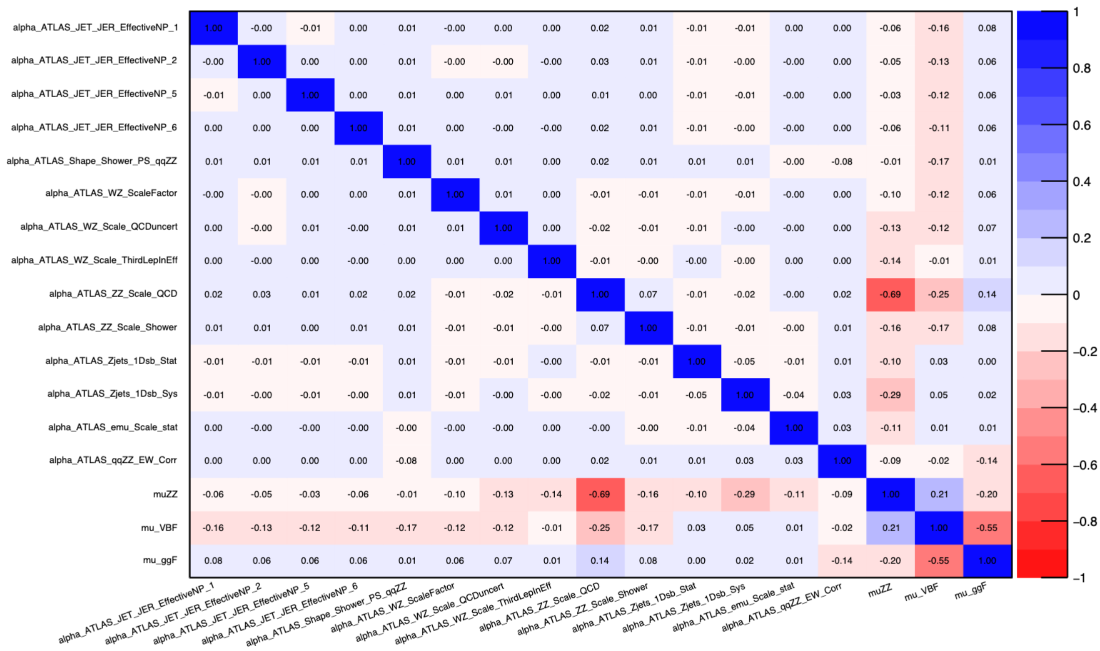

Figure 6.5.7.: Correlation matrix of the data fit for a signal mass point of $m_H = 1$ TeV in the $H \to ZZ \to \ell^+\ell^-\nu\bar{\nu}$ search [114].

2959 CL upper limits for heavy Higgs boson production vary between 200 fb at $m_H = 240$ GeV
2960 and 2.6 fb at $m_H = 2000$ GeV in the ggF channel and 87 fb at $m_H = 250$ GeV and 1.9 fb
2961 at $m_H = 1800$ GeV in the VBF channel.

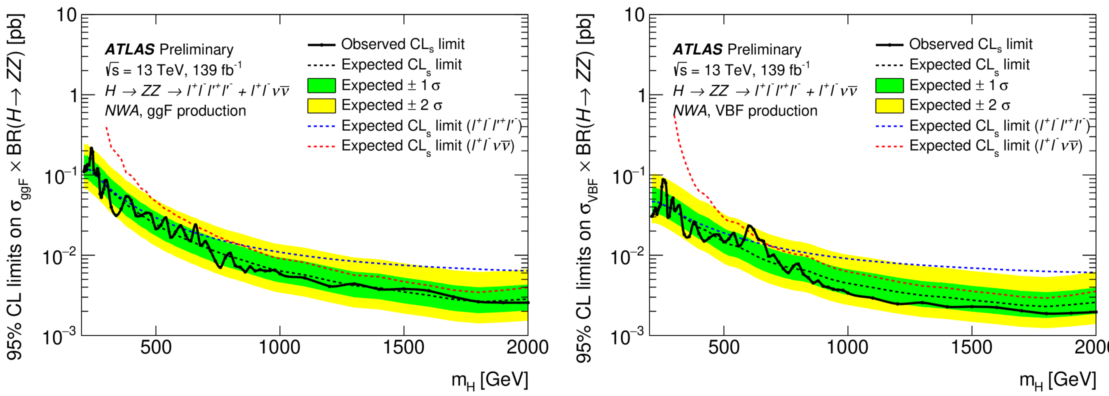

(a) (b)

Figure 6.5.8.: 95% C.L. limits on $\sigma \times$BR($H \to ZZ$) for a narrow width heavy Higgs boson from the combination of $\ell\ell\ell\ell$ and $\ell^+\ell^-\nu\bar{\nu}$ channels produced in (a) ggF and (b) VBF as a function of the heavy resonance mass m_H. The solid black line and points indicate the observed limit. The dashed black line indicates the expected limit and the bands represent the $\pm 1\sigma$ and $\pm 2\sigma$ uncertainty ranges in the expected limit. The dashed coloured lines indicate the expected limits obtained from the individual searches [1].

2962 The NWA model limits presented above are converted in 2HDM exclusion contours in
2963 the tanβ versus cos(β - α) and tanβ versus m_H for Type-I and Type-II 2HDMs. It is

found that the limits have non-trivial dependence on the ggF and VBF production, so the relative rates of the two productions in the fit are set to the prediction of the 2HDM when calculating the limits.

Figure 6.5.9 shows exclusion limits in the tanβ versus cos(β - α) for a heavy Higgs boson with mass m_H = 220 GeV, based on the $\ell\ell\ell\ell$ cross section limits. The white regions in the exclusion plots indicate regions of parameter space not excluded by the present analysis; in these regions, the cross-section predicted by the 2HDM is below the experimental sensitivity.

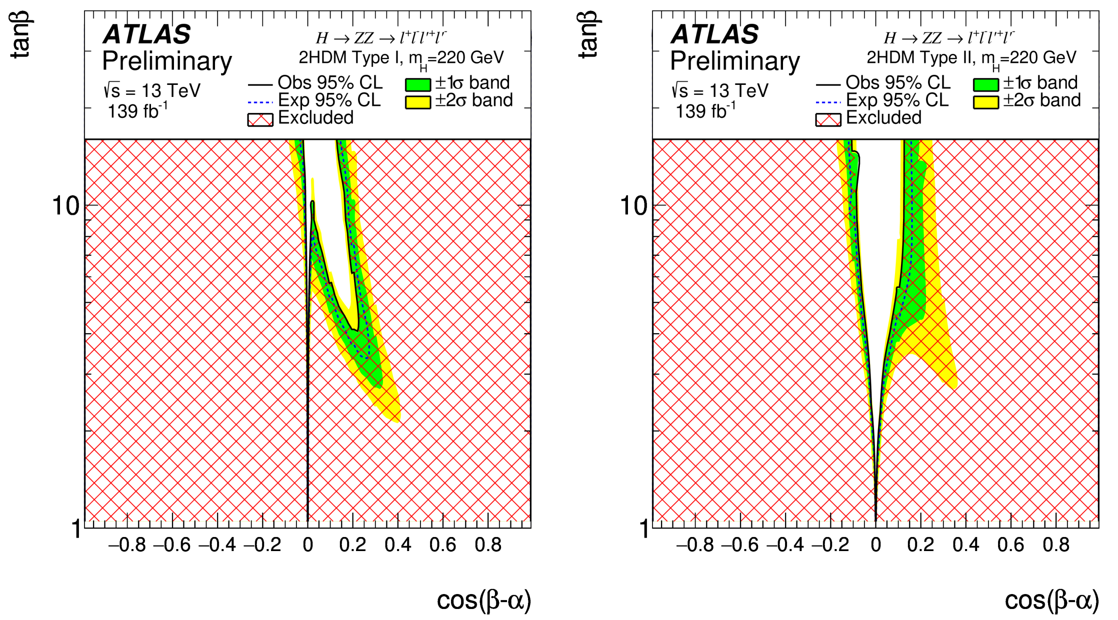

(a) (b)

Figure 6.5.9.: 95% CL exclusion contours in the 2HDM (a) Type-I and (b) Type-II models for m_H = 220 GeV, as a function of the parameters cos(β - α) and tanβ. The shaded area shows the observed exclusion, with the black line denoting the edge of the excluded region. The blue line represents the expected exclusion contour and the shaded bands represent the $\pm 1\sigma$ and $\pm 2\sigma$ uncertainties on the expectation. The limit cos(β - α) $\rightarrow$ 0 corresponds to the decoupling limit [1].

Figure 6.5.10 shows exclusion limits as a function of the heavy Higgs boson mass m_H and the parameter tanβ for 4l and $\ell^+\ell^-\nu\bar{\nu}$ combined channels with cos(β - α) = -0.1.

The analysis results in terms of upper limits are interpreted in terms of the production cross-section of a Randall-Sundrum graviton as well. Only ggF category is considered, and uncorrelated ZZ normalization factors are used in $\ell\ell\ell\ell$ and $\ell^+\ell^-\nu\bar{\nu}$ channels for the combination. The limit setting procedure is very similar to the heavy Higgs search. Figure 6.5.11 gives the predicted and observed limits. Limit lines between each mass are linearly interpolated based on a logarithmic scale on the y-axis. The limits are derived for mass points between 600 GeV and 2 TeV with a 200 GeV interval. The limits span from 25 fb (expected) and 30 fb (observed) at 600 GeV, to approximately 3 fb at the high end of the search range. There is no significant derivation. For this specific model [21], masses $m(G_{KK})$ below 1750 GeV are excluded.

The limit on a graviton signal is better than on the NWA heavy Higgs. There are some possi-

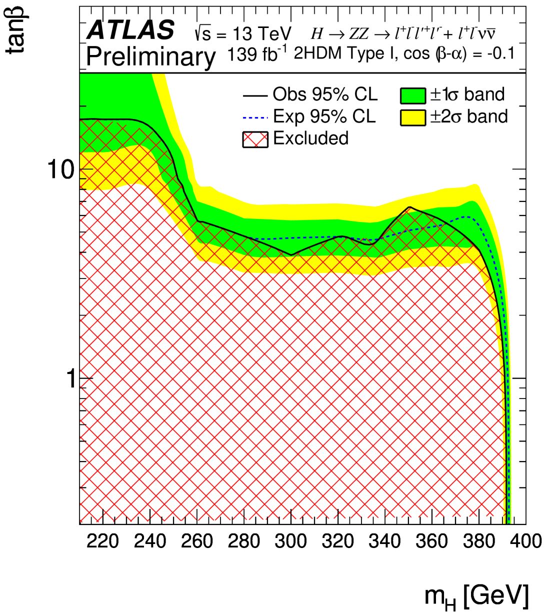

(a)

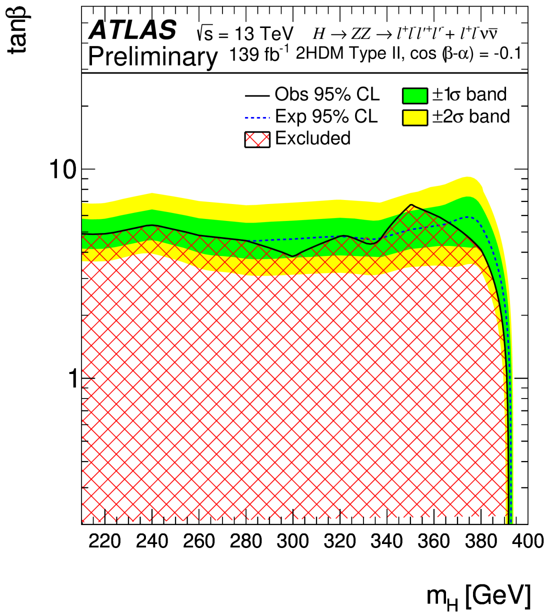

(b)

Figure 6.5.10.: 95% CL exclusion contours in the 2HDM (a) Type-I and (b) Type-II models for cos $(\beta$ - $\alpha)$ = -0.1 as a function of the heavy Higgs boson mass m_H and the parameter tanβ. The shaded area shows the observed exclusion, with the black line denoting the edge of the excluded region. The blue line represents the expected exclusion contour and the shaded bands represent the $\pm 1\sigma$ and $\pm 2\sigma$ uncertainties on the expectation [1].

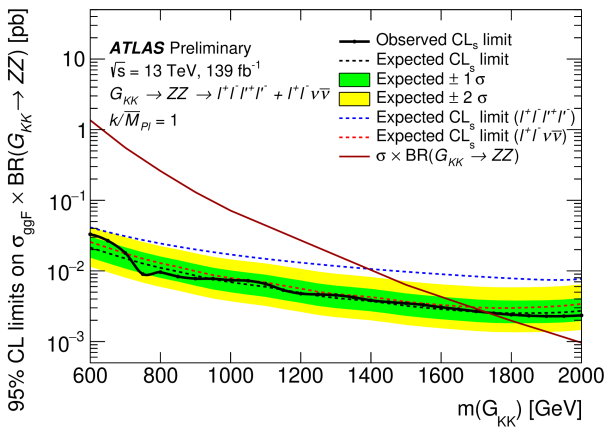

Figure 6.5.11.: 95% C.L. limits on $\sigma_{G^*} \times$BR$(G_{KK} \to ZZ)$ for a KK graviton produced with $k/\bar{M}_{PI} = 1$ as a function of $m(G_{KK})$. The limits are derived using events in both ee and $\mu\mu$ combined channels. The predicted production cross-section times branching ratio as a function of the G_{KK} mass $m(G_{KK})$ is shown by the red solid line [21]. The black line indicates the observed limit [1].

ble reasons to get lower limits: higher signal acceptance and efficiency ($\sigma = N_{sig}$ / Acc $\times$ eff $\times$ L), a smaller number of background events, smaller systematic uncertainties. The first two points are discussed. Firstly, Table 6.5.2 gives the signal acceptances at each mass point compared between graviton and NWA heavy Higgs, but the largest difference is only 2%. Secondly, the key component is from the signal m_{T} shape and its resolution. The graviton signals exhibit a better m_{T} resolution with smaller tails and narrower peaks, which can explain that the graviton signal shapes can be distinguished better from the backgrounds resulting in better limits [114].

Signal acceptances [%]

	e^+e^- channel		$\mu^+\mu^-$ channel	
Signal mass [GeV]	NWA Higgs	Graviton	NWA Higgs	Graviton
600	14.60	15.20	14.83	15.63
800	16.24	17.48	16.33	16.52
1000	17.12	18.12	16.68	17.18
1200	17.61	19.80	16.59	17.22
1400	17.71	19.80	16.59	17.22
1600	17.62	19.31	16.13	15.86
1800	16.50	16.87	15.36	14.67
2000	13.66	12.65	12.76	11.17

Table 6.5.2.: Comparison of signal acceptances between NWA heavy Higgs and Graviton signals.

Chapter 7

Conclusion

A search for heavy resonances decaying into a pair of Z bosons using the $\ell^+\ell^-\nu\bar{\nu}$ final state is performed using proton-proton collision data collected at $\sqrt{s} = 13$ TeV by the ATLAS experiment during 2015−2018 at the LHC. No excess has been observed above expected SM backgrounds. A combination of the results obtained using the $\ell\ell\ell\ell$ and $\ell^+\ell^-\nu\bar{\nu}$ final states is shown, and combined 95% confidence-level upper limits are set on the cross-section times branching ratio of a scalar resonance. Additionally, the results are interpreted in the context of a CP-conserving 2HDM and the Randall–Sundrum model. The 2HDM model predicts the existence of a heavy Higgs boson, trying to explain the observed matter-antimatter asymmetry of the universe. The RS model predicts the existence of gravitons, and it can help solve the hierarchy problem as well.

This thesis shows the development of the $Z\gamma$ method for the estimate of the background contribution from the ZZ process in the $\ell^+\ell^-\nu\bar{\nu}$ channel. Currently the shape of this background is estimated from MC simulation: in addition to the desirability of a more data-driven estimate, the related uncertainties are the dominant systematic uncertainties in the analysis. The $Z\gamma$ method utilizes the fact that at high boson p_{T}, the two processes have very similar kinematics and the cross-sections differ mainly due to the boson couplings. The Matrix and Sherpa generators are used to investigate effects on the cross-section ratio R($ZZ/Z\gamma$) associated with certain event selections. The estimate and the ZZ MC prediction agree within uncertainties. This constitutes an important check of the ZZ MC prediction, in particular the shape.

The systematic uncertainties on the $Z\gamma$ method are also evaluated. A detailed theoretical uncertainty is evaluated by using Matrix, which is based on a NNLO QCD prediction. However, there remains room for improvement. Certain selection cuts are sensitive to radiation, which increases the theoretical uncertainty. Further investigation of the calculation of the higher-order uncertainties and the correlations between the ZZ and $Z\gamma$ processes are needed.

The statistical uncertainties are currently quite large, which is the main reason why the ZZ estimate from the $Z\gamma$ method was only used as a cross-check of the ZZ MC prediction in the heavy Higgs search. More data will help reduce the statistical uncertainty, which of course also depends on the chosen bin widths.

A couple of possible improvements to the $Z\gamma$ method are considered. For example, $Z\gamma$ events in data could be reweighted by a ratio obtained from reconstructed MC events, which could help with more complicated signal regions and discriminants. The selected $Z\gamma$ events can be used in the future as a control region in a simultaneous fit of signal and background, together with $ZZ \rightarrow \ell^+\ell^-\ell'^+\ell'^-$ to constrain the systematic uncertainties on the ZZ estimate. The method also can be used for other analyses with the same final state, like the $Zh(\text{inv})$ search.

The thesis also includes a discussion of improvements to the measurement of $E_{\mathrm{T}}^{\mathrm{miss}}$ in cases when a jet and an electron are close-by. Overlap removal is crucial as failing to account correctly for overlapping objects in the $E_{\mathrm{T}}^{\mathrm{miss}}$ calculation would cause large tails of fake $E_{\mathrm{T}}^{\mathrm{miss}}$, which adversely affects the sensitivity of many analyses.

Scheduled to start in 2027, the HL-LHC will collect an integrated luminosity of 3 ab^{-1} of data in *pp* collisions. This will enhance the probability to find rare production and decay processes. With growing statistics, precise predictions of the SM backgrounds will become even more crucial for BSM searches, and data-driven methods, like the $Z\gamma$ method studied in this thesis, could play an important role.

Appendix A

MET Calculation Issue: crack electrons

A.1. Crack Veto Issues

A larger EMTopo $E_{\mathrm{T}}^{\mathrm{miss}}$ than EMPFlow $E_{\mathrm{T}}^{\mathrm{miss}}$ in tails was noticed when comparing the $E_{\mathrm{T}}^{\mathrm{miss}}$ performance for the $\ell^{+}\ell^{-}\nu\bar{\nu}$ final state analysis. The issue was traced down to an issue in the software that when forming an e/γ super-cluster, satellite topological clusters were erroneously matched with $\Delta\Phi$(seed, satellite) instead of the absolute value of $\Delta\Phi$(seed, satellite). Therefore, there are mismatches between the electron and electron cluster positions in the PFlow $E_{\mathrm{T}}^{\mathrm{miss}}$ map. PFlow $E_{\mathrm{T}}^{\mathrm{miss}}$ having larger tails is due to inefficient overlap removal with jets. The impact on the $E_{\mathrm{T}}^{\mathrm{miss}}$ is described in this section.

In the MC16a sample, PFlow $E_{\mathrm{T}}^{\mathrm{miss}}$ had larger $E_{\mathrm{T}}^{\mathrm{miss}}$ tails than Topo $E_{\mathrm{T}}^{\mathrm{miss}}$, which was not expected as shown in Figure A.1.1 (a). The performance between these two was expected to be similar or better in PFlow $E_{\mathrm{T}}^{\mathrm{miss}}$. The information for these two types of the $E_{\mathrm{T}}^{\mathrm{miss}}$ was:

$$\begin{aligned}
&(\text{EMTopo } E_{\mathrm{T}}^{\mathrm{miss}}) \text{ RMS : 11.98 GeV, Integral } > \text{ 150 GeV : } 454.5 \pm 45.09. \\
&(\text{EMPFlow } E_{\mathrm{T}}^{\mathrm{miss}}) \text{ RMS : 11.74 GeV, Integral } > \text{ 150 GeV : } 827.3 \pm 60.1.
\end{aligned} \tag{A.1.1}$$

The impact of the problem can be seen also in Figure A.1.1 (b), where the electron term is expected to be identical, but the discrepancies were observed in the MC16a PFlow $E_{\mathrm{T}}^{\mathrm{miss}}$.

We developed a work-around for it by applying a crack veto, the $E_{\mathrm{T}}^{\mathrm{miss}}$ tails become similar between EMTopo and EMPFlow as shown in Figure A.1.2 (a). The tails ratio of PFlow and Topo is reduced to 1.4 from 1.82. This significantly reduced the excess when crack veto is applied as shown in Figure A.1.2 (b). Both the geometric crack veto ($1.37 < |\eta| < 1.52$) and the refined selection (the number of calosampling and satellite > 0 and the maximum of dR > 0.15 between its seed and satellite) are removing problematic electrons.

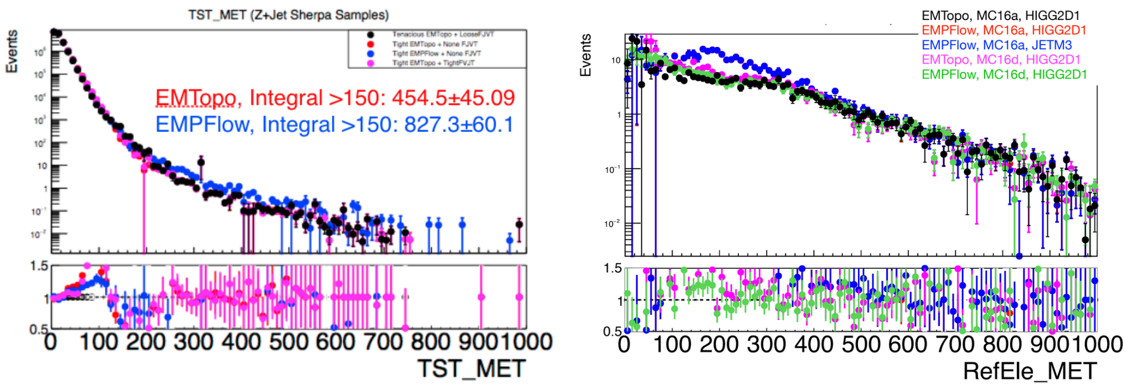

(a) (b)

Figure A.1.1.: $E_{\mathrm{T}}^{\mathrm{miss}}$ distributions with PFlow jets and Topo jets are shown. The Z + jets samples with the Z (ee) selection are applied. (a) Total $E_{\mathrm{T}}^{\mathrm{miss}}$. (b) Electron term. Events are required to have $E_{\mathrm{T}}^{\mathrm{miss}} > 150$ GeV. Different colors represent the distributions were made by using different sample formats.

The remaining tails were expected from the pile-up contamination in the PFlow $E_{\mathrm{T}}^{\mathrm{miss}}$ reconstruction. It was expected to be reduced by another developing technique. There were about 9% events loss if applying a geometric crack veto, while about 0.6% events loss if applying refined selection.

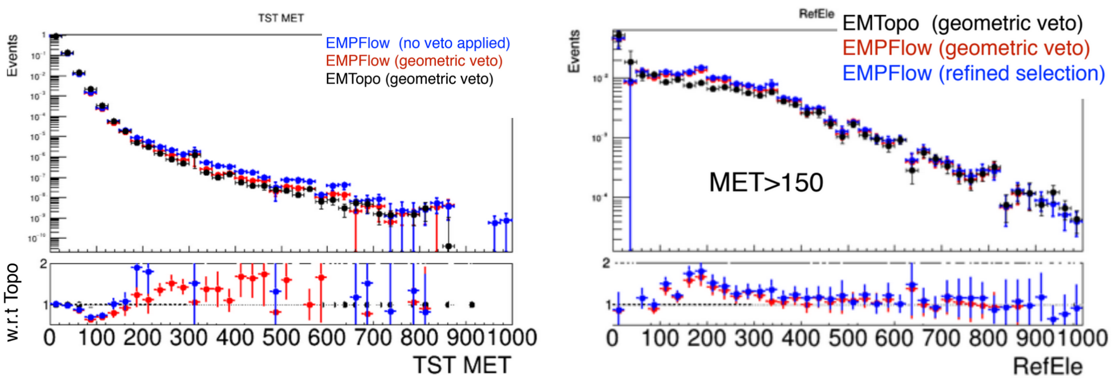

(a) (b)

Figure A.1.2.: $E_{\mathrm{T}}^{\mathrm{miss}}$ distributions with PFlow jets and Topo jets. Electrons are applied either a geometric veto or a refined selection. (a) Total $E_{\mathrm{T}}^{\mathrm{miss}}$. (b) Electron term with $E_{\mathrm{T}}^{\mathrm{miss}} > 150$ GeV cut.

We proposed two ways to solve this crack issue, and the second one is chosen in the analysis in the end:

- veto events which have any electron that would be given to the MET calculation and satisfies 1.37 < | el->caloCluster()->etaBE(2) | < 1.52. This veto has an inefficiency of about 9% for Z-like events with two electrons.
- veto events which have any electron that would be given to the $E_{\mathrm{T}}^{\mathrm{miss}}$ calculation. This veto has a negligible inefficiency, but new derivations need to be produced.

Appendix B

The $Z\gamma$ Method Up to a Z Mass Cut Applied

As a part of the $Z\gamma$ study, we applied a set of cuts (ΔR, $\Delta\phi$, and truth $E_{\mathrm{T}}^{\mathrm{miss}}$ significance) to both ZZ and $Z\gamma$ events in the truth ratio, and for this reason, this section shows the data-driven method with the cuts are applied up to the Z mass window on the truth R and $Z\gamma$ data events as well.

Figure B.0.1 shows the data/MC comparison in the $Z\gamma$ CR. EW corrections applied to $Z\gamma$ MC modeling. The data/MC discrepancies had been observed with the Z mass cut, in particular, $\sim$10% lower data in the m_{T} tails. Figure B.0.2 shows the method validation by comparing the ZZ prediction and the $Z\gamma$ method calculation with $Z\gamma$ MC. There are about 10% that show $Z\gamma$ method overestimation in the m_{T} 400-600 GeV region. Bad agreements are seen by about 5-10% in the low p_{T} region in the $E_{\mathrm{T}}^{\mathrm{miss}}$ distribution with and w/o EW corrections.

Figure B.0.3 shows the result compared to ZZ MC with the R is applied cuts up to the Z mass window. The EW corrections are considered here. The good agreement between $Z\gamma$ data estimate and ZZ MCs is observed. To understand it further, investigations on cut effects and EW corrections would be good.

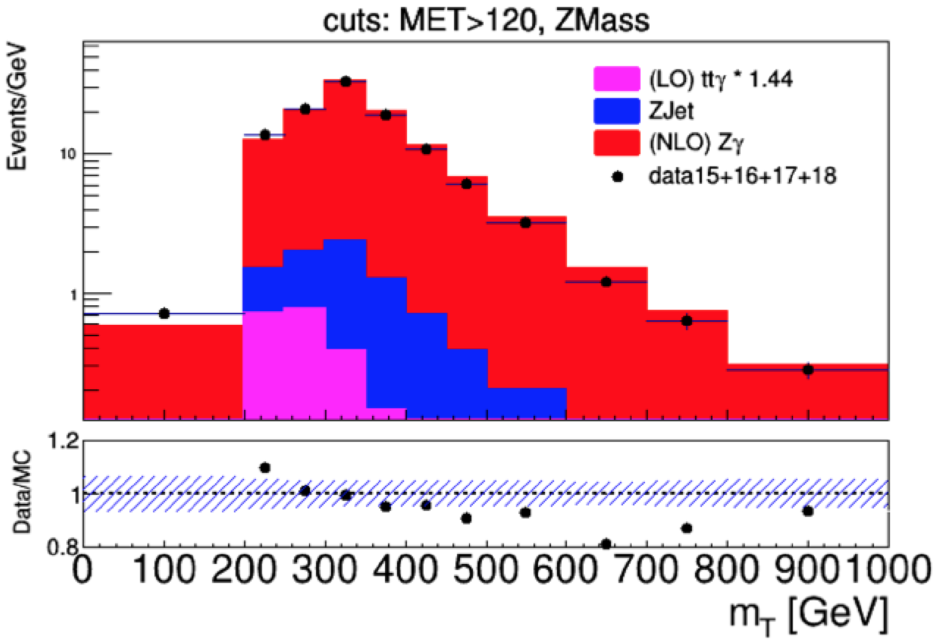

Figure B.0.1.: The m_{T} distribution in the $Z\gamma$ control region with cuts up to the Z mass window. Data points represent collected data from 2015 to 2018 and compared with the predicted Standard Model background contributions in stacked histograms.

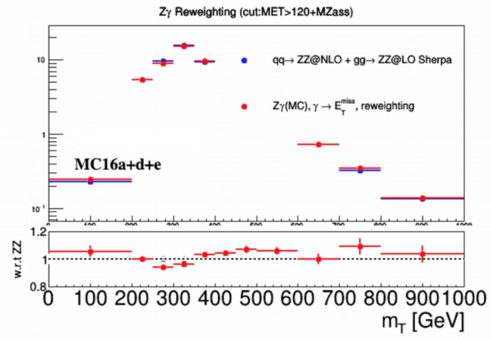

(a)

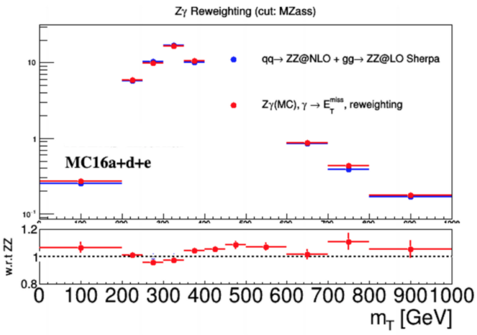

(b)

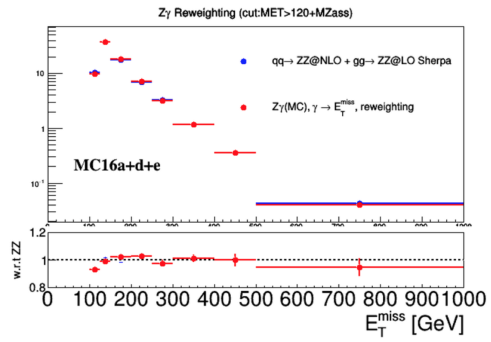

(c)

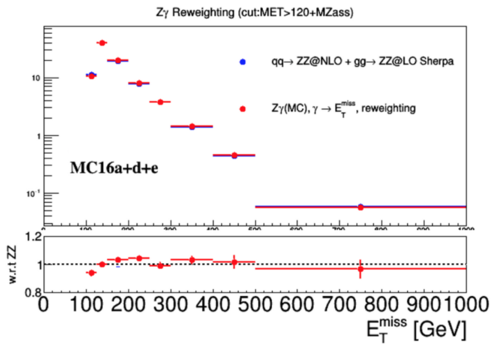

(d)

Figure B.0.2.: Closure checks measured by SHERPA at NLO when applying cuts up to the ZMass in R as well as the ZZ (a) with and (b) without EW corrections applied to $Z\gamma$ MC as a fucntion of m_{T}. ZZ MCs prediction is in blue, and the $Z\gamma$ prediction is in red. (c) with EW (d) without EW corrections to $Z\gamma$ MC as a function of $E_{\mathrm{T}}^{\mathrm{miss}}$ are shown. Caveat: fully correlated in statistics between blue and red.

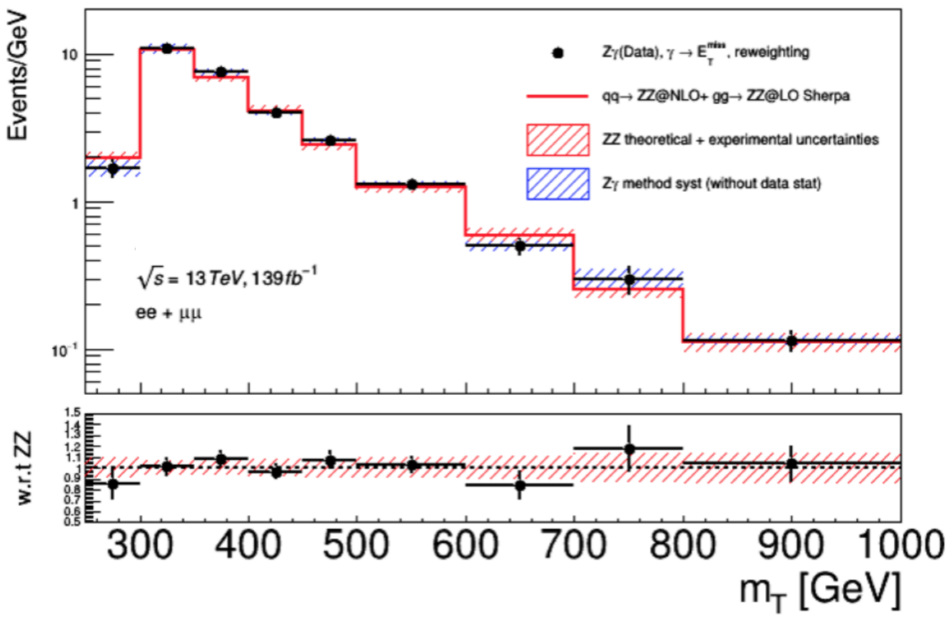

Figure B.0.3.: Comparison of data-driven method with SHERPA R and ZZ MC prediction in the E_T^{miss} distribution with EW corrections. The cut in the ratio R and event selections are applied up to ZMass level.

Appendix C

The $Z\gamma$ Method: inclusive result

This section shows the inclusive results for comparisons between the data-driven method and ZZ MC prediction. The normalization factor (NF) is derived by the ratio of the production from the $Z\gamma$ method and ZZ MC inclusively in the MET distribution:

$$\mathrm{NF} = \frac{N_{data-driven}}{N_{MC}}. \tag{C.0.1}$$

Both the number of events are studied with and without EW corrections as shown in Tables C.0.1 and C.0.2 for HM and LM, respectively. The corresponding uncertainties are not evaluated. The $Z\gamma$ method in Sherpa and Matrix calculations are shown as well. In the search for the heavy Higgs boson, the normalisation factor for the ZZ background is determined from fitting to data. Inclusive studies here indicate the normalisation factor between the $Z\gamma$ CR extrapolated to ZZ and the ZZ MC. With EW corrections, the $Z\gamma$ prediction with HM selections is about 7% greater than the ZZ MC, while without EW corrections, the $Z\gamma$ normalization factor is about 2% smaller than the ZZ MC. The inclusive normalisation estimate for $4l$ CR would be more compatible due to less extrapolation.

	NF
Sherpa R without EW correction	0.98
Sherpa R with EW correction	1.06
Matrix R without EW correction	0.99
Matrix R with EW correction	1.07

Table C.0.1.: NF of the $Z\gamma$ method and ZZ MC prediction with HM selections for the inclusive study.

	NF
Sherpa R without EW correction	0.99
Sherpa R with EW correction	1.06
Matrix R without EW correction	1.02
Matrix R with EW correction	1.09

Table C.0.2.: NF of the $Z\gamma$ method and ZZ MC prediction with LM selections for the inclusive study.

Bibliography

[1] ATLAS Collaboration, *Search for heavy resonances decaying into a pair of Z bosons in the $\ell\ell\ell\ell$ and $\ell^+\ell^-\nu\bar{\nu}$ final states using 139 fb^{-1} of proton-proton collisions at $\sqrt{s}$ = 13 TeV with the ATLAS detector*, (2020), URL: https://atlas.web.cern.ch/Atlas/GROUPS/PHYSICS/CONFNOTES/ATLAS-CONF-2020-032/ (cit. on pp. 2, 24, 48, 64, 99, 136, 137, 139–142).

[2] M. Tanabashi et al., *Review of Particle Physics: Particle Data Group*, Physical Review D **98** (2018) (cit. on p. 6).

[3] *LHCb experiment discovers a new pentaquark*, (2019), URL: https://home.cern/news/news/physics/lhcb-experiment-discovers-new-pentaquark (cit. on p. 6).

[4] M. E. Peskin and D. V. Schroeder, *An Introduction to quantum field theory*, (1995) (cit. on p. 7).

[5] Lectures, *The Dirac equation*, (2007), URL: https://www.ippp.dur.ac.uk/~krauss/Lectures/QuarksLeptons/Dirac/RealDirac_3.html (cit. on p. 8).

[6] T. D. Lee and C. N. Yang, *Question of Parity Conservation in Weak Interactions*, Phys. Rev. **104** (1), URL: https://link.aps.org/doi/10.1103/PhysRev.104.254 (cit. on p. 9).

[7] Particle Data Group, *Review of Particle Physics*, The European Physical Journal C - Particles and Fields **3** (1998) 1, URL: https://doi.org/10.1007/s10052-998-0104-x (cit. on p. 9).

[8] F. Hasert et al., *Observation of Neutrino Like Interactions without Muon or Electron in the Gargamelle Neutrino Experiment*, Nucl. Phys. B **73** (1974) 1 (cit. on p. 10).

[9] ATLAS Collaboration, *Observation of a new particle in the search for the Standard Model Higgs boson with the ATLAS detector at the LHC*, Phys. Lett. B **716** (2012) 1, arXiv: 1207.7214 [hep-ex] (cit. on p. 13).

[10] ATLAS Collaboration, *A combination of measurements of Higgs boson production and decay using up to* 139 *fb^{-1} of proton–proton collision data at $\sqrt{s}$ = 13 TeV collected with the ATLAS experiment*, (2020), URL: http://cds.cern.ch/record/2725733 (cit. on p. 14).

[11] ATLAS and CMS Collaboration, *Combined Measurement of the Higgs Boson Mass in pp Collisions at $\sqrt{s} = 7$ and 8 TeV with the ATLAS and CMS Experiments*, Phys. Rev. Lett. **114** (2015) 191803, arXiv: 1503.07589 [hep-ex] (cit. on p. 14).

[12] ATLAS Collaboration, *Handbook of LHC Higgs Cross Sections: 4. Deciphering the Nature of the Higgs Sector*, **2/2017** (2016), arXiv: 1610.07922 [hep-ph] (cit. on p. 15).

[13] G. Raven, *Measurement of invisible Z decays*, (1995), Presented on 27 Nov 1995, URL: http://cds.cern.ch/record/291887 (cit. on p. 18).

[14] N. Turok and J. Zadrozny, *Electroweak baryogenesis in the two-doublet model*, Nuclear Physics B **358** (1991) 471, ISSN: 0550-3213, URL: http://www.sciencedirect.com/science/article/pii/0550321391903563 (cit. on p. 18).

[15] Branco, G.C. and Ferreira, P.M. and Lavoura, L. and Rebelo, M.N. and Sher, Marc and Silva, Joao P., *Theory and phenomenology of two-Higgs-doublet models*, Phys. Rept. **516** (2012) 1, arXiv: 1106.0034 [hep-ph] (cit. on pp. 18–22).

[16] S. Davidson, E. Nardi, and Y. Nir, *Leptogenesis*, Phys. Rept. **466** (2008) 105, arXiv: 0802.2962 [hep-ph] (cit. on p. 19).

[17] E. A. Paschos, *Diagonal neutral currents*, Phys. Rev. D **15** (7 1977) 1966, URL: https://link.aps.org/doi/10.1103/PhysRevD.15.1966 (cit. on p. 19).

[18] S. L. Glashow and S. Weinberg, *Natural conservation laws for neutral currents*, Phys. Rev. D **15** (7 1977) 1958, URL: https://link.aps.org/doi/10.1103/PhysRevD.15.1958 (cit. on p. 19).

[19] ATLAS Collaboration, *Search for an additional, heavy Higgs boson in the $H \to ZZ$ decay channel at $\sqrt{s} = 8$ TeV in pp collision data with the ATLAS detector*, Eur. Phys. J. C **76** (2016) 45, arXiv: 1507.05930 [hep-ex] (cit. on p. 23).

[20] N. Arkani-Hamed, S. Dimopoulos, and G. Dvali, *The Hierarchy problem and new dimensions at a millimeter*, Phys. Lett. B **429** (1998) 263, arXiv: hep-ph/9803315 (cit. on p. 23).

[21] K. Agashe, H. Davoudiasl, G. Perez, and A. Soni, *Warped Gravitons at the LHC and Beyond*, Phys. Rev. D **76** (2007) 036006, arXiv: hep-ph/0701186 (cit. on pp. 23, 24, 141, 142).

[22] S. J. Huber, *Flavor violation and warped geometry*, Nucl. Phys. B **666** (2003) 269, arXiv: hep-ph/0303183 (cit. on p. 23).

[23] L. Evans and P. Bryant, *LHC Machine*, Journal of Instrumentation **3** (2008) S08001, URL: https://doi.org/10.1088%2F1748-0221%2F3%2F08%2Fs08001 (cit. on p. 25).

[24] *CERN Complex Accelerator*, (2013), URL: https://www.lhc-closer.es/taking_a_closer_look_at_lhc/0.cern_accelerator_complex (cit. on p. 26).

[25] *Magnetic multipoles*, (2013), URL: https://www.lhc-closer.es/taking_a_closer_look_at_lhc/0.magnetic_multipoles (cit. on p. 27).

[26] *Complex Movement*, (2007), URL: https://www.lhc-closer.es/taking_a_closer_look_at_lhc/0.complex_movement (cit. on p. 28).

[27] *Luminosity*, (2018), URL: https://www.lhc-closer.es/taking_a_closer_look_at_lhc/0.luminosity (cit. on p. 29).

[28] J. Pequenao, *Computer generated image of the whole ATLAS detector*, (2008), URL: https://cds.cern.ch/record/1095924 (cit. on p. 30).

[29] ATLAS Collaboration, *The ATLAS Experiment at the CERN Large Hadron Collider*, Journal of Instrumentation **3** (2008) S08003, URL: https://doi.org/10.1088%2F1748-0221%2F3%2F08%2Fs08003 (cit. on pp. 30, 36, 37).

[30] J. Pequenao, *Event Cross Section in a computer generated image of the ATLAS detector.*, (2008), URL: https://cds.cern.ch/record/1096081 (cit. on p. 31).

[31] ATLAS Collaboration, *ATLAS inner detector: Technical Design Report, 1*, Technical Design Report ATLAS (1997), URL: https://cds.cern.ch/record/331063 (cit. on p. 31).

[32] ATLAS Collaboration, *ATLAS inner detector: Technical Design Report, 2*, Technical Design Report ATLAS (1997), URL: https://cds.cern.ch/record/331064 (cit. on p. 31).

[33] J. Pequenao, *Computer generated image of the ATLAS inner detector*, (2008), URL: https://cds.cern.ch/record/1095926 (cit. on pp. 32, 36, 38).

[34] M. Garcia-Sciveres and N. Wermes, *A review of advances in pixel detectors for experiments with high rate and radiation*, Rept. Prog. Phys. **81** (2018) 066101, arXiv: 1705.10150 [physics.ins-det] (cit. on p. 33).

[35] ATLAS Collaboration, *ATLAS tile calorimeter: Technical Design Report*, Technical Design Report ATLAS (1996), URL: https://cds.cern.ch/record/331062 (cit. on p. 33).

[36] ATLAS Collaboration, *ATLAS liquid-argon calorimeter: Technical Design Report*, Technical Design Report ATLAS (1996), URL: https://cds.cern.ch/record/331061 (cit. on p. 33).

[37] ATLAS Collaboration, *Computer Generated image of the ATLAS calorimeter*, (2008), URL: https://cds.cern.ch/record/1095927 (cit. on p. 34).

[38] M. Tanabashi et al. (Particle Data Group), *Review of Particle Physics: Particle Data Group*, Physical Review D **98** (2018), URL: https://pdg.lbl.gov/2019/reviews/rpp2018-rev-passage-particles-matter.pdf (cit. on p. 34).

[39] *Bethe formula*, (2008), URL: https://en.wikipedia.org/wiki/Bethe_formula (cit. on p. 37).

[40] ATLAS Collaboration, *ATLAS muon spectrometer: Technical Design Report*, Technical Design Report ATLAS (1997), URL: https://cds.cern.ch/record/331068 (cit. on p. 37).

[41] ATLAS Collaboration, *Commissioning of the ATLAS Muon Spectrometer with cosmic rays*, The European Physical Journal C **70** (2010) 875 (cit. on p. 38).

[42] ATLAS Collaboration, *Operation of the ATLAS trigger system in Run 2*, (2020), arXiv: 2007.12539 [physics.ins-det] (cit. on pp. 39, 40).

[43] ATLAS Collaboration, *Performance of the ATLAS Trigger System in 2015*, Eur. Phys. J. C **77** (2017) 317, arXiv: 1611.09661 [hep-ex] (cit. on p. 39).

[44] ATLAS Collaboration, *Real time data analysis with the ATLAS Trigger at the LHC in Run-2*, (2018), 8 pages, 23 figures, IEEE conference, URL: https://cds.cern.ch/record/2624583 (cit. on p. 40).

[45] ATLAS Collaboration, *Trigger Operation Public Results*, (2018), URL: https://twiki.cern.ch/twiki/bin/view/AtlasPublic/TriggerOperationPublicResults (cit. on p. 41).

[46] T. Sjöstrand, *The PYTHIA Event Generator: Past, Present and Future*, Comput. Phys. Commun. **246** (2020) 106910, arXiv: 1907.09874 [hep-ph] (cit. on p. 43).

[47] M. Bahr et al., *Herwig++ Physics and Manual*, Eur. Phys. J. C **58** (2008) 639, arXiv: 0803.0883 [hep-ph] (cit. on p. 43).

[48] T.Gleisberg, S. Hoeche, f. Krauss, M. Schoenherr, S. Schuamann, F. Siegert, J. Winter, *Event generation with SHERPA 1.1*, JHEP **02** (2009) 007, arXiv: 0811.4622 [hep-ph] (cit. on pp. 43, 48).

[49] S. Agostinelli, J. Allison, K. Amako and others, *Geant4—a simulation toolkit*, Nuclear Instruments and Methods in Physics Research Section A: Accelerators, Spectrometers, Detectors and Associated Equipment **506** (2003) 250, ISSN: 0168-9002, URL: http://www.sciencedirect.com/science/article/pii/S0168900203013688 (cit. on pp. 43, 48).

[50] S. Alekhin et al., *Proceedings, High-Precision α_s Measurements from LHC to FCC-ee: Geneva, Switzerland, October 2-13, 2015*, (2015), ed. by D. d'Enterria and P. Z. Skands, arXiv: 1512.05194 [hep-ph] (cit. on p. 45).

[51] S. FORTE, *PARTON DISTRIBUTIONS FUNCTIONS*, (2016), URL: http://nnpdf.mi.infn.it/wp-content/uploads/2017/10/freudenstadt-forte-2016.pdf (cit. on p. 46).

[52] M. Whalley, D. Bourilkov, and R. Group, *The Les Houches accord PDFs (LHAPDF) and LHAGLUE*, (2005) 575, arXiv: hep-ph/0508110 (cit. on p. 46).

[53] ATLAS Collaboration, *(Internal ATLAS Ref.) CentralMC15ProductionList*, (2018), URL: shorturl.at/gjmuB (cit. on p. 48).

[54] ATLAS Collaboration, *(Internal ATLAS note) Study of $\ell\ell + E_T^{miss}$ with proton-proton collisions at $\sqrt{s} = 13$ TeV in the HZZ group: introduction of common analysis strategies*, (2018), URL: https://cds.cern.ch/record/2646262 (cit. on p. 48).

[55] F. Caola, K. Melnikov, R. Röntsch, and L. Tancredi, *QCD corrections to ZZ production in gluon fusion at the LHC*, Phys. Rev. **D92** (2015) 094028, arXiv: 1509.06734 [hep-ph] (cit. on p. 48).

[56] T. Melia, P. Nason, R. Rontsch, and G. Zanderighi, *W+W-, WZ and ZZ production in the POWHEG BOX*, JHEP **11** (2011) 078, arXiv: 1107.5051 [hep-ph] (cit. on p. 49).

[57] J. Alwall et al., *The automated computation of tree-level and next-to-leading order differential cross sections, and their matching to parton shower simulations*, JHEP **07** (2014) 079, arXiv: 1405.0301 [hep-ph] (cit. on p. 49).

[58] Alwall, J. and Frederix, R. and Frixione, S. and Hirschi, V. and Maltoni, F. and Mattelaer, O. and Shao, H. -S. and Stelzer, T. and Torrielli, P. and Zaro, M., *The automated computation of tree-level and next-to-leading order differential cross sections, and their matching to parton shower simulations*, JHEP **07** (2014) 079, arXiv: 1405.0301 [hep-ph], URL: https://arxiv.org/pdf/1405.0301.pdf (cit. on p. 49).

[59] M. Grazzini, S. Kallweit, and M. Wiesemann, *Fully differential NNLO computations with MATRIX*, Eur. Phys. J. C **78** (2018) 537, arXiv: 1711.06631 [hep-ph] (cit. on pp. 50, 51, 120).

[60] J. Ohnemus and J. F. Owens, *Order-α_s calculation of hadronic ZZ production*, Phys. Rev. D **43** (11 1991) 3626, URL: https://link.aps.org/doi/10.1103/PhysRevD.43.3626 (cit. on p. 51).

[61] B. Mele, P. Nason and G. Ridolfi, *QCD radiative corrections to Z boson pair production in hadronic collisions*, (1991), URL: https://www.sciencedirect.com/science/article/pii/055032139190475D?via%3Dihub (cit. on p. 51).

[62] S. Kallweit, J. Lindert, S. Pozzorini, and M. Schönherr, *NLO QCD+EW predictions for $2\ell2\nu$ diboson signatures at the LHC*, JHEP **11** (2017) 120, arXiv: 1705.00598 [hep-ph] (cit. on pp. 51, 52, 105, 112).

[63] F. Caola, K. Melnikov, R. Röntsch, and L. Tancredi, *QCD corrections to ZZ production in gluon fusion at the LHC*, Physical Review D **92** (2015) (cit. on p. 51).

[64] B. Heinemann, S. Heim, J. Sabater, FY. Tsai, V. Goumarre, *(Unpublished) Studies of the theoretical uncertainties on the ZZ/Zy cross section ratio*, (2020) (cit. on pp. 53, 55–57).

[65] Lindert, J.M. and others, *Precise predictions for V+ jets dark matter backgrounds*, Eur. Phys. J. C **77** (2017) 829, arXiv: 1705.04664 [hep-ph] (cit. on pp. 54, 120).

[66] J. Butterworth et al., *PDF4LHC recommendations for LHC Run II*, J. Phys. G **43** (2016) 023001, arXiv: 1510.03865 [hep-ph] (cit. on p. 55).

[67] ATLAS Collaboration, *Track and vertex reconstruction in the ATLAS experiment*, Journal of Instrumentation **8** (2013) C02035, URL: https://doi.org/10.1088%2F1748-0221%2F8%2F02%2Fc02035 (cit. on p. 59).

[68] ATLAS Collaboration, *Performance of the ATLAS Track Reconstruction Algorithms in Dense Environments in LHC Run 2*, Eur. Phys. J. C **77** (2017) 673, arXiv: 1704.07983 [hep-ex] (cit. on p. 60).

[69] T. Cornelissen et al., *The new ATLAS track reconstruction (NEWT)*, Journal of Physics: Conference Series **119** (2008) 032014, URL: https://doi.org/10.1088%2F1742-6596%2F119%2F3%2F032014 (cit. on p. 60).

[70] T. G. Cornelissen et al., *Updates of the ATLAS Tracking Event Data Model (Release 13)*, (2007), URL: https://cds.cern.ch/record/1038095 (cit. on p. 61).

[71] ATLAS Collaboration, *Vertex Reconstruction Performance of the ATLAS Detector at $\sqrt{s}$ = 13 TeV*, (2015), URL: http://cds.cern.ch/record/2037717 (cit. on p. 61).

[72] ATLAS Collaboration, *Vertex Reconstruction in the ATLAS Experiment at the LHC*, (2009), Note was a proceeding for IEEE/NSS Dresden 2008 and is now intended for possible publication in TNS., URL: https://cds.cern.ch/record/1176154 (cit. on p. 62).

[73] ATLAS Collaboration, *Electron and photon performance measurements with the ATLAS detector using the 2015–2017 LHC proton-proton collision data*, Journal of Instrumentation **14** (2019) P12006, ISSN: 1748-0221, URL: http://dx.doi.org/10.1088/1748-0221/14/12/P12006 (cit. on pp. 62, 63).

[74] ATLAS Collaboration, *Electron and photon performance measurements with the ATLAS detector using the 2015–2017 LHC proton-proton collision data*, JINST **14** (2019) P12006, arXiv: 1908.00005 [hep-ex] (cit. on p. 62).

[75] ATLAS Collaboration, *Electron reconstruction and identification in the ATLAS experiment using the 2015 and 2016 LHC proton-proton collision data at $\sqrt{s}$ = 13 TeV*, Eur. Phys. J. C **79** (2019) 639, arXiv: 1902.04655 [physics.ins-det] (cit. on p. 64).

[76] ATLAS Collaboration, *Performance of pile-up mitigation techniques for jets in pp collisions at $\sqrt{s} = 8$ TeV using the ATLAS detector*, Eur. Phys. J. C **76** (2016) 581, arXiv: 1510.03823 [hep-ex] (cit. on p. 68).

[77] W. E. Cleland, E. G. Stern, *Signal processing considerations for liquid ionization calorimeters in a high rate environment*, (1993), URL: https://www.nevis.columbia.edu/~haas/documents/cleland_and_stern.pdf (cit. on p. 68).

[78] R. Atkin, *Review of jet reconstruction algorithms*, J. Phys. Conf. Ser. **645** (2015) 012008, ed. by A. S. Cornell and B. Mellado (cit. on p. 69).

[79] G. C. Blazey et al., *Run II jet physics*, (2000) 47, arXiv: hep-ex/0005012 (cit. on p. 70).

[80] ATLAS Collaboration, *Topological cell clustering in the ATLAS calorimeters and its performance in LHC Run 1*, Eur Phys J C (2017) (cit. on p. 71).

[81] ATLAS Collaboration, *Monte Carlo Calibration and Combination of In-situ Measurements of Jet Energy Scale, Jet Energy Resolution and Jet Mass in ATLAS*, (2015), URL: https://cds.cern.ch/record/2044941 (cit. on p. 72).

[82] ATLAS Collaboration, *ATLAS detector and physics performance: Technical Design Report, 1*, Technical Design Report ATLAS (1999), URL: https://cds.cern.ch/record/391176 (cit. on p. 72).

[83] ATLAS Collaboration, *Jet reconstruction and performance using particle flow with the ATLAS Detector*, Eur. Phys. J. C **77** (2017) 466, arXiv: 1703.10485 [hep-ex] (cit. on pp. 73, 74).

[84] S. Schramm, *Searching for Dark Matter with the ATLAS Detector in Events with an Energetic Jet and Large Missing Transverse Momentum*, (2015), Presented 26 Feb 2015, URL: https://cds.cern.ch/record/2014029 (cit. on p. 73).

[85] ATLAS Collaboration, *Jet energy scale measurements and their systematic uncertainties in proton-proton collisions at* $\sqrt{s} = 13$ TeV *with the ATLAS detector*, Phys. Rev. D **96** (7 2017) 072002, URL: https://link.aps.org/doi/10.1103/PhysRevD.96.072002 (cit. on pp. 73, 77).

[86] ATLAS Collaboration, *Jet energy scale and resolution measured in proton-proton collisions at* $\sqrt{s} = 13$ *TeV with the ATLAS detector*, (2020), arXiv: 2007.02645 [hep-ex] (cit. on pp. 75, 76).

[87] ATLAS Collaboration, *Jet energy resolution in 2017 data and simulation*, (2018), URL: https://atlas.web.cern.ch/Atlas/GROUPS/PHYSICS/PLOTS/JETM-2018-005/ (cit. on p. 79).

[88] ATLAS Collaboration, *Tagging and suppression of pileup jets with the ATLAS detector*, (2014), URL: https://cds.cern.ch/record/1700870 (cit. on p. 80).

[89] ATLAS Collaboration, *Selection of jets produced in 13TeV proton-proton collisions with the ATLAS detector*, (2015), URL: https://cds.cern.ch/record/2037702 (cit. on pp. 81, 102).

[90] ATLAS Collaboration, *Commissioning of the ATLAS b-tagging algorithms using* $t\bar{t}$ *events in early Run-2 data*, (2015), URL: http://cds.cern.ch/record/2047871 (cit. on p. 81).

[91] ATLAS Collaboration, *Recommendations of the Physics Objects and Analysis Harmonisation Study Groups 2014*, (2014), URL: https://cds.cern.ch/record/1700874 (cit. on p. 82).

[92] ATLAS Collaboration, E_T^{miss} *performance in the ATLAS detector using 2015-2016 LHC p-p collisions*, (2018), URL: https://cds.cern.ch/record/2625233 (cit. on pp. 83, 92, 94).

[93] Lampl, W and Laplace, S and Lelas, D and Loch, P and Ma, H and Menke, S and Rajagopalan, S and Rousseau, D and Snyder, S and Unal, G, *Calorimeter Clustering Algorithms: Description and Performance*, (2008), URL: http://cds.cern.ch/record/1099735 (cit. on p. 83).

[94] E. Bagnaschi, M. Cacciari, A. Guffanti, and L. Jenniches, *An extensive survey of the estimation of uncertainties from missing higher orders in perturbative calculations*, JHEP **02** (2015) 133, arXiv: 1409.5036 [hep-ph] (cit. on p. 84).

[95] P. Berta, M. Spousta, D. W. Miller, and R. Leitner, *Particle-level pileup subtraction for jets and jet shapes*, JHEP **06** (2014) 092, arXiv: 1403.3108 [hep-ex] (cit. on p. 84).

[96] ATLAS Collaboration, *Performance of Missing Transverse Momentum Reconstruction in Proton-Proton Collisions at 7 TeV with ATLAS*, Eur. Phys. J. C **72** (2012) 1844, arXiv: 1108.5602 [hep-ex] (cit. on p. 84).

[97] ATLAS Collaboration, *Performance of algorithms that reconstruct missing transverse momentum in $\sqrt{s} = 8$ TeV proton-proton collisions in the ATLAS detector*, Eur. Phys. J. C **77** (2017) 241, arXiv: 1609.09324 [hep-ex] (cit. on p. 84).

[98] ATLAS Collaboration, *Performance of missing transverse momentum reconstruction with the ATLAS detector using proton-proton collisions at $\sqrt{s} = 13$ TeV*, Eur. Phys. J. C **78** (2018) 903, arXiv: 1802.08168 [hep-ex] (cit. on p. 84).

[99] TJ Khoo, *(talk) Missing transversE momenTum*, (2016), URL: https://indico.cern.ch/event/565211/contributions/2293331/attachments/1347838/2033199/SWTut_070616.pdf (cit. on p. 85).

[100] P. Z. Skands, *Tuning Monte Carlo Generators: The Perugia Tunes*, Phys. Rev. D **82** (2010) 074018, arXiv: 1005.3457 [hep-ph] (cit. on p. 86).

[101] ATLAS Collaboration, *Measurement of the Z/γ^* boson transverse momentum distribution in pp collisions at $\sqrt{s} = 7$ TeV with the ATLAS detector*, JHEP **09** (2014) 145, arXiv: 1406.3660 [hep-ex] (cit. on p. 86).

[102] ATLAS Collaboration, *Object-based missing transverse momentum significance in the ATLAS detector*, (2018), URL: https://cds.cern.ch/record/2630948 (cit. on p. 89).

[103] ATLAS Collaboration, *Missing transverse momentum performance using the full run 2 pp data at 13 TeV*, (2019), URL: https://atlas.web.cern.ch/Atlas/GROUPS/PHYSICS/PLOTS/JETM-2019-03/ (cit. on pp. 97, 98).

[104] Balthasar Schachtner, *Search for electroweak production of supersymmetric particles with the LHC experiment ATLAS at high luminosities*, (2014), URL: https://www.etp.physik.uni-muenchen.de/publications/theses/download/master_bschachtner.pdf (cit. on p. 100).

[105] Le, My Phuong, *Searches for new physics at colliders*, (2011) (cit. on p. 100).

[106] ATLAS Collaboration, *(Internal ATLAS note) Search for an additional heavy Higgs boson in the $H \to ZZ \to ll\nu\nu$ final state in pp collisions at $\sqrt{s} = 13$ TeV with the ATLAS detector*, (2015), Authors: The ll+MET HZZ group, URL: https://cds.cern.ch/record/2058243 (cit. on p. 101).

[107] ATLAS Collaboration, *Public Egamma Trigger Plots for Collision Data*, (), URL: https://twiki.cern.ch/twiki/bin/view/AtlasPublic/EgammaTriggerPublicResults (cit. on p. 102).

[108] *Data Preparation Check List For Physics Analysis*, (2011), URL: https://twiki.cern.ch/twiki/bin/view/Atlas/DataPreparationCheckListForPhysicsAnalysis (cit. on p. 101).

[109] ATLAS Collaboration, *Luminosity determination in pp collisions at $\sqrt{s} = 13$ TeV using the ATLAS detector at the LHC*, (2019), URL: https://cds.cern.ch/record/2677054 (cit. on p. 102).

[110] ATLAS Collaboration, *The new LUCID-2 detector for luminosity measurement and monitoring in ATLAS*, Journal of Instrumentation **13** (2018) P07017, URL: https://doi.org/10.1088%2F1748-0221%2F13%2F07%2Fp07017 (cit. on p. 102).

[111] ATLAS Collaboration, *Measurement of the $Z(\to \ell^+\ell^-)\gamma$ production cross-section in pp collisions at $\sqrt{s} = 13$ TeV with the ATLAS detector*, JHEP **03** (2020) 054, arXiv: 1911.04813 [hep-ex] (cit. on pp. 108, 116, 117, 120).

[112] ATLAS Collaboration, *(Internal ATLAS note) Measurement of the $Z\gamma$ cross-section in pp collisions at $\sqrt{s} = 13$ TeV with the ATLAS Detector*, (2018), URL: https://cds.cern.ch/record/2644987 (cit. on pp. 117, 122).

[113] ATLAS Collaboration, *Measurements of inclusive and differential fiducial cross-sections of $t\bar{t}\gamma$ production in leptonic final states at $\sqrt{s} = 13$ TeV in ATLAS*, Eur. Phys. J. C **79** (2019) 382, arXiv: 1812.01697 [hep-ex] (cit. on p. 117).

[114] ATLAS Collaboration, *(Internal ATLAS note) Search for heavy resonances in the $H' \to ZZ \to \ell\ell\nu\nu$ channel with proton-proton collisions at $\sqrt{s} = 13$ TeV for 2015-2018 data with the ATLAS detector*, (2018), URL: https://cds.cern.ch/record/2646258 (cit. on pp. 131, 132, 135, 138–140, 143).

[115] L. Lista, *Practical Statistics for Particle Physicists*, (2017) 213, arXiv: 1609.04150 [physics.data-an] (cit. on p. 133).